Positive Contrast Magnetic Resonance Imaging with Multifunctionalised Magnetic Nanoparticles

Krueger, Dirk

Awarding institution:
King's College London

Positive Contrast Magnetic Resonance Imaging with Multifunctionalised Magnetic Nanoparticles

Dirk Krüger

A dissertation submitted in partial fulfilment of the requirements for the degree of

Doctor of Philosophy

of

King's College London

Division of Imaging Sciences & Biomedical Engineering

Faculty of Life Sciences & Medicine

London, United Kingdom, 2018

Acknowledgements

I would like to express my sincerest gratitude to my supervisor Prof. René Botnar for the continuous support and patience. Working with René has truly been a pleasure and a very enriching experience.

I am very thankful for my colleagues from the Botnar lab, in a particular Dr. Silvia Lorrio Gonzalez. Their support, advice and collaborative attitudes were a huge motivation. Their passion for research is inspiring.

I would like to thank both my examiners for their insightful discussions and comments that helped improve this work considerably.

Finally, I would like to thank my mother for her love and continuous support. What she has given me goes beyond what I thought possible. She is a true inspiration and none of my achievements would have been possible without her.

In loving memory of my grandparents Ewald & Frida Krüger.

Abstract

Superparamagnetic iron oxide nanoparticles (SPIONs) are used in many biomedical applications such as drug delivery, as therapeutic agent for hyperthermia treatment and contrast agent for molecular magnetic resonance imaging (MRI). Apart from the synthesis of novel SPIONs there have been technical developments such as new MRI pulse sequences for positive contrast imaging. The most prominent are GRadient-echo Acquisition for Superparamagnetic particles with Positive contrast (GRASP), Inversion Recovery with ON-resonant water suppression (IRON) and Susceptibility Gradient Mapping (SGM).

Four novel SPIONs of different sizes, coatings and surface charges were assessed in terms of their application as MR contrast agents. The r_2 and r_2^* relaxivities in water and breast cancer cells were investigated *in vitro* and the effects on the relaxivity when SPIONs move from a free to a bound state were described. The most promising SPION was also investigated in vivo with a multi echo gradient-echo sequence and a range of positive contrast imaging techniques. For the GRASP and IRON technique a dynamic preparation phase was devised to optimise the positive contrast imaging parameters. We developed a novel positive contrast imaging technique based on the Dixon multi echo sequence for improved SPION visualisation and quantification. The Dixon positive contrast technique was compared to already established techniques such as GRASP, IRON and SGM. Finally, it was determined that fat suppression with Dixon is superior to SPIR for positive contrast imaging with the IRON technique.

Overall, this work makes a contribution to the development of novel SPIONs for nanotheranostic applications. In particular, new developments for positive contrast imaging with SPIONs are presented that could further improve the usability of these techniques in future diagnostic applications.

Table of Contents

1. Introduction

1.1. Multimodal Nanotheranostic Approach

The most essential factors in the battle against cancer are early detection and effective treatment options [1]. Currently, anti-cancer drugs have severe limitations such as poor biodistribution and pharmacokinetics [2]. Combination of diagnostic (e.g. contrast agent for medical imaging modality) and therapeutic (e.g. anti-cancer drug) agents in one multifunctional unit is referred to as nanotheranostics [2]–[4]. Ideally, theranostic nanoparticles should be able to selectively accumulate in the tumour, enable early tumour detection, deliver anti-cancer drugs of therapeutic doses, and be biodegradable and biocompatible [1]. Nanotheranostics can be used to assess biodistribution and accumulation at the target site, monitor release of the anti-cancer drug, enhance therapeutic efficacy, and predict the therapeutic response [2].

Superparamagnetic iron oxide nanoparticles (SPIONs) are well suited for theranostic purposes. They have large surface areas to form SPION-conjugates and are good MR and multi-modal imaging contrast agents [5], [6]. SPIONs are subject to opsonisation *in vivo* where salts, proteins, and cells bind to the SPION surface leading to recognition by the mononuclear phagocytic system (MPS) and eventually clearance from the blood stream. In particular macrophages in the liver, bone marrow, and spleen are responsible for removal of SPIONs from the circulation [7]. Surface modification by poly(ethyleneglycol) (PEG) coating provides stealth characteristics which limit phagocytosis. In order to deliver a drug, it can be loosely attached to the coating through physical interactions or covalently bound to the surface with a linker molecule [8]. Alternatively, SPIONs can be encapsulated into nanocarriers together with anti-cancer drugs for a theranostic cancer strategy [9].

The accumulation of the theranostic particles in the tumour through the enhanced permeability and retention (EPR) effect (leaky neovasculature at the tumour site) [10] is referred to as passive targeted delivery [11]–[17]. The cellular uptake primarily happens via micropinocytosis [18], [19]. This target strategy depends heavily on the neovascularisation of the tumour. However, the vascularisation of a tumour is highly heterogeneous. It depends on the tumour type, location, and disease state, as well as the patient. This makes tumour targeting via the EPR effect an inconsistent phenomenon [20], [21].

Through the attachment of ligands to the surface of the theranostic particle targeting can be improved (active targeting approach). Specific ligands bind to overexpressed receptors at angiogenic endothelial or cancer cells [22], [23]. These ligands promote cell internalisation of

the theranostic particle via receptor mediated endocytosis [3], [24] which leads to an increased cellular uptake [25], [26]. This improves anti-cancer efficacy by shifting the nanoparticle intratumour distribution from the extracellular to the intracellular compartment [27], [28]. Popular targeting ligands for cancer cells are the folate receptor [29]–[32] and the RGD peptide [33]–[35] that binds to $\alpha_v\beta_3$ integrin [36], [37].

An alternative to passive and active targeting is stimuli-mediated targeting where the drug carrier releases its content as a result to an external stimulus [38]–[40]. The tumour microenvironment has a pH that is lower than the normal physiological pH [41]. This phenomenon can be used for acid triggered drug release [42], [43]. SPIOs exposed to an alternating magnetic field (AMF) are able to absorb this energy and convert it into heat [6], [26]. Cancer tissue has a higher sensitivity to heat than healthy tissue. Therefore, SPIOs can be used for hyperthermia treatments to destroy cancerous tissue through the localised application of heat. Hyperthermia has been investigated in several pre-clinical studies [44], [45] and clinical trials [46], [47]. Ultrasound can be used for the disruption of the blood-brain barrier, permeabilisation of tissue membranes, extravasation of carriers, triggering of temperature-depending drug release, and the ablation of tumour tissue [48]–[51]. Another strategy uses an external magnetic field to accumulate the superparamagnetic theranostic probes at the tumour [25], [52]–[57].

In addition to the above targeting strategies, it is also possible to combine these to create multifunctional platforms. Popular combinations are active and acid-triggered drug release [58] and magnetic targeting combined with hyperthermia using SPIOs [59]. Instead of hyperthermia, magnetic targeting has also been successfully combined with ultrasound to open the blood-brain barrier and deliver the therapeutic agent [60]. Photodynamic therapy (PDT) is the accumulation of a drug containing a photosensitiser at the tumour cells where the drug becomes activated upon radiation with light. Combining active targeting and PDT increases specificity thereby decreasing the damage to normal tissue from the latter [61], [62]. Further combinations reported in the literature are active and magnetic targeting [63], magnetic targeting and PDT [64], and photothermic therapy which is the local heating of cancer tissue caused by near infrared light resulting in hyperthermia-induced destruction of cancer cells [54], [65], [66].

Most in vivo data in the literature only focuses on diagnostic or therapeutic efficacy of theranostics [67]. Those studies that show efficacy for both, diagnostic and therapeutic purposes, are often using a combination of targeting strategies. Theranostic probes using SPIOs have limitations that result in challenges for *in vivo* applications and the translation into the clinic. These limitations are inappropriate biodistribution [68], [69], formulation challenges (i.e.

high manufacturing costs and complexity of production) [70], [71], and opposing concentrations and time lines for diagnostic and therapeutic probes [72]. The main challenge is certainly poor tumour accumulation in vivo that leads to difficulties for the imaging and anti-tumour efficacy. By combining different targeting strategies in a single nanoprobe, the limitations of each individual strategy can be overcome which is called a multimodal nanotheranostic approach.

1.2. Aims

- To investigate and compare different novel SPIONs in terms of their suitability as MRI contrast agents (relaxivities) with respect to their chemical nature. R_2 and R_2^* can be used to differentiate between free and cell-bound SPIONs by MRI as demonstrated elsewhere. The aim of the present work was to extent this approach to five SPIONs by investigating the ability to differentiate whether a particular particle is cell-bound or free by MRI.
- Assess the most promising new SPION *in vivo* in tumour-bearing mice and compare it their imaging characteristics with quantitative T_2^* mapping and susceptibility gradient mapping.
- Investigate different new SPIONs in terms of their ability to produce positive contrast with several well established positive contrast techniques (i.e. GRASP, IRON, SGM).
- Devise and develop dynamic preparation phase for GRASP and IRON to optimise the positive contrast imaging parameters.
- Implement and assess a novel positive contrast technique based on the Dixon method and compare it to established positive contrast techniques.
- Investigate an effective fat suppression technique that can be combined with an off-resonance imaging technique to allow *in vivo* positive contrast imaging without interference from fat signal.

1.3. Thesis Overview

Chapter 2 is an overview of the MR physics starting with a description of the nuclear magnetic resonance phenomenon, its quantum-mechanical origin and a practical description using classical mechanics (i.e. Bloch equations) for the understanding of the signal generation. The radiofrequency excitation of spins and their relaxation properties are discussed in the laboratory and rotating frame of reference. This chapter furthermore describes signal acquisitions methods such as spin echo and gradient-echo acquisitions. Finally, signal encoding and a brief introduction to k-space are provided.

Chapter 3 reviews established methods for T_1 and T_2 mapping. For the former, basic inversion and saturation recovery techniques are described. The focus is on the inversion recovery techniques, specifically the Look-Locker sequence. Developments of the Look-Locker such as MOLLI, ShMOLLI, Look-Locker-EPI and FLASH are reviewed. This chapter also described important T_2 mapping sequences such as multi echo spin-echo sequences, DESPOT2 and the T_2prep.

Chapter 4 reviews established positive contrast imaging techniques. Popular sequences are the GRadient-echo Acquisition for Superparamagnetic particles with Positive contrast (GRASP or whiter marker imaging), Inversion Recovery with ON-resonant water suppression (IRON) and Susceptibility Gradient Mapping (SGM) which is a postprocessing technique. Another method described uses a balanced steady-state free precession (b-SSFP) sequence for positive contrast imaging which is called Fast Low Angle Positive contrast Steady-state free precession (FLAPS).

Chapter 5 provides an overview of the background of superparamagnetic iron oxide nanoparticles (SPIONs). These inorganic particles have been intensely investigated in the past 20 years as MRI contrast agents. This chapter will introduce the different types of magnetisation in the context of superparamagnetism and molecular structures of iron oxides, their synthesis and stabilisation strategies. The main part of this chapter will review the biomedical applications of SPIONs via passive and active targeting routes with an emphasis on cancer and cardiovascular application.

Chapter 6 describes my own work on the implementation of two established positive contrast sequences (GRASP and IRON). The changes made to the Philips GOAL-C pulse programming environment are described in detail. The implemented sequences were tested and the scan parameter evaluation and optimisation is discussed.

Chapter 7 describes my own work on the implementation of the Dixon technique as a positive contrast imaging technique. I describe the optimisation in a phantom study of different SPION concentrations. The Dixon positive contrast method was compared with other more established positive contrast techniques such SGM, GRASP and IRON. In addition to utilising Dixon as a positive contrast imaging technique, I have investigated its capability as a fat suppression technique on IRON images and compared those results to fat suppression using spectral pre-saturation with inversion recovery (SPIR).

Chapter 8 describes my own work on the characterisation (i.e. the T_1, T_2 and T_2^* mapping for relaxivity determination) of 24 novel iron-oxide nanoparticles and a comparison in terms of their application as MRI contrast agents. These nanoparticles were developed by the MultiFun project and synthesised by collaborators. For comparison, four commercial samples were also evaluated. Furthermore, it has been reported in the literature that R_2 and R_2^* mapping can be used to differentiate between free and cell-bound SPIONs by MRI. In this *in vitro* study I reproduce and extend these results with our novel iron-oxide nanoparticles.

Chapter 9 describes my own on the investigation of two SPIONs, ferumoxytol (commercial sample) and MF66-PEG *in vivo* in a mouse model of cancer. Both SPIONs were compared for their abilities to produce negative contrast using a gradient echo sequence and positive contrast using SGM as a post-processing technique.

Chapter 10 is a discussion chapter on the general role and novel aspects of the thesis within the field.

Chapter 11 presents a concise conclusion of this thesis.

2. Introduction to Magnetic Resonance Imaging

2.1. History of Magnetic Resonance Imaging

The history of magnetic resonance imaging (MRI) can be traced back to Wolfgang Pauli [73], one of the great physicists of the 20th century. Pauli helped in the discovery of the neutrino and discovered the quantum mechanical exclusion principle for which he was awarded the Nobel Prize for physics in 1945 [74]. In 1924 Pauli noticed irregularities in spectra on which basis he suggested that atomic nuclei must possess a magnetically related spin property [73]. Following Pauli's assumption, Isidor Rabi used varying fields to influence magnetic resonance in gases which proved the existence of magnetic spin in 1938 [75]. He was honoured with the Nobel Prize for physics in 1944 [76]. Two years later in 1946, Edward Mills Purcell and Felix Bloch independently discovered that the nuclear magnetic resonance (NMR) effect [77], [78] described by Rabi could also be observed in solids for which they shared the 1952 Nobel Prize in physics [79]. The discovery of Purcell and Bloch was monumental as it allowed the study of NMR of different materials and biological samples. More than 20 years later in 1971, Raymond Damadian measured relaxation times on tumours and found that the spin-spin relaxation time was longer in tumours than in healthy tissue [80]. This made the scientific community aware of the fact that NMR could potentially have a use in medical diagnostics. In 1974, Paul Lauterbur thought of the concept of using magnetic field gradients in all three orthogonal directions in addition to the static magnetic field to have a slightly different magnetic field strength at each position in the sample under investigation [81]. One year later in 1975, Richard Ernst showed how data sets from various volume elements could be acquired at the same time which would lead to a complex mix of frequencies and how to use a Fourier transform to extract different frequency components [82]. The Fourier transform is central to the development of MRI. It is a mathematical approach invented by Jean Baptiste Joseph Fourier in the early 1880's. The Fourier transform allows the dissection of a signal that is oscillating in the time domain into its frequency components [83]. It was finally Peter Mansfield who developed the right mathematical approaches to produce an image from NMR signals [84]. So it was really Lauterbur, Mansfield and Ernst who transformed the NMR phenomenon into the medical imaging device that is an essential part of today's medical diagnostics. Lauterbur and Mansfield were honoured in 2003 with the Nobel Prize in medicine for their discoveries concerning magnetic resonance imaging [85].

2.2. Nuclear Magnetic Resonance

"Nuclear magnetic resonance (NMR) is the study of magnetic properties and energies of nuclei" [86] which are the building blocks of matter. The structure of matter is described with quantum

mechanics. However, magnetic resonance imaging is concerned with human bodies that represent a huge number of nuclei that behave collectively [87]. Therefore, this work will wherever possible use classical vector mechanics to gain the required understanding of the processes involved.

2.2.1. Nuclear Spin

Matter is made up of molecules that are built from atoms. Every atom has a nucleus consisting of protons and neutrons. The nucleus is surrounded by electrons that sit in so-called orbitals. Electrons are pure primary particles that cannot be further subdivided whereas protons and neutrons are made up of even smaller particles called quarks. But for the description of the NMR phenomenon, it is sufficient to remain at the nuclear level. Every nucleus with an odd atomic number (number of protons) and/or an odd atomic mass (sum of protons and neutrons) possesses a spin. The concept of the spin property of nuclei which enables Magnetic Resonance Imaging is not only difficult but also highly abstract. Spin is a quantum mechanical property and it may well be that humans are incapable of understanding the full depth of quantum mechanics. However, nuclear spins can be thought about in a physical and geometrical way and such a classical viewpoint allows understanding the majority of MRI concepts. Classically, the nuclear spin can be imagined as a physical rotation of the nucleus which is why it is often referred to as spin angular momentum $\vec{S}$. Both names, nuclear spin and spin angular momentum, are interchangeable. In that sense it can be thought of as a sphere of electromagnetic charge that is spinning about its own axis as shown in figure 1. According to classical electromagnetism, this will create a current loop that gives rise to a magnetic dipole moment [87], [88].

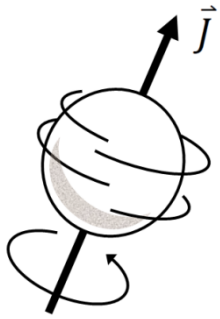

Figure 1: Illustration of a nucleus as a sphere rotating about its own axis with nuclear angular momentum $\vec{J}$ (reproduced from Liang and Lauterbur [87], p. 59).

2.2.2. Nuclear Magnetic Dipole Moment

Every nucleus has a nuclear angular momentum $\vec{J}$ that is made up of two contributions. One stems from orbital motion $\vec{L}$ and one stems from the intrinsic spin or spin angular momentum $\vec{S}$.

$$\vec{J} = \vec{L} + \vec{S} \tag{1}$$

The magnitude of the spin angular momentum is defined with a spin quantum number s that can be an integer or half-integer value.

$$S = \hbar\sqrt{s(s+1)} \tag{2}$$

In equation (2) the constant $\hbar$ is the Planck constant divided by 2π, $\hbar = \frac{h}{2\pi}$. Every nucleus that has a spin can be seen as a particle with electric charge that rotates around its own axis (figure 1). According to classical electromagnetism, a spinning charged object creates a magnetic field. Such a microscopic magnetic field has a direction (left-hand rule) which is represented by the nuclear magnetic dipole moment $\vec{\mu}$. The magnetic moment is related to the spin angular momentum $\vec{S}$ according to equation (3).

$$\vec{\mu} = \gamma\vec{S} \tag{3}$$

The proportionality constant is the gyromagnetic ratio and it depends on the nucleus. It can be positive or negative. If the gyromagnetic ratio is positive so is the magnetic moment parallel to the spin angular momentum. A negative gyromagnetic ratio means that magnetic moment and spin angular momentum have an antiparallel position to each other. For hydrogen, the most important nucleus in MRI applications, the gyromagnetic ratio is $\frac{\gamma}{2\pi} = 42.58\ MHz/T$. By combining equations (2) and (3), the magnitude of the magnetic moment is defined as

$$\mu = \gamma\hbar\sqrt{s(s+1)} \tag{4}$$

The nuclear spin quantum number can take integer and half-integer values, $= 0, \frac{1}{2}, 1, \frac{3}{2}, 2, \frac{5}{2}, \ldots$. Only nuclei with $s \neq 0$ possess the NMR phenomenon. Hydrogen has a nuclear spin quantum number of $\frac{1}{2}$. That is determined by a set of quantum mechanical rules where it is described that nuclei with an odd mass number have half-integer spins. Equation (4) determines the magnitude of the magnetic dipole moment but its orientation in space is completely random at thermal equilibrium as shown in figure 2 [87].

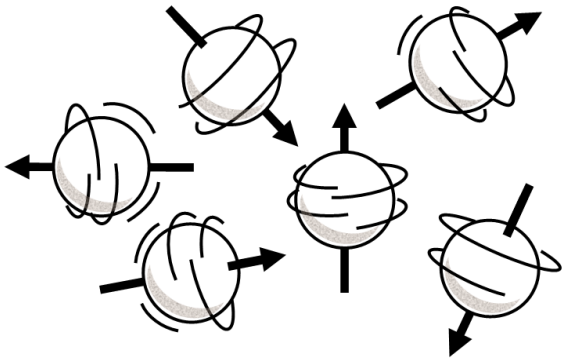

Figure 2: Random spatial orientation of dipole moments each associated with a spinning nucleus (reproduced from Liang and Lauterbur [87], p. 62).

2.2.3. Magnetisation

A spin system in MRI is the entity of all spins of the same type (e.g. spin of hydrogen atom) in a sample. Those spins with the same resonance frequency (i.e. spins in the same tissue that have the same chemical environment) are called an isochromat. All the magnetic dipole moments of a spin system cancel each other out macroscopically and no net magnetisation is observed. However, a net macroscopic magnetisation vector $\vec{M}$ can be defined that will take values other than zero when an external magnetic field of strength B_0 is applied. A spin system with N_s spins where $\vec{\mu}_n$ is the nth nuclear spin, $\vec{M}$ is the sum of the magnetic moments of all nuclei in the sample.

$$\vec{M} = \sum_{n=1}^{N_s} \vec{\mu}_n \tag{5}$$

In the presence of a static magnetic field of strength B_0 that has a direction, the individual spin vectors start to align with the magnetic field lines and macroscopic magnetism is observed. The three orthogonal directions in space are referred to as x-, y-, and z-direction. This is called the laboratory frame of reference with the unit directional vectors $\vec{\imath}, \vec{\jmath}$, and $\vec{k}$. At thermal equilibrium the z-component of the spin angular momentum $\vec{S}$ is given by $S_z = m_s\hbar$. The z-component of the magnetic moment is then

$$\mu_z = \gamma m_s \hbar \tag{6}$$

In equation (6), m_s is called the magnetic or azimuthal quantum number that can have $2s + 1$ values, $m_s = -s, -s+1, \dots, s-1, s$. For a proton with 'spin one-half', which means $s = \frac{1}{2}$ and $m_s = \pm\frac{1}{2}$ there are two possible orientations for μ_z, pointing up (parallel to $\vec{B}_0$) or pointing down (antiparallel to $\vec{B}_0$). If no external magnetic field is present, then all $2s + 1$ energy states with the same spin quantum number s but different magnetic quantum numbers m_s have the same energy (degeneracy). However, with an external magnetic field present, the magnetic moment can only take discrete values which lead to discrete energy levels of the two different orientations given by

$$E = -\vec{\mu}\,\vec{B}_0 = -\mu_z B_0 = -\gamma\hbar m_s B_0 \tag{7}$$

Substituting the magnetic quantum number into equation (7) leads to

$$m_s = \frac{1}{2}\ (spin\ up\ \uparrow): \qquad E_\uparrow = -\frac{1}{2}\gamma\hbar B_0 \tag{8}$$

$$m_s = -\frac{1}{2}\ (spin\ down\ \downarrow): \qquad E_\downarrow = \frac{1}{2}\gamma\hbar B_0 \tag{9}$$

The energy difference between the two orientations can be calculated to $\Delta E = E_\downarrow - E_\uparrow = \gamma\hbar B_0$. The splitting of nuclear energy under the application of an external magnetic field is called the Zeeman splitting. In the case of a hydrogen nucleus, the degeneracy turns into two energy levels

in which the spin up (parallel) orientation is the lower energy state and therefore more likely (figure 3).

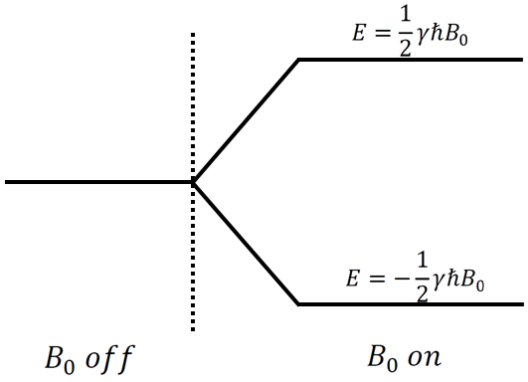

Figure 3: Zeeman splitting of a system with spin $\frac{1}{2}$ such as that of a hydrogen nucleus (reproduced from Liang and Lauterbur [87], p. 65).

Thermal energy is responsible for some of the spins to overcome the energy separation and also occupy the spin down (antiparallel) position. The magnitude of the Zeeman splitting depends on the difference in spin population which is given by the Boltzmann relationship.

$$\frac{N_\uparrow}{N_\downarrow} = e^{\Delta E/kT} \tag{10}$$

In equation (10), N is the number of spins in the up (↑) or down (↓) position, T is the absolute temperature in Kelvin and k is the Boltzmann constant $(1.38 \times 10^{-23} J/K)$. According to equation (10), there are $\frac{\gamma\hbar B_0}{4\pi kT}$ more spins in the lower and more stable energy state. This difference in population gives rise to the measurable net magnetisation $\vec{M}$ that points along the direction of $\vec{B}_0$.

$$\begin{aligned}\vec{M} = M_x\vec{\imath} + M_y\vec{\jmath} + M_z\vec{k} &= \left(\sum_{n=1}^{N_s}\mu_{x,n}\right)\vec{\imath} + \left(\sum_{n=1}^{N_s}\mu_{y,n}\right)\vec{\jmath} + \left(\sum_{n=1}^{N_s}\mu_{z,n}\right)\vec{k} \\ &= \left(\sum_{n=1}^{N_s}\mu_{z,n}\right)\vec{k} = \left(\sum_{n=1}^{N_\uparrow}\frac{1}{2}\gamma\hbar - \sum_{n=1}^{N_\downarrow}\frac{1}{2}\gamma\hbar\right)\vec{k} \\ &= \frac{1}{2}(N_\uparrow - N_\downarrow)\gamma\hbar\vec{k} = \frac{\gamma^2\hbar^2 B_0 N_s}{4kT} = M_z^0\end{aligned} \tag{11}$$

The transverse terms of $\vec{\mu}_n$ are zero because of random phase distribution of the precessing magnetic dipole moments [87], [88].

2.2.4. Free Precession and Larmor Frequency

According to classical mechanics, the nuclear magnetic dipole vector $\vec{\mu}$ will experience a torque when placed in a magnetic field which equals the rate of change of its angular momentum.

$$\frac{d\vec{S}}{dt} = \vec{\mu} \times B_0 \vec{k} \tag{12}$$

With equation (3), equation (12) can be written as

$$\frac{d\vec{\mu}}{dt} = \gamma \vec{\mu} \times B_0 \vec{k} \tag{13}$$

Equation (13) is a first-order differential equation that has the following solutions.

$$\mu_{xy}(t) = \mu_{xy}(0) e^{-i\gamma B_0 t} \tag{14}$$

$$\mu_z(t) = \mu_z(0) \tag{15}$$

Equations (14) and (15) are the mathematical descriptions of a precessional motion in z-direction of $\vec{\mu}$ about the $\vec{B}_0$ field direction as shown in figure 4. The angular frequency of the nuclear precession is called the Larmor frequency ω_0 and it is a central quantity in MRI.

$$\omega_0 = \gamma B_0 \tag{16}$$

The Larmor frequency is important because the net magnetisation vector $\vec{M}$ precesses at that frequency. It depends on the gyromagnetic ratio γ, which is a constant unique to every nuclei, and the static magnetic field strength B_0 [87], [88].

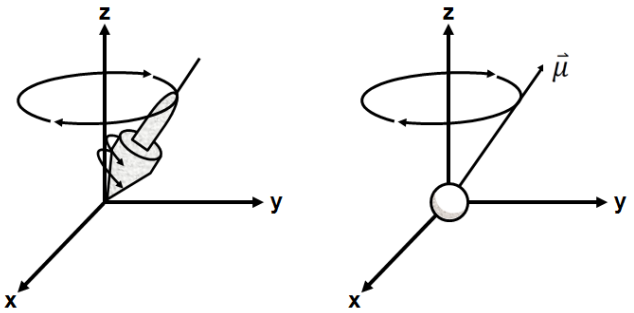

Figure 4: Illustration of the precessional motion of $\vec{\mu}$ about the $\vec{B}_0$ which can be compared to the wobbling of a spinning top under the influence of the gravitational field of the earth (reproduced from Liang and Lauterbur [87], p. 62).

2.2.5. Bloch Equation

The net magnetisation vector $\vec{M}$ changes with time when in addition to the static magnetic field $\vec{B}_0$ a second short-lived magnetic field $\vec{B}_1(t)$ is applied. The next section will discuss $\vec{B}_1(t)$ fields in more detail. However, there is a central equation in MRI that describes the dynamics of nuclear magnetisation called the Bloch equation.

$$\frac{d\vec{M}}{dt} = \gamma \vec{M} \times \vec{B} - \frac{M_x \vec{\imath} + M_y \vec{\jmath}}{T_2} - \frac{(M_z - M_z^0)\vec{k}}{T_1} \tag{17}$$

In equation (17), $\vec{\imath}$, $\vec{\jmath}$, and $\vec{k}$ are unit vectors in x-, y-, and z-direction, respectively. The exponential terms in the Bloch equation are approximations to represent what is observed. The

time constants T_1 and T_2 will be discussed in more detail below. They demonstrate that the magnetisation changes as a function of time [87], [88].

2.2.6. Radiofrequency Excitation

The resonance phenomenon is central to the description of MRI. Resonance is the achievement of phase coherence among the spins in a particular spin system that is precessing in a random fashion. In order to achieve phase coherence, an oscillating, time-dependent, magnetic field $\vec{B}_1(t)$ is used. Such a magnetic field is referred to in the literature as a radiofrequency (rf) field. Other names include rf excitation, rf pulse, or $\vec{B}_1$ field. The radiofrequency field described by classical mechanics can be pictured as rotating equally to the precessing spins. According to quantum mechanics, an oscillating magnetic field of energy $E_{rf} = \hbar\omega_{rf}$ can transfer spins between energy states if E_{rf} is equal to the difference in energy between the two spin states $\hbar\omega_{rf} = \Delta E = \gamma\hbar B_0$. Such a transition can establish coherence. From that follows the resonance condition which simply says that the Larmor frequency ω_0 is equal to the frequency of the radiofrequency field ω_{rf}.

2.2.6.1. Rotating Frame of Reference

So far a static orthogonal axes system was used for the description of the behaviour of various vector quantities in space. This was called the *laboratory reference frame*. Before starting the explanation of rf excitations, the *rotating reference frame* shall be introduced. It offers conceptual simplicity in describing rf excitations of a spin system. Spins align with a static magnetic field and a constant precession of the spins about that field results. Precession can also be understood as a rotation. Any magnetic moment that interacts with a magnetic field undergoes an instantaneous rotation. Of particular interest in MRI is the application of a short-lived rf field perpendicular to the static magnetic field. Such an rf field is capable of tipping the aligned spins in the transverse plane or in fact by any angle with respect to the static magnetic field. The rotating reference frame consists of three orthogonal axes but in comparison to the laboratory frame is rotating about an axis at angular frequency ω. In the easiest case the rotation is about one of the three orthogonal axes. In figure 5a, the laboratory and rotating reference frames are shown from the perspective of the positive z-axis. The rotating frame of reference is rotating clockwise about the z-axis which is also the direction of the static magnetic field $\vec{B}_0$S.

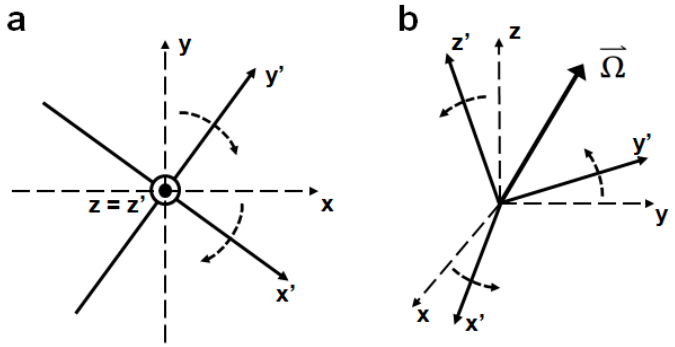

Figure 5: Laboratory and rotating reference frames. a: Perspective from and rotation about the z-axis. b: Rotation about an arbitrary axis (reproduced from Brown et al. [89], p. 38f).

The rotating reference frame can also rotate about any arbitrary axis as shown in figure 5b. A rotational angular velocity vector $\vec{\Omega}$ can be defined where the rotation is about the vector direction of $\vec{\Omega}$. The magnitude of this vector is the angular speed of rotation. A vector $\vec{C}$ that is rotating in the laboratory reference frame with angular frequency ω can be defined. Such a vector will be fixed in the rotating reference frame which will make the discussion of certain concepts to do with radiofrequency fields easier. The mathematical treatment of the rotating reference frame is given below for a rotation about the z-axis. The three orthogonal axes will be labeled analogous to the laboratory frame but primed $(x', y', \text{and } z')$ to allow distinguishing them. The same will be done for the unit directional vectors $\vec{\imath}$, $\vec{\jmath}$, and $\vec{k}$. The mathematical definition of the transformation of the laboratory frame to the rotational frame and vice versa is given by equation (18).

$$\begin{cases} \vec{\imath}' = cos(\omega t)\vec{\imath} - sin(\omega t)\vec{\jmath} \\ \vec{\jmath}' = sin(\omega t)\vec{\imath} + cos(\omega t)\vec{\jmath} \\ \vec{k}' = \vec{k} \end{cases} \tag{18}$$

Two rotating reference frames are of particular interest, the Larmor-rotating frame where the transverse plane rotates at $\omega = \omega_0$ (Larmor frequency) and the rf rotating frame where the transverse plane rotates at the frequency of the $\vec{B}_1$ field $\omega = \omega_{rf}$. The time derivatives of the unit vectors defined in equation (18) in the rotating reference frame are

$$\begin{cases} \dfrac{d\vec{\imath}'}{dt} = \vec{\omega} \times \vec{\imath}' \\ \dfrac{d\vec{\jmath}'}{dt} = \vec{\omega} \times \vec{\jmath}' \\ \dfrac{d\vec{k}'}{dt} = \vec{\omega} \times \vec{k}' \end{cases} \tag{19}$$

The net magnetisation vector in the laboratory $(\vec{M})$ and rotating reference frame $(\vec{M}_{rot})$ are defined as

$$\vec{M} = M_x\vec{\imath} + M_y\vec{\jmath} + M_z\vec{k} \tag{20}$$

$$\vec{M}_{rot} = M_{x\prime}\vec{\imath}' + M_{y\prime}\vec{\jmath}' + M_{z\prime}\vec{k}' \tag{21}$$

The transformation in equation (18) can be used to set $\vec{M} = \vec{M}_{rot}$.

$$\begin{bmatrix} M_{x\prime} \\ M_{y\prime} \\ M_{z\prime} \end{bmatrix} = \begin{bmatrix} \cos\omega t & -\sin\omega t & 0 \\ \sin\omega t & \cos\omega t & 0 \\ 0 & 0 & 1 \end{bmatrix} \begin{bmatrix} M_x \\ M_y \\ M_z \end{bmatrix} \tag{22}$$

The same can be done for the $\vec{B}_1$ field. It is important to remember that the rf excitation is usually applied in the transverse plane and therefore no z-component is considered.

$$\vec{B}_1 = B_{1,x}\vec{\imath} + B_{1,y}\vec{\jmath} \tag{23}$$

$$\vec{B}_{1,rot} = B_{1,x\prime}\vec{\imath}' + B_{1,y\prime}\vec{\jmath}' \tag{24}$$

$$\begin{bmatrix} B_{1,x\prime} \\ B_{1,y\prime} \end{bmatrix} = \begin{bmatrix} \cos\omega t & -\sin\omega t \\ \sin\omega t & \cos\omega t \end{bmatrix} \begin{bmatrix} B_{1,x} \\ B_{1,y} \end{bmatrix} \tag{25}$$

Equations (22) and (25) which are the conversions of the magnetisation and excitation vectors between the static and rotating reference frames can also be given in complex numbers.

$$M_{x\prime y\prime} = M_{xy}e^{i\omega t} \quad \Rightarrow \quad \begin{cases} M_{xy} = M_x + iM_y \\ M_{x\prime y\prime} = M_{x\prime} + iM_{y\prime} \end{cases} \tag{26}$$

$$B_{1,rot}(t) = B_1(t)e^{i\omega t} \quad \Rightarrow \quad \begin{cases} B_1 = B_{1,x} + iB_{1,y} \\ B_{1,rot} = B_{1,x\prime} + iB_{1,y\prime} \end{cases} \tag{27}$$

The time derivatives of the net magnetisation in the laboratory and rotating reference frame are given as

$$\frac{d\vec{M}}{dt} = \frac{dM_x}{dt}\vec{\imath} + \frac{dM_y}{dt}\vec{\jmath} + \frac{dM_z}{dt}\vec{k} \tag{28}$$

$$\frac{\partial\vec{M}_{rot}}{\partial t} = \frac{dM_{x\prime}}{dt}\vec{\imath}' + \frac{dM_{y\prime}}{dt}\vec{\jmath}' + \frac{dM_{z\prime}}{dt}\vec{k}' \tag{29}$$

From that it can be concluded that

$$\frac{d\vec{M}}{dt} = \frac{\partial\vec{M}_{rot}}{\partial t} + \vec{\omega}\times\vec{M}_{rot} \tag{30}$$

The time derivative of the net magnetisation in the laboratory frame is $\frac{d\vec{M}}{dt}$. The rate of change of the net magnetisation in the rotating frame is $\frac{\partial\vec{M}_{rot}}{\partial t}$, hence $\frac{d\vec{M}}{dt} = \frac{d\vec{M}_{rot}}{dt} \neq \frac{\partial\vec{M}_{rot}}{\partial t}$.

2.2.6.2. Description of the B_1 Field

The $\vec{B}_1$ field is only applied for a very short time in the microsecond or millisecond range. Its oscillating frequency is in the radiofrequency range. The $\vec{B}_1$ field is significantly weaker than the static magnetic field (around 50 mT) and applied perpendicular to $\vec{B}_0$. Mathematically, the $\vec{B}_1$ field is described as

$$\vec{B}_1(t) = 2B_1^e(t)cos\big(\omega_{rf}t + \varphi\big)\vec{\imath} \tag{31}$$

In equation (31), $B_1^e(t)$ is the pulse envelope function, ω_{rf} is the carrier frequency, and φ is the phase angle. The linearly polarised field from equation (31) oscillates along the x-axis. It is also possible to describe $\vec{B}_1(t)$ with two fields that are circularly polarised where the two terms rotate on opposite directions.

$$\begin{aligned}\vec{B}_1(t) = B_1^e(t)\big[cos\big(\omega_{rf}t+\varphi\big)\vec{\imath} - sin\big(\omega_{rf}t+\varphi\big)\vec{\jmath}\big] \\ + B_1^e(t)\big[cos\big(\omega_{rf}t+\varphi\big)\vec{\imath} + sin\big(\omega_{rf}t+\varphi\big)\vec{\jmath}\big]\end{aligned} \tag{32}$$

The second term rotates counter clockwise in a direction opposite to the precessing spins and therefore has very little effect when the carrier frequency ω_{rf} is approaching the Larmor frequency ω_0. As a result of that, the effective $\vec{B}_1$ field is only the first term of equation (31).

$$\vec{B}_1(t) = B_1^e(t)\big[cos\big(\omega_{rf}t+\varphi\big)\vec{\imath} - sin\big(\omega_{rf}t+\varphi\big)\vec{\jmath}\big] \tag{33}$$

The x-component is represented by the cosine term and the y-component by the sine term.

$$B_{1,x} = B_1^e(t)cos\big(\omega_{rf}+\varphi\big) \tag{34}$$

$$B_{1,y} = -B_1^e(t)sin\big(\omega_{rf}+\varphi\big) \tag{35}$$

Equations (34) and (35) can also be represented in a complex notation.

$$B_1(t) = B_{1,x}(t) + iB_{1,y}(t) = B_1^e(t)e^{-i(\omega_{rf}t+\varphi)} \tag{36}$$

The carrier frequency ω_{rf} is determined by the Larmor frequency and constant for most of the popular rf pulses used in practice. Shape and duration of an rf pulse and therefore its excitation property is determined by the envelope function $B_1^e(t)$. Two widely used rf pulses are the rectangular and the sinc pulse.

Rectangular pulse: $$B_1^e(t) = B_1 \prod\left(\frac{t-\tau_p/2}{\tau_p}\right) = \begin{cases} B_1 & 0 \le t \le \tau_p \\ 0 & otherwise \end{cases} \tag{37}$$

Sinc pulse: $$B_1^e(t) = \begin{cases} B_1\, sinc\big[\pi f_\omega(t-\tau_p/2)\big], & 0 \le t \le \tau_p \\ 0, & otherwise \end{cases} \tag{38}$$

The quantity τ_p in equations (37) and (38) is the pulse width.

2.2.6.3. On-resonance Excitation

For simplicity it is assumed that there is a spin system containing only one isochromat that is precessing at the Larmor frequency ω_0. The initial phase angle φ in equation (33) is assumed to be zero. Equation (25) can be used to define an rf pulse in the rotating reference frame as

$$\vec{B}_{1,rot} = B_1^e(t)\vec{\imath} \tag{39}$$

The effective field seen by the isochromats is

$$\vec{B}_{eff} = B_0\vec{k}' + B_1^e(t)\vec{\imath}' + \frac{\vec{\omega}_{rf}}{\gamma} = \left(B_0 - \frac{\omega_{rf}}{\gamma}\right)\vec{k}' + B_1^e(t)\vec{\imath}' \tag{40}$$

Because excitation occurs on-resonance, the excitation frequency is $\omega_{rf} = \omega_0$ which means $\vec{B}_{eff} = B_1^e(t)\vec{\imath}'$. The Bloch equation in the rotating reference frame has the form

$\frac{\partial \vec{M}_{rot}}{\partial t} = \gamma \vec{M}_{rot} \times \vec{B}_{eff}$ and $\vec{B}_{eff} = \vec{B}_{rot} + \frac{\vec{\omega}}{\gamma}$. The Bloch equation for the on-resonance excitation is then

$$\frac{\partial \vec{M}_{rot}}{\partial t} = \gamma \vec{M}_{rot} \times B_1^e(t)\vec{\imath}' \tag{41}$$

Equation (41) describes the motion of the net magnetisation $\vec{M}$ that can also be stated in scalar form.

$$\begin{cases} \dfrac{dM_{x'}}{dt} = 0 \\ \dfrac{dM_{y'}}{dt} = \gamma B_1^e(t) M_{z'} \\ \dfrac{dM_{z'}}{dt} = \gamma B_1^e(t) M_{y'} \end{cases} \tag{42}$$

Before the excitation, there is no transverse magnetisation which means $\left(M_{x'}(0) = M_{y'}(0) = 0\right)$. The magnetisation in z-direction equals the initial net magnetisation $(M_{z'}(0) = M_z^0)$. Under these conditions, a solution of equation (42) is

$$\begin{cases} M_{x'}(t) = 0 \\ M_{y'}(t) = M_z^0 \, sin\left(\int_0^t \gamma B_1^e(\hat{t}) d\hat{t}\right) \\ M_{z'}(t) = M_z^0 \, cos\left(\int_0^t \gamma B_1^e(\hat{t}) d\hat{t}\right) \end{cases} \quad 0 \le t \le \tau_p \tag{43}$$

This shows that the application of an on-resonance excitation results in a rotation of the net magnetisation vector about the x'-axis. This is expected because the effective field $\vec{B}_{eff}$ extends along that direction. In order to illustrate the effect of an on-resonance excitation in the rotating reference frame, the solution of the Bloch equation of a rectangular pulse shall be found. The solution of the Bloch equation for a rectangular $\vec{B}_1$ field is

$$\begin{cases} M_{x'}(t) = 0 \\ M_{y'}(t) = M_z^0 \, sin(\omega_1 t) \\ M_{z'}(t) = M_z^0 \, cos(\omega_1 t) \end{cases} \quad 0 \le t \le \tau_p \tag{44}$$

The angular velocity with which the net magnetisation vector rotates about the x'-axis is $\vec{\omega}_1 = -\gamma \vec{B}_1$. Figure 6 illustrates that the time dependent magnetisation in y'- and z'-direction can be calculated by using simple trigonometric relations. When the net magnetisation is rotated away from the z'-axis by a $\vec{B}_1$ field to create transverse magnetisation $\vec{M}_{x'y'}$, an angle can be defined between the z'-axis and $\vec{M}$. This flip angle α can be calculated by

$$\alpha = \int_0^{\tau_p} \omega_1(t) dt = \int_0^{\tau_p} \gamma B_1^e(t) dt \tag{45}$$

If the applied pulse is of rectangular shape, then α is defined as

$$\alpha = \omega_1 \tau_p = \gamma B_1 \tau_p \tag{46}$$

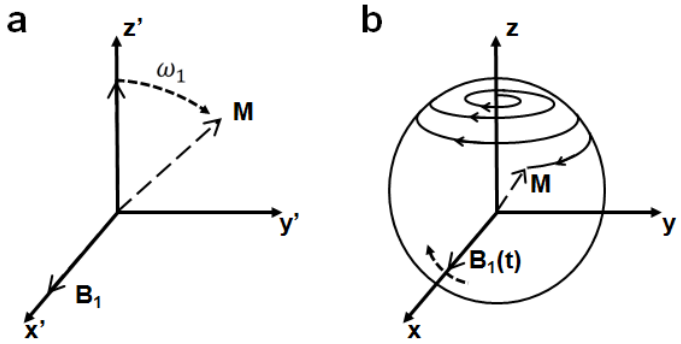

Figure 6: Behaviour of the time dependent magnetisation $\vec{M}$ under the application of a $\vec{B}_1$ field in the rotating frame (a) and the laboratory frame (b) (reproduced from Liang and Lauterbur [87], p. 79).

2.2.6.4. Off-resonance Excitation

In the previous chapter, on-resonance excitations were discussed. However, in most situations static field inhomogeneities are present that result in imperfect excitations of some isochromats. In such an off-resonance excitation, the effective magnetic field takes the form

$$\vec{B}_{eff} = \left(B_0 - \frac{\omega_{rf}}{\gamma}\right)\vec{k}' + B_1^e(t)\vec{\imath}' = \frac{\Delta\omega_0}{\gamma}\vec{k}' + B_1^e(t)\vec{\imath}' \tag{47}$$

In equation (47), $\Delta\omega_0 = \omega_0 - \omega_{rf}$ is a measure of how off-resonance the excitation occurs. In comparison to the effective field of an on-resonance excitation there is an additional component along the z'-axis as shown in figure 7.

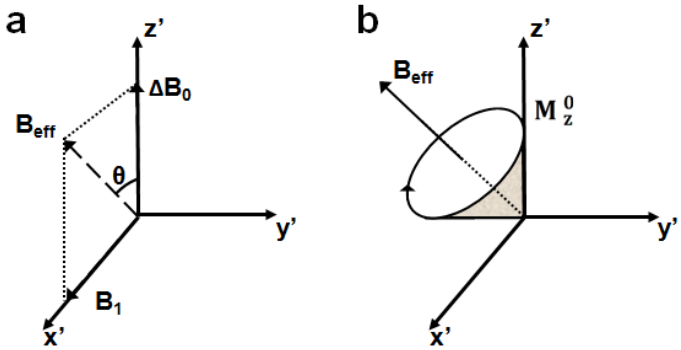

Figure 7: Effective field $\vec{B}_{eff}$ of an off-resonance excitation. a: $\vec{B}_{eff}$ in the rotating frame. b: Rotating magnetisation vector precessing about $\vec{B}_{eff}$ (reproduced from Liang and Lauterbur [87], p. 89).

As before, equation (48) which is the Bloch equation of motion of the net magnetisation during application of an rf pulse needs to be solved.

$$\begin{cases} \dfrac{dM_{x'}}{dt} = \Delta\omega_0 M_{y'} \\ \dfrac{dM_{y'}}{dt} = -\Delta\omega_0 M_{x'} + \gamma B_1^e(t) M_{z'} \\ \dfrac{dM_{z'}}{dt} = -\gamma B_1^e(t) M_{y'} \end{cases} \tag{48}$$

The solution of equation (48) for the specific case of a rectangular envelope function $B_1^e(t) = B_1 \Pi\left(\frac{t-\tau_p/2}{\tau_p}\right)$ can be given as

$$\begin{cases} M_{x'}(t) = M_z^0 \sin\theta \cos\theta \left[1 - cos(\omega_{eff} t)\right] \\ M_{y'}(t) = M_z^0 \sin\theta \, sin(\omega_{eff} t) \\ M_{z'}(t) = M_z^0 \left[cos^2\theta + sin^2\theta \, cos(\omega_{eff} t)\right] \end{cases} \qquad 0 \le t \le \tau_p \tag{49}$$

The effective frequency is given as $\omega_{eff} = \sqrt{\Delta\omega_0^2 + \omega_1^2}$ and the angle θ is defined as $\theta = arctan(\omega_1/\Delta\omega_0)$. Immediately after the application of the rf pulse, the flip angle about $\vec{B}_{eff}$ is $\alpha = \omega_{eff}\tau_p$. This changes the solution to

$$\begin{cases} M_{x'}(0_+) = M_{x'}(\tau_p) = M_z^0 \ \sin\theta \cos\theta \ (1 - \cos\alpha) \\ M_{y'}(0_+) = M_{y'}(\tau_p) = M_z^0 \ \sin\theta \sin\alpha \\ M_{z'}(0_+) = M_{z'}(\tau_p) = M_z^0 \ (cos^2\theta + sin^2\theta \cos\alpha) \end{cases} \tag{50}$$

where $t = 0_+$ denotes the time immediately after the application of an rf pulse. The main difference to the on-resonance excitation is that the transverse magnetisation is not limited to the y'-axis. A phase shift φ_0 has occurred that can be calculated as

$$\begin{aligned} \tan\varphi_0 = \frac{M_x(0_+)}{M_y(0_+)} &= \frac{\sin\theta\cos\theta \ (1-\cos\alpha)}{\sin\theta\sin\alpha} = \frac{(1-\cos\alpha)}{\sin\alpha}\frac{\Delta\omega_0}{\omega_{eff}} \\ &= \tan\frac{\alpha}{2}\frac{\Delta\omega_0}{\omega_{eff}} \end{aligned} \tag{51}$$

The magnitude of the magnetisation in the transverse plane is

$$\begin{aligned} M_{x'y'}(0_+) &= \sqrt{M_{x'}^2(0_+) + M_{y'}^2(0_+)} \\ &= M_z^0 \sin\theta \sqrt{sin^2\,\alpha + (1-\cos\alpha)^2\, cos^2\,\theta} \end{aligned} \tag{52}$$

From equations (51) it can be seen that an almost linear increase of the phase shift φ_0 with the frequency shift $\Delta\omega_0$ occurs. Equation (52) shows that a decrease of the magnitude of transverse magnetisation results when the frequency offset is increased.

2.2.7. Relaxation

The application of an rf pulse to a spin system causes the net magnetisation vector $\vec{M}$ to lose longitudinal magnetisation M_z and gain transverse magnetisation M_{xy}. Once the $\vec{B}_1$ field is no longer applied, $\vec{M}$ will return to its equilibrium state which is parallel to the static magnetic field

$\vec{B}_0$. When $\vec{M}$ returns to equilibrium it will precess about the static magnetic field. At the same time, two relaxation processes take place. One is the regrowth of longitudinal magnetisation that is governed by the longitudinal relaxation time constant T_1. The other is the decay of transverse magnetisation that is described by the transversal relaxation time constant T_2. Relaxation occurs because of microscopic magnetic fields in the surrounding of the nuclei. Longitudinal and transverse relaxation processes can be mathematically described using the Bloch equation. It is important to note that the following exponential expressions for longitudinal and transverse relaxation are only valid for weak spin-spin interactions as it is the case in biological tissues and liquids. This means they are correct for most applications in MRI. The relaxations time constants T_1 and T_2 are different for different spin systems and depend on the type of tissue and surroundings [87].

2.2.7.1. Longitudinal Relaxation

Longitudinal relaxation is the recovery of longitudinal magnetisation. In the Larmor-rotating frame it takes the form

$$\frac{dM_{z\prime}}{dt} = -\frac{M_{z\prime} - M_z^0}{T_1} \tag{53}$$

The term of the Bloch equation can be neglected because $\vec{B}_{eff} = (B_0 - \omega_0/\gamma)\vec{k}' = 0$. By solving the first order differential equation an expression is obtained that describes the behaviour of the longitudinal magnetisation over time.

$$M_{z\prime}(t) = M_z^0\left(1 - e^{-t/T_1}\right) + M_{z\prime}(0_+)e^{-t/T_1} \tag{54}$$

The term M_z^0 is the longitudinal magnetisation without the application of a $\vec{B}_1$ field. After an excitation that would rotate $\vec{M}$ by 90° in the transverse plane, $M_{z\prime}(0_+) = 0$.

$$M_{z\prime}(t) = M_z^0\left(1 - e^{-t/T_1}\right) \tag{55}$$

Simple arithmetical operations can provide a definition for the longitudinal relaxation time constant T_1.

$$M_{z\prime}(T_1) \approx 63\%\, M_z^0 \tag{56}$$

This means the longitudinal magnetisation will have recovered 63% of its equilibrium magnitude in the time T_1 as shown in figure 8b. The longitudinal relaxation time constant is also referred to as the spin-lattice time constant as it describes the exchange of energy between the spins of a nuclei and the surrounding. The longitudinal relaxation is improved (shortening of T_1) by small randomly distributed magnetic fields caused by surrounding dipoles [87], [88].

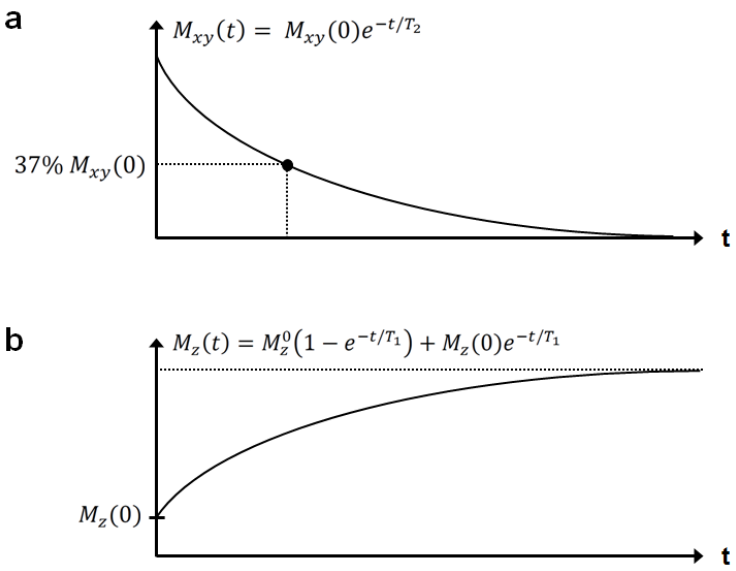

Figure 8: Time dependent relaxation of the transverse (a) and longitudinal (b) magnetisation (reproduced from Liang and Lauterbur [87], p. 93).

2.2.7.2. Transverse Relaxation

The decay of the transverse magnetisation established during application of an rf pulse is referred to as transverse relaxation and described by

$$\frac{dM_{x'y'}}{dt} = -\frac{M_{x'y'}}{T_2} \tag{57}$$

The solution of this first order differential equation gives an expression that describes the change of transverse magnetisation over time.

$$M_{x'y'}(t) = M_{x'y'}(0_+)e^{-t/T_2} \tag{58}$$

Contrary to the longitudinal magnetisation, the transverse magnetisation is immediately after a 90° rotation equal to the full magnetisation at equilibrium, $M_{x'y'}(0_+) = M_z^0$.

$$M_{x'y'}(t) = M_z^0\, e^{-t/T_2} \tag{59}$$

This allows to determine the transverse relaxation time constant T_2.

$$M_{x'y'}(T_2) \approx 37\%\, M_{x'y'}(0_+) \tag{60}$$

Transverse magnetisation will be reduced down to 37% of its initial value within the time T_2 as shown in figure 8a. The transverse relaxation time constant is also called the spin-spin time constant. The name refers to the fact that at a microscopic level, the magnetic fields of various dipoles interact with each other which causes a broadening of the resonance frequencies of the spins. These spin-spin interactions contribute to the loss of phase coherence of the transverse magnetisation. This process is also called dephasing of the spins. T_2 relaxation processes depend to some extent on longitudinal field fluctuations which is why T_2 is always shorter than T_1 [87], [88].

2.2.8. Chemical Shift

The resonance frequency of nuclear spins is determined by the gyromagnetic ratio which is the same for all nuclei of the same element even in different molecules. However, the resonance frequency also depends on the chemical environment of the nucleus. This phenomenon, the change in the resonance frequency of a specific nucleus, is called the chemical shift. It occurs because nuclei are shielded from the external magnetic field by the electrons orbiting them. Once a nucleus is exposed to a static magnetic field, its electrons start to rotate about $\vec{B}_0$ in the opposite direction to the nuclear spin precession. Because electrons are charged, moving particles, a magnetic moment $\vec{\mu}$ is created. The magnetic moment of the electrons opposes the static magnetic field $\vec{B}_0$ as shown in figure 9. As a result, the effective magnetic field experienced by the nucleus is changed and smaller than $\vec{B}_0$. This also leads to a different Larmor frequency.

$$B_{eff} = B_0 - B_{0\sigma} = B_0(1-\sigma) \tag{61}$$

$$\omega_{eff} = \omega_0 - \omega_{0\sigma} = \omega_0(1-\sigma) \tag{62}$$

This phenomenon is also called electronic shielding. The shielding constant σ is dimensionless and depends on the chemical environment of the nucleus. In order to define the chemical shift numerically, a reference frequency ω_R is needed. The chemical shift δ of a sample with frequency ω_S can be calculated as follows.

$$\delta = \frac{\omega_S - \omega_R}{\omega_R} \times 10^6 = \frac{\sigma_R - \sigma_S}{1-\sigma_R} \times 10^6 \approx (\sigma_R - \sigma_S) \times 10^6 \tag{63}$$

The chemical shift is commonly expressed in parts per million (ppm) in order to make it independent of the magnetic field strength. The most abundant molecule with hydrogen in humans is water. For that reason water protons are the reference in MRI. Of interest is often the chemical shift of fat (lipids) which was shown to be at a resonance frequency with respect to water of about 3.5 ppm [86], [88].

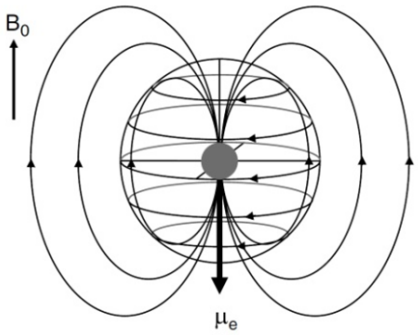

Figure 9: Illustration of the opposing nature of the static magnetic field $\vec{B}_0$ and the magnetic moment of an electron (source: de Graaf [86], p. 19).

2.3. Signal Acquisition Methods

2.3.1. Free Induction Decay

Free induction decay (FID) signals are the easiest signals produced by a spin system. They are generated by a single rf excitation pulse and the free precession of the net magnetisation vector $\vec{M}$ about the static magnetic field $\vec{B}_0$. The frequency of precession depends on the applied rf pulse according to the Larmor equation. As the magnetisation returns back to its equilibrium position while precessing about the z-axis, it has a longitudinal and transverse component. The transverse component can be detected with the same rf coil that produced the excitation pulse. As the name indicates, the signal is based on electromagnetic induction as described by Michael Faraday. An electromotive force ε is induced by a change in flux in the coil that is caused by the rotating magnetisation vector [88].

$$\varepsilon = -\frac{\partial \Phi}{\partial t} \tag{64}$$

The FID signal decreases over time and takes the following mathematical form:

$$S(t) = \sin\alpha \int_{-\infty}^{\infty} \rho(\omega) e^{-t/T_2(\omega)} e^{-i\omega t} d\omega \tag{65}$$

The characteristics of an FID signal is determined by the spectral density function $\rho(\omega)$ which is the number of spins in the sample and described by its amplitude and the rate at which it decays. The maximum amplitude is always directly after the application of the α-pulse at $t = 0$.

$$A_f = \sin\alpha \int_{-\infty}^{\infty} \rho(\omega) d\omega = M_z^0 sin\alpha \tag{66}$$

As can be seen, the maximum amplitude depends on the flip angle and the net magnetisation at thermal equilibrium. A typical FID signal is shown in figure 10. If the sample and the static magnetic field are both homogeneous, the FID signal decays with the time constant T_2. This process which results in a decrease of the transverse magnetisation is also called dephasing of the spins. It is irreversible and stems from intrinsic magnetic fields of adjacent spins and is therefore also referred to as spin-spin relaxation [90]. In the case that inhomogeneities are present in the static magnetic field, the signal decays faster. The reason for that is that isochromats in the sample will have slightly different phases which means that their magnetic moments will cancel each other. This results in a smaller net magnetisation or a faster decay of the signal. In order to differentiate the signal loss due to field inhomogeneities from the T_2 decay, a different time constant T_2^* is used to characterise this faster decay. If a Lorentzian distribution is assumed of the field inhomogeneity, the FID signal can be described mathematically as

$$S(t) = \sin\alpha \int_{-\infty}^{\infty} M_z^0 \frac{(\gamma\Delta B_0)^2}{(\gamma\Delta B_0)^2 + (\omega - \omega_0)^2} e^{-\frac{t}{T_2}} e^{-i\omega t} d\omega$$

$$= \sin\alpha \int_{-\infty}^{\infty} \left[M_z^0 \frac{(\gamma\Delta B_0)^2}{(\gamma\Delta B_0)^2 + \omega^2} e^{-i\omega t} d\omega \right] e^{-t/T_2} e^{-i\omega_0 t} \qquad t \geq 0 \qquad (67)$$

$$= \pi M_z^0 \gamma\Delta B_0 \sin\alpha \, e^{-\gamma\Delta B_0 t} e^{-t/T_2} e^{-i\omega_0 t}$$

$$= \pi M_z^0 \gamma\Delta B_0 \sin\alpha \, e^{-t/T_2^*} e^{-i\omega_0 t}$$

From equation (67) we can see that

$$\frac{1}{T_2^*} = \frac{1}{T_2} + \gamma\Delta B_0 \qquad (68)$$

From the derivation it is obvious that equation (68) only applies if the spectral density function takes a Lorentzian shape. However, due to its simplicity it is a very common and popular expression in the literature to express the relation between T_2 and T_2^*. Other spectral density functions will not produce an exponential term for the FID envelope function and hence T_2^* is the time constant of an approximating exponential. In practice, the time it takes for an FID signal to decay depends on the inhomogeneities present in the static magnetic field which is described by T_2^* [87].

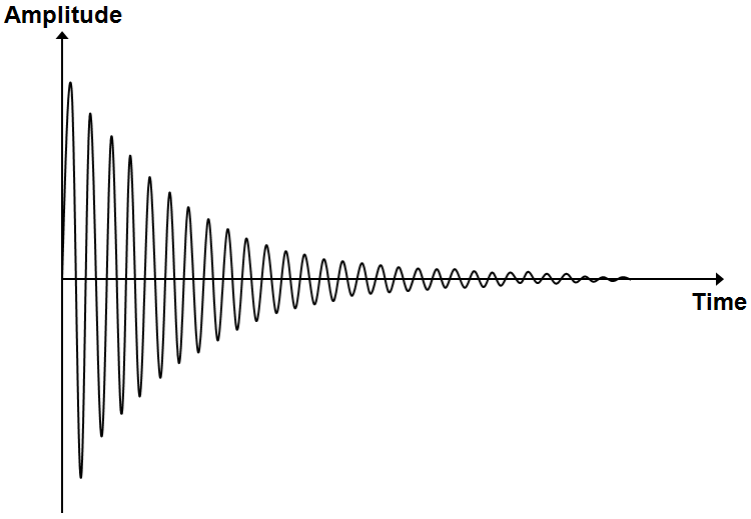

Figure 10: Decrease of amplitude with time of a typical FID signal (reproduced from Liang and Lauterbur [87], p. 113).

2.3.2. Spin Echo

In the previous chapter the free induction decay was introduced as a MR signal. Another MR signal is called an echo. There are two ways to generate an echo, by applying multiple rf pulses (spin echo signal) or by reversing a previously applied magnetic field gradient (gradient echo signal). This chapter will describe the spin echo (SE) signal which was discovered in 1950 by Erwin L. Hahn. The basic concept of it is to use refocusing rf pulses to realign dephasing

magnetisation vectors. The simplest spin echo sequence consists of two rf pulses (90° and 180°) with a time delay τ in between.

$$90° - \tau - 180°$$

MR sequences based on spin echo signals are very common and of particular importance. Figure 11 is a vector diagram that displays the behaviour of the magnetisation and the formation of a spin echo. The first 90° rf pulse and the second 180° rf pulse are applied along different axes which are the x'- and y'-axis, respectively. For simplicity a sample with two isochromats is assumed; one precessing at a slow (ω_s) and one precessing at a higher (faster) frequency (ω_f). The first 90° pulse rotates the magnetisation vectors of both isochromats onto the y'-axis as shown in figure 11a where they immediately start to precess about the z'-axis. Because the two isochromats precess at different frequencies, they will continuously go out of phase over time which is depicted in figure 11b. After the time delay τ, the phase angle between the two magnetisation vectors in the transverse plane will be $(\omega_f - \omega_s)\tau$. At that point the second 180° rf pulse is applied which causes the vectors to flip-over in the transverse plane as shown in figure 11c. Both vectors will precess in the same direction (i.e. clockwise) as before the 180° rf pulse. The faster vector of frequency ω_f that was ahead of the slower vector is now lagging behind. However, due to the faster precessional frequency it will have caught up with the slower vector after a time τ. That means both vectors are again in phase at time $t = 2\tau$ as shown in figure 11d.

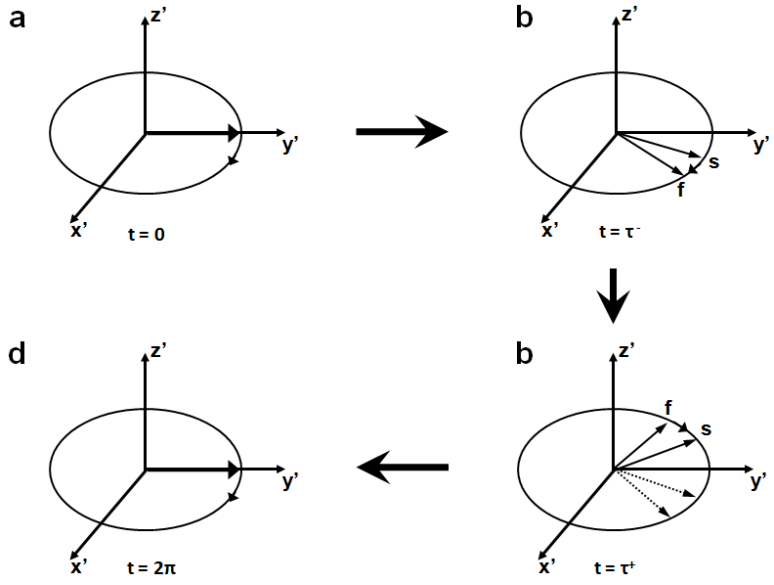

Figure 11: Behaviour of the magnetisation vector during spin echo formation. a: 90° pulse rotates the magnetisation vectors two isochromats onto the y'-axis. b: Isochromats precess at different frequencies and will go out of phase. c: Application of 180° rf pulse causes the vectors to flip –over in the transverse plane. d: Vectors continue to precess in the same direction and rephase at time $t = 2\tau$ (reproduced from Liang and Lauterbur [87], p. 115).

In a real sample, the number of isochromats with many different precessional frequencies will be much higher. Therefore, at time $t = \tau$ the transverse magnetisation $M_{x'y'}$ will have completely disappeared due to total dephasing. $M_{x'y'}$ grows again after the 180° refocusing pulse until all isochromats achieve phase coherence at $t = 2\tau$. Ignoring the T_2 relaxation, the same physical effect is responsible for the dephasing of the spins before the refocusing pulse as for the regaining of phase coherence after the 180° rf pulse. This means the transverse magnetisation is symmetrical about τ.

$$\left|M_{x'y'}(\tau - t)\right| = \left|M_{x'y'}(\tau + t)\right| \text{ for } 0 \leq t \leq \tau \tag{69}$$

The rephasing of the transverse magnetisation for $\tau < t < 2\tau$ is responsible for one side of the echo signal that has its highest amplitude when all isochromats are in phase again at 2τ. After that a dephasing occurs again for $t > 2\tau$ which is responsible for the other side of the echo signal as shown in figure 12.

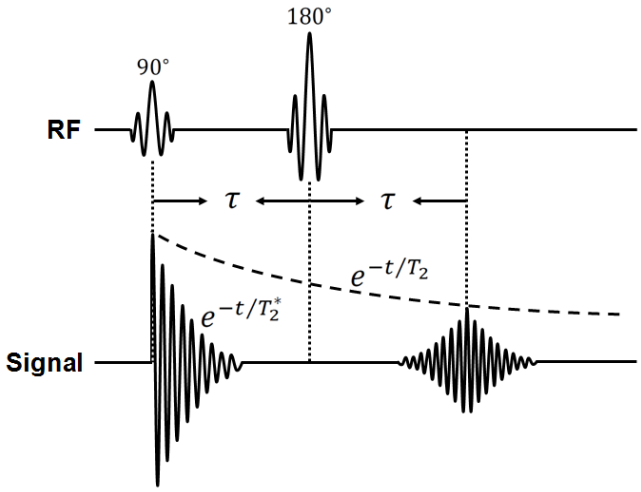

Figure 12: Signal behaviour in a spin echo sequence also showing the difference between T_2 and T_2^* decay (reproduced from Liang and Lauterbur [87], p. 116).

An extension to the described simple two-pulse spin echo sequence is the CPMG echo train sequence. The difference is that instead of using only one 180° refocusing pulse a sequence of 180° rf pulses is employed. As a result a train of spin echoes will be produced. The timeline of this sequence can be described as follows. The initial 90° pulse is applied at $t = 0$. This means that the series of 180° pulses is applied at $(2n - 1)\tau$ where $n = 1,2, \dots, N$ corresponds to the first, second, up to the nth refocusing pulse. The corresponding echoes are generated at $t = 2n\tau$. The amplitudes of each echo are weighted by

$$E_n = e^{-2n\tau/T_2} \tag{70}$$

All the echoes formed after the first, the primary echo, are called secondary echoes because they are echoes of the preceding echo. The CPMG echo train sequence is often employed for T_2

mapping measurements as the amplitude of the echoes depends on T_2 as can be seen from equation (70) and shown in figure 13.

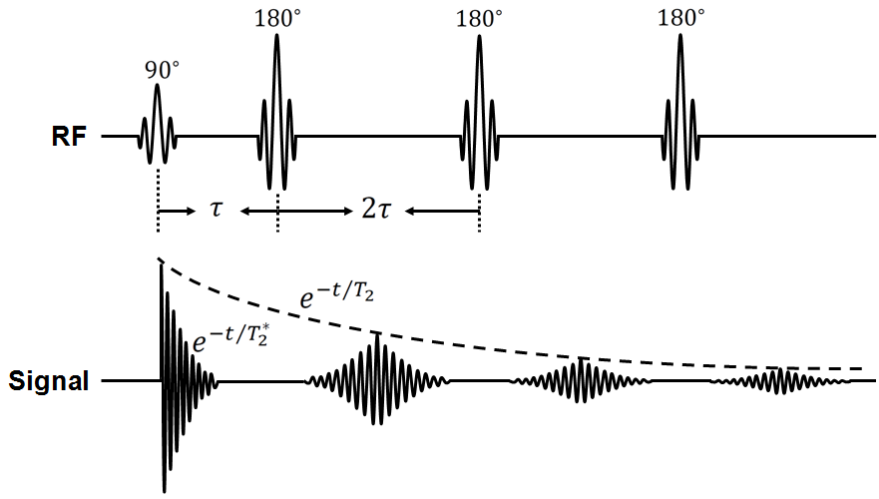

Figure 13: CPMG echo train sequence with three echoes where the amplitude of these depends on T_2 making it a standard T_2 mapping sequence (reproduced from Liang and Lauterbur [87], p. 130).

This sequence was initially invented by Carr and Purcell in 1954. However, cumulative phase errors occurred due to imperfections in the train of 180° pulses. The solution to this problem was given by Meiboom and Gill in 1958 who proposed to stop applying all pulses along the same axis. Instead the refocusing pulses should be applied orthogonal to the 90° excitation pulse. CPMG stands for Carr-Purcell-Meiboom-Gill, the surnames of the four scientists who invented it.

2.3.3. Gradient Echo

Gradient echo signals are produced by employing time-varying magnetic gradient fields. These gradient fields are used to dephase and rephase the magnetisation vectors of the different isochromats in a sample to generate one or a series of echoes.

2.3.3.1. Gradient Fields

The z-component of a gradient field $\vec{B}_G$ changes in one direction linearly. That direction is called the gradient direction which can be in x-, y-, or z-direction. $\vec{B}_G$ will then be called an x-, y-, or z-gradient field accordingly. The gradient coils in a MR scanner system also produce gradient fields in the x- and y-direction ($B_{G,x}$ and $B_{G,y}$). Due to the strong static magnetic field along the z-direction, the gradient fields in the x- and y-direction are negligible and $B_{G,z}$ is simply referred to as B_G. The total magnetic field is the summation of the static magnetic field and the gradient field.

$$\vec{B} = \left(B_0 + B_{G,z}\right)\vec{k} \tag{71}$$

In the case that not only one gradient coil is producing a gradient field but all three in x-, y-, and z-direction, $B_{G,z}$ takes the following form:

$$B_{G,z} = G_x x + G_y y + G_z z \tag{72}$$

It is quite common to combine the three gradients in x-, y-, and z-direction into a gradient vector $\vec{G}$.

$$\vec{G} = \left(G_x, G_y, G_z\right) = G_x\vec{\imath} + G_y\vec{\jmath} + G_z\vec{k} \tag{73}$$

The gradient direction of $\vec{B}$ or $\vec{B}_G$ is defined as the direction of $\vec{G}$. It is essential to understand that $\vec{G}$ can point along the x-, y-, z-direction, or any arbitrary direction which is a combination of the three orthogonal directions. However, this must not be the direction of B_G which is typically unknown. This means one needs to differentiate between the direction of the gradient field and the gradient direction of $B_{G,z}$.

2.3.3.2. Formation of Gradient Echoes

An rf pulse is applied to excite the spin system followed by a negative gradient in x-direction. This will cause spins that have a different position along the x-axis to have a different phase.

$$\phi(x,t) = \gamma \int_0^t -G_x x d\hat{t} = -\gamma G_x x t \qquad 0 \le t \le \tau \tag{74}$$

Equation (74) shows that the phase difference of spins in different x-positions increases with time. Due to the negative gradient, the spins dephase and the signal decays to zero after a time τ three times larger than the time constant that describes the decay. However, this time constant is of negligible importance for most applications. After application of the negative gradient, a positive gradient is switched on which causes the signal to regrow as the transverse magnetisation components rephase again. The spin phase angle takes the form

$$\phi(x,t) = -\gamma G_x x\tau + \gamma \int_\tau^t G_x x d\hat{t} = -\gamma G_x x\tau + \gamma G_x x(t-\tau) \qquad \tau \le t \le 2\tau \tag{75}$$

The dispersion of the phase of different spins caused by the negative gradient is reversed by the positive gradient that is switched on at $t = \tau$. After another delay time τ all spins have rephased and an echo is produced as shown in figure 14.

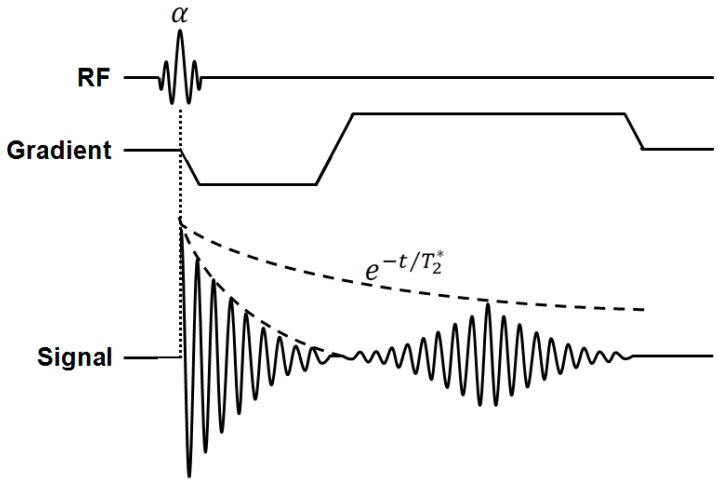

Figure 14: Signal behaviour in a gradient echo sequence where the echo is formed by reversing the gradient switched on at the time of the excitation pulse (reproduced from Liang and Lauterbur [87], p. 134).

At that point the spin phase ϕ is zero for all spins at different x-positions. The dephase and rephase gradients do not necessarily have to be of the same strength. However, this would result in an echo time different to 2τ. It is important to note that in reality $\vec{B}_0$ inhomogeneities are usually present. This means that the spins will not be perfectly rephased in the centre of the rephasing gradient and the amplitude of the formed echo is T_2^*-weighted. This is an important difference to a spin echo signal where T_2^*-weighting is prevented by the 180° refocusing pulses.

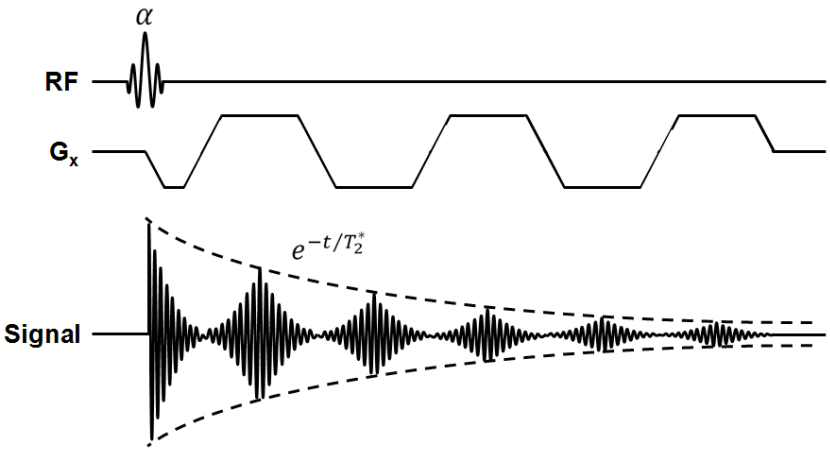

Figure 15: Train of gradient echoes produced by switching between positive and negative gradient strength (reproduced from Liang and Lauterbur [87], p. 135).

Similarly to the CPMG echo train it is also possible to create a train of gradient echo signals. This can be achieved by switching between positive and negative gradient strengths as illustrated in figure 15. Such a multi-echo gradient echo (ME-GRE) approach leads to a stack of images where each image corresponds to one gradient echo [91]. The time constant T_2^* and the

speed of gradient switching determine how many echoes can be collected. The switching between positive and negative refocusing gradients will lead to differences in the amplitude of the echoes. For that reason, only even or odd echoes should be considered for T_2^* calculation. The key difference in measuring T_2^* compared to T_2 is that only a single excitation is required and no refocusing pulses which makes T_2^* mapping faster [89].

2.4. Signal Encoding

In order to produce an MR image it is essential to be able to differentiate spins in the sample (e.g. different tissues). Three orthogonal magnetic field gradients are used in MRI to spatially localise the obtained signal. First, a slice in the sample is selected with a slice-select gradient. For simplicity it is assumed that a conventional slice is selected in the transverse orientation which means the slice-select gradient is applied along the z-direction. Once a slice is selected, spatial localisation within a slice is done with two gradients that produce a grid-like structure. These two gradients are a frequency-encoding gradient along the x-direction and a phase-encoding gradient along the y-direction. The description of spatial localisation in this work will focus predominantly on 2D imaging to illustrate the basic principles. In comparison to the topics above, explanations in this chapter will be less mathematical to allow for a phenomenological understanding of the mechanisms of image formation in MRI.

2.4.1. Slice-select Gradients

The slice-select gradient is switched on during rf excitation to only generate signal in a well-defined area of the sample. Signal will only originate from a single slice along the z-direction where the resonance condition is fulfilled while all other protons are oblivious to the excitation pulse. The slice-select gradient is a magnetic field gradient that causes the magnetic field strength to vary linearly along the z-direction which has a direct influence of the slice thickness as shown in figure 16a.

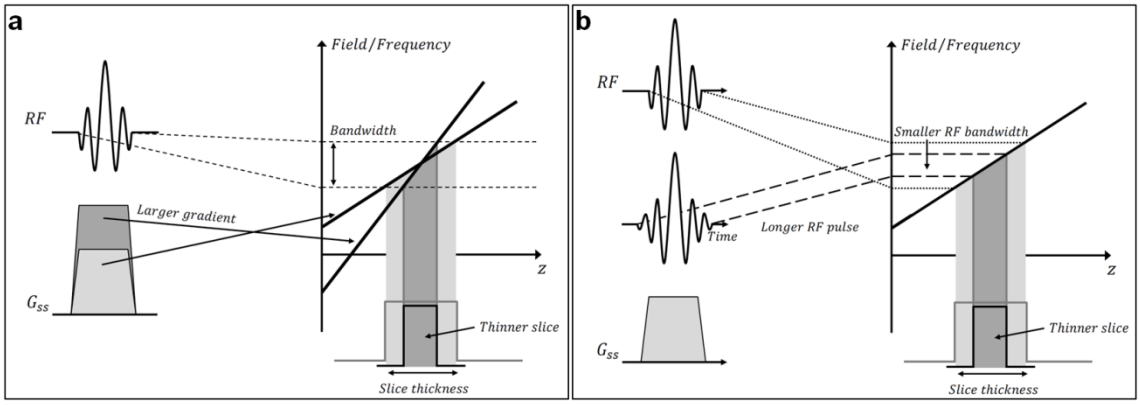

Figure 16: Slice thickness changes with the strength of the slice-select gradient (a) or the transmit bandwidth of the rf excitation pulse (b) (reproduced from McRobbie et al. [92], p. 118).

An rf excitation pulse will include a well-defined range of frequencies referred to as the transmitter bandwidth. This width is controlled by the operator and defines the slice thickness (figure 16b). The slice-select gradient strength is determined by the change in magnetic field strength ΔB_0 over a certain distance Δd. The change in magnetic field strength can be expressed in terms of the transmitter frequency Δf by using the Larmor equation:

$$G_z = \frac{\Delta B_0}{\Delta d} = \frac{\Delta f}{\gamma \Delta d} \tag{76}$$

From equation (76) it is obvious that in order to decrease the slice thickness, the transmitter frequency needs to be decreased and/or the gradient strength increased (figure 16b).

2.4.1.1. Slice Profile

When considering slice-selection, the slice profile is an important concept. It describes the excitation of spins in the selected slice as well as in the rest of the sample. Ideally, only spins within the selected slice are excited while all other spins experience no excitation. The excitation profile is determined by the Fourier transformed rf pulse. The Fourier transform contains the frequency components of an rf pulse. These frequencies define the slice borders as they correspond to different spatial locations along the slice-select gradient. The ideal slice profile would be a rectangular Fourier transform whereby the spins in the slice are uniformly excited with no excitation outside the selected slice. This can only be approximated as such a perfectly rectangular Fourier transform can only be achieved with a sinc function of infinitely length. In practice, truncated sinc functions are used for rf excitation pulses. The majority of the frequency information is located in the central peak and truncating such a function after a few side ripples provides a fairly good approximation to an ideal slice profile. The result of truncating an rf pulse is that the edges of the selected slice might be excited slightly less or more than desired. Furthermore, some excitation may also occur outside of the slice. These effects result in a decrease in image quality and contrast and can be minimised by including as many periods in the truncated pulse as possible. A stronger slice-select gradient can be used to shorten the rf pulse and allow for more periods to be included. This is because a stronger slice-select gradient increases the transmitter bandwidth as can be seen in equation (76). A higher transmitter frequency results in a more “compressed” rf pulse. It can be concluded that by increasing the strength of the slice-select gradient, the duration of the rf pulse is reduced and the slice profile can be improved while keeping the slice thickness constant.

2.4.1.2. Rephasing Lobe

Slices are not infinitesimally thin to allow inclusion of only one spin (proton) along the slice-select direction. Spins with different frequencies will be present within a slice which dephase and cancel each other out. It is therefore necessary to apply a gradient of opposite sign to the slice-select gradient to rephase the magnetic moments. This rephasing lobe is half the area of the slice-select gradient. A rephasing lobe is only necessary for gradient echo sequences where the slice-select gradient is applied during the rf excitation pulse. For spin-echo sequences on the other hand, the slice-select gradient is turned on during the 90° excitation as well as the 180° refocusing pulse. The reason that no rephasing gradient is needed for spin-echo sequences is that dephasing and rephasing occur during the application of the 180° pulse as described in more detail above.

2.4.2. Frequency-encoding Gradients

After a slice is selected, gradients along the x- and y-direction are applied to localise the signal within a given slice. For signal localisation along the x-direction, a process called frequency-encoding is applied where the gradient is turned on while the echo is collected. This gradient encodes the location of a spin along the x-direction based on the frequency of the measured signal. The frequency-encoding gradient is also sometimes called a readout gradient because it is applied during echo sampling. This also means that the echo will contain a range of frequencies and resemble a sinc function. The characteristic of a sinc function is that the more frequency components it comprises the more compressed it will be. In order to extract spatial information along the x-axis out of an echo a Fourier transform needs to be applied. Due to the presence of the frequency-encoding gradient during echo sampling, frequencies are linearly distributed in the x-direction. A Fourier transform will then provide information on the total signal at each location which again depends on tissue properties such as T_1 and T_2 relaxation times as well as sequence parameters such as repetition time (TR) and echo time (TE). All gradients cause dephasing of spins and therefore, analogous to the slice-select gradient, a rephasing gradient lobe is required to compensate for that. However, unlike with the slice-select gradient, the reverse frequency-encoding lobe is applied first to cause the spins to dephase. After that the frequency-encoding gradient is applied where rephasing is greatest in the centre of the gradient because the dephasing lobe is chosen to be half of the area of the rephasing gradient. In the case of a gradient echo sequence, it is the frequency-encoding gradient that produces the echo. For spin echo sequences, the frequency-encoding gradient adds a gradient echo contribution to the sampled echo. For gradient echo imaging it can be concluded that by increasing the strength of the frequency-encoding gradient, the duration of the echo can be

shortened as well as TR and TE. This is contrary to spin echo sequences where the total imaging time is normally not affected by the time required to sample the echo.

2.4.2.1. Receiver Bandwidth

The range of frequencies collected while the frequency-encoding gradient is turned on is referred to as the receiver bandwidth. It widens as the strength of the frequency-encoding gradient is increased for a constant field of view. The difference to the earlier mentioned transmitter bandwidth is that the receiver bandwidth applies to the sampled echo and the range of frequencies it is comprised of whereas the transmitter bandwidth refers to the rf excitation pulse. The receiver bandwidth is constrained by the sampling frequency. When increasing the frequency-encoding gradient and consequently the receiver bandwidth, the signal-to-noise ratio (SNR) is decreased.

2.4.2.2. Sampling Frequency

The sampling frequency describes the rate of echo sampling and its digitalisation. An analogue-to-digital converter (ADC) is used for digitalisation of the signal and the rate at which that conversion occurs is given by the sampling frequency. Because the sampling frequency cannot be increased infinitely, the measured echo might be different to the original echo and some information might get lost. The relationship between the highest-frequency component and the sampling frequency determines how accurate the original echo is digitised and called the Nyquist theorem of sampling. According to that sampling of a signal must be at least at twice the frequency of the signal in order to get an acceptable representation of the original signal. The time necessary to sample a full echo is determined by the sampling frequency.

2.4.3. Phase-Encoding Gradient

The final step to achieve spatial localisation of a voxel is the application of a phase-encoding gradient along the y-direction. At this stage the reader is reminded that the direction of each gradient is arbitrary but for this work the convention is that slice-select, frequency-encoding, and phase-encoding gradients are applied along z-, x-, and y-direction, respectively. While the first two gradients used for spatial localisation slightly change the frequency of spins, the phase-encoding gradient changes the phase. All gradients cause dephasing of spins because different precession frequencies cause differences in phase accumulated over time. Dephasing occurs faster the stronger the gradient is and the phase dispersion is larger the longer the gradient is applied. If there is no gradient present, the spins precess at the Larmor frequency. However, any accumulated phase dispersion is maintained. The phase shift caused by the phase-encoding

gradient changes linearly along the y-direction and is a result of the strength and duration of the gradient. In contrast to the slice-select and frequency-encoding gradients, the phase encoding gradient is not applied during rf excitation or echo sampling but at some time point in between. The idea here is that the part of the MR sequence from rf excitation to echo sampling is repeated several times with a different phase-encoding gradient every time that results in different phase shifts for each run. The number of phase-encoding steps N_{PE} (i.e. number of repetitions) depends on the number of voxels along the phase-encoding direction. The echo sampled at each phase-encoding step will be different. After the application of the frequency-encoding gradient and the Fourier transformation of the echo, there will be as many frequencies as columns along the x-direction. Each frequency belongs to one column that is an unknown combination of the signals from each voxel along the y-direction. Phase-encoding now allows to solve the unknown voxel values in each column along the x-direction by providing enough equations (i.e. different combinations of the unknown voxel values) so that each of them can be determined. Spatial localisation is always linked with the concept of k-space which will be discussed in more detail in the next chapter. But it shall be mentioned at this point that each line in k-space is filled by one echo which differ based on the phase-encoding gradient used. When zero phase-encoding is applied, the respective echo has the largest amplitude because all spins are in phase. Contrary to that, higher phase-encoding gradients have lower amplitudes because the introduced phase shift causes dephasing of the spins.

2.4.4. k-Space

The echoes that are sampled during the application of an MRI pulse sequence are stored in k-space which is the Fourier transformation of the anatomical representation of the sample (i.e. the MR image). Mathematically, the Fourier transform of an image can be written as

$$\begin{aligned} H(k_x, k_y) &= \int_{-\infty}^{\infty} h(x,y) e^{-i(k_x x + k_y y)} dx dy \\ &= \int_{-\infty}^{\infty} h(x,y)\left[cos(k_x x + k_y y) - i\, sin(k_x x + k_y y)\right] dx dy \end{aligned} \tag{77}$$

The function $H(k_x, k_y)$ is the Fourier transform or spatial frequency map and $h(x,y)$ describes the image, specifically the spatial distribution of the voxel signal intensities. This so-called image space can be imagined as a 2D grid of numbers where at each location, which is defined by two coordinates, there is a value of the signal intensity. The centre of the image space is at $(x,y) = (0,0)$ which means that for a grid or image matrix with 256 by 256 coordinate pairs, the x- and y-axes would start at -127 and go up to +128 as shown in figure 17.

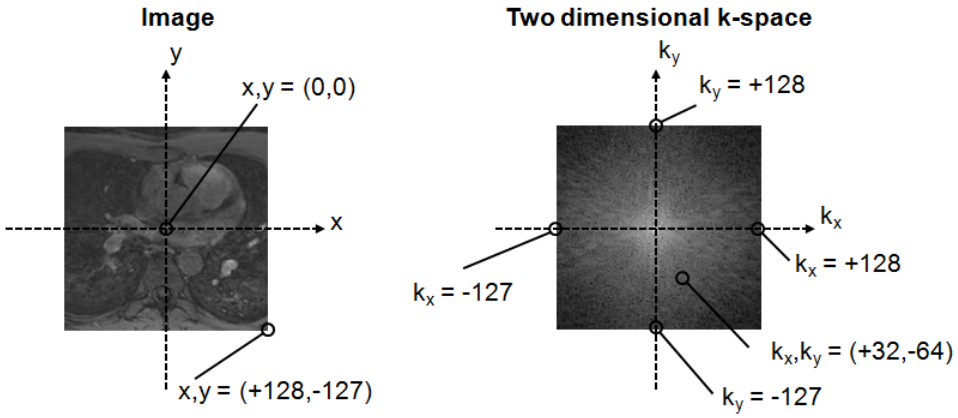

Figure 17: Comparison of image space and k-space for an image with a matrix of 256x256 coordinate pairs (i.e. pixels or voxels) (reproduced from Lee [93], p. 105).

The k-space represented by $H(k_x, k_y)$ also adopts a grid of numbers where position is defined by a pair of coordinates (k_x, k_y). Those coordinates refer to spatial frequencies $cosk_x x$ and $cosk_y y$. Because the same grid is used for $h(x, y)$ and $H(k_x, k_y)$, the signal intensity at a point in the grid is directly linked to $H(k_x, k_y)$ and describes the amount of spatial frequency components in the image at that point. Analogous to the image space, k-space is centred at $(k_x, k_y) = (0,0)$. A value in k-space at a certain location (k_x, k_y) refers to the amplitude of the sinusoidal function of the image. Because the cosine function is symmetric, there is always a second value in k-space at $(-k_x x, -k_y y)$. According to equation (77), a multiplication of the image with $cos(k_x x + k_y y) - i\, sin(k_x x + k_y y)$ needs to be performed followed by a summation across the image for all values of x and y in order to get a k-space value at a certain frequency determined by (k_x, k_y).

As previously explained, linear gradients are used for spatial localisation. These gradients introduce phase shifts that can be understood as a sinusoidal modulation. The amplitudes of the magnetisation vectors are not affected by the gradients and only depend on the pulse sequence parameters and the properties of the sample. But the direction of the magnetisation vectors is modulated in a sinusoidal fashion. Sinusoidal motion in phase is always associated with a frequency which is called "k". Phase dispersion is greater the longer the gradient remains switched on. A strong gradient causes the phase shifts to increase faster. In terms of the sinusoidal function of which k is the frequency, k is larger if the gradient is switched on for longer and increases faster the stronger the gradient is. A positive gradient causes k to progressively increase while a negative gradient has the opposite effect. Accumulated phase differences are preserved after the gradient is turned off because all the spins in the sample will then return to precessing at the Larmor frequency. In order to produce an image, echoes during

the readout period are collected with a receiver coil which sums the contributions from all the spins in the sample slice. These spatial frequencies are stored in a grid (k-space). Fourier transform of k-space produces the MR image. Values for all combinations of k_x and k_y must be collected in order to fill k-space. The coordinates k_x and k_y are proportional to the area under the curves described by G_x and G_y. For a k-space matrix of 256×256 the receiver coil must sample a signal when the frequencies k_x and k_y of the sinusoidal modulation caused by the area under G_x and G_y change from -127 to $+128$ and all possible combinations of the two frequencies.

2.4.4.1. k-Space Trajectories

There are different ways in which k-space can be filled which is described by the k-space trajectories. The three most common ways to fill k-space are with a linear, spiral, or radial trajectory (figure 18). For the linear (Cartesian) trajectory, each horizontal line in k-space is filled during the sampling of one echo with a given phase-encoding step while running through all possible frequency-encoding steps. This ensures an evenly distribution of k-space filling. As the name suggests, a spiral k-space trajectory runs through k-space in a spiral pattern. This results in an oversampling of the centre of k-space where the low spatial frequencies are contained that provide contrast information. If the centre of k-space has high amplitude frequencies then the Fourier transformed image will show high signal intensity. The periphery of k-space contains the high spatial frequencies that are associated with information regarding image resolution. The radial method of filling k-space uses diagonal lines that all go through the centre of k-space.

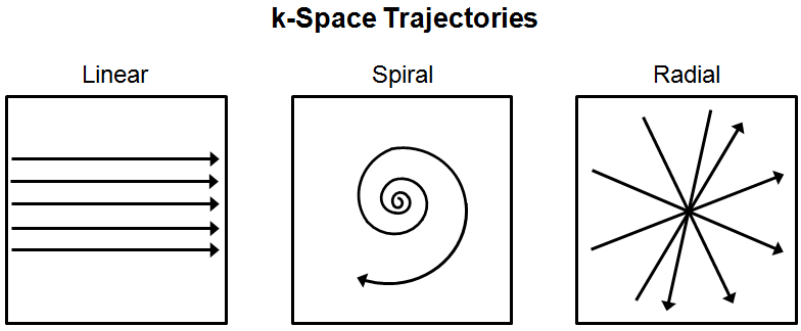

Figure 18: The most common trajectories to fill k-space, linear, spiral, or radial (reproduced from Lee [93], p. 109).

2.4.4.2. Magnitude and Phase Images

As shown in equation (77), k-space is generated by sine and cosine functions which means that k-space contains two sets. One of the sets is for the spatial frequencies of the cosine function which is symmetrical and a second is for the spatial frequencies of the sine function which is

asymmetrical. The sine frequencies are the imaginary part of a complex number (i.e. imaginary component of k-space) and the cosine frequencies are the real part (i.e. real component of k-space). However, real and imaginary components are stored separately. The sine function represents asymmetries in the image as well as contains information regarding orientation (i.e. left, right, superior, or inferior). The imaginary component of k-space produces an imaginary image and the real component of k-space produces a real image. Imaginary and real images can be combined to calculate magnitude (modulus) images and phase images. The magnitude image is the "normal" MR image that is used in most clinical settings.

$$Magnitude\ image = \sqrt{(Real\ image)^2 + (Imaginary\ image)^2}$$

The phase of the phase image goes from $-180°$ to $+180°$ and is defined as:

$$Phase\ image = arctan\left(\frac{Imaginary\ image}{Real\ image}\right)$$

k-space possess a symmetry called the Hermitian conjugate symmetry where two quadrants are identical. This applies to the first and third quadrants as well as the second and fourth quadrants. This has the advantage that by only acquiring parts of k-space the other missing parts can be inferred and therefore acquisition times can be reduced. Hermitian conjugate symmetry only applies in the case of a perfectly homogenous magnetic field and inhomogeneities will therefore introduce phase errors.

2.4.4.3. Voxel Size and Field of View

There are two important concepts that are related to k-space which are voxel size and field of view (FOV). Similar to the image, k-space is of finite length and made up of voxels with dimensions Δk $\left(\Delta k_x, \Delta k_y, \Delta k_z\right)$ that when multiplied by the matrix size for a specific dimension give the overall k-space size $k_{total}\left(k_{x,total}, k_{y,total}, k_{z,total}\right)$. Normally, the image matrix and the matrix of k-space are the same size. The inverse of the overall image size is the voxel size in k-space:

$$\Delta k_x = \frac{1}{FOV_x} \tag{78}$$

The same inverse relationship also applies between spatial resolution of the image (voxel size) and the total k-space size:

$$voxel\ size(x) = \frac{1}{k_{x,total}} \tag{79}$$

The relationships shown in equations (78) and (79) say that if spatial resolution is kept constant, increasing the FOV by a factor of two will half the voxel size in k-space. But if FOV is kept constant, then doubling spatial resolution (i.e. halving the image voxel size) will double the overall size of k-space. It is important to note that the strength of the gradients only alter the

duration of the echo during readout but they do not change the spacing or dimensions of k-space.

3. T_1 and T_2 Mapping

T_1 and T_2 mapping is the quantitative estimation of the longitudinal and transverse relaxation time constant, respectively. MRI pulse sequences that are designed to measure T_1 and T_2 are becoming increasingly important. Many diseased tissues show significant changes in their relaxation times that can be used for diagnosis by MRI.

3.1. T_1 Mapping

The aim of T_1 mapping is to calculate a parametric map from multiple MR images, typically acquired along the temporal evolution of the M_z magnetisation where every pixel has a quantitative T_1 value reflecting the average longitudinal relaxation time constant of the associated voxel of the tissue under investigation. T_1 mapping sequences are commonly used for the characterisation of nanoparticle-based contrast agents for cancer imaging applications [94]. The reason for T_1 changes can be due to changes in water content or in the molecular environment [95]. Another application is in cardiovascular MRI where various disease states of the myocardium cause a change in the longitudinal relaxation time constant [96]–[99]. T_1 mapping has also been successfully demonstrated in the human brain [100] where it can be used to better understand the effects of multiple sclerosis on white and grey brain matter [101].

The two main techniques used for T_1 mapping are the inversion recovery (IR) and saturation recovery (SR) methods. Within these two main categories, various modifications and specialised techniques have been developed such as the Modified Look-Locker Inversion Recovery (MOLLI) and the Saturation Recovery Single-Shot Acquisition (SASHA). In addition, the estimation of T_1 from a series of spoiled gradient echo (SPGR) images (DESPOT1) will be described.

3.1.1. Basic Inversion Recovery (IR) and Saturation Recovery (SR) Sequences

A generic inversion recovery (IR) sequence (figure 19) starts with an inversion pulse θ_{inv} that tips the bulk magnetisation vector from the positive z-axis to the negative z-axis. The inversion pulse does not necessarily be exactly 180°, as long as it is larger than 90° negative longitudinal magnetisation is created. The inversion pulse can be slice-selective or nonselective. The spin system is assumed to be at thermal equilibrium before the application of the inversion pulse, which means the magnetisation vector is defined as $\vec{M} = (0, 0, M_0)$. The transverse magnetisation immediately after the inversion pulse is $M_{xy} = M_0 \sin\theta_{inv}$ and the longitudinal magnetisation is given by $M_z = M_0 \cos\theta_{inv}$.

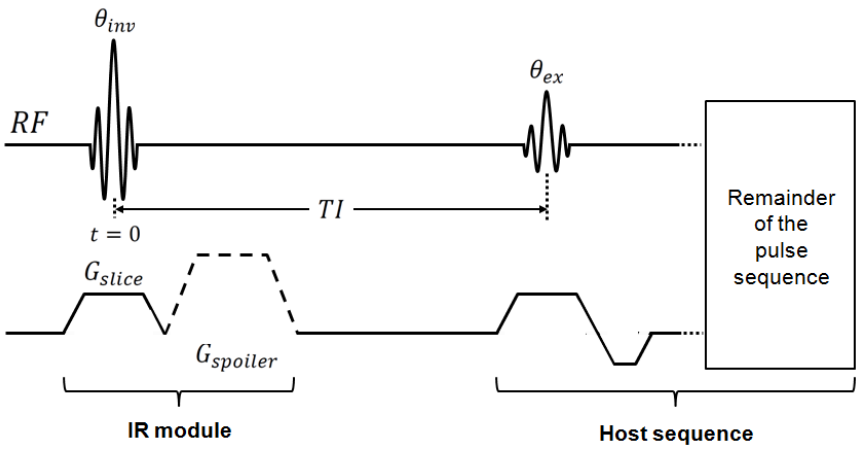

Figure 19: Generic inversion recovery sequence with the initial inversion pulse followed by a time delay (inversion time, TI) during which the longitudinal magnetisation will undergo relaxation. At the end of the inversion time a excitation pulse is applied in order to acquire an image (reproduced from Bernstein et al. [91], p. 607).

It is common practice to apply a spoiler gradient after the application of the inversion pulse to dephase the transverse magnetisation. Such a spoiler gradient does not affect the longitudinal magnetisation. The time delay after the inversion pulse is called the inversion time (TI). The longitudinal magnetisation will undergo relaxation in its attempt to return to equilibrium magnetization M_0, and align with the positive z-axis parallel to the static magnetisation vector $\vec{B}_0$. The T_1 relaxation is described by the Bloch equation (80).

$$\frac{dM_z}{dt} = \frac{M_0 - M_z}{T_1} \tag{80}$$

When using $M_z = M_0 \cos\theta_{inv}$ as the initial condition of the Bloch equation, a solution for the longitudinal magnetisation is given by

$$M_z(t) = M_0\left[1 - (1 - \cos\theta_{inv})e^{-t/T_1}\right] \tag{81}$$

The inversion recovery pulse sequence can be structured into two parts. The first part being an IR module consisting of the inversion pulse, with optional slice-select and spoiler gradients, and inversion time. The second part is the remainder of the pulse sequence referred to as the imaging sequence (figure 19). The imaging sequence is self-contained and produces the image while the IR module only prepares the magnetisation to achieve a certain contrast effect. It is possible to execute more than one IR module before the imaging sequence. Two and three IR modules lead to double and triple inversion recovery sequences, respectively. Equation (81) is only valid if the repetition time (TR) between successive inversion pulses is at least 5 times the longest T_1 measured. In practice, TR is always finite and the definition of $M_z(t)$ depends on the imaging sequence. In the case of a spin echo sequence it is given by equation (82).

$$M_z(t) = M_0\left[1 - (1 - \cos\theta_{inv})e^{-t/T_1} + e^{-TR/T_1}\right] \tag{82}$$

For the specific case of a complete inversion i.e. $\theta_{inv} = 180°$, the time-dependent longitudinal magnetisation is

$$M_z(t) = M_0\left(1 - 2e^{-t/T_1} + e^{-TR/T_1}\right) \tag{83}$$

When the inversion pulse has an angle of 90°, i.e. $M_z(0) = 0$, the sequence is referred to as a saturation recovery (SR) sequence because the longitudinal magnetisation is tipped completely in the transverse plane and therefore 'saturated'.

$$M_z(t) = M_0\left(1 - e^{-t/T_1}\right) \tag{84}$$

Figure 20 shows two graphs, one of an inversion recovery and one of a saturation recovery curve.

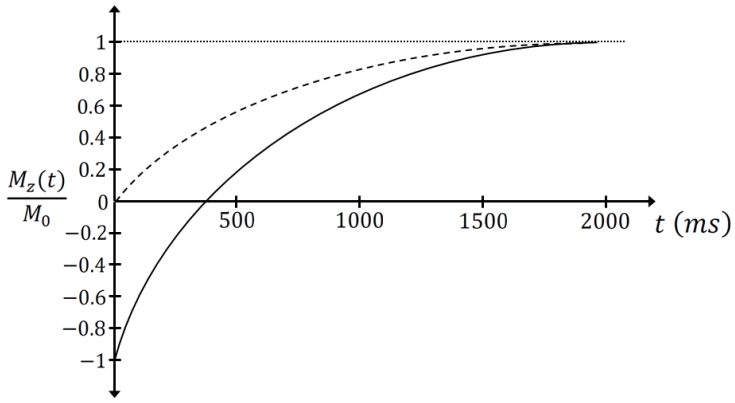

Figure 20: Comparison of inversion recovery (solid line) and saturation recovery (dashed line) (reproduced from Bernstein et al. [91], p. 610).

Longitudinal magnetisation recovers along the z-axis for as long as the time delay is chosen by the operator. Relaxation is interrupted by an excitation pulse of the imaging sequence that performs the actual imaging. In the case that the repetition time between inversion pulses is much larger than the longitudinal relaxation time of the sample, i.e. $TR \gg T_1$, the magnetisation available for imaging at the start of the imaging sequence is given by

$$M_z(TI) = M_0\left(1 - 2e^{-TI/T_1}\right) \tag{85}$$

Apart from T_1 mapping, inversion recovery sequences are also used for the nulling of magnetisation of a particular tissue by carefully selecting TI such as for black blood imaging [102]. A major disadvantage in practical applications is the long TR that is required. For that reason, it is common to use fast imaging techniques and 2D sequences are preferred over 3D.

Due to its importance to fully understand T_1 and T_2 mapping pulse sequences, the physics of an inversion pulse will be briefly discussed in the following paragraph. A radiofrequency pulse is referred to as an inversion pulse if its application results in a negative z-component in the magnetisation vector. At equilibrium, $\vec{M}_0$ is completely aligned with the static magnetic field $\vec{B}_0$ along the positive z-axis. The normal flip angle for an inversion pulse is 180° and ideally no

transverse magnetisation is produced (figure 21a). In reality, imperfections in the inversion of magnetisation are present that result in residual transverse magnetisation (figure 21 b).

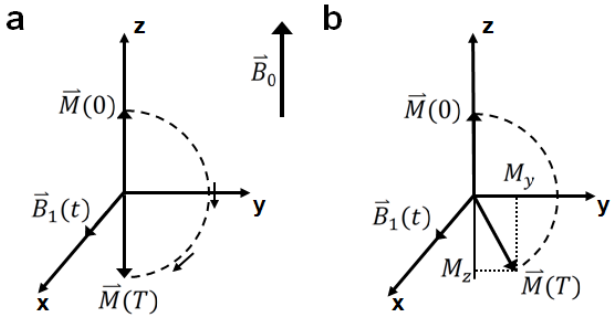

Figure 21: Behaviour of the magnetisation vector for the application of an on-resonance inversion pulse in the rotating frame of reference. a: Ideal behaviour with the magnetisation vector being aligned along the negative z-axis. b: Imperfections result in incorrect alignment of the magnetisation vector with the z-axis which leads to residual transverse magnetisation residual (reproduced from Bernstein et al. [91], p. 77).

A spoiler gradient is often applied immediately after the inversion pulse to dephase any transverse magnetisation (figure 19). Inversion pulses can be selective or nonselective which depends on the pulse width and shape. Those pulses with constant rf amplitude are usually nonselective. Pulses that have been amplitude modulated are typically frequency selective. The application of a frequency selective inversion pulse in the presence of a slice-select gradient results in a spatially selective inversion pulse. In the case that the inversion pulse is applied along the x-axis and spins are on-resonance, a precession of the magnetisation about $\vec{B}_1$ in the transverse plane results. Mathematically, the magnetisation can be described as

$$\vec{M}(t) = M_0 \begin{bmatrix} 1 & 0 & 0 \\ 0 & \cos\theta(t) & \sin\theta(t) \\ 0 & -\sin\theta(t) & \cos\theta(t) \end{bmatrix} \begin{bmatrix} 0 \\ 0 \\ 1 \end{bmatrix} \tag{86}$$

and

$$\theta(t) = \gamma \int_0^t B_1(t')dt' \tag{87}$$

If the spins are off-resonance, an off-resonance term $(\Delta\omega/\gamma)$ along the z-axis is established (figure 22).

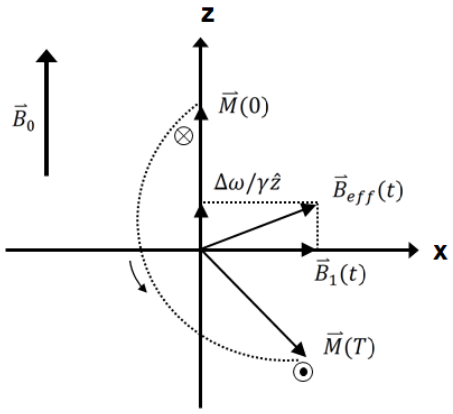

Figure 22: Magnetisation vector rotates about the effective field which creates a transverse component. This off resonance effect on an inversion pulse is caused by the off-resonance term $(\Delta\omega/\gamma)$ (reproduced from Bernstein et al. [91], p. 80).

This causes the effective magnetic field $\vec{B}_{eff}$ to be no longer aligned with the x-axis and M_x has a nonzero value because the magnetisation vector rotates now about $\vec{B}_{eff}$. Even with a flip angle of 180°, this results in a transverse component of the magnetisation vector. Spins that are off-resonance can come from magnetic field inhomogeneities, changes in magnetic susceptibility, chemical shift, and application of a slice-select gradient. The usual solution to off-resonance effects in an inversion recovery pulse sequence is to use an adiabatic inversion pulse which is insensitive to B_1 inhomogeneities.

3.1.1.1. Adiabatic inversion pulse

Adiabatic pulses are fundamentally different to normal, amplitude modulated rf pulses. They are frequency (or phase) and amplitude modulated. The type of frequency and amplitude modulation determines the flip angle. Through changing the two modulation functions (i.e. frequency and amplitude) it is possible to uniformly flip spins exposed to different B_1 fields with the same flip angle.

Adiabatic pulses must fulfil the adiabatic condition. According to that the bulk magnetisation vector follows the effective magnetic field $\vec{B}_{eff}$. As the bulk magnetisation also precesses about the effective field in a cone-shape, it is important that the direction of $\vec{B}_{eff}$ only changes negligibly during one precession period. The adiabatic condition can be mathematically expressed as

$$\left|\frac{d\psi}{dt}\right| \ll \gamma\left|\vec{B}_{eff}\right| \tag{88}$$

For an rf pulse of the form $B_1(t) = A(t)e^{-i\omega_{rf}(t)t}$ where the frequency is described by a cosine function $\left(\omega_{rf}(t) = \omega - \gamma B_z \cos \xi t\right)$ and the amplitude is described by a sine function $(A(t) = B_x \sin \xi t)$, the effective magnetic field, i.e. its direction ψ and amplitude $\left|\vec{B}_{eff}\right|$, are as follows

$$\psi = \arctan\left(\frac{B_x \sin \xi t}{B_z \cos \xi t}\right) \tag{89}$$

$$\left|\vec{B}_{eff}\right| = \sqrt{(B_x \sin \xi t)^2 + (B_z \cos \xi t)^2} \tag{90}$$

The adiabatic condition is satisfied if the modulation frequency ξ is slow and/or $\vec{B}_{eff}$ is strong. Because the bulk magnetisation follows the effective field under the adiabatic condition, when ψ has completed a 180° rotation $(t = \pi/\xi)$ the magnetisation vector has also completed a full inversion. However, the inversion trajectory is different compared to normal inversion pulses.

For the application of a full inversion, the hyperbolic secant pulse is usually used. This adiabatic pulse is also sometimes referred to as the Silver-Jospeh-Hoult pulse after the scientists who first described it. Mathematically it is given as

$$B_1(t) = [A_0 \operatorname{sech}(\beta t)]^{1+i\mu} \tag{91}$$

In that equation, A_0 is the amplitude, μ is a parameter (dimensionless) and β is the angular frequency of the modulation function. The frequency and amplitude modulation functions are given as

$$A(t) = A_0 \operatorname{sech}(\beta t) \tag{92}$$

$$\Delta\omega(t) = -\mu\beta \tanh(\beta t) \tag{93}$$

From equations (92) and (93) it becomes apparent that as the time variable t goes from $-\infty$ to ∞, the two modulation functions behave very differently. The frequency modulation function starts at its maximum (i.e. $\mu\beta$), crosses the ordinate line (i.e. zero line) at $t = 0$ and continues with negative polarity until its minimum (i.e. $-\mu\beta$). The amplitude modulation function starts with zero amplitude, increases to its maximum value at $t = 0$ after which it returns back to zero (figure 23).

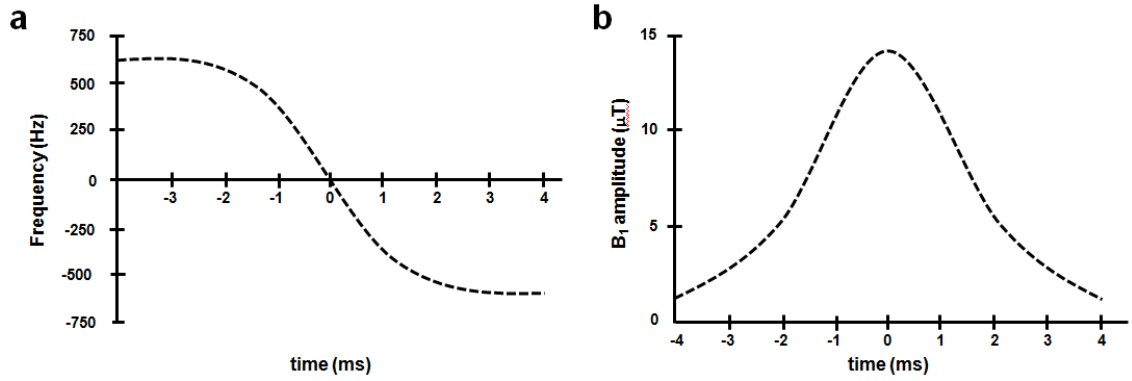

Figure 23: Modulation functions for a adiabatic inversion pulse (hyperbolic secant pulse). a: Frequency modulation function. b: Amplitude modulation function (reproduced from McRobbie et al. [92], p. 235).

Adiabatic inversion pulses are a popular choice when using surface coils as the transmission of B_1 fields is very nonuniform. They have also been used with short TI inversion recover (STIR) sequences for the inversion of lipid signals and in fluid-attenuated inversion recovery (FLAIR) to attenuate the cerebrospinal fluid for neuroimaging. Tissue perfusion measurements using arterial spin tagging is another common application [91].

3.1.2. Look Locker Sequence

A problem of the classical IR sequence is its time inefficiency. This is because a very long longitudinal recovery period is employed to ensure full recovery of the M_z magnetisation which results in a long acquisition time. In order to increase efficiency, a set of rf pulses with small angles α are employed to sample the longitudinal magnetisation after application of the inversion pulse. These imaging pulses of angle α are separated by a time τ. A separate phase encoding gradient of constant gradient strength is employed for each rf pulse. For a longitudinal recovery time of $N\tau$, a total of N data points on the longitudinal relaxation curve can be collected. If $TR = N\tau$, the sequence is conducted in the most efficient way. The N data points or images after reconstruction are inversion recovery curves at different inversion times $TI_n = n\tau, n \in \{0,1,2,\dots,N\}$.

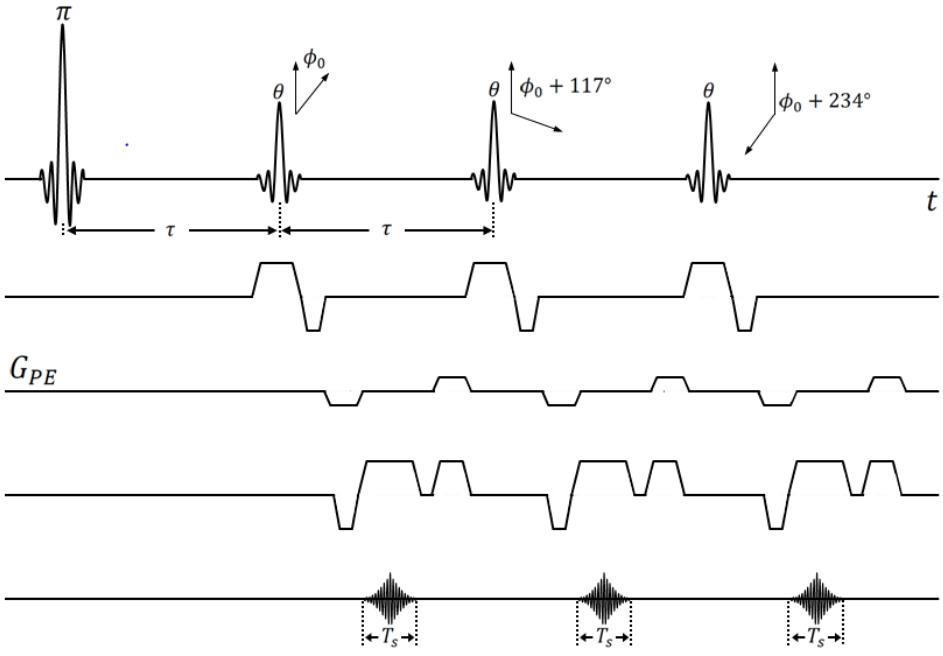

Figure 24: Sequence diagram of a Look-Locker acquisition where an inversion pulse is followed by a train of small flip angle rf pulses between which an echo is formed (reproduced from Brown et al. [89], p. 653).

A typical Look-Locker sequence diagram is illustrated in figure 24. The following mathematical description of the Look-Locker technique will mainly follow Brown et al. [89]. After an inversion pulse θ follows a train of $(N-1)$ small angle α rf pulses each separated by a time delay τ. The N^{th} pulse will be an inversion pulse again with which a new cycle starts. It shall be assumed that before each α-pulse no remnant transverse magnetisation will be present. The longitudinal magnetisation immediately prior to the n^{th} rf pulse is symbolised as M_n^- with $n \in \{1,2,\dots,N\}$ and given as

$$M_n^- = M_1^-(E_1\cos\alpha)^{n-1} - M_\infty^-((E_1\cos\alpha)^{n-1} - 1) \tag{94}$$

In the specific case of M_1^- it takes the form

$$M_1^- = -E_1 M_N^- + M_0(1-E_1) \tag{95}$$

In equation (94) and (95), M_∞^- is the steady-state value and M_0 is the equilibrium magnetisation. The magnetisation prior to the next inversion pulse in the steady-state is given by

$$M_N^- = \frac{M_\infty^-(1-(E_1\cos\alpha)^{N-1}) + M_0(1-E_1)(E_1\cos\alpha)^{N-1}}{(1+\cos\alpha\,(E_1\cos\alpha)^{N-1})} \tag{96}$$

The signal after the n^{th} rf pulse is mathematically described by

$$S(\tau_n) = \beta\left\{1 - DR_{norm}\cdot e^{-(n-1)\tau/T_1^*}\right\} \tag{97}$$

with DR_{norm} being the dynamic ratio which is the difference in the limiting values of the signal and $\beta \equiv M_\infty^-\sin\alpha$.

$$DR_{norm} \equiv \frac{M_1^- - M_\infty^-}{M_\infty^-} = \frac{\cos\theta\,(1-(E_1\cos\theta)^{N-1})}{1+\cos\theta(E_1\cos\theta)^{N-1}} + 1 \tag{98}$$

This leads to the definition of the apparent T_1^*.

$$\frac{\tau}{T_1^*} \equiv \frac{\tau}{T_1} - \ln(\cos\alpha) \tag{99}$$

In the case that the flip angle α is made vanishingly small ($\alpha \to 0$)

$$\lim_{\alpha\to 0}\left(\frac{\tau}{T_1^*}\right) \to \frac{\tau}{T_1} \tag{100}$$

$$\lim_{\alpha\to 0}(\beta) \to \alpha M_\infty^- \tag{101}$$

and for $N \gg 1$

$$\lim_{\alpha\to 0}(DR_{norm}) \to \frac{(1-E_1^{N-1})}{(1+E_1^{N-1})} + 1 = \frac{2}{(1+E_1^{N-1})} \simeq 2 \tag{102}$$

The measured signal will then approximate the following for a small flip angle α.

$$\lim_{\alpha\to 0} S(\tau_n) \simeq M_\infty^-\alpha 1 - 2e^{-(n-1)\tau/T_1} \tag{103}$$

As long as the flip angle α is small, the relaxation of the longitudinal magnetisation back to equilibrium after an inversion pulse is not disrupted. Because of the exponential signal behaviour between α-pulses, it is possible to do a nonlinear least square fit using equation (97) with the three parameters β, DR and T_1^*. Once the apparent longitudinal relaxation time is determined, T_1 can be found using equation (99).

3.1.2.1. Modified Look-Locker Inversion Recovery (MOLLI)

MOLLI was developed by Messroghli et al. [97] to overcome the limitations of the conventional Look-Locker (LL) sequence that up to this point was the gold standard for T_1 mapping. The main problem of the LL technique was its limitation for cardiac imaging. Because the data acquisition happens continuously irrespective of the cardiac motion, T_1 mapping can only be done for manually defined regions of interest and not pixel-by-pixel. This leads irrevocably to errors from misregistration. MOLLI allows for accurate T_1 mapping of the myocardium within a single breath hold. That is achieved with two modifications compared to the LL approach. MOLLI allows selective data acquisition at a specific point of time in the cardiac cycle over a series of successive heart beats. That means that only one image needs to be acquired per heartbeat. Second, the multiple LL data sets with different inversion times that make up the MOLLI sequence can be merged into one data set. Having multiple LL data sets with different TIs available is invaluable to sample the relaxation curve sufficiently to get an accurate T_1 value. The readout of MOLLI is usually done with a balanced steady-state free precession (bSSFP) sequence [103], [104] because of better SNR compared to conventional gradient echo readout. For a more detailed description of bSSFP please refer to chapter 4.5.1. and appendix I. The steady-state that is reached through the readout is less than the initial magnetisation M_0. The longitudinal recovery is described by an apparent relaxation time T_1^* that is less than T_1. T_1 can be found from T_1^* according to equation (105). Figure 25 illustrates the MOLLI sequence scheme.

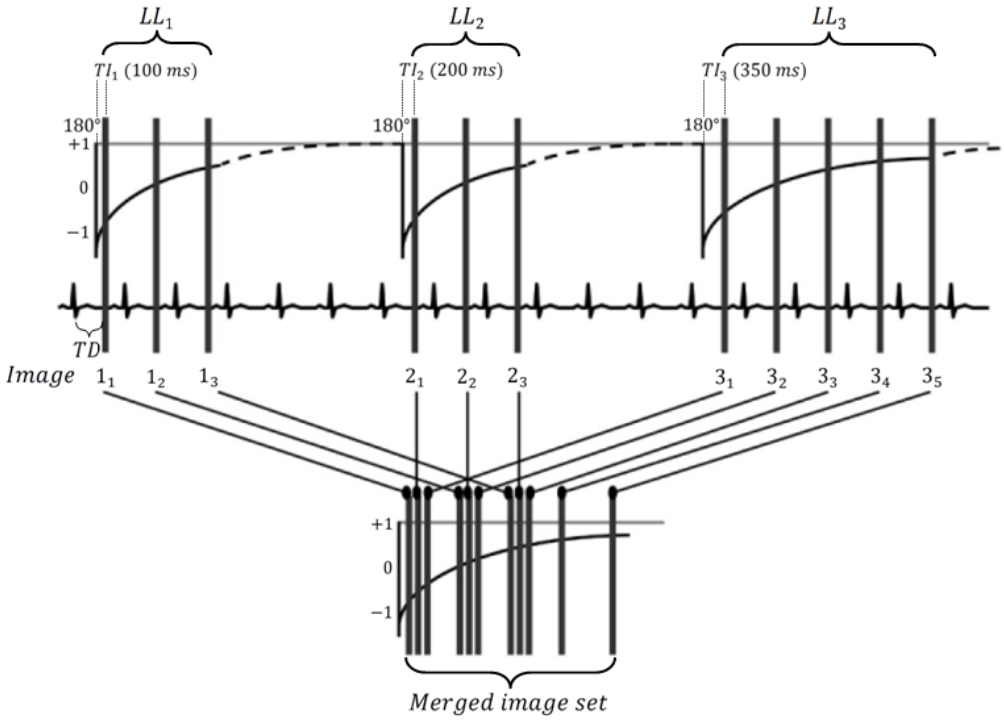

Figure 25: Illustration of the MOLLI sequence scheme. Three Look-Locker experiments are performed with three different TIs. In a postprocessing step the images are regrouped to reflect their effective inversion time (reproduced from Messroghli et al. [97], p. 142).

In the original publication, it was described with three successive LL acquisitions that are ECG triggered for application in cardiac imaging. The first and second LL acquisition (LL_1, LL_2) acquired three frames each, one frame per heart beat. The third LL acquisition (LL_3) acquires five frames. Each frame is a single shot acquisition and a recovery time of at least 4 seconds was given for the magnetisation to recover fully after each LL experiment. This is important to ensure the same initial magnetisation is flipped and therefore the same sampling at different LL experiments is from the same recovery curve. All three LL acquisitions start with a non-selective 180° adiabatic inversion pulse. The inversion time to the first single shot readout changes for each LL experiment (TI_1, TI_2, TI_3). However, the trigger delay (TD) from the R-wave to the first readout remains constant to ensure images are always acquired at the same point of the cardiac cycle. That means that the time of the inversion pulse changes in each of the three LL experiments. The time delay between two readouts is a heartbeat interval and therefore depends on the subjects heartbeat. In order to receive one data set at the end, images have to be sorted according to $t = TI + (n-1)RR$. In that equation, n is the number of images in a specific LL acquisition and RR is the heart beat interval. After sorting the images, the Levenberg-Marquardt algorithm for non-linear curve fitting problems with three parameters can be applied [97]

$$SI = A - Be^{-(t/T_1^*)} \tag{104}$$

Once A, B, and T_1^* have been found, T_1 can be determined with

$$T_1 = T_1^* \left(\frac{B}{A} - 1\right) \tag{105}$$

Precision of the MOLLI method depends on the number of frames sampled along the recovery curve. The factor $\left(\frac{B}{A} - 1\right)$ is called the Look-Locker correction factor and stems from the fact that several readouts are being used with low flip angles.

3.1.2.2. Shortened Modified Look-Locker Inversion Recovery (ShMOLLI)

ShMOLLI was developed for cardiac MRI to acquire high precision and high resolution T_1 maps of the heart in a short breath-hold of 9 heartbeats. The ShMOLLI sequence uses a 5(1)1(1)1 sampling scheme (7 images) in 3 IR intervals that are separated by one RR interval (T_{RR}) (figure 26) [95].

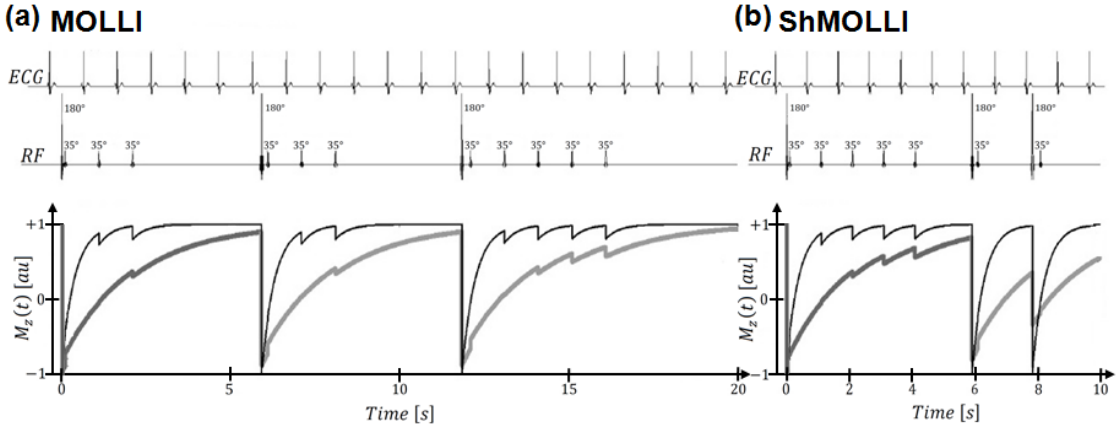

Figure 26: Comparison of simulated signal behaviour of the MOLLI (a) and ShMOLLI (b) sequences steady-state free precession readouts (reproduced from Piechnik et al. [105], p. 3).

Because of the shortened recovery period, the longitudinal magnetisation cannot fully recover and will significantly be affected by the preceding IR interval. As a result, the data collected in the 2nd and 3rd IR interval cannot simply be combined with the 1st IR interval to produce one data set as it was done for MOLLI. Therefore, conditional data analysis is used to solve this problem. If T_1 of the tissue is long, only acquisitions 1-5 are used for the fitting. Sample 6 is included in the fitting if T_1 is shorter than T_{RR} but larger than $0.4T_{RR}$. For T_1 shorter than $0.4T_{RR}$, all 7 acquisitions are utilised. The thresholds T_{RR} and $0.4T_{RR}$ are adopted according to the errors of the fit as T_1 is unknown [105]. When all 7 images are acquired and used for the fitting of the magnetisation recovery curve, approximately 30% in precision is sacrificed because of exclusion of data and the faster acquisition time compared to MOLLI [95].

3.1.2.3. Look-Locker Echo Planar Imaging Sequence (LL-EPI)

The LL-EPI sequence consists of a magnetisation preparatory Look-Locker module (nonselective inversion pulse followed by multiple small flip angle α acquisitions) and an echo planar imaging (EPI) module (figure 27) [91]. The description of EPI is beyond the scope of this work but detailed description can be found in Brown et al [89], Bernstein et al. [91], Schmitt et al. [106] and DeLaPaz [107] among others.

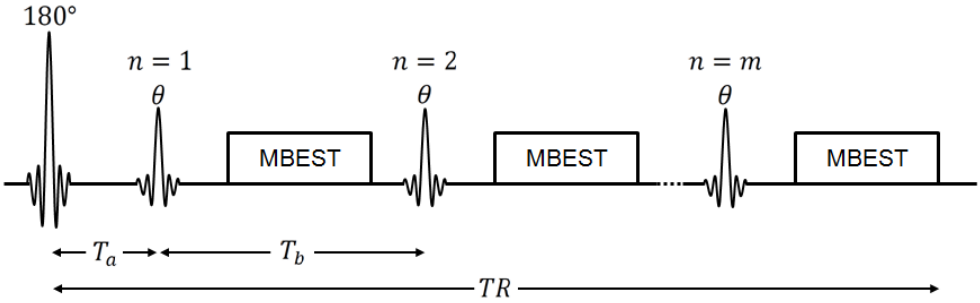

Figure 27: Fast T_1 measurement with a Look-Locker sequence that uses an EPI module for a one-shot acquisition (reproduced from Gowland and Mansfield [108], p. 352).

For $TR \gg T_1$, the signal after the n[th] readout is given by

$$S_n = \int_{-\infty}^{+\infty} M_{z,n} \sin\alpha \; e^{-TE/T_2^*} dz \tag{106}$$

in which $M_{z,n}$ is given by

$$M_{z,n} = M_0 \left[\frac{(1-B)(1-(AB)^{n-1})}{1-AB} + AB^{n-1}(1-C) - C(AB)^{n-1} \right] \tag{107}$$

In equation (107), $A = \cos\alpha$, $B = e^{-T_b/T_1}$, and $C = e^{-T_a/T_1}$. The time constants T_a and T_b are defined in figure 27. The echo time is defined as the time from the application of the readout pulse α to the point in time when the signal from the centre of k-space is collected. A T_1 map is obtained by fitting the data from each EPI image to equation (106) by using a nonlinear least squares method [108]–[110]. This technique is able to produce T_1 maps with high temporal and spatial resolution in less than 3 seconds. The fast acquisition brings the disadvantage of low SNR which means finding the optimal sequence parameters is important to achieve the best possible T_1 map. There are several applications that require such fast imaging techniques such as for the study of contrast agent uptake in the brain [111] or the MRI of fetal organs [112].

3.1.3. Look-Locker with a Fast Low Angle Shot (FLASH) Readout

The concept of this technique as with the other Look-Locker methods is to acquire a series of images (here: snapshot FLASH images) to sample the recovery curve of the magnetisation after an inversion pulse. Because rf pulses are applied during sampling the recovery curve, an

apparent relaxation time T_1^* and a saturation value for the equilibrium magnetisation M_0^* must be considered. After application of the inversion pulse to a spin system at equilibrium, the temporal recovery of the magnetisation is given by [113], [114]

$$M(t) = M_0^* - (M_0 + M_0^*)e^{-t/T_1^*} \tag{108}$$

and

$$\frac{1}{T_1^*} = \frac{1}{T_1} - \frac{1}{TR}\ln(\cos\alpha) \tag{109}$$

In equation (109), α is the flip angle and M_0^* is given by

$$M_0^* = M_0 \frac{1 - e^{-TR/T_1}}{1 - e^{-TR/T_1^*}} \tag{110}$$

A condition of this method is that $TR < T_1^*$ which means equation (110) can be written as

$$M_0^* = M_0 \frac{T_1^*}{T_1} \tag{111}$$

A three-parameter fit can be performed with the signal intensities according to

$$S(t) = A - Be^{-t/T_1^*} \tag{112}$$

Equation (112) yields values for A, B, and T_1^* from which T_1 can be found according to

$$T_1 = T_1^* \left(\frac{B}{A} - 1\right) \tag{113}$$

3.1.4. Saturation Recovery Single Shot Acquisition (SASHA)

Saturation recovery methods have a lower dynamic range compared to inversion recovery techniques but they could potentially offer improved accuracy. The advantage SR methods have is that each acquisition is independent of the other. By saturating the magnetisation before each measurement, the history of what has happened before the current measurement to the magnetisation vector is erased. SASHA is using a bSSFP [103], [104] readout (see chapter 4.5.1.) that offers good SNR and blood-tissue contrast. The SASHA scheme for T_1 mapping of the heart is shown in figure 28 [95].

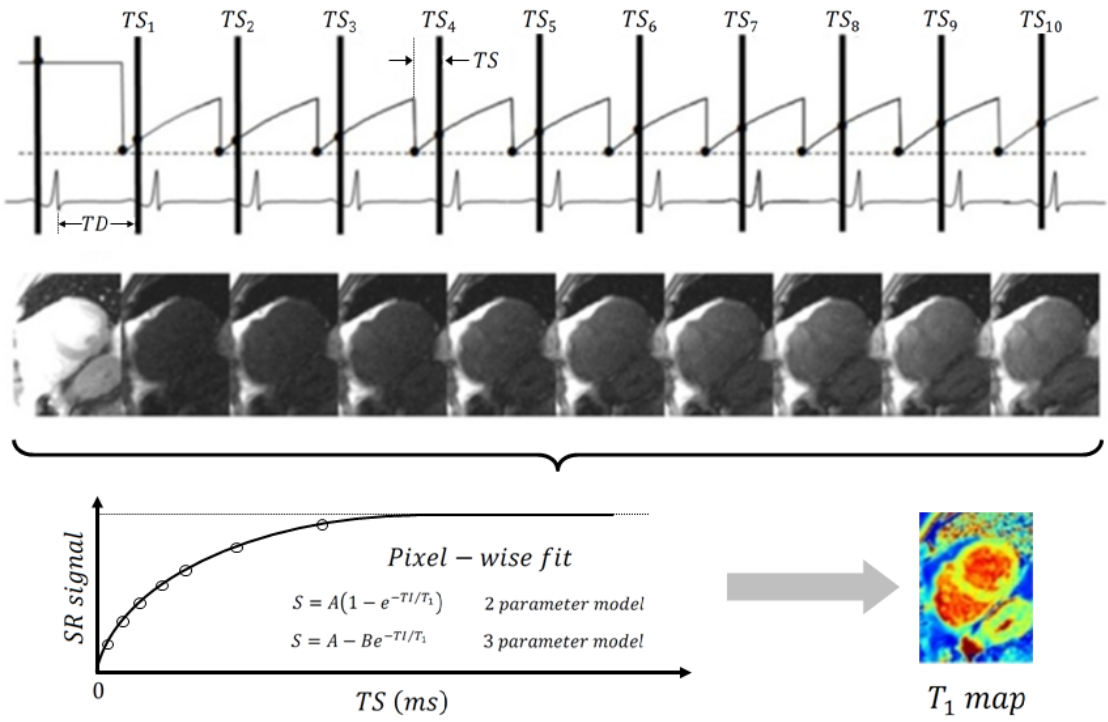

Figure 28: T_1 mapping of the heart with saturation recovery single shot acquisition (SASHA). The first image is acquired before the application of any saturation preparation which is followed by a series of images acquired with a 90° saturation pulse (reproduced from Kellman and Hansen [95], p. 5).

In the original publication, ten images were acquired where the first image is acquired before the application of any saturation preparation. After that a 90° saturation pulse is applied and one image is acquired in every RR interval. The saturation recovery time (TS) which is the time from the end of the saturation pulse to the centre line of k-space changes for every heartbeat. That way, multiple points along the SR curve are sampled. In addition, a variable trigger delay is added before the saturation pulse to ensure a constant cardiac phase is achieved for all images. The magnetisation at the start of a SASHA acquisition is

$$M(0) = 1 - \eta_{actual} e^{-(TS-A)/T_1} \tag{114}$$

In equation (114), η_{actual} is the saturation pulse efficiency and Δ describes the time from the beginning of imaging to the centre of k-space [115]. The recovery of the magnetisation is not affected by the readout which means no apparent $T_1^* < T_1$ has to be considered and therefore no correction is needed. Because no apparent T_1^* is produced, a higher flip angle can be utilised for the readout. The advantage of using a higher flip angle is that the signal-to-noise ratio (SNR) of the sequence can be increased. However, this might also slightly change the shape of the SR curve which means that instead of a two-parameter signal model $S(TS) = A\left(1 - e^{-TS/T_1}\right)$ a three-parameter model must be used for the fitting procedure.

$$S(TS) = A - Be^{-TS/T_1} \tag{115}$$

An additional fitting parameter however leads to a decrease in precision [95].

3.1.5. Driven Equilibrium Single Pulse Observation of T_1 (DESPOT1)

DESPOT1 is based on a spoiled gradient echo (SPGR) sequence (see appendix I) which is a fast gradient echo sequence in which the longitudinal magnetisation reaches a nonzero steady state. It is also referred to as steady-state incoherent (SSI) sequence in the literature [89]. The repetition time is selected to be shorter than the transverse relaxation time of the tissue. Residual transverse magnetisation at the end of each TR interval is spoiled which means a steady state is only achieved in the longitudinal magnetisation [104]. In the DESPOT1 sequence, after an initial inversion pulse of 180° and the time delay TI, a series of small flip angle excitations α-pulses are applied. The magnetisation will eventually reach a steady-state for which the effective time constant T_1^* can be defined as

$$T_1^* = \frac{TR}{TR/T_1 - \ln(\cos\alpha)} \tag{116}$$

The signal intensity of the spoiled gradient echo (SI_{SPGR}) depends on T_1, TR, α, and the equilibrium magnetisation M_0.

$$SI_{SPGR} = \frac{M_0(1 - E_1)\sin\alpha}{1 - E_1\cos\alpha} \quad and \quad E_1 = e^{-TR/T_1} \tag{117}$$

Equation (117) describes a curve that is highly T_1 weighted when TR is kept constant and the flip angle α is incrementally increased (figure 29a). By rearranging equation (117), it can be represented in a linear form (figure 29b) where the ordinate intercept is given as $M_0(1 - E_1)$ and the gradient is defined as E_1.

$$\frac{SI_{SPGR}}{\sin\alpha} = E_1\frac{SI_{SPGR}}{\tan\alpha} + M_0(1 - E_1) \tag{118}$$

Performing a linear regression allows to determine T_1 and M_0 as follows

$$T_1 = -\frac{TR}{\ln m} \quad \text{and} \quad m \Rightarrow gradient \tag{119}$$

$$M_0 = \frac{b}{1 - m} \quad \text{and} \quad b \Rightarrow ordinate\ intercept \tag{120}$$

The advantage of this method is that the overall measurement time can be shortened by a lot while maintaining a good SNR. This becomes even more important when measuring tissues with long relaxation times. It is often employed for 3D imaging because the DESPOT1 sequence can easily combined with fast imaging techniques and possess a high inherent 3D resolution [89].

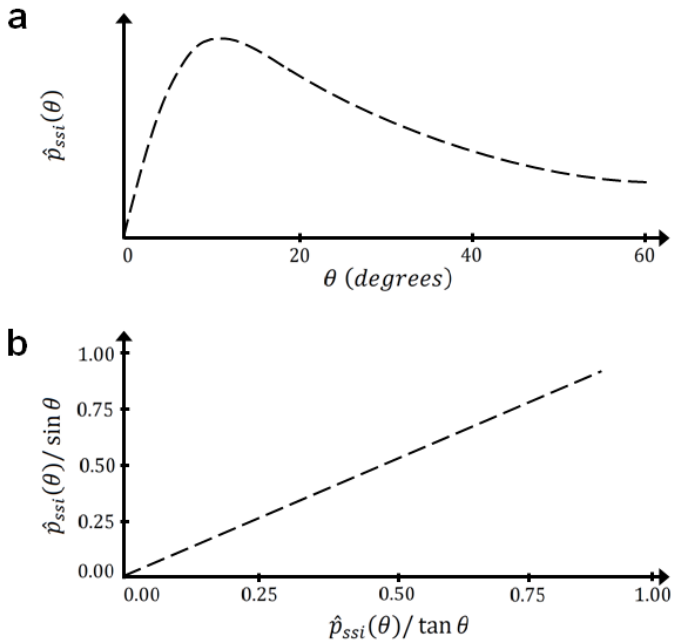

Figure 29: Driven equilibrium single pulse observation of T_1 (DESPOT1). a: Curve of spoiled gradient echo for a range of different flip angles α which is highly T_1 weighted. B: Rearranging the signal equation defining the spoiled gradient echo allows its representation in linear form (reproduced from Brown et al. [89], p. 655).

The effectiveness of this method in providing an accurate T_1 map depends on finding the optimum flip angle for the measurement. This can be done numerically or analytically [116].

3.1.5.1. Numerical Method

It was shown that it is sufficient to just measure the signal with two flip angles optimised for a particular TR/T_1 combination [117]. The regression line described by equation (118) contains data points of the form $\left(\frac{SI_{\alpha,i}}{\tan\alpha_i}, \frac{SI_{\alpha,i}}{\sin\alpha_i}\right)$. If only two measurements are needed with flip angles α_1 and α_2, then only two data points are available for the linear regression. If it is assumed that each point has the same intrinsic error, then the gradient of the linear regression becomes better to estimate the further apart the two data points are. The ordinate distance between two data points is called the normalised dynamic range (DR).

$$DR = \frac{SI_{\alpha,2}}{M_0 \sin\alpha_2} - \frac{SI_{\alpha,1}}{M_0 \sin\alpha_1} \tag{121}$$

When the location of the data points determines the precession, a fractional signal of the points can be defined.

$$FS = \left(SI_{\alpha,1} + SI_{\alpha,2}\right)/2SI_{\alpha,E} \tag{122}$$

In equation (122), $SI_{\alpha,E}$ is the Ernst signal which is obtained with the Ernst angle. By maximising $DR{\times}FS$, the optimal angles for any TR/T_1 combination can be found [116].

3.1.5.2. Analytical Method

The above defined product $DR{\times}FS$ has its maximum when $SI_{\alpha,1} = SI_{\alpha,2}$ which means the following simplification can be made.

$$f = \frac{SI_{\alpha,1}}{SI_{\alpha,E}} = \frac{SI_{\alpha,2}}{SI_{\alpha,E}} \tag{123}$$

Deoni et al. [116] have plotted the product $(DR{\times}f)$ versus TR/T_1 and f and used a polynomial to fit the data and find its maximum. It was shown that the best precision for determining T_1 is achieved with flip angles that lead to $SI_{\alpha,1} = SI_{\alpha,2} = 0.71SI_{\alpha,E}$. By expanding the signal intensity from equation (117) to $SI = f{\times}SI_{\alpha,E}$ and after some algebraic rearrangements an analytic solution for the optimal angles is found [116].

$$\alpha = \cos^{-1}\left(\frac{f^2E_1 \pm \left(1 - E_1^2\sqrt{1-f^2}\right)}{1 - E_1^2(1-f^2)}\right) \tag{124}$$

3.2. T_2 Mapping

The aim of T_2 mapping is to calculate an image from multiple MR images where every pixel has a quantitative T_2 value reflecting the average transverse relaxation time constant of the associated voxel of the tissue under investigation. A major application of reliable T_2 mapping techniques is molecular imaging such as the cell tracking with MRI contrast agents [118]. The active and passive targeting of tumour cells with iron-oxide nanoparticles is of particular interest. A decrease in the signal intensity of the tumour area on T_2 maps has been shown to correlate with successful targeting in xenograft models [119]. Several authors have also reported the successful application of T_2 mapping for the detection [120], [121] and characterisation [122], [123] of prostate cancer in patients. Another application is in cardiac MR where elevated T_2 values have been reported for acute myocardial infarction [124], [125] and myocarditis [126]. Neurologic diseases such as multiple sclerosis [127], epilepsy [128] and schizophrenia [129] show differences in transverse relaxation times compared to healthy brains.

This work will describe three techniques that have been shown to provide successful T_2 mapping results. Traditionally, a multi-echo spin echo (ME-SE) sequence is used with incrementally increasing echo times. More recent methods include the estimation of T_2 from multiple bSSFP (see chapter 4.5.1. and appendix I) images (DESPOT2) and the use of a T_2-weighted magnetisation preparation (T_2 Prep) technique.

3.2.1. Multi-echo Spin Echo (ME-SE) Sequence

The basic spin echo sequence consists of an initial 90° excitation pulse which brings the magnetisation vector in the transverse plane. After a time delay a second 180° refocusing pulse is applied that flips the dephasing spins about the transverse plane and brings them back together to form an echo. After the formation of an echo, the spins start to dephase again which means that multiple refocusing pulses can be applied to produce a series of spin echoes that have alternating positive and negative amplitudes (figure 13, chapter 2). Such a series of echoes is referred to as an echo train. A typical echo train length for T_2 mapping is about 16 echoes long although shorter trains can also be sufficient. The range of echo times should go up to roughly three times the estimated T_2 value [91]. Nonideal slice profiles can cause problems in 2D imaging techniques of the spatially varying flip angles of the slice-selective excitation and refocusing pulses. The echo amplitude of a spin echo for a $90^{\circ} - \tau - 180^{\circ}$ pulse sequence is proportional to $\sin^3\theta$ where θ is the flip angle of the excitation pulse. All other echoes have a reduction in amplitude by $\sin^2\theta$. The amplitude of the spin echo after the nth 180°-pulse is therefore proportional to $\sin^{2n+1}\theta$. The signal of the nth echo can be calculated by integrating the slice profile $p(\theta)$.

$$SI(TE_n) = M_0 e^{-TE_n/T_2}\left[\int d\theta\, p(\theta)\sin^{2n+1}\theta\right] \tag{125}$$

In equation (125) it is assumed that all echoes are separated by a time TE and that the slice profile is normalised $\int d\theta\, p(\theta) = 1$. With increasing n, the bracketed expression is decreasing which is the signal loss. The exponential e^{-nf} with $f > 0$ can approximate that signal loss because when plotting the bracketed expression of equation (125) for a time-truncated sinc pulse, it resembles an exponential decay. The signal expression of equation (125) can therefore be written as

$$SI(TE_n) = M_0 \sin\theta\, e^{-TE_n/T_2} e^{-nf} \tag{126}$$

When fitting $SI(TE_n)$ to an exponential function, an incorrect T_2 value is obtained that underestimates the "true" T_2 value. It is therefore called 'apparent' T_2 value or $T_{2,app}$.

$$\frac{1}{T_{2,app}} = \frac{1}{T_2} + \frac{f}{TE} \tag{127}$$

The underestimation of the transverse relaxation time can be reduced by increasing the echo time to its maximum. However, making the echo time too large also decreases the SNR. To resolve this problem, nonselective 'hard' pulses can be used for the refocusing pulses [89]. Named after its inventors, this sequence is called the Carr-Purcell T_2 mapping sequence. Compared with individual spin echo experiments, the Carr-Purcell sequence compensates for irreversible dephasing from the diffusion of spins through magnetic field inhomogeneities as well as considerably shortens acquisition times.

$$SI(TE) = M_0 \left[e^{\left(\frac{-TE}{T_2}\right)} \cdot e^{\left(\frac{-\gamma^2 \Delta B^2 D \tau^2 TE}{3}\right)} \right] \tag{128}$$

In equation (128), D is the diffusion coefficient, 2τ is the echo spacing and ΔB the magnetic field inhomogeneity. For a small echo spacing, the second term approaches 1 and the signal is described by the first exponential term that depends on T_2. A well known problem is imperfections in the 180° refocusing pulses which over the duration of the echo train can start to accumulate and cause incorrect T_2 estimates. The Carr-Purcell-Meiboom-Gill (CPMG) sequence which is a modification of the above sequence compensates for B_1 field inhomogeneities by applying the excitation pulse $\left(90^{\circ}_{x}\right)$ and the train of refocusing pulses $\left(180^{\circ}_{y}\right)$ 90° out of phase. All refocusing pulses are still equally spaced by a distance of 2τ but all echoes are positive in this case (figure 30).

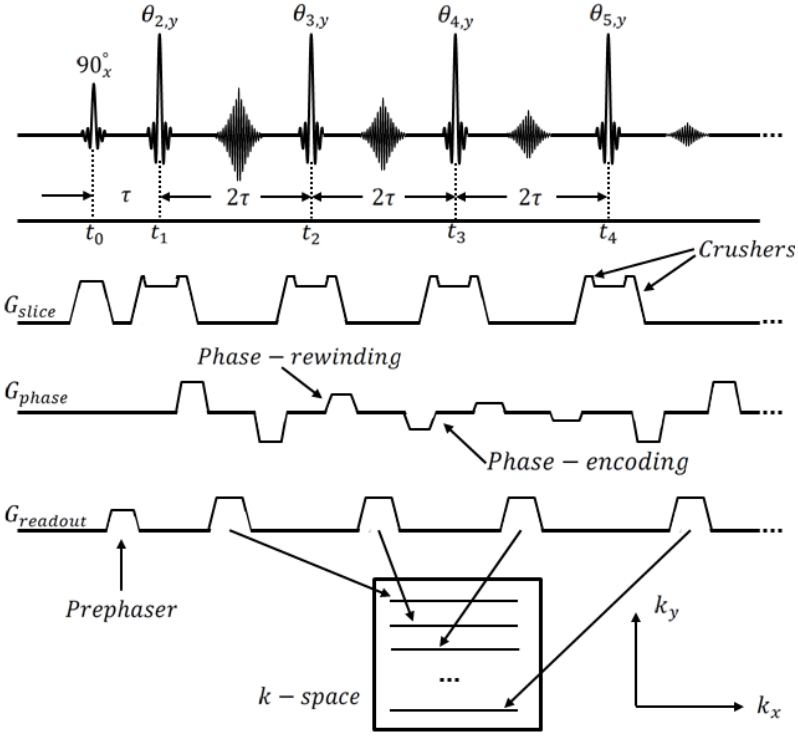

Figure 30: Sequence diagram of a Carr-Purcell-Meiboom-Gill (CPMG) sequence showing slice-select, phase-encoding, and readout gradients used to fill k-space (reproduced from Bernstein et al. [91], p. 778).

Imperfections in the refocusing pulses cause the first and every odd numbered 180° pulse to be too small. However, the even refocusing pulses will have the correct height and precise T_2 measurements are possible by only considering the even echoes. It must be noted that T_1-weighting can potentially be introduced in the measured signal by the stimulated echoes which will interfere in the analysis when trying to fit the data to a monoexponential decay curve. Magnitude reconstruction causes the noise floor to be nonzero which leads to an overestimation

of the T_2 values. This can be resolved by utilising a three parameter nonlinear fitting model of the form $S(TE) = N + Ae^{-TE/T_2}$.

3.2.2. Driven Equilibrium Single Pulse Observation of T_2 (DESPOT2)

The driven equilibrium single pulse observation of T_2 technique uses a preexcitation refocused SSFP sequence [104] (appendix I) that includes a series of small flip angle excitation pulses [130]. The echo is formed before the excitation pulse and originates from refocusing residual echo at the time of the next rf pulse. This sequence is strongly T_2-weighted [104]. The signal intensity (SI_{SSFP}) depends on the flip angle α, TR, T_1, T_2, and M_0. The signal equation can take several forms depending on the conditions under which the sequence is run. For this description, the signal equation is given in the same form as in the original publication of this technique [116].

$$SI_{SSFP} = \frac{M_0(1 - E_1)\sin\alpha}{1 - E_1E_2 - (E_1 - E_2)\cos\alpha} \tag{129}$$

Equation (129) is particular useful for short repetition times that are less than 10 ms and excitation pulses with alternating phase with $E_1 = e^{-(TR/T_1)}$ and $E_2 = e^{-(TR/T_2)}$. The TR is to be kept constant while increasing the flip angle α incrementally. The data generated will show dependency on both T_1 and T_2. Equation (129) can be rearranged to take on a linear form.

$$\frac{SI_{SSFP}}{\sin\alpha} = \frac{E_1 - E_2}{1 - E_1E_2} \times \frac{SI_{SSFP}}{\tan\alpha} + \frac{M_0(1 - E_1)}{1 - E_1E_2} \tag{130}$$

In equation (130), $\frac{E_1 - E_2}{1 - E_1E_2}$ is the gradient m of a linear function and $\frac{M_0(1-E_1)}{1-E_1E_2}$ is the ordinate intercept b. From gradient and intercept, a value for T_2 and M_0 can be found given that T_1 and hence E_1 is known.

$$M_0 = \frac{b(1 - E_1E_2)}{(1 - E_1)} \tag{131}$$

$$T_2 = -\frac{TR}{\ln\left(\frac{m - E_1}{mE_1 - 1}\right)} \tag{132}$$

The optimal flip angle α can be determined in a similar way as above for the DESPOT1 method which is finding those flip angles that lead to optimal precession of the T_2 value for a specific set of TR, T_1, and T_2. The vector product of DR (equation (121)) and FS (equation (122)) can be evaluated and were found to be maximised for $SI_{\alpha,1} = SI_{\alpha,2}$. Note that for the case of DESPOT2, the signal intensity in equation (130) comes from the SSFP sequence. Similar to the description of DESPOT1, FS can be subsidised with f. Using a polynomial fitting method, Deoni et al. [116] concluded that the optimal T_2 precession is achieved for flip angles $SI_{\alpha,1} =$

$SI_{\alpha,2} = 0.71SI_E$. Identical to the SPGR case presented above, an analytical solution can also be found for the ideal preexcitation refocused SSFP flip angles as

$$\alpha = \cos^{-1}\left(\frac{-B \pm \sqrt{B^2 - 4AC}}{2A}\right) \tag{133}$$

with

$A = 2E_1E_2 + 2E_1E_2\Psi - 2E_1E_2(E_1 - E_2)\Psi + E_1^2E_2^2 + (E_1 - E_2)^2\Psi^2 - \mathrm{f}^2(1 - \Psi)(\mathrm{E}_1 - \mathrm{E}_2)^2$

$B = 2f^2(1 - \Psi)(E_1 - E_2) - 2f^2(1 - \Psi)E_1E_2(E_1 - E_2)$

$C = 1 - 2E_1E_2 - 2(E_1 - E_2)\Psi + 2E_1E_2(E_1 - E_2)\Psi + E_1^2E_2^2 + (E_1 - E_2)^2\Psi^2 - f^2(1 - \Psi)$
$+ 2f^2(1 - \Psi)E_1E_2 - f^2(1 - \Psi)E_1^2E_2^2$

and $\Psi = \frac{E_1 - E_2}{1 - E_1E_2}$.

3.2.3. T_2-weighted Magnetisation Prepared (T_2Prep) Sequence

This technique uses a T_2-weighted magnetisation prepared sequence called the T_2prep to quantitatively measure the transverse relaxation time constant. T_2-weighted magnetisation prepared methods have been introduced to the scientific community in 1990 by Haase [131]. It was demonstrated in the past that this method can also be used for T_2 measurements [132], [133]. The principle technique is that a 90°_x excitation pulse is followed by a train of equally separated 180°_y refocusing pulses. When the echo of the final refocusing pulse is established, a tipup pulse returns the T_2-weighted magnetisation back along the longitudinal direction. The number N of refocusing pulses applied can vary and depends on the specific conditions [134].

$$90^\circ_x - \left(\tau - 180^\circ_y\right)_N - \tau - tipup_{-x}$$

Because the transverse magnetisation after the initial excitation pulse dephases according to spin-spin relaxation, the refocused and flipped back longitudinal magnetisation at the end of the train of refocusing pulses is strongly T_2-weighted [91]. The T_2 Prep sequence is nonselective and designed so that it is independent of B_0 and B_1 field inhomogeneities by weighing the refocusing pulses in an MLEV pattern [135], [136] or utilising composite 180°_x pulses [137]. After the T_2 Prep sequence, spoiler gradients usually dephase any residual transverse magnetisation before the readout part of the sequence. The T_2 Prep can be combined with any other readout sequence depending on the imaging requirements (figure 31) [91].

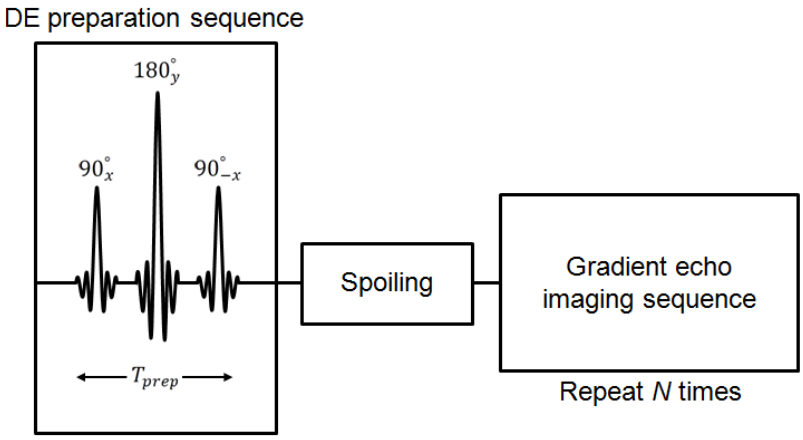

Figure 31: T_2 Prep module preceding other elements (e.g. Spoiling) and the sequence acquisition (e.g. gradient echo sequence) (reproduced from Bernstein et al. [91], p. 889).

Quantitative T_2 mapping using the T_2 Prep sequence was recently demonstrated by Ding et al. [138]. The authors performed a three-dimensional whole heart T_2 mapping at 3T using a T_2prep rf spoiled gradient echo (SPGR) sequence together with a saturation prepulse and a navigator. The adiabatic T_2prep [139] was used to achieve different T_2 weightings by selecting different T_2prep echo times (i.e. time between the initial 90°_{x} excitation pulse and the tipup pulse). The first image was acquired without a T_2 Prep $\left(TE_{T_2\ Prep} = 0\ ms\right)$ and then at echo times of 25ms and 45 ms.

3.2.4. T_2^* Mapping

The presence of magnetic field inhomogeneities contribute to the dephasing of spins and cause the transverse magnetisation to decay faster which is described in chapter 2.3. Magnetic field inhomogeneities that change over the size of a voxel are referred to as microscopic and provide information about the microstructure of the tissue [140]. The magnetic field distortions introduced by superparamagnetic iron oxide nanoparticles (SPIONs) are an example of this kind of inhomogeneity that produces T_2^* decay. The other form of inhomogeneities are macroscopic that are constant over the size of a voxel such as imperfections in the static magnetic field caused by air/tissue interfaces or gradient fields [141].

Multi-echo GRE sequences use increasing echo times and therefore the T_2^* decay curve can be obtained from pixel-wise fitting of the signal intensity along the time axis [91]. T_2^* mapping sequences use small flip angles to reduce the T_1 influence and large voxel sizes. Because T_2^* mapping is usually done with a 2D sequence, the slice thickness is normally considerably larger than the in-plane resolution to increase T_2^*-weighing and provide a good SNR [142].

A problem with quantitative T_2^* mapping is that for many applications such as molecular imaging with SPIONs [143] and the investigation of the vascular morphology of tumours [144], macroscopic inhomogeneities are unwanted. Therefore, it is important to correct for macroscopic magnetic field inhomogeneities in order to generate T_2^* maps that reflect the microscopic inhomogeneities present in the tissue of interest. Various correction methods have been proposed such as the manipulation of the slice-select gradient [145] or the application of a $\vec{B}_1$ field [140], [146]. Wild et al. [147] proposed the combination of three successive ME-GRE images where slice refocus gradients are incremented in succession after using a numerical simulation to determine optimal incrementation. Other authors have developed a postprocessing method such as the correction for the sinc modulation generated by the macroscopic inhomogeneities under the assumption that these inhomogeneities are linear across the slice thickness [148]. Dahnke and Schaeffter [143] later simplified this method which led to widespread use.

4. Positive Contrast Imaging

Positive contrast methods for MR imaging take advantage of local differences in susceptibility [149]. Local magnetic field susceptibilities are e.g. introduced by superparamagnetic iron oxide nanoparticles (SPIONs) or at tissue interfaces. The water molecules affected by the dipole field of SPIONs is visualised as signal loss with conventional spin echo or gradient echo sequences (negative contrast). A problem with depicting SPION accumulating areas with negative contrast is its ambiguity with other sources of signal loss such as air cavities in the abdomen [150]. Furthermore, it is generally easier to identify a white or bright signal on a T1 weighted MR image than it is to identify a black or dark area on a T2 weighted or proton density weighted MR image.

Several techniques have been developed to generate positive contrast with SPIONs. These techniques can be grouped into three categories. The first category treats the dipole field introduced by SPIONs as local magnetic field gradients that add to the imaging gradients and cause a shift in k-space [150]. Examples are **GR**adient-echo **A**cquisition for **S**uperparamagnetic particles with **P**ositive contrast (GRASP) [151] and **S**usceptibility **G**radient **M**apping (SGM) [152]. The second group of techniques utilise the fact that SPIONs change the local Larmor frequency [150]. **I**nversion **R**ecovery with **ON**-resonant water suppression (IRON) [153] is an example of a method that utilises off-resonance imaging to depict SPIONs as positive contrast. The final group of techniques exploits the different phase accumulation, specifically the different phase rotation angle, of on- and off-resonant protons [150]. An example of this is the **F**ast **L**ow **A**ngle **P**ositive contrast **S**teady-state free precession (FLAPS) [154] technique that is based on a balanced steady-state free precession sequence [103].

4.1. Background Physics

Superparamagnetic iron oxide nanoparticles have a different magnetic susceptibility than the background tissue. This introduces local magnetic field inhomogeneities which causes magnetic field variations within adjacent voxels. A change of the magnetic field strength leads to a change of the Larmor frequency according to the Larmor equation introduced in chapter 2. Hence, spins in an adjacent voxel will be precessing at different frequencies which results in a signal decay within the voxel due to intravoxel dephasing. The signal within a voxel can be described as

$$S_{voxel} = \frac{1}{V}\int_V \rho(r)e^{-i\varphi}d^3r \quad \text{and} \quad \varphi = \gamma B_{z,inh}(x,y,z)TE \tag{134}$$

In equation (134) the additional phase component in z-direction due to the distortion of the local magnetic field $B_{z,inh}$ is represented by φ. The voxel volume in mm^3 is represented by V, $\rho(r)$ is the spin density, TE is the echo time, and γ is the gyromagnetic ratio. The field distortion caused by SPIONs is a dipole field that can be mathematically described as

$$B_{z,inh}(x,y,z) = c\frac{x^2+y^2-2z^2}{(x^2+y^2+z^2)^{5/2}} \quad \text{with} \quad c = \frac{B_0 \Delta\chi V}{4\pi} \tag{135}$$

In equation (135) B_0 is the external magnetic field along the z-direction. The difference in magnetic susceptibility per volume between the environment and the SPION is given by $\Delta\chi V$. When integrating equation (135) over the slice-selection direction, the normalized complex signal expression for a voxel (equation 136) is obtained as

$$S(x,y) = \frac{1}{d}\int_{-d/2}^{d/2} \rho(x,y,z) e^{-i\gamma B_{z,inh}(x,y,z)TE} dz \tag{136}$$

where d is the slice thickness in millimetre and $\rho(x,y,z)$ is the spin density in all three directions.

4.2. GRadient-echo Acquisition for Superparamagnetic particles with Positive contrast

GRadient-echo **A**cquisition for **S**uperparamagnetic particles with **P**ositive contrast (GRASP) was first described by Seppenwoolde et al. [151]. This method treats the field distortion as a local time invariant magnetic field gradient that is overlaid onto the imaging gradients such as the slice-selection gradient. A change in gradient strength results in a shift of the signal in k-space. In the original publication, GRASP was referred to as the "white marker phenomenon" or "white marker imaging". Both names, GRASP and whiter marker (WW), are used nowadays.

4.2.1. Technical description of GRASP

The addition of a gradient in the z-direction will change the local magnetic field experienced by the spins. The phase accumulation during acquisition will also change as a result of that. Mathematically, having an additional phase contribution from an additional gradient will change equation (136) according to

$$S(x,y) = \frac{1}{d}\int_{-d/2}^{d/2} \rho(x,y,z) e^{-i\gamma B_{z,inh}(x,y,z)TE + G_s \tau_s z} dz \tag{137}$$

Equation (137) contains additional components such as the strength of the susceptibility gradient G_s (mT/m) and the time τ_s (ms) during which the spins experience this gradient. The

spatial dependence of the phase φ can be shown by treating the slice thickness as a summation of subslices of infinitesimal small thickness dz. For each subslice the phase will be

$$\varphi = \frac{\partial B_{z,inh}}{\partial z}(x, y, z)TE + G_s\tau_s \tag{138}$$

Signal conservation occurs when the phase described by equation (138) is zero at the point where the echo is acquired (TE) because the dephasing will be zero. This is called gradient compensation and illustrated by figure 32.

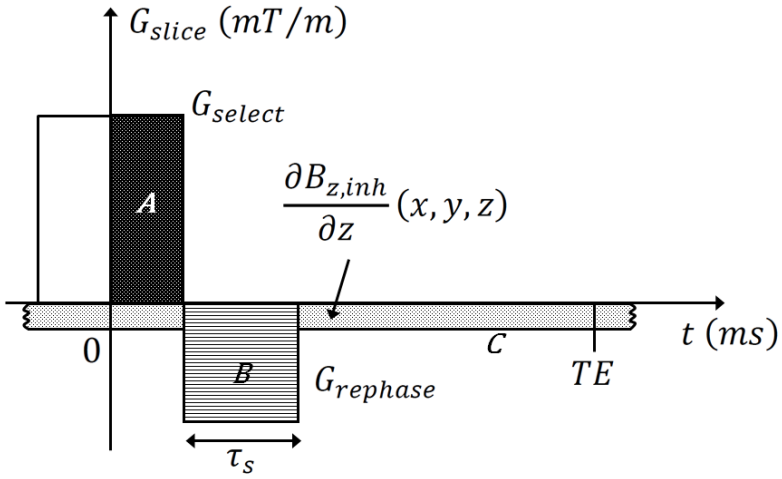

Figure 32: Gradient compensation in the slice-select direction where the field inhomogeneities interpreted as gradient C add to the rephasing gradient B which will therefore need to be reduced in strength to rephase area A (reproduced from Seppenwoolde et al. [151], p. 785).

In order to rephase the spins after the application of a slice-select gradient, the rephasing lobe (B) must be equal to area (A) which is half of the applied slice-select gradient. For a gradient echo sequence, this will produce a conventional gradient-echo at the echo time. If the strength of the rephasing lobe is decreased, the signal available at the echo time to produce an image will also be decreased due to a gradient imbalance. The reason for that is that not all spins will be rephased at the echo time which results in less available signal. Areas where there is an additional local gradient (C) due to the presence of the SPIONs, the spins can get fully rephased because the local additional gradient is added to the rephasing lobe and together compensate for the applied slice-select gradient. Therefore, for spins that are affected by the local magnetic field distortion of the SPIONs represented as an additional gradient, a fully rephased gradient-echo will occur with maximum signal intensity. The gradients in z- and x-direction can be found by finding the derivatives of equation (135).

$$\frac{\partial B_{z,inh}}{\partial z}(x, y, z) = 3cz\frac{-3x^2 - 3y^2 + 2z^2}{(x^2 + y^2 + z^2)^{7/2}} \tag{139}$$

$$\frac{\partial B_{z,inh}}{\partial x}(x, y, z) = -3cx\frac{x^2 + y^2 - 4z^2}{(x^2 + y^2 + z^2)^{7/2}} \tag{140}$$

Different region in the vicinity of the SPIONs will cause the phase to be zero according to equation (138). The reason for that is the spatial variation of different derivatives which means that the signal conservation occurs at different regions around the SPIONs [151], [155], [156]. Because the dephasing of spins is of central importance for the GRASP technique, all acquisition parameters that influence dephasing have a significant influence on the image quality. This means that the echo time, slice thickness, and strength of background gradients are parameters of vital importance for this technique. As shown by Seppenwoolde et al. [151] the transition from normal gradient-echo contrast behaviour to a positive contrast image is sudden when varying the background gradient. If the gradient is higher, i.e. the SPIONs introduce stronger magnetic field inhomogeneity, the signal near the SPIONs decreases. However, signal intensity relative to the background signal increases which means better contrast.

4.2.2. Applications of GRASP

Mani et al. [155] conducted a comprehensive phantom study with Feridex® (Advanced Magnetics, Cambridge, MA) which is a dextran coated SPION with a core size of 4.8 ± 1.0 nm. The authors prepared membrane phantoms of 1% agarose gel with different SPION concentrations to eliminate effects of the glass/gel interface and compared these with glass phantoms. A good positive signal was observed between 0.05 – 0.8 mM on clinical scanners of 1.5T and 3T. The authors demonstrated that the positive signal was directly related with the signal loss on conventional gradient-echo images. However, when comparing the results at 1.5T and 3T the sensitivity of GRASP was greatly reduced at the higher field strength for the detection of low SPION concentrations. This might have implications for in vivo imaging at 3T or higher field strengths when only small SPION concentrations are delivered to the target region. The susceptibility difference at the glass/gel interface was significant and plastic or glass tubes are therefore not recommended for phantom experiments. The authors furthermore concluded that GRASP provides best results when the SPIONs are highly compartmentalised with limited iron particle uptake.

The same research group also conducted a study to determine if ferritin depositions in a thrombus model could be determined with GRASP in vitro and in vivo. Incubating blood with ferritin was used for the in vitro thrombi model in which the GRASP sequence successfully verified the deposition of ferritin. GRASP and conventional T_2^*-weighted gradient-echo sequences were performed in vivo on a crush injury model in rabbits. The authors showed that signal enhancement by GRASP correlated with signal loss in the gradient-echo images which was confirmed by histology [156].

Signal variations within voxels caused by partial volume effects also produce positive contrast using the GRASP sequence. The authors who first described the GRASP technique reported in 2007 a strategy to eliminate partial volume effects during imaging with GRASP. The normal signal response curve as a function of the applied gradients is asymmetric. Symmetrical signal responses must stem from partial volume effects and can therefore be subtracted. This technique was probed in vitro and in vivo in brain regions affected by susceptibility and partial volume effects. Partial volume effects were successfully eliminated in vitro and became negligibly small *in vivo* [157].

Mani et al. [158] used GRASP in an in vivo mouse model of myocardial infarction to dynamically track implanted stem cells. A complex of Feridex® (Berlex Laboratories, Wayne, NJ) and protamine sulphate was bound to embryonic stem cell-derived cardiac-precursor-cells. Half a million magnetically labelled stem cells were injected in infarcted mice and gradient-echo and GRASP images were acquired at 9.4T at three different time points (baseline, 24h and one-week post injection). The negative contrast images acquired with the gradient echo sequence were in good agreement with the GRASP images which was confirmed by positive staining for iron with histology.

4.3. Inversion Recovery with ON-resonant water suppression

The first group to use an **I**nversion **R**ecovery with **ON**-resonant water suppression (IRON) to achieve positive contrast with SPIONs was Stuber et al. [153]. The difference to the above described GRASP method is that the field inhomogeneities introduced by the SPIONs are not treated as an additional gradient but as the cause of a frequency shift of spins in the vicinity of the SPIONs.

4.3.1. Technical description of IRON

If SPIONs can be assumed to be spherical, then the magnetic field distortion they introduce can be mathematically described by

$$\Delta B(r,\Theta)_{External} \sim \frac{\Delta K\, a^3}{3r^3}(3\cos^2\Theta - 1)B_0 \tag{141}$$

In equation (141) ΔK is the susceptibility gradient coefficient of the spherical object (SPIONs). The radius of the sphere is represented by a and $\vec{r}$ describes the distance from the magnetic sphere to any given point in space where r shall be larger than the radius of the sphere ($|\vec{r}| > a$). The angle between $\vec{r}$ and the direction of the main magnetic field $\vec{B}_0$ is represented by Θ. Due to a disturbance of the magnetic field, a shift in frequency results according to the Larmor equation

$$\Delta\omega_{External} = \gamma \Delta B_{External} \quad (142)$$

Equations (141) and (142) demonstrate that by introducing objects such as SPIONs with a susceptibility gradient coefficient ΔK into the main magnetic field of an MRI scanner adds frequency components different to the Larmor frequency ω_0 (figure 33a). IRON utilises the shift in resonance frequency of spins affected by the magnetic field disturbance by applying a saturation rf pulse that is spectrally selective to spins resonating at the Larmor frequency ω_0 (on-resonant protons) (figure 33b). This saturation pulse has a limited bandwidth ($\mathrm{BW_{Sat}}$) and is applied prior to the actual imaging part in the magnetisation preparation phase of the sequence. This results in the signal normally coming from on-resonant protons to be suppressed while only minimally affecting the off-resonant protons influenced by the SPIONs. This means that positive contrast can be generated in areas close to susceptibility introducing particles.

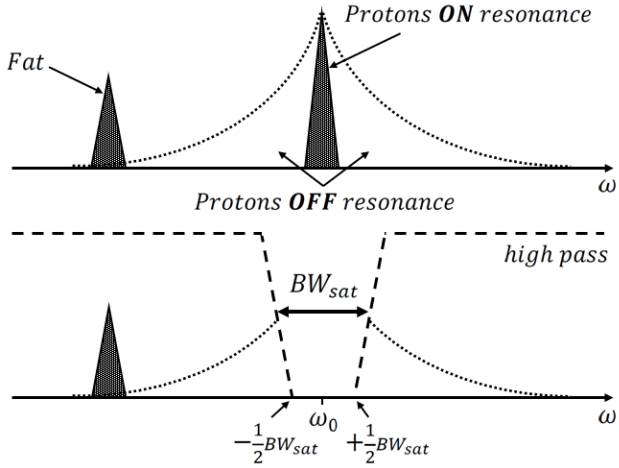

Figure 33: MR signals in the frequency domain where a narrow bandwidth IRON pulse is used to suppress on-resonant protons while preserving the off-resonant components and the fat signal (reproduced from Stuber et al. [153], p. 1073).

The angle of the applied saturation pulse α_{Sat} can be changed and used to control the level of background suppression. The bandwidth of the saturation pulse $\mathrm{BW_{Sat}}$ controls the size of the area with positive contrast. Figure 34a shows the pulse sequence diagram. The temporal development of the longitudinal magnetisation of the off-resonant spins is displayed in figure 34b. The behaviour of the on-resonant spins is illustrated in figure 34c.

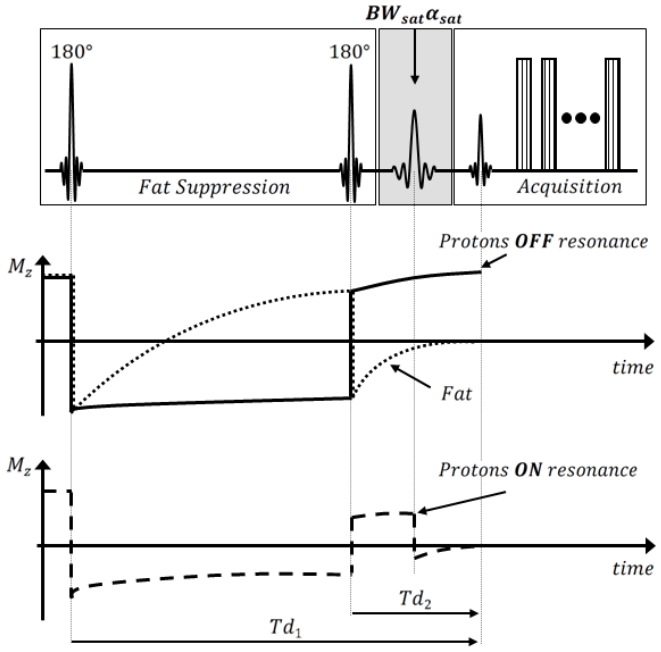

Figure 34: Signal behaviour over time of the on- and off-resonant frequency components for an acquisition preceded by fat suppression (dual-inversion) and the IRON prepulse (reproduced from Stuber et al. [153], p. 1073).

The saturation pulse nulls the on-resonant protons at the time of the imaging sequence. The signal of fat and off-resonant protons however remains unaffected. In order to also remove the fat signal from the image, a dual inversion saturation pulse can be applied prior to the on-resonant saturation pulse that only affects protons of short longitudinal relaxation time such as fat [150], [153], [159].

4.3.2. Applications of IRON

In the original IRON publication, Stuber et al. [153] demonstrated the feasibility of generating positive contrast with IRON in a gelatine phantom containing a 0.5 mm diameter stainless steel sphere as well as with SPION-labelled stem cells in vitro and *in vivo*. For the stem cell experiments the authors used an agarose gel phantom that contained wells with mineral oil (fat) and wells with two million labelled canine mesenchymal stem cells. The in vivo experiments were conducted with New Zealand White Rabbits intramuscularly injected with SPION-labelled canine mesenchymal stem cells. The authors successfully demonstrated in vitro and in vivo that positive contrast can be achieved with IRON in the surrounding of SPION-labelled cells.

Advantages of IRON are that the imaging part of the sequence does not need to be modified such as with GRASP. The in vitro studies of Stuber et al. [153] demonstrated a high correlation of SPION-labelled cells to the amount (i.e. volume) of positive contrast and could potentially be

used for non-invasive cell quantification. Furthermore, 2D and 3D images can be easily acquired and fast imaging techniques can be employed. A limitation of IRON is the increased power deposition when using a fast spin echo sequence. Moreover, positive contrast may also result at tissue borders or air-tissue interfaces for which higher order volumetric shimming is required. Local over- or undertipping of the magnetisation can be caused by B_1 inhomogeneities at higher field strengths. For fat suppression, a second spectrally selective prepulse is preferred over a dual inversion technique to avoid T_1 dependence of the longitudinal magnetisation from the off-resonant protons. Finally, the positive contrast achieved depends not only on the amount of cells successfully labelled with SPIONs but also their local spatial distribution and concentration which are highly variable factors *in vivo* [153].

Korosogiou et al. [159] administered monocrystalline iron oxide nanoparticles (MIONS) via a single bolus injection into rabbits. IRON images displayed very strong positive contrast in the paraaortic lymph nodes. Three days post injection the CNR in the blood vessels had approached baseline while the CNR in the lymph nodes was still highly enhanced. This technique has therefore potential to be used for nodal staging in cancer screening.

Gitsioudis et al. [160] investigated the ability of IRON for steady-state equilibrium phase MR angiography (MRA) of a SPION coated with an amino-alcohol derivative of glucose. IRON was compared to a conventional T_1-weighted MRA sequence by imaging the abdominal and thoracic aorta of 12 rabbits. For a wide range of SPION dosages, the vessel sharpness and quantitative contrast-to-noise-ratio (CNR) was consistently higher for the IRON images. This demonstrates the potential of IRON to be used for vessel imaging in conjunction with a suitable iron-based MR contrast agent.

4.4. Susceptibility Gradient Mapping

The two approaches for positive contrast imaging discussed so far (GRASP and IRON) have been very successful in displaying SPIONs but also suffer from major disadvantages. GRASP only compensates for susceptibility gradients along the slice-select direction. Furthermore, knowledge about the strength of the susceptibility gradient is necessary to optimise the strength of the slice rephasing lobe. IRON also requires a priori knowledge about the expected shift of frequency and is easily affected by chemical shift artefacts and other field inhomogeneities. **S**usceptibility **G**radient **M**apping (SGM) similarly to GRASP perceives the field distortions introduced by SPIONs as local susceptibility gradients. However, SGM is a postprocessing method that can be applied to any gradient-echo data set that has been saved together with the

complex data. Furthermore, SGM does not suffer from the above mentioned disadvantages of GRASP and IRON [152], [161].

4.4.1. Technique

Any object with a magnetic susceptibility different to its surrounding creates a local inhomogeneity in an external magnetic field. As described for the GRASP technique, inhomogeneities that are larger than the voxel size change the applied imaging gradients which lead to a shift in the associated echo of a gradient echo sequence in k-space. In the case of a first-order approximation only the susceptibility gradient G_x^{sus} is considered. This resembles the linear part of the main magnetic field inhomogeneity. The susceptibility gradient and the imaging gradient G_x^{imag} are additive and result in a different timing of the echo at the echo time. Mathematically, the readout signal of a 1D gradient-echo sequence is given by

$$\mathrm{S(t)} = \sum_{\mathrm{n=0}}^{\mathrm{N-1}} \rho(\mathrm{n}\cdot\Delta\mathrm{x})\mathrm{e}^{-\mathrm{i}2\pi\gamma\mathrm{G}_\mathrm{x}^{\mathrm{imag}}\mathrm{t}\mathrm{n}\Delta\mathrm{x}}\mathrm{e}^{\mathrm{i}2\pi\gamma\mathrm{G}_\mathrm{x}^{\mathrm{sus}}(\mathrm{t}+\mathrm{TE})\mathrm{n}\Delta\mathrm{x}} \tag{143}$$

In equation (143), $\Delta\mathrm{x}$ is the dimension of the pixel and $\rho(\mathrm{n}\cdot\Delta\mathrm{x})$ is the spin density. The assumption for equation (143) is that there are no other sources of phase distortions. In order to better understand the influence the susceptibility gradient has on the signal, equation (143) can be rewritten as

$$\mathrm{S(t)} = \sum_{\mathrm{n=0}}^{\mathrm{N-1}} \rho(\mathrm{n}\cdot\Delta\mathrm{x})\mathrm{e}^{-\mathrm{i}2\pi\gamma\mathrm{G}_\mathrm{x}^{\mathrm{imag}}\mathrm{t}\left(1+\frac{\mathrm{G}_\mathrm{x}^{\mathrm{sus}}}{\mathrm{G}_\mathrm{x}^{\mathrm{imag}}}\right)\mathrm{n}\Delta\mathrm{x}} \times \mathrm{e}^{\mathrm{i}2\pi\gamma\mathrm{G}_\mathrm{x}^{\mathrm{sus}}\,\mathrm{TE\,n\,\Delta x}} \tag{144}$$

From equation (144) the modification of the k-space trajectory can be isolated.

$$\mathrm{k'(t)} = \left(1+\frac{\mathrm{G}_\mathrm{x}^{\mathrm{sus}}}{\mathrm{G}_\mathrm{x}^{\mathrm{imag}}}\right)\cdot\gamma\cdot\mathrm{G}_\mathrm{x}^{\mathrm{imag}}\cdot\mathrm{t} = \left(1+\frac{\mathrm{G}_\mathrm{x}^{\mathrm{sus}}}{\mathrm{G}_\mathrm{x}^{\mathrm{imag}}}\right)\cdot\mathrm{k(t)} \tag{145}$$

Equation (144) and (145) make it evident that a susceptibility gradient leads to scaling in k-space and adds a position dependent phase term. This ultimately results in a shift of the echo. At the time $\mathrm{t} = \mathrm{m}\tau_\mathrm{x}$ the imaging gradient completely cancels the susceptibility gradient when the total phase from equation (143) becomes zero.

$$-2\pi\cdot\gamma\cdot G_x^{imag} m\cdot\tau_x\cdot n\Delta x - 2\pi\cdot\gamma\times G_x^{sus}(m\cdot\tau_x + TE)\cdot n\Delta x = 0 \tag{146}$$

From equation (146), m can be determined with $\frac{1}{\tau_x}$ being the sampling rate

$$m = -\frac{G_x^{sus}\cdot TE}{\left(G_x^{imag} + G_x^{sus}\right)\cdot\tau_x} \tag{147}$$

By using a short-term Fourier transform (STFT), local susceptibility gradients $\mathrm{G}_\mathrm{x}^{\mathrm{sus}}(\mathrm{n}\Delta\mathrm{x})$ can be investigated. These gradients are usually much smaller in comparison to the imaging gradients. Therefore, the scaling of k-space can be disregarded. Furthermore, $\mathrm{G}_\mathrm{x}^{\mathrm{sus}}(\mathrm{n}\Delta\mathrm{x})$ is assumed to be constant within a specified region denoted by r. The prior assumptions mean that the complete

data set can be divided into R regions in the image domain. This is achieved by summing over a rectangular window function that scans through all regions of the data set.

$$S(k) = \sum_{r=0}^{R-1} \sum_{n=0}^{N-1} \rho(n \cdot \Delta x) \cdot \mathrm{rect}_{\frac{N \cdot \Delta x}{R}}\left(\left(n - r \cdot \frac{N}{R}\right)\Delta x\right) \cdot e^{-i \cdot 2\pi \cdot \gamma \cdot G_x^{sus}(r) \cdot TE \cdot n \cdot \Delta x} \tag{148}$$

and

$$\mathrm{rect}_{\frac{N \cdot \Delta x}{R}}\left(\left(n - r \cdot \frac{N}{R}\right)\Delta x\right) = \begin{cases} 1; & r \cdot \frac{N}{R} \leq n \leq (r+1)\frac{N}{R} \\ 0; & \text{otherwise} \end{cases} \tag{149}$$

Equation (148) resembles the summation of Fourier transforms of data that lies within the rectangular window function at a specific position $r \cdot \frac{N}{R} \cdot \Delta x$:

$$S(k) = \sum_{r=0}^{R-1} \mathrm{STFT}\left(\rho(n \cdot \Delta x) \cdot e^{-i \cdot 2\pi \cdot \gamma \cdot G_x^{sus}(\gamma) \cdot TE \cdot n \cdot \Delta x}\right), \quad \text{with} \quad k_{sus}(r) = \gamma \cdot G_x^{sus}(r) \cdot TE \tag{150}$$

and

$$S(k - k_{sus}) = STFT\left(\rho(n \cdot \Delta x) \cdot e^{-i \cdot 2\pi \cdot \gamma \cdot G_x^{sus}(\gamma) \cdot TE \cdot n \cdot \Delta x}\right) \tag{151}$$

Equation (150) shows that the signal in k-space $S(k)$ is the sum over STFTs where each Fourier transform has been shifted by k_{sus} which is given by $G_x^{sus}(n\Delta x)$. The rectangular window function is very short which results in a change of the shape of the STFT due to convolution. However, this does not change the position of the maximum. In each region r the susceptibility gradient can be determined by finding the position of the maximum in k-space. This is called an echo-shift approach which also works for 2D and 3D data sets. In that case, the shift of the echo simply occurs in more than one direction. In the case of a 3D data acquisition, the susceptibility gradient for a particular voxel will take the form

$$G_{x,y,z}^{sus} \approx -\frac{m_{x,y,z} \cdot G_{x,y,z}^{imag} \cdot \tau_{x,y,z}}{m\tau_{x,y,z} + TE} \tag{152}$$

The shift of the echo in k-space has been illustrated in figure 35. The shift in two different regions is shown where arrows symbolise in what way that particular voxel is affected by the susceptibility gradient.

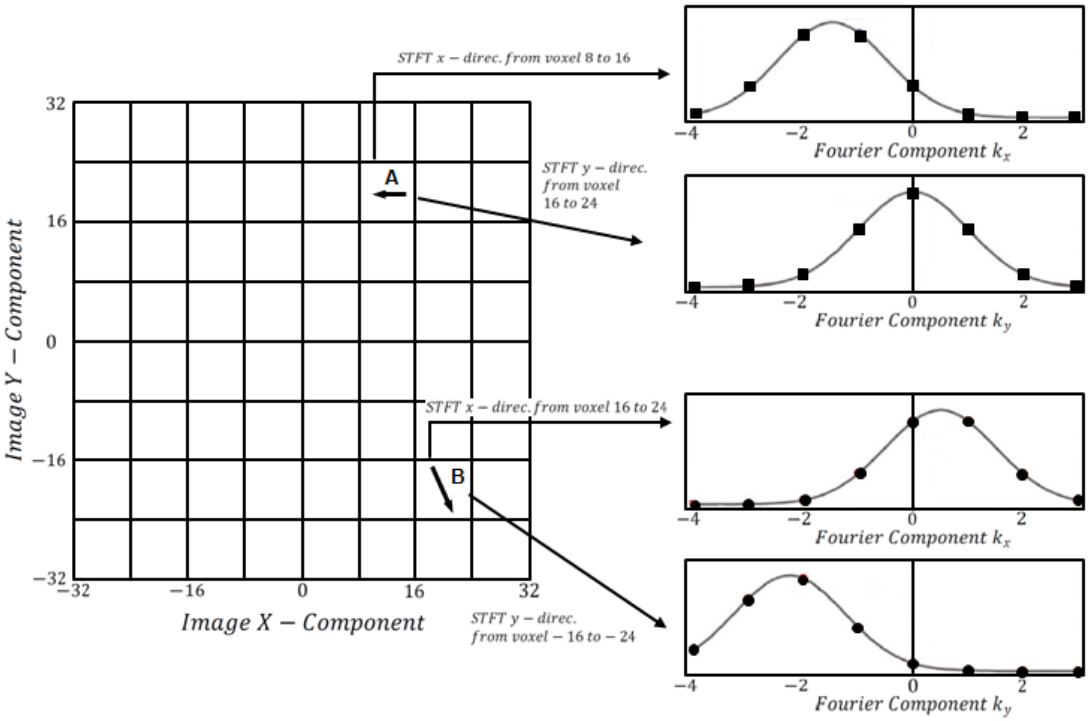

Figure 35: Illustration of the echo shift in k-space caused by inhomogeneities that can be understood as susceptibility gradients. The maximum of the shift can be found by fitting Lorentzian curve to the data (reproduced from Dahnke et al. [152], p. 598).

By determining the position of the maximum in the "short term" k-space of the different regions allows finding the vector components of the susceptibility gradient. By summing over all "short term" k-space data, a representation of the global k-space is obtained [152], [161].

The reason local "short term" k-space is repeatedly used in this description has to do with the fact that in an object almost free of B_0 inhomogeneities, a small susceptibility gradient in one region would be difficult to detect. This is because the small echo shift would be overlapped by the main echo in the global k-space. The "short term" k-space of a particular region only includes local information which allows detection of even small echo shifts of low resolution. The STFTs used to determine the local echo shifts are performed in the different parts of the image space separately [152].

4.4.2. Applications of SGM

Dahnke et al. [152] who first described SGM also performed a phantom and in vivo study to demonstrate the ability of SGM to produce positive contrast. A gelatine phantom with holes filled with different SPION concentrations and one hole (i.e. control) filled with agarose was imaged with a gradient-echo sequence. Agarose and SPIONs could not be distinguished in the

gradient-echo image but all SPION holes produced bright positive signal on the calculated SGM image while the agarose hole remained dark. Furthermore, holes with a higher SPION concentration were displayed brighter on the SGM magnitude image. The authors also subcutaneously implanted SPION-labelled and unlabelled (i.e. control) glioma cells in the flanks of nude rats. On gradient-echo images two weeks post implantation, the tumour has visibly grown and the tumour cells have been diluted. The calculated SGM image selectively shows the labelled cells as bright signals whereas the unlabelled cells remain unenhanced.

The same research group compared SGM as a positive contrast method with GRASP and IRON in phantom experiments and in vivo in a preclinical study. The authors used a water phantom containing three vials of different Fe concentrations with SPION-labelled C6 glioma cells suspended in agarose gel. Six female nude rats had SPION-labelled C6 glioma cells implanted in the flanks and imaged with GRASP, IRON, and a gradient-echo sequence from which SGM magnitude images were calculated. SGM images showed the highest amount of positive contrast for small tumours (~5mm) compared to GRASP and IRON as these only covered parts of the labelled tumour. For larger tumours (~20mm), IRON could not detect labelled cancer cells while GRASP and SGM generated similar amount of positive contrast. A major disadvantage the authors pointed out is the inability to differentiate haemorrhage within the tissue and SPION-labelled cells. When comparing SGM for 2D versus 3D imaging, the sensitivity might decrease for the detection of SPION-labelled cells [161].

Varma et al. [162] compared SGM to GRASP and IRON in a phantom containing prostate marker seeds. SGM images were generated from a gradient-echo data set of SPION uptake in a balloon-injured swine carotid model. These authors agree that the SGM technique provided the greatest positive contrast. However, gradient echo images provided greater sensitivity to regions in the subject where susceptibility effects were weaker.

Makowski et al. [163] utilised the SGM technique together with very small iron oxide particles (VSOPs) to assess the progression of atherosclerotic plaques in $ApoE^{-/-}$ mice. The authors demonstrated the feasibility of SGM in visualising and quantifying the increasing uptake of VSOPs in atherosclerotic plaques during different stages of plaque development.

4.4.3. SGM using the original resolution (SUMO)

A disadvantage of the SGM technique is that during the generation of the positive contrast magnitude image, the spatial resolution of the image is reduced. This makes it difficult to visualise small structures effectively. To overcome this limitation, a development of SGM that

retains the original resolution called SUMO has been proposed [164]. In the technical description of the SGM technique, whenever the maximum occurs at the edge of the rectangular window function, the window size is increased (i.e. $N = N + 1$). The influence of the local susceptibility gradient becomes less relevant in the constructed parameter map when increasing the window size because of an increase of neighbouring pixels that are unaffected by it. In order to detect local susceptibility gradients high spatial resolution is required to avoid compensation of the gradient by adjacent pixels included in the STFT. As an alternative, Varma et al. [164] suggested a filter in k-space $F(k, s_k)$ to null an entire line in k-space at position s_k. The Lorentzian shaped filter function is given by

$$F(k, s_k) = 1 - \frac{\Delta k^2}{\Delta k^2 + (k - s_k)^2} \tag{153}$$

The filter is applied to k-space like a sliding window. The centre of the filter (s_k) will separately move in all three orthogonal directions. At every position s_k in k-space the filter is applied, the value will be set to zero and an inverse Fourier transform is used to calculate the corresponding image.

$$S(k_x) = \int M(x) \cdot e^{-i\pi k_x x} dx \tag{154}$$

$$M^{s_k}(x) = \left| \int S(k_x) \cdot F(k_x, s_k) \cdot e^{+i\pi x k_x} dk_x \right|_{s_k = k_{min}}^{k_{max}} \tag{155}$$

From that, a plot can be generated of the signal amplitude of every pixel for all possible positions of the filter. The echo shift in k-space is then found on a pixel-by-pixel basis by finding the minimum along the s_k axis

$$k_s = \min\{M^{s_k}(x)\}_{s_k = k_{min}}^{k_{max}} \tag{156}$$

Finding k_s for all pixels in each orthogonal direction permits the construction of a parameter map of the k-space echo shift. This will then provide information about the susceptibility gradient G_s. It is possible to also set a threshold to only visualise pixels with k_s values above that threshold.

The authors showed that the SUMO technique is able to resolve small local susceptibility gradients that were acquired with a low resolution acquisition while the SGM technique was unable to depict these. Furthermore, SUMO was used on in vivo MR images of a nitinol stent graft and produced positive contrast images that allowed good visualisation of the implant.

4.5. Fast Low Angle Positive Contrast Steady-State Free Precession (FLAPS)

Fast **L**ow **A**ngle **P**ositive contrast **S**teady-state free precession (FLAPS) is based on the bSSFP sequence (see below chapter 4.5.1.). The FLAPS method is a very fast positive contrast imaging technique that does not require any additional imaging pre-pulses or postprocessing efforts. Because it uses only small flip angles the power deposition is very low and the sequence can be used without concern at higher field strengths [150].

4.5.1. Balanced Steady-State Free Precession

In a gradient-echo sequence each excitation pulse is separated by a time delay, the repetition time TR. During TR the dephasing of the spins due to imaging gradients or field inhomogeneities occurs as well as T_1 and T_2 relaxation. The former causes the longitudinal magnetisation component to increase while T_2 relaxation results in a decrease of the transverse magnetisation. As described in chapter 1 these two processes, T_1 and T_2 relaxation, occur at the same time. Because there is a train of excitation pulses, the next rf pulse will act on the changed magnetisation after which dephasing and relaxation occurs again. This process is repeated over and over which means that for a constant flip angle α, TR, and constant dephasing the magnetisation will reach a steady-state after a few repetition times. This is referred to as steady-state free precession (SSFP).

A special type of steady-state free precession sequences is where the dephasing caused by the imaging gradients is zero which is then called a balanced steady-state free precession (bSSFP). This means that each gradient applied will be fully compensated with another gradient of opposite polarity. The main difference between balanced and non-balanced SSFP (nbSSFP) is that the magnetisation in the latter is dephased after the echo formation by a spoiler gradient. The bSSFP sequence has an additional read gradient lobe that compensates for the dephasing at the end of the TR interval. This means that the net transverse magnetisation is zero at the end of TR in nbSSFP due to the complete dephasing of spins. In the case of bSSFP the spins are refocused at the end of the TR interval which means the magnetisation at the beginning and at the end of the TR period is very similar. Balanced SSFP sequences are usually run with a very short TR as it makes the sequence less sensitive to off-resonance effects (i.e. field inhomogeneities) [103], [104].

The contrast of bSSFP is composed of contributions from T_1 and T_2. The signal intensity for on-resonant spins depends on T_1, T_2, TR, and α.

$$M_{ss} = M_0 \frac{\sqrt{E_2(1-E_1)\sin\alpha}}{1-(E_1-E_2)\cos\alpha - E_1E_2} \tag{157}$$

In equation (157), $E_1 = e^{-TR/T_1}$ and $E_2 = e^{-TR/T_2}$. If TR is much smaller than either T_1 or T_2, then equation (157) can be simplified to

$$M_{ss} = M_0 \frac{\sin\alpha}{1+\cos\alpha+(1-\cos\alpha)\left(\frac{T_1}{T_2}\right)} \tag{158}$$

The optimal flip angle α can be determined from the longitudinal and transverse relaxation times.

$$\cos\alpha = \frac{\frac{T_1}{T_2}-1}{\frac{T_1}{T_2}+1} \tag{159}$$

for which the signal amplitude is given by

$$M_{ss} = \frac{1}{2}M_0\sqrt{\frac{T_2}{T_1}} \tag{160}$$

The highest signal is obtained when T_1 and T_2 have similar values and for a flip angle between 70-90°. Under these conditions a signal of 50% of M_0 can be achieved. No other sequence achieves such a high signal continuously. Compared to all other sequences bSSFP has the highest signal-to-noise ratio per unit time. It is important to note that despite it being a gradient-echo sequence, bSSFP is not T_2^*-weighted. Dephasing due to field inhomogeneities is almost completely refocused at $TE = TR/2$. This means a spin echo rather than a gradient-echo is formed. As can be seen in equation (157) the signal of a bSSFP sequence contains an additional weighing factor of $e^{-TE/T_2} = \sqrt{E_2}$ for $TE = TR/2$ [103].

4.5.2. Technical description of FLAPS

The transverse magnetisation in the steady-state at a point in space described by $\vec{r}$ can be written as

$$M_{xy} = M_0 \sin\alpha \frac{\sqrt{2(1+\cos\beta(\vec{r}))}}{\left[2\frac{T_1}{T_2}(1-\cos\alpha)+\cos\beta(\vec{r})(1+\cos\alpha)+\cos\alpha+1\right]} \tag{161}$$

In equation (161), $\beta(\vec{r})$ is called the phase rotation angle. During the repetition time spins experience a phase rotation because of the magnetic field perturbation ΔB_z along the longitudinal direction.

$$\beta \equiv \beta(\vec{r}) = \gamma \Delta B_z(\vec{r}) TR \tag{162}$$

The difference in signal intensity of the off-resonant (β) and on-resonant $(\beta = 0)$ spins (i.e. contrast) is defined as

$$C(\beta) \equiv M_{xy}(\beta) - M_{xy}(\beta = 0)$$
$$= M_0 \sin\alpha \left[\frac{\sqrt{2(1+\cos\beta)}}{\left[2\frac{T_1}{T_2}(1-\cos\alpha) + \cos\beta(1+\cos\alpha) + \cos\alpha + 1\right]} \right. \quad (163)$$
$$\left. - \frac{1}{\frac{T_1}{T_2}(1-\cos\alpha) + \cos\alpha + 1} \right]$$

Positive contrast is generated when $C(\beta) > 0$. A peak contrast C_p can be derived from equation (163) as

$$C_p = M_0 \left[\frac{1}{2}\sqrt{\frac{T_2}{T_1}} - \frac{\sin\alpha}{\left(\frac{T_1}{T_2}\right)(1-\cos\alpha) + \cos\alpha + 1} \right] \quad (164)$$

Equations (163) and (164) are valid for a specific set of flip angles that satisfy equation (165) and a medium of given longitudinal and transversal relaxation times that is exposed to a repeated phase-cycle rf excitation of flip angle α. The maximal achievable positive contrast depends on the ratio of T_1 and T_2 as well as the flip angle α. In the presence of field inhomogeneities, steady-state free precession signal behaviour is identical for specific β values. This means that no signal is detected from on-resonant spins while strong signal peaks are observed around the null points of $\beta = \pm n\pi$ (n → non-zero, odd integer). This is because across the null points the phase of the magnetisation changes at low flip angles but is relatively independent of any other β value. By increasing the flip angle the signal changes between on- and off-resonant spins decrease due to smoother phase transitions. The peak signal from a SSFP sequence for on-resonant spins (equation 160) is achieved for a flip angle according to equation (159). But as α approaches the ideal value, C_p approaches zero which means no positive contrast is achieved at the optimal on-resonant SSFP signal conditions. In order to achieve positive contrast with SSFP, the following flip angle criterion must be met

$$0 < \alpha < \arccos\left(\frac{\frac{T_1}{T_2} - 1}{\frac{T_1}{T_2} + 1}\right) \quad (165)$$

From equation (165) it becomes evident that as the ratio of T_1 and T_2 increases, the suitable range of flip angles that enable positive contrast imaging becomes smaller [154], [165].

4.5.3. Applications of FLAPS

Dharmakumar et al. [154] proved the capability of FLAPS to produce positive contrast images on simple SPION phantoms. Cylindrical and spherical Perspex and rubber cases where filled with a Ferumoxide solution without any air inclusions. These were then immersed in a water

bath doped with gadolinium. The appropriate selection of the flip angle was essential to receive good positive contrast images. Moreover, the range of flip angles that allowed positive contrast imaging depends strongly on the ratio of T_1 and T_2. The spatial distribution of the positive contrast varied as suspected with the geometry of the SPION-filled object as well as the ratio of T_1 and T_2.

In a follow up study, the same group showed in phantom studies that FLAPS can easily be combined with fat suppression in the form of a fat saturation prepulse which does not compromise quality of the positive contrast images. Furthermore, the positive contrast achieved with FLAPS is predominantly dependent on the imaging parameters [165].

Vonken et al. [150] compared several positive contrast techniques in a phantom study and concluded that the amount of positive contrast achievable with FLAPS and the background suppression are both lower compared to GRASP, IRON, and SGM. The authors also noticed that non-ideal shimming has a significant effect on positive contrast images acquired with FLAPS that manifests in artefacts in the form of dark bands in the image.

4.6. Other relevant positive contrast techniques

So far we have categorised positive contrast imaging techniques in three categories. Those that treat the dipole field of SPIONs as a local magnetic field gradient [151], a shift in the Larmor frequency [153] or the change in phase accumulation [166]. Positive contrast techniques can also be classified in those that use modified MRI pulse sequences and those that produce positive contrast images in a post-processing step from regular gradient and spin echo sequences [167].

4.6.1. Techniques with modified MRI pulse sequences

Prominent examples of techniques that use modified pulse sequences are GRASP and IRON. The latter uses a spectrally selective inversion pulse to saturate on-resonant water at the time the image is acquired [153]. However, it is also possible to use a spectrally selective rf pulse to specifically excite those water protons affected by the dipole field of the SPIONs (off-resonant water) [168], [169]. The excitation of off-resonance water protons can also be achieved with a low-angle steady-state free precession sequence [154], [165], [166], [170], [171]. Apart from the techniques described in chapter 4, other positive contrast imaging techniques have been reported where the pulse sequence is modified. Kim et al. [172] reported the positive contrast imaging by acquiring a spin echo image and then subtracting an image acquired with a **S**usceptibility-**W**eighted **E**cho time **E**ncoding **T**echnique (SWEET). SPIONs are considered T_2

contrast agents that mainly affect the T_2^* relaxation time. Girard et al. [173] have also explored T_1 shortening properties by acquiring positive contrast images with an ultra-short echo time (UTE) sequence. Ultra-short spin echo sequences can be used for susceptibility mapping techniques [174]. There are many examples in the literature for UTE sequences for positive contrast [175], [176]. Seevinck et al. [177] described a frequency-encoded, 3D imaging technique using ultra-short TE (UTE) acquisition method [178] for a **c**enter-**o**ut **RA**dial **S**ampling with **O**ff-**R**esonance reception (co-RASOR). The technique uses off-resonance reception and a large excitation bandwidth. An off-resonance frequency offset is introduced (Δf_0) to the central reception frequency (f_0) the radial signal can be shifted to the centre of the paramagnetic particle which therefore will be displayed with a hyperintense signal. The co-RASOR method relies on knowledge of the susceptibility value of the paramagnetic particle as the shift of the off-resonance signal to the location of the particle depend on it.

4.6.2. Post-processing technique

Positive contrast imaging can also be based on phase recognition [179] and be implemented as part of a post-processing step. There are two main post-processing techniques, SGM and PGM [180], [181]. SGM measures the echo shift in k-space due to the susceptibility-induced gradients [182] which has been described in detail in chapter 4. Other techniques explored measuring the echo shift in the imaging space. PGM was shown to be likely to produce improved accuracy when acquiring images at higher resolution [180]. Two different methods to generate phase gradient maps have been described. One uses a standard forward difference operation on normal phase images in order to determine the phase gradient [183]. The phase gradient can also be calculated by implementing difference operation in the Fourier domain using a fast Fourier transform (FFT) without phase unwrapping [184]. Phase gradient maps can be used for the analysis of phase perturbations introduced by macroscopic objects [183], tissue differentiation of tissues with different susceptibilities through contrast enhancement [185] and for the detection of local field inhomogeneities for positive contrast imaging of SPIONs [184].

5. Superparamagnetic Iron Oxide Nanoparticles (SPIONs)

Superparamagnetic iron oxide nanoparticles and gadolinium chelates are two classes of MRI contrast agents that are in the focus of medical imaging research but also readily used in clinical practice. SPIONs are biocompatible and display no remnant magnetisation outside of the MR environment making them ideal for applications in MRI. In this chapter, the different types of magnetisms will be described and the physicochemical nature of iron oxides explained. The most popular synthesis strategies and common stabilisers will be discussed. The chapter finishes with a short literature review of current biomedical applications of SPIONs where the focus will be on MR imaging and treatment of cancer.

5.1. Magnetism

The nature of magnetic dipole moments and how they can be explained using quantum mechanical concepts was introduced in chapter 2. MR contrast agents based on iron (SPIONs) possess a specific type of magnetic characteristic called superparamagnetism. In the following the main types of magnetic behaviour that materials can display, dia-, para-, ferro-, and superparamagnetism will be described to understand why it is important for SPIONs to be superparamagnetic.

5.1.1. Diamagnetism

Atoms where each quantum mechanical sublevel contains an electron pair (one with spin up ↑ and one with spin down ↓) do not possess a net magnetic dipole moment. Each individual electron has a magnetic moment but due to the pairing of electrons, the overall atom will have no magnetic moment. Diamagnetism describes the existence of an induced magnetic dipole moment by an external magnetic field. The reason for that is a small alteration of the electrons orbital motion by the external magnetic field that leads to an extremely weak magnetic moment in the atom or molecule. The macroscopic induced magnetic moment is antiparallel to the applied magnetic field which means the induced magnetic field opposes the applied field. Diamagnetism is an omnipresent property of all materials but it might be obscured due to the presence of a stronger magnetic property such as para- or ferromagnetism. The strength of the induced diamagnetic field is directly proportional to the applied magnetic field and not dependent on temperature [89], [186].

5.1.2. Paramagnetism

Contrary to diamagnetism, when an atom has an unpaired electron in its outer shell, it possesses a permanent intrinsic magnetic dipole moment in the absence of an external magnetic field. This magnetic property is called paramagnetism. However, a sample of many paramagnetic atoms will not have a net magnetic moment because the individual magnetic dipole moments will be randomly distributed and cancel each other out. A bulk magnetisation can be achieved by applying an external magnetic field. The individual magnetic dipole moments preferentially align parallel to the external magnetic field and the strength of the bulk paramagnetic moment depends on the field strength of the applied field. The difference to diamagnetism is that the paramagnetic dipole moment is much stronger than the diamagnetic moment. Furthermore, the strength of the paramagnetic dipole moment heavily depends on the temperature. Similar to the nuclear magnetic dipole effect discussed in chapter 1, thermal energy accounts for the fact that not all individual spin moments will align parallel to the applied magnetic field. Some might align antiparallel to it. The proportion of spins that are aligned antiparallel to the applied field increases with temperature. Saturation magnetisation is therefore achieved in the region close to absolute zero (-273 °C) [89], [186], [187].

5.1.3. Ferromagnetism

Ferromagnetism is fundamentally different to dia- and paramagnetism in the sense that the latter are properties of individual atoms or molecules while ferromagnetism can only be exhibited by a group of atoms or molecules that are combined in a crystal structure. When paramagnetic atoms are closely packed in a crystal structure, the magnetic dipole moments of neighbouring atoms will interact with each other and align in a parallel fashion. Such materials are magnetically ordered and within the material permanently magnetised domains are established. Each of these magnetic domains contains a vast number of spin dipole moments. A limiting factor in terms of their size is the range of the spin-spin forces. Normally, the magnetic domains are dispersed randomly and no net magnetisation is observed. However, upon the application of a magnetic field the magnetic domains will readily start to align parallel to the applied magnetic field and the material becomes magnetised. Ferromagnetic materials can be magnetised to the maximal potential (saturation magnetisation = almost all domains align parallel to applied field) with low external magnetic fields. Furthermore, a remnant magnetisation remains even when the applied magnetic field is completely removed. To remove the remnant magnetisation and demagnetise a ferromagnet, energy in the form of heat is required. That is because by aligning in a parallel fashion, the magnetic dipole moments of the individual magnetic domains have taken a low energy state which the system likes to retain. In order to demagnetise a ferromagnetic material it would need to be heated above a critical temperature (Curie

temperature) which depends on the ferromagnetic material. Above the Curie temperature, ferromagnetic materials show paramagnetic characteristics including the lack of remnant magnetisation. Examples of ferromagnetic elements are iron, cobalt, nickel, as well as several alloys and transition metal oxides [89], [186], [187].

5.1.4. Superparamagnetism

Superparamagnetism [188] is a magnetic property obtained when decreasing a ferromagnetic particle until it only contains one magnetic domain. Particles that are superparamagnetic have unique characteristics that make them well suited for many applications especially as MRI contrast agents. Upon application of an external magnetic field, superparamagnetic particles will similarly to ferromagnetic materials exhibit a very strong magnetic field by achieving saturation magnetisation. However, once the external field is removed, no remnant magnetisation is observed because the magnetic dipole moments disperse in a random fashion due to thermal motion. That means, superparamagnetic particles show a similar magnetisation behaviour as paramagnetic materials with the difference that they are readily able to achieve saturation magnetisation and therefore can get much stronger magnetised [89], [186], [187], [189].

5.2. Iron Oxides

The most common forms of iron oxide in nature are magnetite (Fe_3O_4), maghemite (γ-Fe_2O_3), hematite (α-Fe_2O_3) [190]. The former two exhibit superparamagnetism at room temperature if the particle size is smaller than ~20 nm [191], [192]. Iron oxide particles of that size are a single magnetic domain crystal which possesses superparamagnetism. SPIO exhibit a much stronger susceptibility effect than just paramagnetic materials such as gadolinium because the whole crystal aligns with the external field and saturation magnetisation is achieved [193]. This characteristic as well as the biocompatibility and biodegradability of magnetite and maghemite [194] makes them particularly well suited for biomedical applications.

5.2.1. Magnetite (Fe_3O_4)

From all transition metal oxides, the magnetism exhibited by magnetite is the strongest. It is ferromagnetic and has a lattice parameter of 8.396 Å. Because of its black-brown colour it is also referred to as black iron oxide [190], [195]. The crystal structure is an inverse spinel with planes of oxygen anions in a cubic arrangement. The Fe^{2+} ions occupy octahedral (O_h) interstitial sites and the Fe^{3+} ions are randomly distributed between tetrahedral (T_d) and octahedral positions [196]. The spins of the ions occupying the tetrahedral and octahedral sites take antiparallel positions to each other when exposed to an external magnetic field [194].

Because magnetite has Fe^{2+} and Fe^{3+} in its octahedral positions, electrons can move between the two at room temperature [197].

5.2.2. Maghemite (γ-Fe_2O_3)

Maghemite is formed from other iron oxides through heating or as a result of the weathering process of magnetite. In a laboratory setting, maghemite is the product of oxidising magnetite. It can easily be distinguished from magnetite because of its red-brown colour. Maghemite is ferrimagnetic and has a lattice parameter of 8.347 Å. Its crystal structure is similar to the one of magnetite but the spinel structure possesses vacancies in the cation sublattice (defect spinel). Fe^{3+} ions occupy two-third of the crystal sites which are arranged so that one vacant site follows two occupied sites [190]. The ordering of the vacancy decreases as the maghemite particle size becomes smaller [198]. Maghemite has a lower saturation magnetisation than magnetite [193].

5.3. Synthesis and Stabilisation of SPIONs

In the last 20 years superparamagnetic iron oxide nanoparticles have been intensely investigated for their biomedical applications. New and improved synthetic routes have been proposed with the aim to produce monodisperse SPIONs while having good control over the particle size. Furthermore, SPIONs need to be stable in aqueous solution and be biocompatible.

5.3.1. Synthesis strategies

The simplest way to synthesise SPIONs that also offers the most control is via a wet chemical route. In the following the two main methods, coprecipitation and thermal decomposition, are described and further references are provided for the interested reader.

5.3.1.1. Coprecipitation

Superparamagnetic iron oxide nanoparticles such as magnetite and maghemite precipitate from an aqueous iron salt solution in an alkaline environment [199]–[203]. The size, shape, and composition of the SPIONs depend on the iron salt (e.g. nitrates, sulphates, chlorides, etc.) as well as the ratio of ferrous to ferric ions (i.e. Fe^{2+}/Fe^{3+}) and the pH [204], [205]. Isolation of the iron oxide precipitate is achieved by centrifugation or magnetic decantation. Usually the precipitate is washed with either nitric acid or perchloric acid and colloidally dispersed [193]. For a Fe^{2+}/Fe^{3+} ratio of 2:1, the chemical reaction equation can be written as [190], [206]

$$Fe^{2+} + 2Fe^{3+} + 8OH^- \rightarrow Fe_3O_4 + 4H_2O \quad (166)$$

It is important to ensure that the reaction environment is alkaline (i.e. pH 9 – 14) and free of oxygen by conducting the reaction in a nitrogen environment to avoid oxidation of Fe_3O_4 [187].

In order to stabilise the SPIONs and prevent agglomeration, the iron oxide particles are often coated during the precipitation procedure through the presence of surface complexing agents [193]. There are several other methods that are based on the coprecipitation method that have been used successfully to synthesise SPIONs. Among those, the most common approaches are the microemulsion technique [207], the reduction precipitation [208]–[211] where an iron salt is reduced in the presence of an surfactant agent and the sol-gel approach [212].

According to Bagwe et al. [213] a microemulsion is a thermodynamically stable isotropic dispersion of two immiscible liquids. The microemulsion can either be oil-in-water or water-in-oil. Iron oxides for biomedical applications are mostly synthesised with the water-in-oil approach [193]. The aqueous iron salt phase will form microdroplets by separating it with a surfactant coating from the organic phase (i.e. reverse micelle). Upon adding nanodroplets of a base, the two aqueous nanodroplets will collide, coalesce and break and iron oxide particles precipitate within the micelles [214]–[217]. SPION synthesis by microemulsion results in a uniform population [218] and offers good control over size and shape [219] of the nanoparticles. A disadvantage of this approach has been described where larger nanoparticles resulted because of poor crystallinity of the SPIONs [197].

5.3.1.2. Thermal Decomposition

The decomposition of an organometallic precursor complex by applying heat or light is one of the simplest methods to synthesise SPIONs [192]. Thermal decomposition has also been popular because it is considered to produce monodisperse particles while allowing good control over the particle size. Common organometallic precursors are iron cupferron ($Fe(Cup)_3$) [220], iron pentacarbonyl ($Fe(OH)_5$) [221], [222], and iron triacetylacetonate ($Fe(acac)_3$) [223]. The morphology and size of the resulting SPIONs is determined by the ratios and concentrations of the reactants, the temperature, reaction times, as well as the nature of solvents and precursors [224]. Rockenberger et al. [220] were able to receive monodisperse maghemite particles from a thermal decomposition reaction of $Fe(Cup)_3$ in the presence of octylamine and trioctylamine. Hyeon et al. [225] described the synthesis of highly monodisperse maghemite particles of sizes between 4-16 nm from $Fe(OH)_5$ in oleic acid at 100°C. Sun et al. [209] reported the synthesis of monodisperse magnetite particles (4-20 nm) from $Fe(acac)_3$ that reacted with 1,2-hexadecanediol in the presence of oleic acid and oleylamine. Li et al. [226] described the synthesis of magnetite from an iron salt ($FeCl_3$) by thermal decomposition in an acidic or alkaline environment.

5.3.2. Stabilisation of SPIONs

The surface of bare superparamagnetic iron oxide nanoparticles is hydrophobic. For biomedical applications these particles need to be in an aqueous solution. Uncoated SPIONs in an aqueous solution try to minimise contact with the solvent by exhibiting hydrophobic interactions that causes the particles to agglomerate and decrease their surface area to volume ratio. Larger SPION cluster exhibit dipole-dipole interactions and the magnetic behaviour changes from superparamagnetic to ferromagnetic. Nanoparticles with a remnant magnetisation agglomerate and can block blood vessels in biomedical applications [195], [227]. In addition, flocculation can occur because of the van der Waals force. Biomedical applications require monodisperse, stable, biocompatible particles which is why SPIONs are usually stabilised with a coating material [228]. The coating can be done in situ (during the synthesis of the SPION) or after the synthesis reaction in a separate step. Common coating materials are monomeric stabilisers such as carboxylates [229]–[232] and phosphates [190], [233]. Various long-chained polymers such as dextran [234] and polyethylene glycol (PEG) [235] have also been extensively studied as SPION stabilisers. Finally, inorganic materials such as silica [236], [237], gold [238], [239], or gadolinium [240], [241] have been utilised to coat bare iron oxide nanoparticles because they allow the binding of biological ligands to the surface of the SPION [224].

5.3.2.1. Monomers

Citric acid is a carboxylate that has been used to stabilise magnetite particles in an aqueous medium [229]. Citric acid possesses three carboxylic acid groups of which one or two are used for the coordination to the surface of magnetite. The uncoordinated carboxylic acid group(s) give the coated SPION surface a negative charge and therefore hydrophilic character [224]. One well described SPION that is coated with citric acid and has undergone clinical investigation is VSOP C184. It is synthesised by coprecipitation in the presence of citrate ions. The particle is very small with a hydrodynamic diameter of 8.6 nm [242], [243]. It was reported by Bee et al. [199] that the size of maghemite particles depend on the concentration of citrate ions. Krishnamurti and Huang [244] describe that the citrate has an effect on the Fe^{2+} kinetics. Moreover, the higher the concentration of citric acid during synthesis of the SPION the lower its crystallinity [245]. Changes in the surface geometry of the iron oxide nanoparticles have been reported because of citrate and other carboxylate coatings [246], [247]. Other carboxylates that have been used for coating SPIONs are dimercaptosuccinic acid (DMSA) [231], phosphorylcholine [232], [248], and gluconic acid [230]. The effectiveness of these coating materials in stabilising the SPION is highly dependent on pH.

5.3.2.2. Polymers

Dextran is one of the most popular coating materials for iron oxide nanoparticles because of its biocompatibility [234], [249]. It is made up of α-D-glucopyranosyl units making it a polysaccharide polymer [224]. The first publication that described the coating of magnetite with dextran was by Molday and Mackenzie [250] in 1982. Ferumoxtran-10 [251] that has a hydrodynamic diameter between 15-20 nm was synthesised according to the method described by Molday and Mackenzie [250] and coated with dextran. Closely related to dextran are carboxydextran and carboxymethyl dextran that have been used to coat Resovist® [252] and ferumoxytol [253], respectively. The dextran chains have been reported to lead to ideal polar interactions with the surface of iron oxide nanoparticles. This is because of the relatively high bonding energy of all the hydrogen bonds formed by the hydroxyl groups over the length of a dextran molecule [254]. Polyethylene glycol (PEG) is hydrophobic and water-soluble. It increases blood circulation time and biocompatibility [255], [256]. PEG-coated SPIONs with hydrodynamic diameters between 60-100 nm (small) and 20-35 nm (ultra small) have been synthesised [257]. Polyethylenimine (PEI) [258], [259] can form cationic complexes when used to stabilise SPIONs. Negatively charged biomolecules such as DNA therefore interact with PEI electrostatically and allow PEI to enter cells via endocytosis [190]. Polyvinyl Alcohol (PVA) is hydrophilic and biocompatible and aids in the production of monodisperse nanoparticles by hindering agglomeration [260], [261]. Lee et al. [262] synthesised stable SPIONs in situ by precipitating an iron salt in an aqueous solution of PVA. It has been suggested that the binding of PVA to magnetite is irreversible.

5.4. Biomedical applications

Superparamagnetic iron oxide nanoparticles can be used for diagnostic and therapeutic applications as magnetite and maghemite are both biocompatible with a low cytotoxicity [195], [227]. It is common for biomedical applications with SPIONs to differentiate between passive and active targeting. This section will describe these two targeting approaches and provide examples with an emphasis on cancer applications in imaging and treatment.

5.4.1. Passive targeting

Superparamagnetic iron oxide nanoparticles that have been coated with a stabiliser but have not undergone any further functionalisation reach their target sites via distinct anatomic or physiological processes. The hydrodynamic diameter and surface charge of the SPION determine its targeting route. The blood circulation time, tissue uptake, opsonisation, as well as type and rate of cell uptake of the SPIONs are all determined by these two parameters [193].

5.4.1.1. Clearance pathways

The reticuloendothelial system (RES) is comprised of macrophages, monocytes, and their precursor cells. It is also referred to as the mononuclear phagocyte system (MPS). Monocytes are produced by progenitor cells and are released into the circulatory system. This allows monocytes to migrate to different tissues. Once they have diffused into a particular tissue, they can differentiate into macrophages that will have functional and morphologic qualities according to a particular function. This means that macrophages in different tissue have different functions. One common task all reticuloendothelial cells share is the clearance of damaged cells and external particles [263].

Plasma proteins such as albumin or immunoglobulins are adsorbed by SPIONs because of their large surface area to volume ratio. The adsorption of plasma proteins lead to a recognition of the SPIONs by Kuppfer cells of the liver and macrophages which are part of the RES. Coating with polyethylene glycol (PEG) [264] minimises protein adsorption and increases blood circulation time [265]. SPIONs with hydrodynamic diameters larger than 200 nm are taken up by the spleen due to mechanical filtration where cells of the RES remove the SPIONs. Nanoparticles with hydrodynamic diameters smaller than 10 nm are removed from the system by the kidneys. The ideal size for SPIONs in order to have a long blood circulation time is a hydrodynamic diameter between 10 and 100 nm. This size allows the SPIONs to reach small capillaries while avoiding the RES [187].

5.4.1.2. Cancer applications

Fast tumour growth is accompanied by rapid angiogenesis [266] to ensure sufficient blood supply to the tumour. As a result, the neovasculature of tumours is damaged and leaky [267], [268] which results in an increased permeability for SPIONs. The nanoparticles are retained inside the tumour because of an underdeveloped lymphatic drainage system. This phenomenon is called the enhanced permeability and retention (EPR) effect which was first described by Maeda et al. [269]. The EPR effect will only lead to increased SPION accumulation in tumours if the nanoparticles are adequately coated to allow for a prolonged blood circulation times [270].

Moore et al. [270] have reported that SPIONs coated with dextran injected in a rat gliosarcoma model were taken up 10-fold more by cancerous tissue compared to healthy tissue. The maximum accumulation of SPIONs in the tumour occurs 24 hours post injection [271]. The internalisation of SPIONs by tumour cells most likely happens via pinocytosis rather than receptor-mediated endocytosis [270], [272]. Nanoparticles with smaller hydrodynamic

diameters are better suited to move into the tumour interstitium [273]. SPIONs also tend to accumulate in sites of inflammation where no cancer cells are present which decreases the cancer specificity of this approach [267]. Bone marrow lesions have been detected with SPIONs with high sensitivity [274]. Jordan et al. [275] showed *in vitro* the selective uptake of aminosilane nanoparticles by glioblastoma cells while healthy glial cells did not internalise the nanoparticles. However, these results do not directly translate in vivo as described by van Landeghem et al. [276]. SPIONs have also been used for the detection of focal splenic tumours [277] and the differentiation of metastatic and inflammatory tumours [278]. A general problem of molecular imaging with MRI remains its lower sensitivity compared to nuclear or optical imaging modalities [273].

Hyperthermia is based on magnetic induction where tumours with an accumulation of magnetic particles are exposed to an alternating magnetic field [279]. Magnetic nanoparticles such as SPIONs generate heat when brought into an alternating magnetic field because of the magnetic hysteresis loss. The temperature of the generated heat depends on various factors such as the magnetic field strength, the magnetic nature of the particles, the oscillation frequency and biological factors such as the blood flow rate in the target area. Most cancer cells die at temperatures above 43°C while healthy cells can withstand these temperatures [280]. Tumours exhibit a high interstitial pressure which can hinder the diffusion into the tumour interstitium for SPIONs larger than 50 nm. Therefore, MR imaging applications commonly use smaller SPIONs. However, these cannot generate enough heat to kill tumour cells for hyperthermia applications [273]. Preclinical experiments reported side effects such as oedema, cerebral necrosis, infarction, and focal haemorrhage [281]. For hyperthermia applications, SPIONs can be directly injected into the tumour. The aim of passive targeting in this case is to maximise the uptake of nanoparticles by cancer cells [273]. Dextran-coated magnetite particles have successfully been used for hyperthermia treatment of oral cancer. The particles where directly injected in the tumour on the tongue and temperatures between 43-45°C were reached [282]. The only hyperthermia application so far that was applied in a clinical trials study is for the treatment of the brain and prostate [46], [283], [284].

5.4.1.3. Other applications

SPIONs with hydrodynamic diameters of more than 100 nm are taken up by the Kupffer cells of the liver which enables SPION-enhanced hepatic MRI [285]. Reimer et al. [286] demonstrated the improved detection of hepatic lesions with this approach. SPIONs with hydrodynamic diameters of around 30 nm can get from the vasculature to the interstitial space and move on from there via the lymphatic vessels to the lymph nodes where they accumulate [270], [287].

The absence of SPIONs in the lymph nodes after intravenous injection could indicate metastases of a primary tumour that are blocking the lymphatic vessels [288].

Stem cells have the unique ability to divide in different cell types. They can therefore be used for tissue repair by replacing necrotic or damaged cells. By labelling stem cells with SPIONs, the migration of the stem cells can be monitored in vivo by MRI [289]. The labelling must not affect the functionality, vitality and mobility of the stem cell. Approaches for stem cell labelling mainly focus on SPION uptake by endocytosis [290]. Successful labelling depends on shape, size, surface charge and chemistry of the SPION as well as type of cell. SPIONs can be functionalised with peptides that are able to translocate the cell membrane or other surface ligands that aid in interactions with the cell membrane [291]. Specific examples of where this technique has been applied are for the treatment of brain trauma [292], Type 1 diabetes [293], chronic spinal cord injury [294], multiple sclerosis [295] and to monitor cell therapy in melanoma patients [296]. A current problem is the inability of MRI to quantify iron oxide nanoparticles. Furthermore, the differentiation between stem cells labelled with SPIONs and other sources of hypointense MRI signals is difficult. SPION-labelled stem cells might also undergo asymmetric cell division [297].

Apart from magnetite and maghemite, chemically more sophisticated iron oxides have also been explored for their passive targeting ability. Examples are shape modified iron oxides such as nanocubes [298] and polyhedral nanoparticles [299]. Another option are iron oxides that have another transition metal incorporated in their crystal structure such as quantum dot-capped magnetite nanorings [300], cobalt nanoparticles [301], and manganese nanoparticles [302].

5.4.2. Active targeting

Active targeting describes the conjugation of ligands with a particular affinity or functional groups to the surface coating of SPIONs to make their agglomeration in biological tissue highly specific [273]. Polymer coatings are popular because they provide many reactive parts such as carboxyl and amine groups useful in a variety of conjugation strategies [193]. Ligands that possess a particular affinity are aptamers, peptides, and antibodies. Antibodies are relatively large biomolecules which significantly increases the hydrodynamic diameter of the functionalised SPION. This decreases the chances of extravasation from the circulation and diffusion in the interstitium. However, antibodies possess a very high affinity which makes them interesting targeting agents. Antibodies that originated from a different organism than the one they are applied to might cause an immune response [273]. Active targeting provides information about physiological and molecular mechanisms [193].

5.4.2.1. Cancer applications

SPIONs usually target the surface antigen in tumours because they are easily accessible. There are many early markers of cancer that can be targeted with functionalised iron oxide nanoparticles. These markers need to be specifically overexpressed on a particular cancer cell type and also accumulate the SPIONs intracellularly [193]. Examples are HER-2/neu receptor, mucin-1 antigen, carcinoembryonic antigen, folate receptor, transferrin receptor, CD-20 antigen, and integrins. The transferrin receptor has been described as a target for breast cancer [303]–[305]. Several authors have described the targeting of the folate receptor overexpressed in several cancer cells [306]–[308]. Common in epithelial cell adenocarcinomas (i.e., pancreatic, breast, lung, colorectal, prostate, and gastric) is the underglycosylated mucin-1 antigen that can be targeted with the EPPTI peptide [309]. Gliomas upregulate matrix metalloproteinase-2 that can be targeted with the chlorotoxin peptide [310]. Breast cancer metastases overexpress the HER-2/neu tyrosine kinase receptor that attracts Herceptin [311], [312]. Hepatic carcinomas are in the focus of current targeting strategies because metastases from primary tumour sites in the lungs, breasts, colon, and rectum often form in the liver. Reimer et al. [313] have reported that the asialoglycoprotein (ASG) receptors are present in a healthy liver but absent in hepatocytes of metastatic or primary malignant tumours. SPIONs functionalised with annexin V have been described to successfully detect apoptotic cancer cells after therapy [314].

Active targeting of tumours after intravenous injection for hyperthermia applications remains a problem because the amounts of SPIONs accumulated in the tumour are considerably lower compared to intratumoral injection. The dosages of SPIONs required for a sensible hyperthermia effect have to be much higher than for MRI because of limited heating capacities of current iron oxide nanoparticles formulations. A reason for insufficient SPION accumulation in the tumour could be opsonisation processes. These might mask the ligand used for active targeting conjugated to the SPION surface. The functionalisation generally increases the uptake of SPIONs by cells but does not increase its overall accumulation (permeability) at the tumour site [273]. Ito et al. [315] combined the gene therapy for cancer treatment with hyperthermia. The therapeutic gene expression is induced by the heat generated from the hyperthermia effect. The authors described the positive effect the combined therapeutic approach had on hindering tumour growth in a preclinical mouse model.

5.4.2.2. Cardiovascular applications

Molecular imaging with SPIONs has also been applied to major cardiovascular diseases such as thrombosis, myocardial infarction, and atherosclerosis. Cyclic arginine-glycine-aspartic acid (RGD) peptides [316] can be conjugated to SPIONs to target the $\alpha_{IIb}\beta_3$ integrin that is expressed on activated thrombosis platelets [317]. Another marker, the activated coagulation

factor XIII(FXIIIa), can be detected with an alpha$_2$AP peptide conjugated to iron oxide nanoparticles. FXIIIa is a transglutaminase that plays a vital role in the formation of stable thrombi by crosslinking plasmin and fibrin inhibitors [318], [319]. Weissleder et al. [320] attached R11D10 to SPIONs and successfully targeted an infracted area with this monoclonal antibody specific to necrotising cardiac myocites. Kelly et al. [321] described the detection of atherosclerosis targeting the vascular adhesion molecule-1 (VCAM-1) which is an early marker for endothelial inflammation. Another proinflammatory marker of endothelial cells is E-selectin that is also associated with angiogenesis and tumour vascular endothelial proliferation [322], [323].

5.4.2.3. Other applications

Apoptosis is of vital importance in acute myocardial infarction, cancer, and chronic inflammation. Zhao et al. [324] targeted apoptotic cells in vivo with SPIONs which offers real-time monitoring via MRI of drug effects. SPIONs have also been successfully employed to aid with tissue repair. SPIONs coated with proteins or synthetic polymers can be directed between two tissue surfaces where tissue soldering is taking place at temperatures higher than 50°C [325]. Furthermore, SPIONs coated with inorganic materials such as gold or silica have been described as strongly light absorbing. When placed at the surfaces of tissue sites that need to be joined, these particles can aid the soldering upon application of laser light [326]. SPIONs can also transport and direct stem cells to a specific target site as well as proteins and growth factors that can help with tissue development [327]. Another application is the use of iron oxide nanoparticles as drug carriers for a targeted delivery. The pharmaceutical drug is conjugated on the surface of the coating and should be released at the target site. Of particular importance are charge, size and the nature of the coating material of the SPION for this application [328]. Magnetite antrapped in albumin was described as an approach to release anti-cancer drugs (adriamicin, mitomicin) at a tumour site [329]. Another author has reported that magnetite particles coated with poly(DL-lactide) can be used as polymeric spheres that are loaded with a pharmaceutical drug [330]. The overall advantage of developing and employing a targeted drug delivery approach is that the drug dose can be reduced and therefore potential side effects minimised [187].

6. Implementation and optimisation of existing positive-contrast MRI methods

6.1. Introduction

This chapter describes the implementation and optimisation of GRASP and IRON. The changes made to the code in the pulse programming environment are detailed and scan parameter optimisations are evaluated and discussed.

A theoretical description of GRASP, IRON, SGM and FLAPS has been provided in chapter 4. To avoid repetitions, these techniques will not be described in detail again and the reader is referred to chapter 4 for further information. Chapter 4 also contains a brief literature overview about other relevant positive contrast imaging techniques for SPIONs. These techniques were not implemented or used as part of this thesis. However, these techniques should be mentioned within the thesis to put the experimentally utilised techniques in context and give the reader an overview of alternative methods.

6.2. GOAL-C and the Philips pulse programming environment

All MR experiments presented in this work were conducted on a clinical 3T Philips Achieva System. Philips provides a pulse programming environment to associated research institutions that allows to make changes to the built-in MRI sequences. The Philips pulse programming environment is called *PARADISE* that can be run in a virtual machine (e.g. VMware Workstation). *PARADISE* encompasses a file directory that includes the code for the built-in sequences, a simulation tool and a tool that graphically displays sequence (timing of gradients, radiofrequency pulses etc) that were run in a simulator. Files containing code were opened and edited in Microsoft Visual Studio C++ .NET version 2003.

The MR pulse sequences are written in GOAL-C (**G**yroscan **O**bject-oriented **A**cquisition **L**anguage) which is similar of C++. Code files are categorised in three broad folders, MPF files, PDF files and global files. The latter is able to communicate across MPF and PDF.

Code files are clearly labelled to indicate their function. As an example, the file ‘mmiffe’ is in the MPF (because of ‘mm’, a file in the PDF would start with ‘mp’), the content is related to imaging (because of the ‘i’) and describes a gradient echo sequence (because of ‘ffe’ which stands for ‘fast field echo’ and means gradient echo in Philips terminology). There are three main file types, text files (.txt), include files (.h) and source files (.gc).

6.3. Implementation of GRASP and IRON

We first describe the implementation of GRASP and IRON in the pulse programming environment with examples of changes that were made to the code. The optimisation of the implementation will be discussed following on from that.

6.3.1. Parameter definition and initialisation

As a first step, the parameters for GRASP and IRON had to be defined. For GRASP, three parameters were required:

- GRASP (Yes/No parameter, i.e. ON or OFF)
- Gradient step (float, shows a default value that the user can change)
- Gradient strength (float, shows a default value that the user can change)

For IRON seven parameters were defined:

- IRON (Yes/No parameter)
- Frequency offset (float)
- Bandwidth (float)
- Frequency loop (Yes/No parameter)
- Frequency step (float)
- Bandwidth loop (Yes/No parameter)
- Bandwidth step (float)

All parameters that will be enabled for display and visible to the user must be included in a text file. Parameters are assigned a unique ID (e.g. MDXNIACQ125). The name of the parameter as displayed on the user interface is specified (e.g. gradient step [mT]). By using an indent, parameters can be shown as subordinate to other parameters.

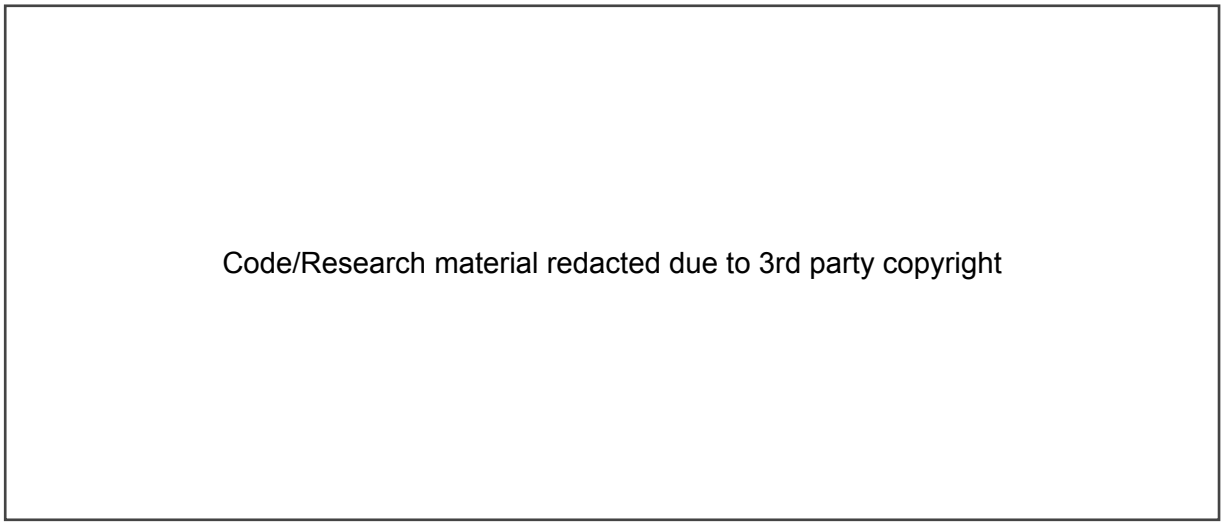

All parameters were set up in relevant include files (".h"). There are different types of parameters, MP parameters (available globally), UGN1 and EX parameters. An overview of parameter definitions for GRASP are shown below.

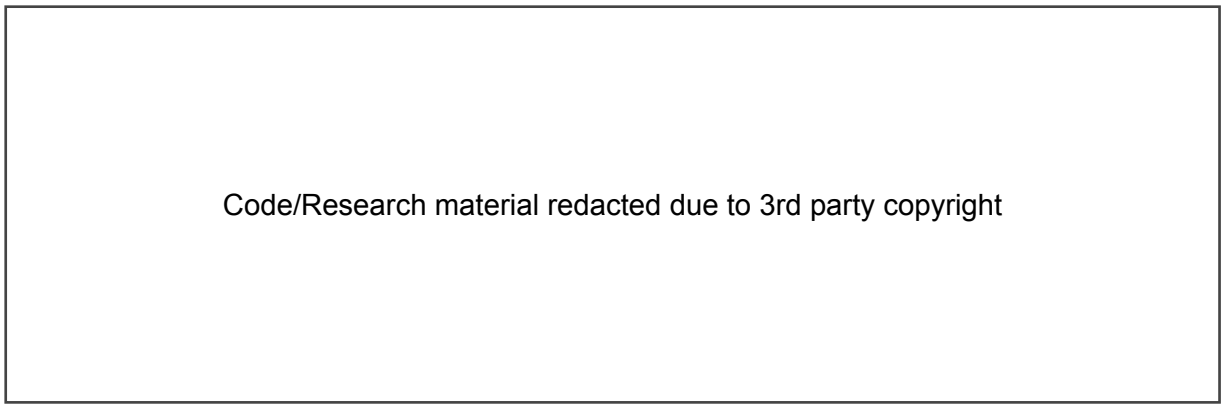

The EX parameter for GRASP and IRON were specified in mpuexrcd.h. The other GRASP parameters were defined in include files labelled 'acq' (acquisition). To ensure parameters are globally available, i.e. in the PDF as well as MPF, they must also be defined in a global include file (mguacqrcd.h).

In the file mpuacqrcd.h, the EX parameters were defined for the user interface by providing specific characteristics. EX_ACQ_GRASP is a YES/NO parameter which means the user can either have it on (Yes) or off (No). The other two parameters, EX_ACQ_GRASP_gradient_step and EX_ACQ_GRASP_gradient_strength were defined as float parameters. For both, characteristics such as the allowed range, default value and increment step were specified. The name tag is taken from the text files. After defining GRASP parameters for the user interface, they also had to be added to the IEX_ACQ parameter group. The three GRASP variables also needed to be defined as UGN1 parameters.

The IRON parameters were defined in the following include files

- mpuexrcd.h
- mpuspirrcd.h
- mguspirrcd.h

Because IRON was implemented using SPIR (see below for more information), the relevant include files (PDF and global) to define the IRON parameters were those labelled ‘spir’. The executables (EX parameters) were defined in the same include file as the GRASP parameters (mpuexrcd.h). Global MP parameters for the three Yes/No parameter (IRON, frequency loop, bandwidth loop) were defined in mgspirrcd.h.

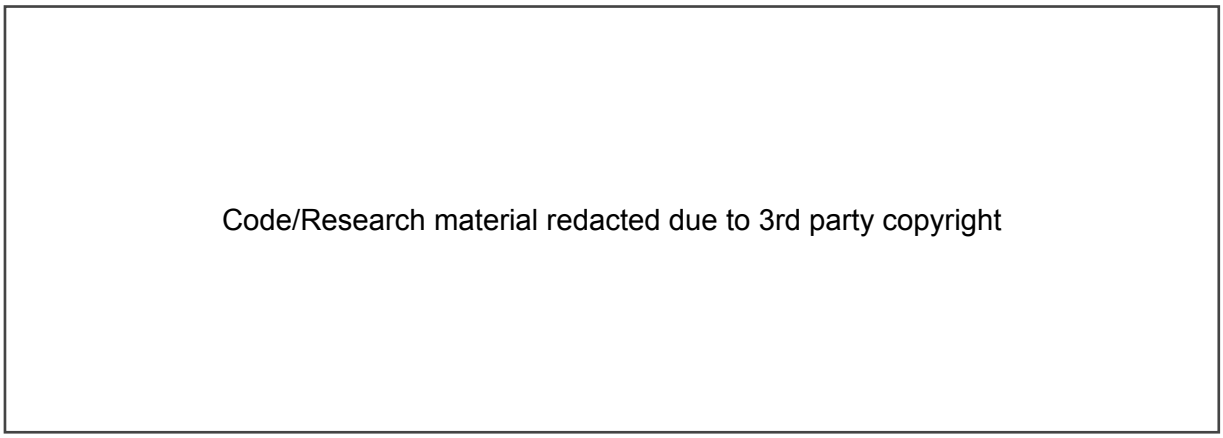

Definitions for the user interface (parameter characteristics) were done in mpuspirrcd.h for EX and UGN1 parameters.

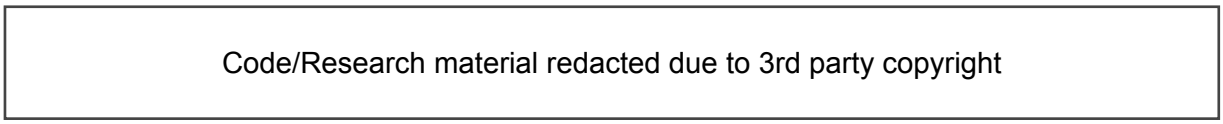

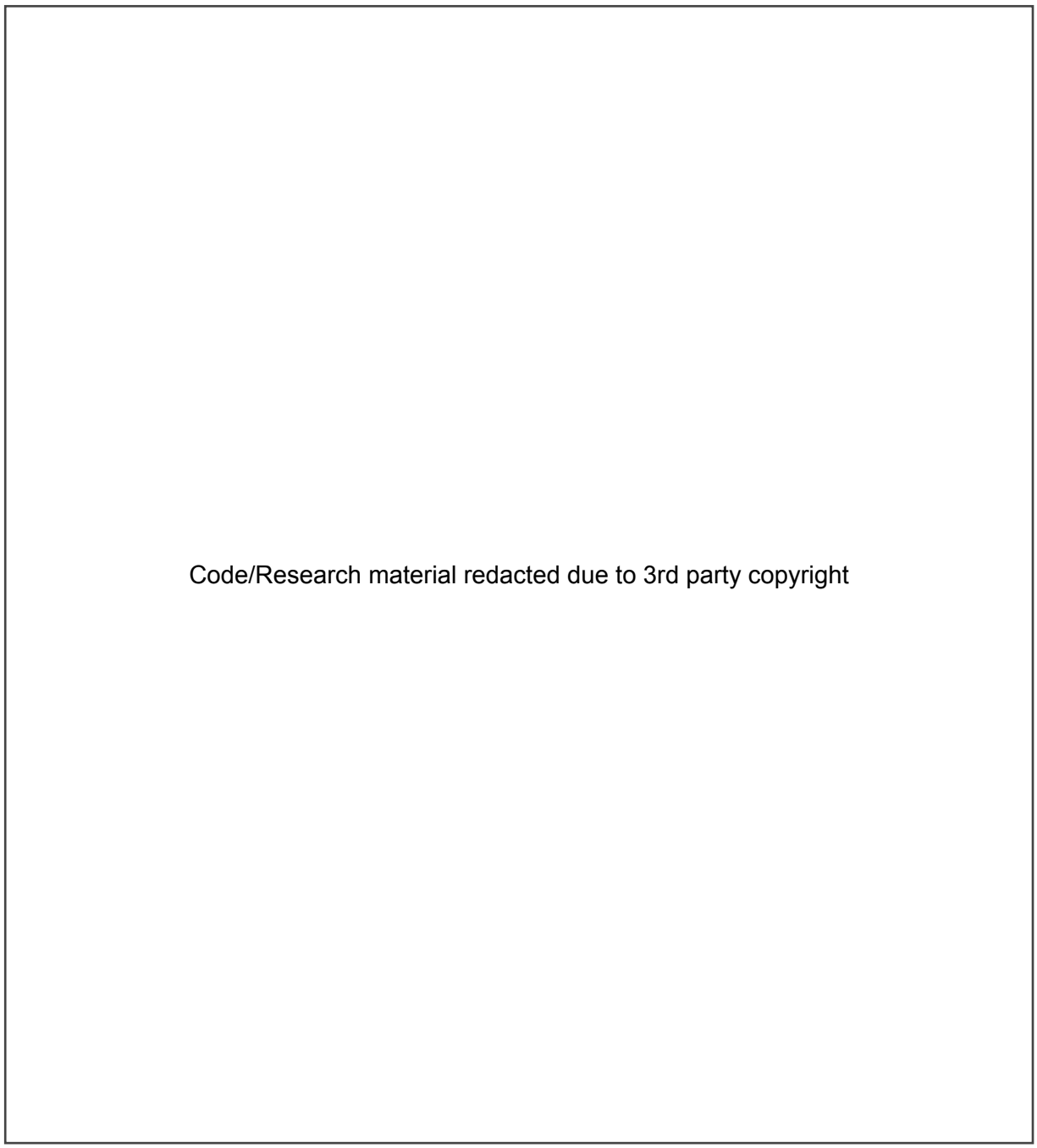

6.3.2. Implementation in PDF and MPF

In all source files where we made changes to the code, a trace was added so that parameters could be logged during scanning. Include files where relevant parameters had been defined were added to the source files.

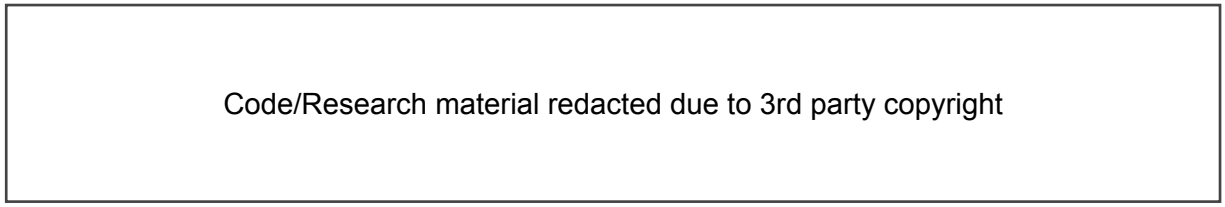

For GRASP, changes were made in two PDF source files, mpiffe_sq_g.c and mpirfe_sq_g.c. The former refers to gradient echo sequences (FFE = Fast Field Echo) and the latter to spin echo sequences (RFE = Refocused Field Echo). We set the gradient strength and gradient step of the slice-select gradient to the parameters that the user could control via the user interface.

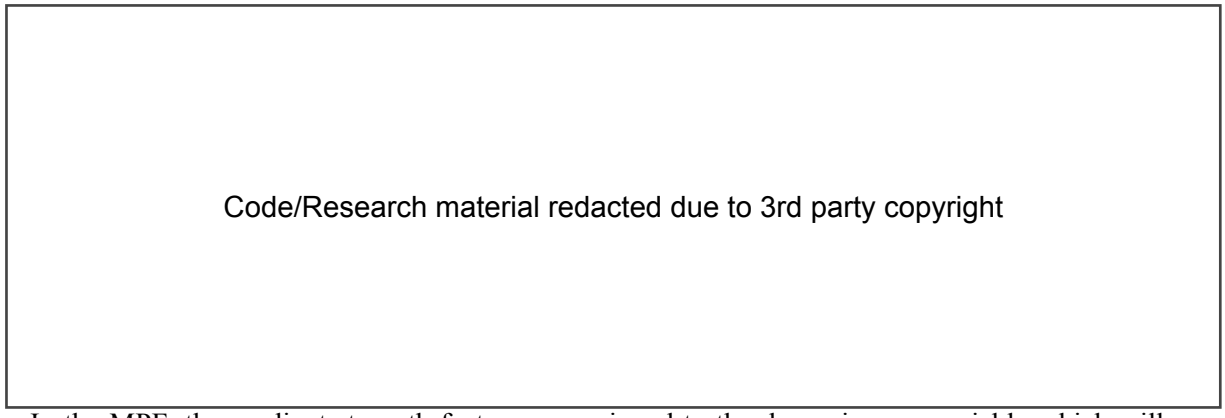

In the MPF, the gradient strength factor was assigned to the dynamic scan variable which will start at zero and increase by 1 with every iteration (the dynamic scan functionality must be selected by the user). This was implemented for gradient (mmiffe_mxg.c) and spin echo (mmirfe_mxg.c) and also enabled for fast imaging (turbo field echo).

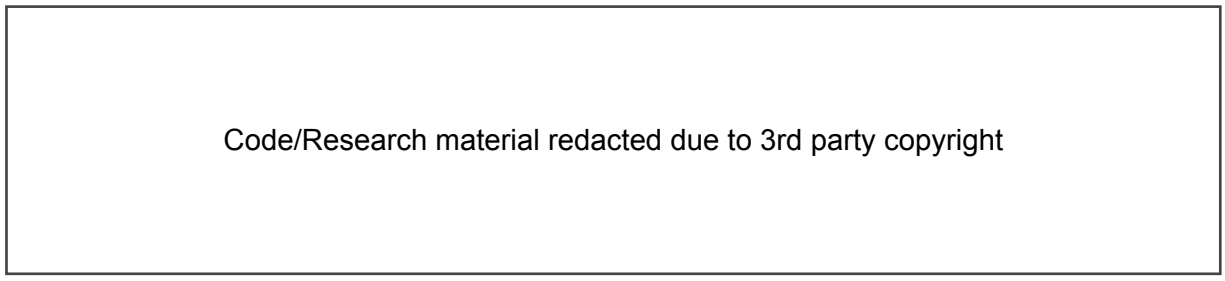

IRON uses an rf pulse to suppress the signal from on-resonant protons during the image acquisition. We decided to use the SPIR pulse for that purpose which was already implemented in the code. Specifically, the code contained three SPIR function, spir1, spir2 and spir3. Spir1 is used for fat and water suppression. Spir2 is used for the respiratory navigator. The spir3 function was not enabled and had no functionality yet which is why we made some changes to the global source file mpuspir_g.c to be able to use spir3 for IRON. Furthermore, we wanted to be able to use SPIR fat suppression in combination with IRON and for that reason did not want to use spir1.

As spir3 was not used by the code for any other functionality, it first had to be initialised including definition of the shot ID. The IRON offset was set to be equal to the standard SPIR offset as a default value. After that, all relevant IRON parameter were enabled for display. We added the function ‘uspir_calc_sq_spir3’ that defines the SQ’spir3 and adds it to the SOR’cycle. Within the validation function MPUSPIR_val13, we defined when the system should provide the user with a conflict. SPIR water and fat suppression must not be used at the same time. The

frequency and bandwidth loops can only be used when the dynamic study was selected and frequency and bandwidth looping cannot happen at the same time either. The IRON bandwidth was defined using the *set_min_dur* function. The frequency and frequency step were defined together with the bandwidth.

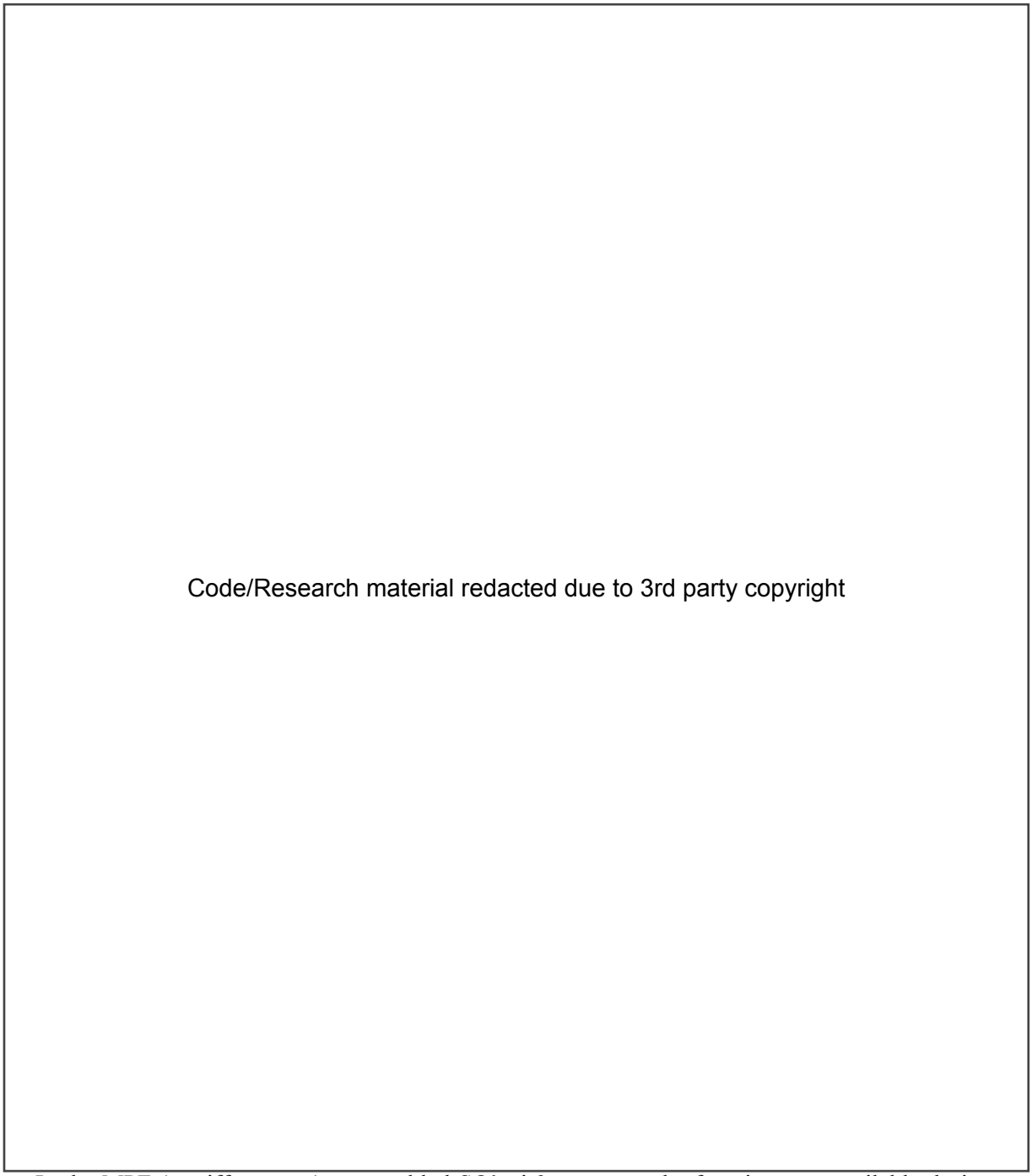

In the MPF (mmiffe_mxg.c), we enabled SQ'spir3 to ensure the function was available during scanning. To ensure the general SPIR functionality was available even when SPIR was not directly selected, we added ('MP_SPIR_IRON == YES) throughout the mmiffe_mxg.c to all 'iffe_enable_spir' functions. This is important because IRON was implemented based on SPIR but we wanted to ensure IRON and SPIR can be used separate from each other, i.e. IRON works

even when no SPIR fat suppression was selected. For the IRON implementation, it was important for us to be able to loop through different frequencies. We defined a frequency factor and frequency step from which the actual frequency could be calculated. At the beginning, the frequency factor ('RFspir3:freq_factor3) is equal to the dynamic variable (iffe_dynamic_scan) which starts at zero and increases by one for each loop. For spir3, we defined three frequency factors. When the dynamic is zero, hence the frequency factor3 is zero, the frequency equals the frequency defined on the user interface and frequency factor1 is set to zero (only needed for the next loop). When the frequency factor3 (dynamic) is larger than frequency factor 1, then the frequency is increased by the amount defined by the frequency step (determined by the operator on the user interface). The frequency does no longer increase when the dynamic has reached its final value as defined by the operator.

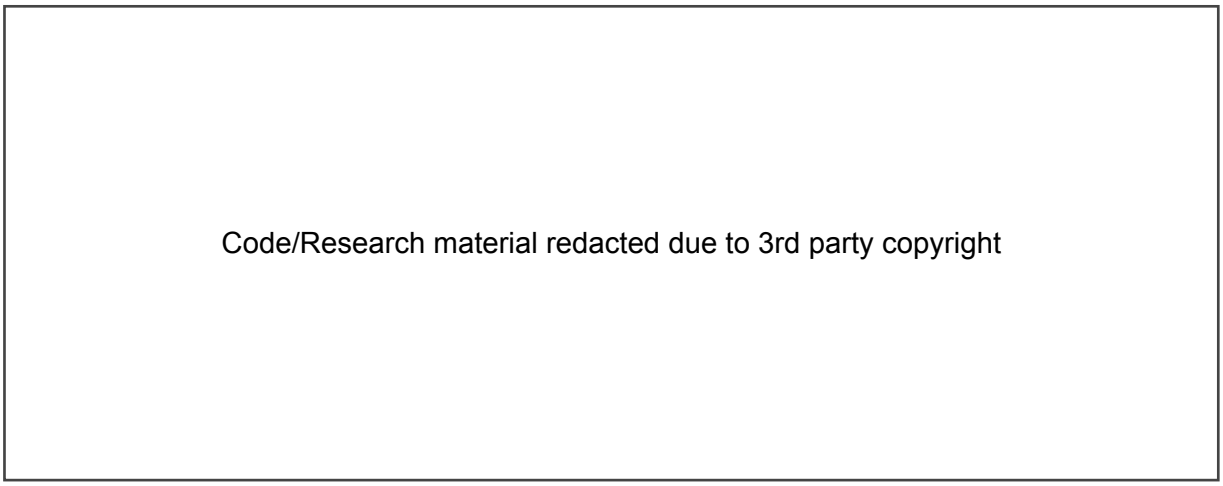

6.4. Optimisation of positive contrast imaging techniques

6.4.1. Test phantoms

We used four different phantom setups for the sequence optimisation. Phantoms A, B and C consisted of a 140 mm crystallising dish (Technische Glasswerke Ilmenau GmbH, Ilmenau, Germany) with 5 mm thick custom-made Perspex holder capable of holding up to six 1.5 ml PCR tubes. Phantoms A, B and C had different vial setups and utilised different SPIONs (see below). Phantom D used the same crystallising dish filled with Gelatine that contained a ball 2.5 mm steel ball bearing in the centre.

Phantom A was loaded with five PCR tubes of very small superparamagnetic iron oxide particles vials (VSOP-200, Ferropharm, Teltow, Germany) of different concentrations (1.2 mM, 0.6 mM, 0.3 mM, 0.15 mM and 0.075 mM) prepared by two-fold serial dilution. **Phantom B** was similar to phantom A but we added a vial of olive oil in the centre of the water phantom. **Phantom C** contained a centre vial filled with superparamagnetic iron oxide nanoparticle F1566 (Liquid Research Ltd., Bangor, UK). The iron concentration was selected to be very

high, 7.56 mg/ml which is equal to 135.37 mM. The centre SPION vial was surrounded by five water vials. The water vials were added to be able to investigate the effects of the presence of the PCR tubes on the centre vial, compare water within the PCR tube to the water in the phantom and to compare the different vial positions with each other in case of local magnetic field differences. **Phantom D** contained a steel sphere of 2.5 mm diameter which was embedded in 600 ml gelatine (6%) which was contained by a 1000 ml glass beaker (Schott). The gelatine was allowed to fully harden before the measurement. The steel ball bearing was completely encompassed in gelatine without any air pockets.

6.4.2. GRASP

The first gradient echo sequence we tested with GRASP was a turbo field echo (TFE) sequence in phantom A (figure 36) with the following scan parameters: echo train length = 15, flip angle = 5, echo time = 3.08 ms, repetition time = 6.8 ms. The slice refocusing gradient was varied between 0 mT and 2.5 mT in steps of 0.5 mT.

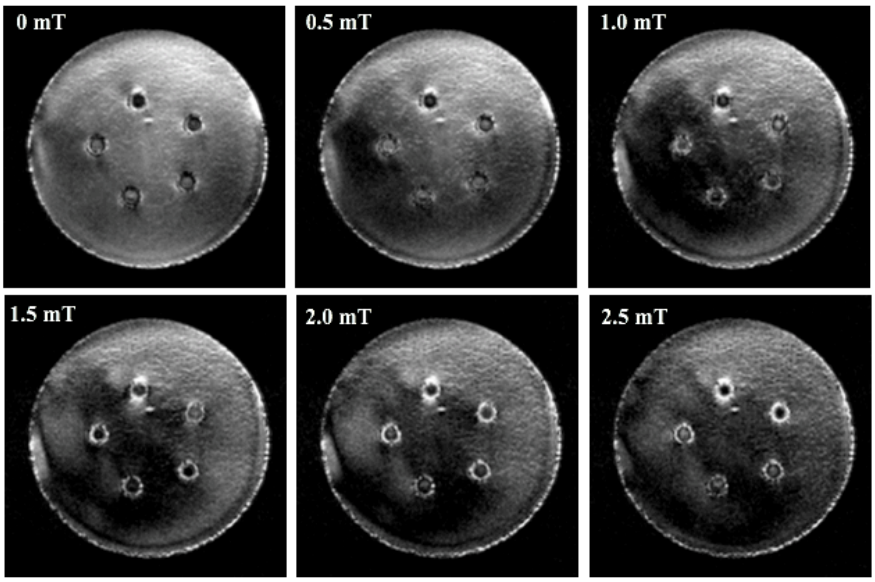

Figure 36: First attempt to receive GRASP images with a TFE sequence with varying slice refocusing gradient strength (0 mT to 2.5 mT).

The general quality of the images is poor and the water phantom is insufficiently suppressed. Hyperintensity is seen around the edges of all PCR tubes on all images, displaying non-specificity regarding Fe concentration and strength of refocusing gradient strength applied. Hyperintensity is most likely the result of the phase change from water to the PCR tube. The vial with the highest Fe concentration shows increased hyperintensity on all images. The vials with the two highest VSOP concentrations showed increased hyperintensity in the 2.0 mT and 2.5 mT images.

The same sequence was tested in phantom C that contained a centre vial filled with F1566 from Liquid research of a high iron concentration (7.56 mg/ml or 135.37 mM). The images obtained from this experiment are shown in figure 37 and several interesting effects can be observed. At a refocusing gradient strength of -3.5 mT, the inhomogeneity introduced through the highly concentrated SPION solution is visible on the gradient echo image. At -2.0 mT, the signal from the on-resonant water protons in the phantom body starts to decrease (i.e. onset of background darkening). At a refocusing gradient strength of 1.0 mT, the majority of on-resonant protons in the water phantom have darkened (i.e. low signal intensity) while the inhomogeneity introduced by the SPION vial is displayed hyperintense. The SPION vial itself does not display any hyperintensity. Instead, the dipole field introduced by the SPION particles becomes hyperintense. We can eliminate an effect of the PCR tubes as 5 other PCR tubes filled with water are present that do not display the same hyperintensity effect.

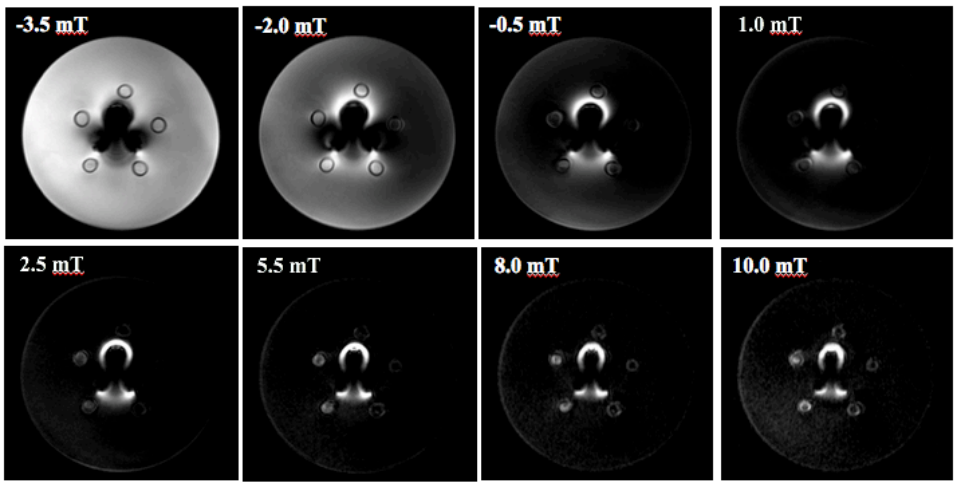

Figure 37: GRASP TFE sequence tested on phantom C. Good background suppression is achieved at a refocusing gradient strength of 1.0 mT. Inhomogeneity introduced by SPION is hyperintense.

As the refocusing gradient is further increased, the on-resonant water signal remains dark but the image quality decreases (e.g. 10.0 mT). As this is the same sequence as before (figure 36), it appears GRASP works better with a higher inhomogeneity.

We optimised the above described sequence by increasing the flip angle to 19 degrees and tested it on phantom D (steel ball bearing embedded in gelatine).

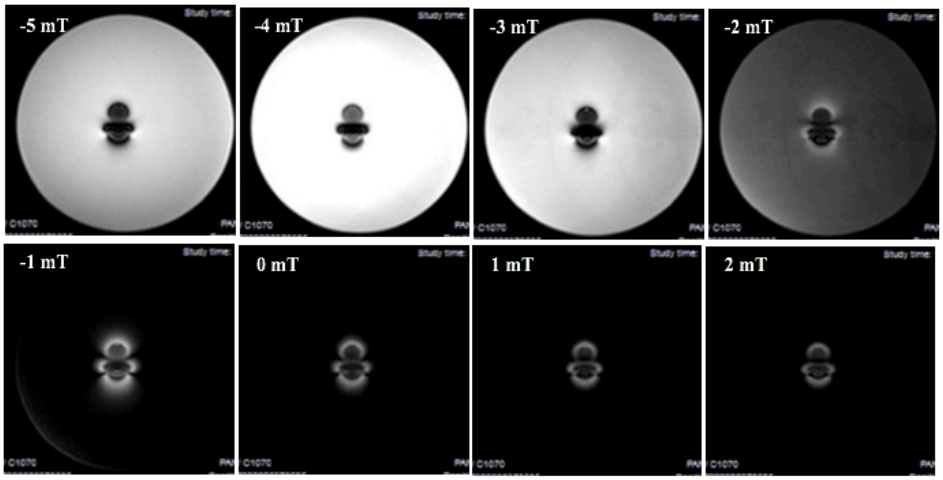

Figure 38: GRASP TFE sequence tested on phantom D. Complete background suppression is achieved at a refocusing gradient strength of -1.0 mT while displaying the dipole field of the steel ball bearing hyperintense.

In figure 38, signal darkening of the on-resonant protons (gelatine phantom) starts at -2.0 mT. Before that, the dipole field introduced by the steel bearing is visible in the gradient echo image. At a refocusing gradient strength of -1.0 mT or higher, a positive contrast image is visible, displaying the dipole field hyperintense while darkening all on-resonant protons. As the refocusing gradient increases, hyperintensity of the dipole field decreases. At -1.0 mT, hyperintensity is at a maximum. A disadvantage at that refocusing gradient strength is that the phantom edges are slightly visible in head/toe-direction.

In another optimisation step, we used the VSOP phantom B (vial of olive oil in the centre). We used the same sequence as before but increased the TFE factor from 15 to 20, selected a water-fat shift of 2, the flip angle was changed back to 5 degrees, echo time was set to shortest (3.1 ms) and the repetition time was kept at 6.8 ms. In addition, we switched on the SPIR fat suppression (default settings). Figure 39 shows the images that were obtained.

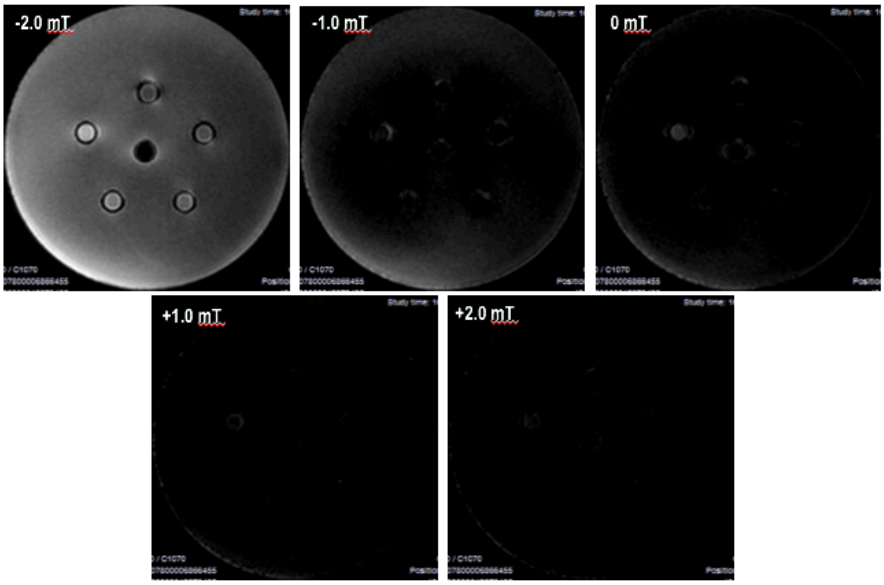

Figure 39: GRASP TFE sequence tested on phantom B. Little hyperintensity is visible from the VSOP vials while background suppression onsets at -2.0 mT.

Similar to previous results, on-resonant water darkening starts at -2.0 mT. In this sequence, the darkening is a lot more consistent. However, we obtained very little hyperintensity from the VSOP vials.

So far we have focused GRASP testing on a TFE sequence. However, the implementation should also allow to test GRASP with a spin echo sequence (figure 40). We used a 2D turbo spin echo sequence (TSE factor 20) with the following scan parameter: echo time = 11 ms, repetition time = 855 ms, water-fat shift = 1.5, SPIR fat suppression switched on.

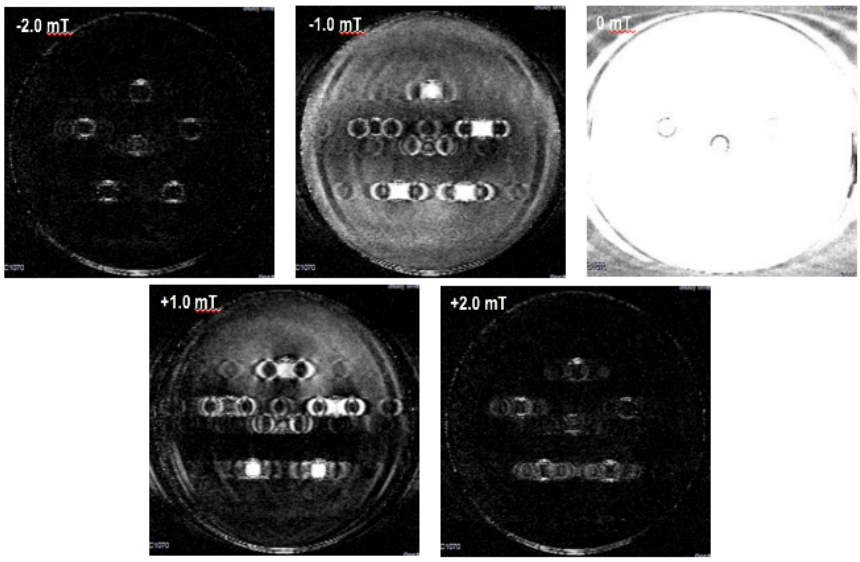

Figure 40: GRASP spin echo sequence (TSE) tested on phantom B. Images show artefacts and no consistent positive contrast image was obtained.

Artefacts for positive and negative refocusing gradients are visible. These only appear along the frequency encoding direction. The MR frequency of the water phantom and the SPIO tubes will be considerably different and impact spatial encoding. The shift in the TSE readout was likely caused because the receive bandwidth was set too low. The hyperintensity also appeared inconsistent. The visible artefacts could have been optimised, but the inconsistent positive contrast behaviour let us to focus our optimisation efforts on the TFE sequences.

In the previously tested TFE sequence we increased the repetition time to 12.8 ms and scanned phantom B again (figure 41) in which SPIR fat suppression was switched on.

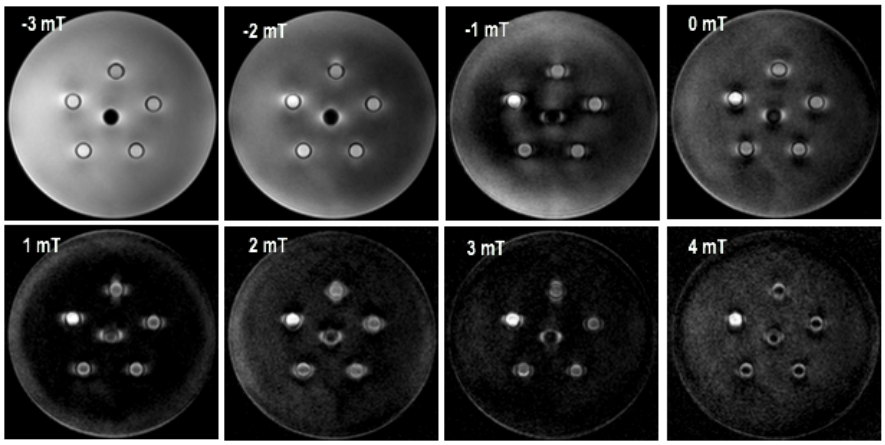

Figure 41: GRASP TFE sequence with TR = 12.8 ms and SPIR fat suppression.

As before, background suppression onsets at -2.0 mT refocusing gradient strength. The increase in repetition time to 12.8 ms led to hyperintensity in the vial with lowest VSOP concentration. Surprisingly, not the vials with the highest Fe concentration produced the strongest hyperintense signal. Fat suppression worked for the vial content but small lobes of hyperintense signal are visible on all vials which predominantly results from the PCR vials themselves. As VSOP 5 shows the strongest hyperintensity, it can be assumed that GRASP will need to be optimised for a specific iron concentration to achieve the desired contrast effects.

All attempts to produce positive contrast images so far using GRASP have not led to images that showed good background suppression while displaying the VSOP vials hyperintense with hyperintensity being concentration dependent. We therefore tested phantom B with a TFE sequence based on the work by Vonken et al. [150]. The scan parameters were as follows: flip angle = 10, echo time = 1.64 ms (shortest), repetition time = 3.1 ms (shortest), water-fat = minimum and SPIR fat suppression was applied. The images we obtained are displayed in figure 42.

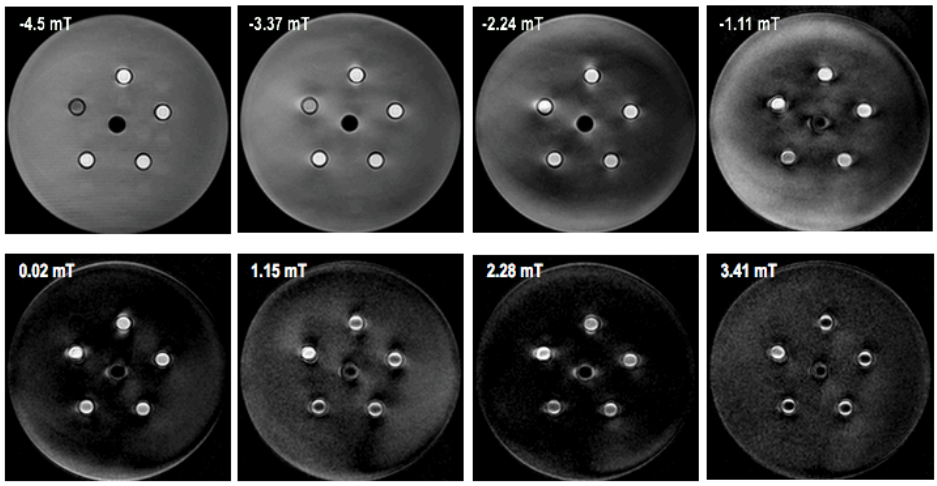

Figure 42: GRASP TFE sequence (based on [150]). Background suppression for refocusing gradient strengths greater than around 0 mT.

Background suppression is inconsistent and not as good as with the steel sphere phantom (phantom D). The hyperintense signal from the VSOP vials do not allow a concentration differentiation. Plotting the signal intensity for different refocusing gradient strengths for the different VSOP concentrations, oil vial, water vial and phantom water is shown in figure 43.

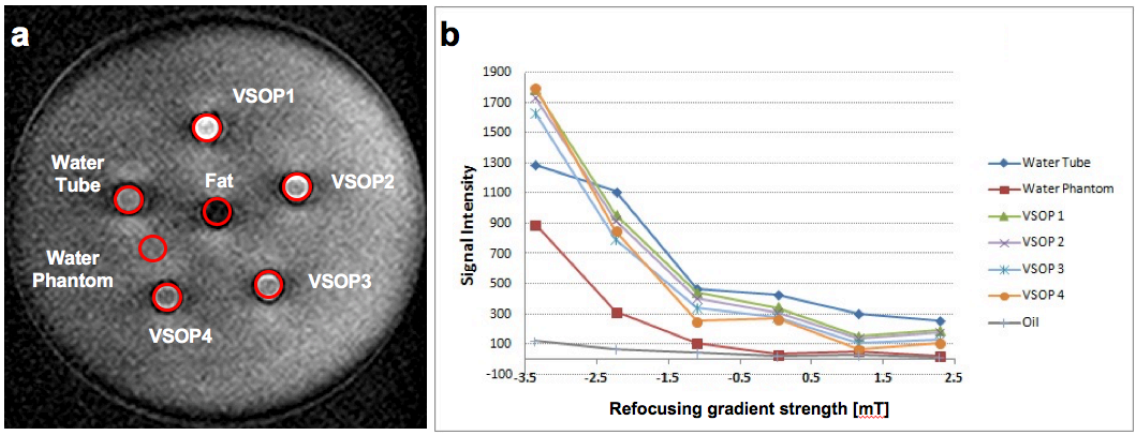

Figure 43: Analysis of GRASP images. a: Overview of ROI measurements. The phantom water was measured to estimate the effect the PCR tube has on the water vial. b: Diagram of the different signal intensities for different refocusing gradient strengths.

Higher hyperintensity is achieved than at previous experiments but the highest is recorded for the vial containing only water. This suggests that the hyperintense signal is due to the PCR tube and not the SPION particles.

According to figure 43, background suppression occurs for refocusing gradient strengths of greater than zero. However, the steps by which the refocusing gradient was changed were larger than 1 mT. We therefore repeated the above experiment and set the step to 0.1 mT. We obtained positive contrast images at a refocusing gradient strength of -4.4 and -4.5 mT (figure 44).

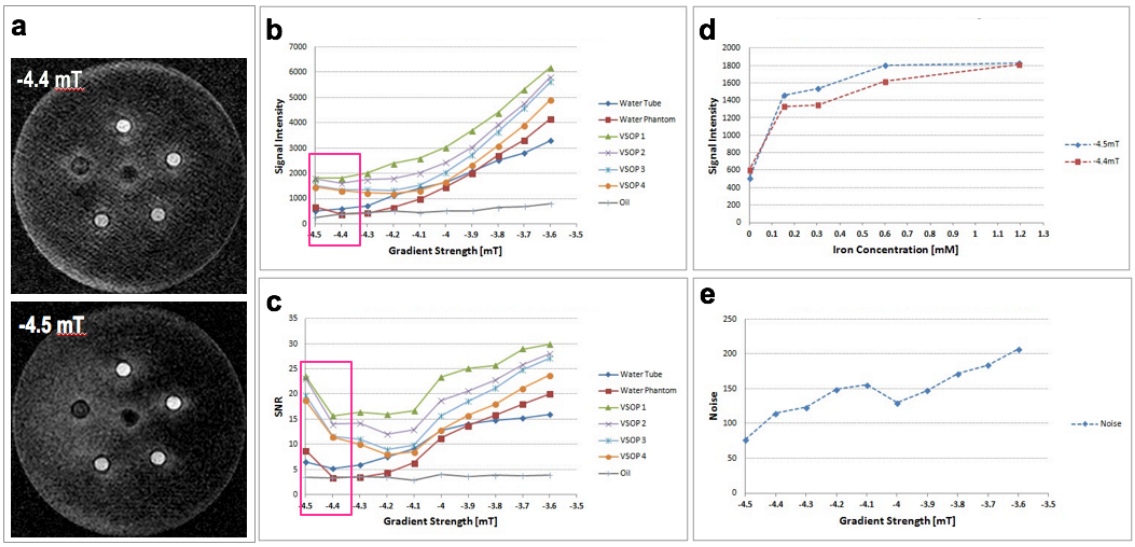

Figure 44: a: GRASP positive contrast images obtained with a TFE sequence at a refocusing gradient strength of -4.4 and -4.5 mT. b: Diagram of signal intensity over gradient strength for different phantom vials. c: Diagram of signal-to-noise ratio (SNR) over gradient strength. d: Diagram of signal intensity over Fe concentration for the images at -4.4 and -4.5 mT. e: Diagram of noise over gradient strength.

From figure 44b and c it is obvious that the greatest difference in signal intensity and SNR between the VSOP vials and the water ROIs is at -4.4 and -4.5 mT. Figure 44d shows that if ignoring the lowest VSOP concentration, the signal intensity almost linearly increases with Fe concentration.

For the next experiment, we used a gradient echo sequence with the following scan parameters: Flip angle = 25, echo time = 4.6 ms, repetition time = 100 ms, water-fat shift = minimum, SPIR fat suppression on. In that experiment, the best image is the one at a refocusing gradient strength of -0.48 mT. The background suppression is not as strong as on some other scans but the VSOP vials are hyperintense (figure 45). After this experiment, we implemented a change to the user interface which allowed the user to select the refocusing gradient strength and the step by which it is increased (dynamic scans) to be a percentage of the original gradient strength. We repeated the experiment with the above described gradient echo sequence and acquired more image around the -0.48 mT (equal to around 50% of original refocusing gradient strength). The best images were obtained at 55.5%, 54% and 52.5% of the original refocusing gradient strength (figure 46).

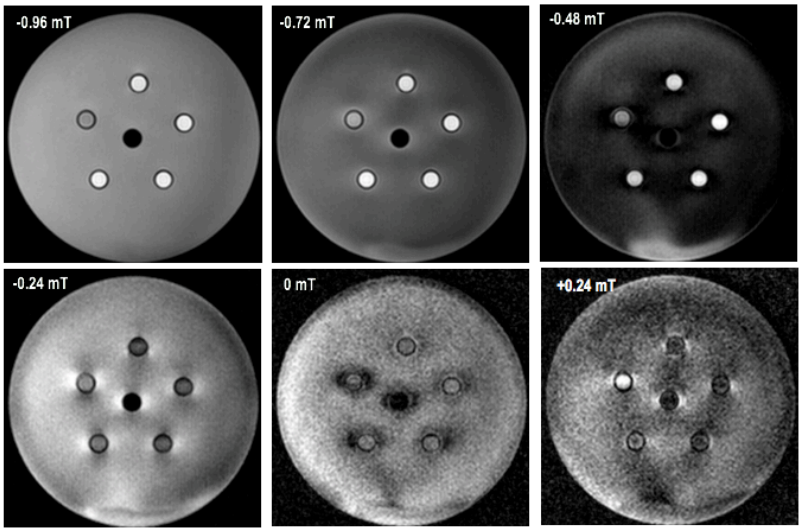

Figure 45: GRASP images obtained with a gradient echo sequence (TE = 4.6 ms, TR = 100 ms, FA = 25). The best image was obtained at a refocusing gradient strength of -0.48 mT.

In figure 46c the signal intensity is plotted over the Fe concentration.

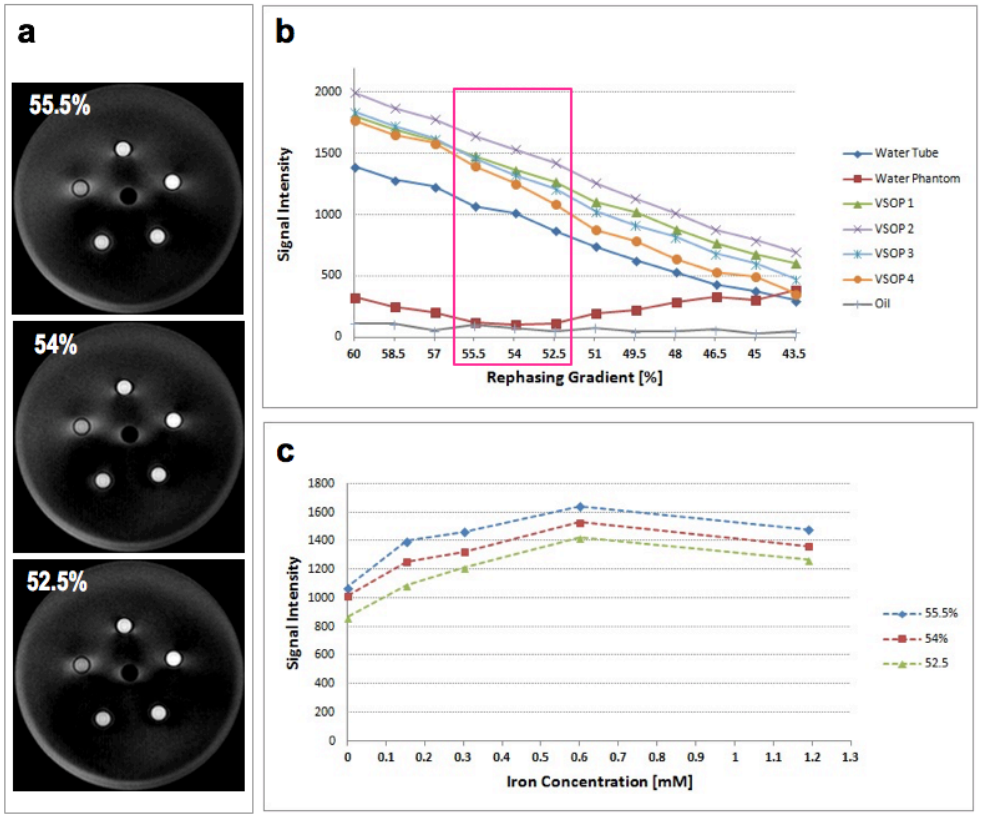

Figure 46: GRASP images and analysis of a gradient echo sequence (TE = 4.6 ms, TR = 100 ms, FA = 25). a: Best positive contrast images obtained at 55.5%, 54% and 52.5% of the original refocusing gradient strength. b: Signal intensity over rephrasing gradient strength. c: Signal intensity over Fe concentration.

The relationship appears linear for lower Fe concentrations up to 0.6 mM. After that a saturation of signal intensity is observed. Because the solutions were prepared by two-fold dilution, the biggest concentration difference is between the highest and second highest concentration (i.e. difference of 0.6 mM). For that reason we cannot determine the exact Fe concentration at which saturation occurs. Saturation of signal intensity at higher Fe concentrations could result from nanoparticles agglomerating and as a result sedimenting within the timeframe of the experiment leaving less SPIO nanoparticles in solution to be captured by the imaging slice.

After we obtained the GRASP images from figure 46, we went back to a TFE sequence. We used the sequence described above which was based on Vonken et al. [150] but made some changes to the echo and repetition times: Flip angle = 10, echo time = 3.1 ms (shortest), repetition time = 6.4 ms (shortest), water-fat = 2, TFE factor = 10, shot interval = 100 ms, profile order low-high. The best image was obtained at 50% refocusing gradient strength (figure 47).

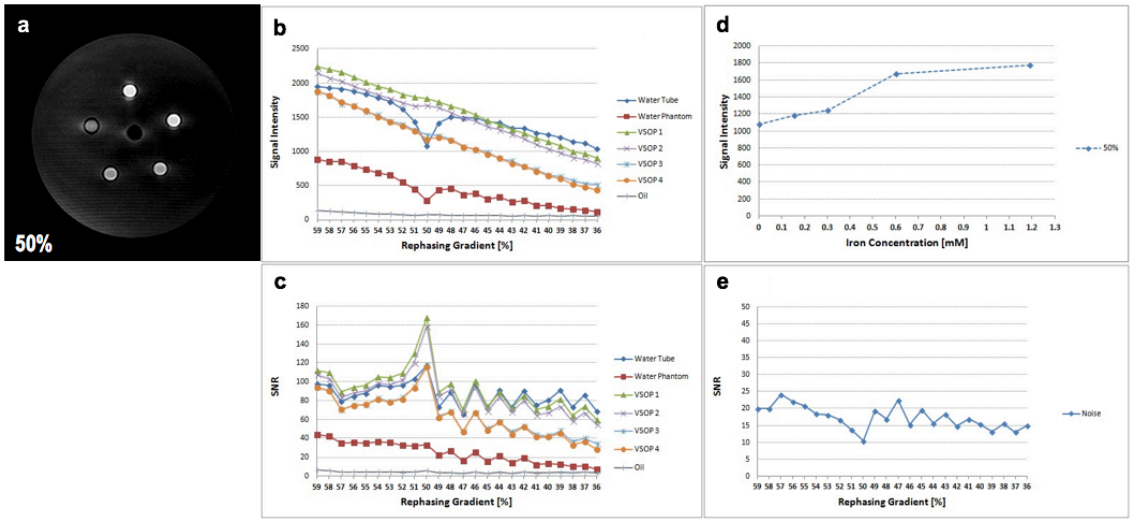

Figure 47: GRASP images obtained with a TFE sequence (TE = 3.1 ms, TR = 6.4 ms, FA = 10). a: The best image was obtained at 50% of the original rephrasing gradient strength. b: Signal intensity over rephrasing gradient strength [percentage of original gradient strength]. c: SNR over rephrasing gradient strength. d: Signal intensity over Fe concentration for the 50% image. e: Noise over rephrasing gradient strength.

From figure 47a, the background suppression and hyperintensity of VSOP vials is much improved to previous experiments. The best background suppression is achieved at a refocusing gradient strength of 50% (figure 47b). The hyperintensity of the VSOP vials appears to correlate linearly with the Fe concentration (figure 47d).

We tested another FFE sequence with the following scan parameters: Flip angle = 25, repetition time = 100 ms, echo time = 1.36 ms, water-fat shift = minimum and SPIR fat suppression on. The best images were obtained at a refocusing gradient between 50 and 60% (figure 48).

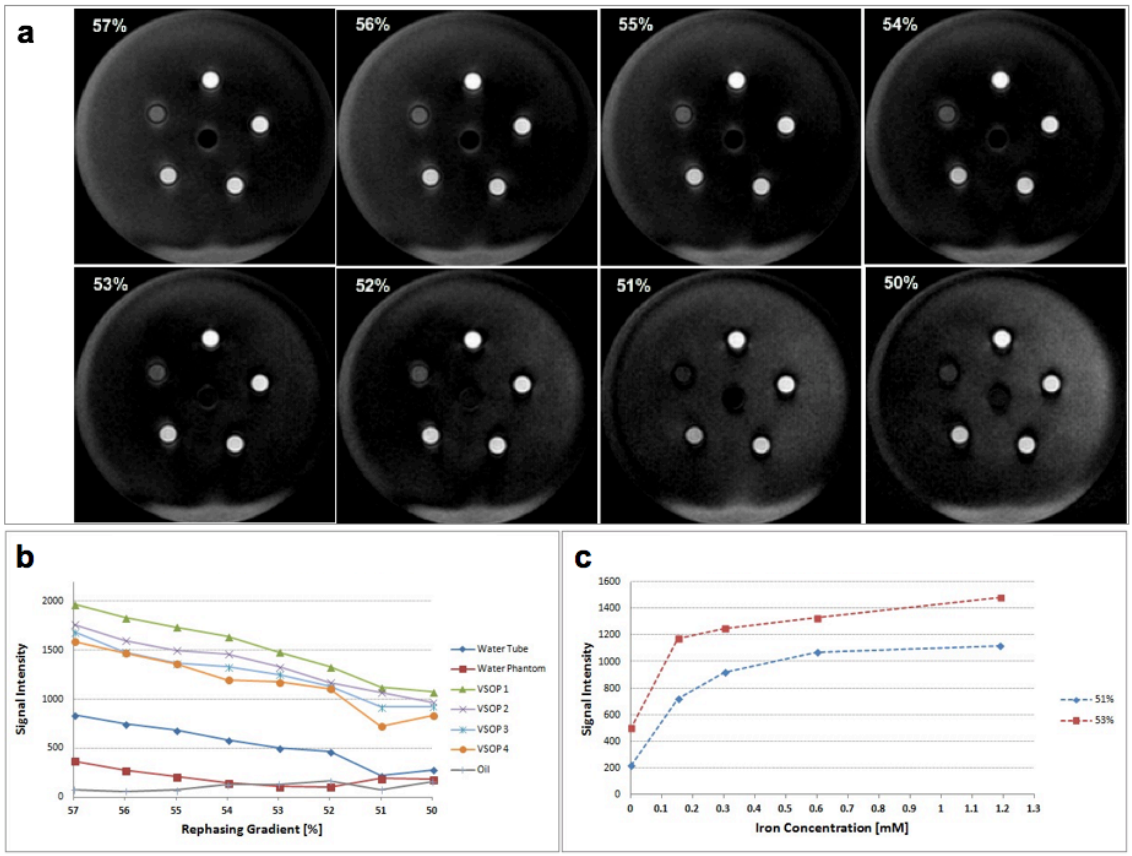

Figure 48: GRASP images obtained with a FFE sequence (TE = 1.36 ms, TR = 100 ms, FA = 25). a: The best image was obtained between 50% and 60% of the original rephrasing gradient strength. b: Signal intensity over rephrasing gradient strength [percentage of original gradient strength]. c: Signal intensity over Fe concentration (51% and 53% images).

The positive contrast images of figure 48a are promising. No signal can be seen from either the water or fat tube. All four VSOP vials are hyperintense and higher signal intensity corresponds to a higher Fe concentration (figure 48c). We also tested the exact same sequence but with half the repetition time, TR = 50 ms (figure 49). According to figure 49c, the relationship between the signal intensity of the VSOP vials and the Fe concentration is more linear, particularly considering the low Fe concentration signal, than with the same sequence but longer repetition time.

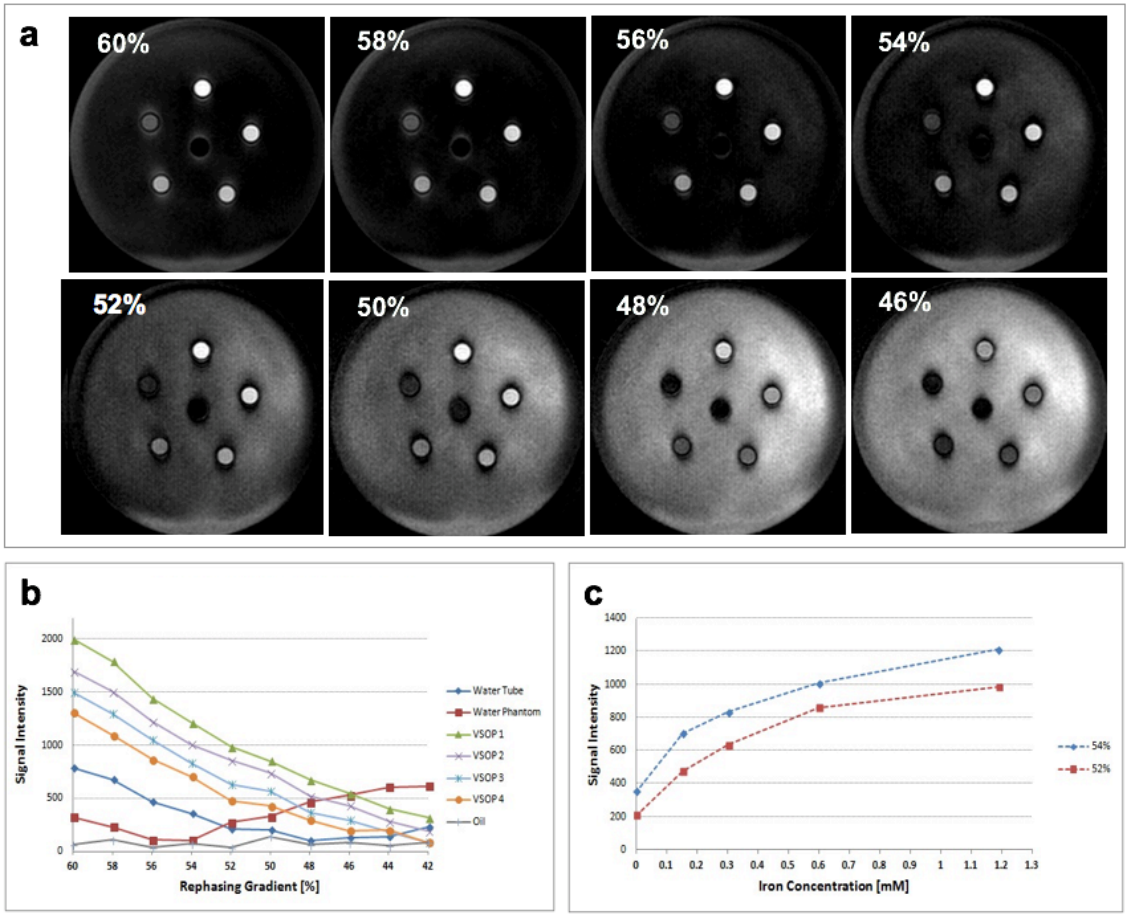

Figure 49: GRASP images obtained with a FFE sequence (TE = 1.36 ms, TR = 50 ms, FA = 25). a: The best image was obtained between 50% and 60% of the original rephrasing gradient strength. b: Signal intensity over rephrasing gradient strength [percentage of original gradient strength]. c: Signal intensity over Fe concentration (52% and 54% images).

Finally, we wanted to try a TFE sequence with a higher flip angle and a very short repetition time: Flip angle = 30, echo time = 23 ms, repetition time = 1.36 ms, water-fat shift = minimum, and SPIR fat suppression on (figure 50). This particular sequence showed a very strong linear correlation between the hyperintense signal within the VSOP vials and the Fe concentration of these vials (figure 50c) which would be important for quantitative experiments.

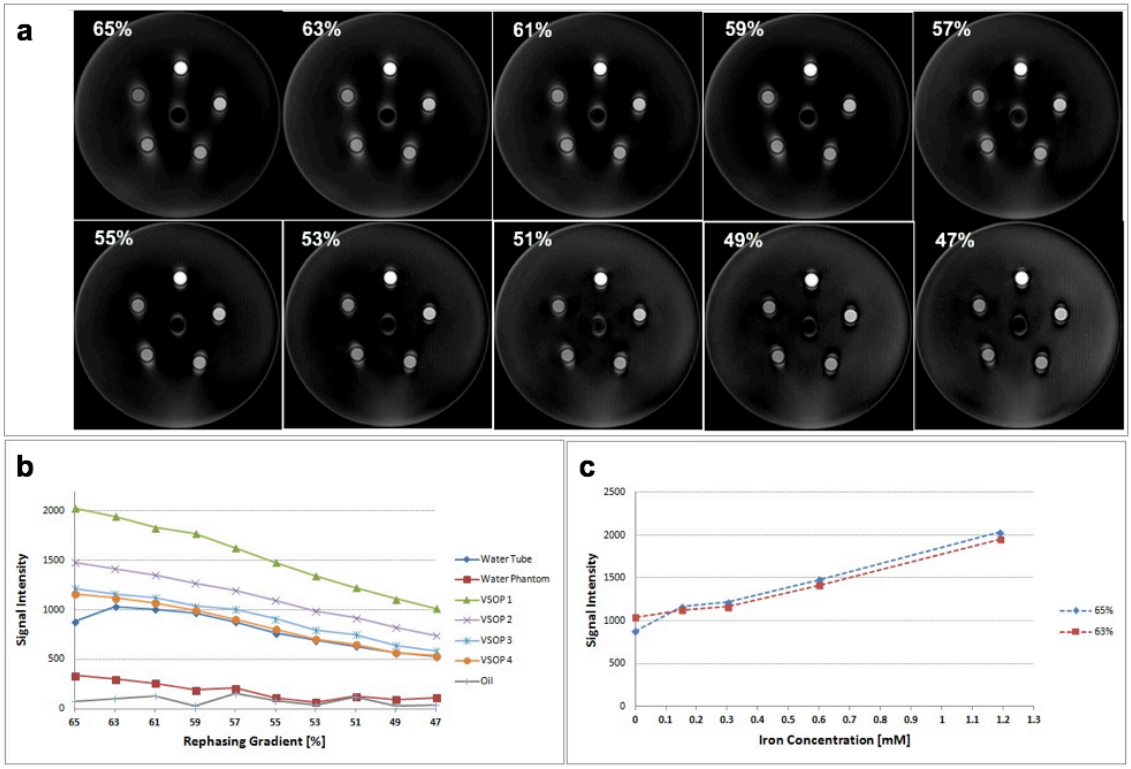

Figure 50: GRASP images obtained with a TFE sequence (TE = 23 ms, TR = 1.36 ms, FA = 30). a: The best image was obtained between 50% and 65% of the original rephrasing gradient strength. b: Signal intensity over rephrasing gradient strength [percentage of original gradient strength]. c: Signal intensity over Fe concentration (52% and 54% images).

6.4.3. IRON

The first optimisation scan was performed on phantom C. We used a turbo spin echo sequence with an echo train length of 9, echo time = 11 ms and repetition time = 855 ms. The IRON bandwidth was set to 100 Hz and the dynamic loop was started at an offset of -100 Hz and increased in steps of 10Hz (figure 51).

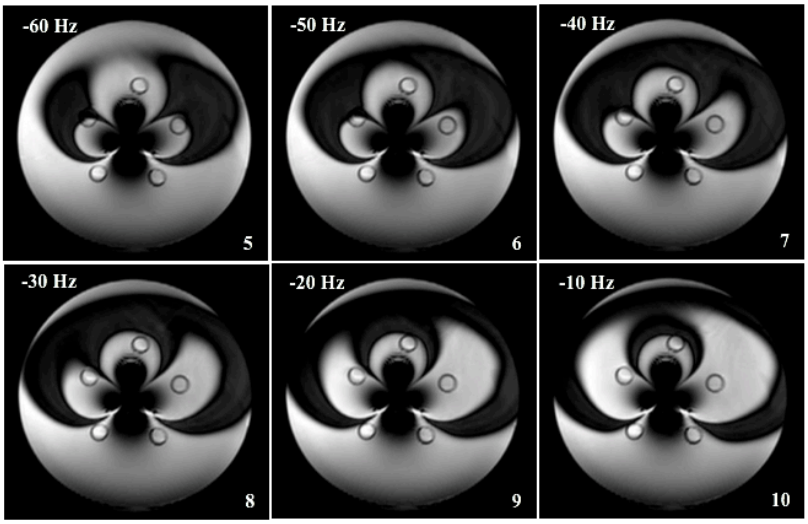

Figure 51: IRON images obtained with a TSE sequence (TE = 11 ms, TR = 855 ms). The strong inhomogeneity which originates from the centre vial does not allow for a complete background suppression.

A satisfactory background suppression could not be achieved. The strong dipole filed of the F1566 vial is visible as a dark shadow in the centre which has a strong influence on the IRON implementation as the sequence loops through different IRON offsets.

We tested a fast gradient echo sequence on the same phantom with an echo train length of 15, flip angle = 10 degrees, echo time = 3.3 ms and repetition time = 6.8 ms. In order to assess the effect of the bandwidth of the IRON pulse, we ran this experiment twice, the first time with IRON bandwidth of 120 Hz and after that with 200 Hz (figure 52 and 53).

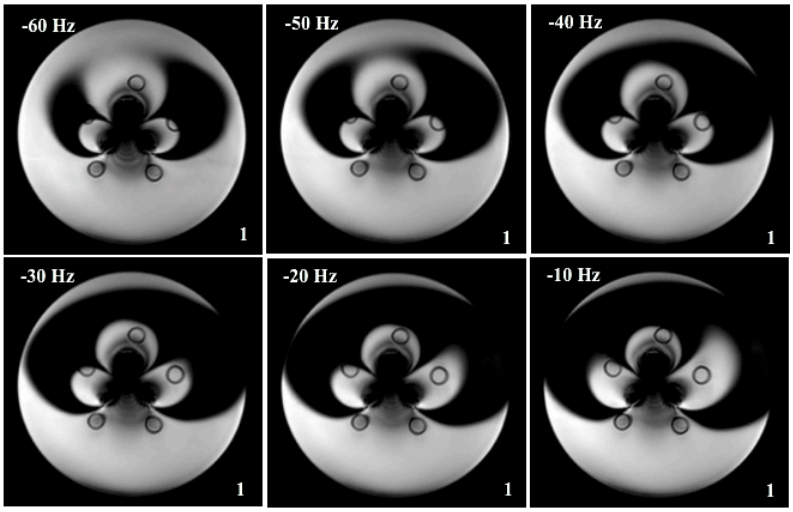

Figure 52: IRON images obtained with a TFE sequence (FA = 10, TE = 3.3 ms, TR = 6.8 ms). The bandwidth of the IRON pulse was set to 120 Hz.

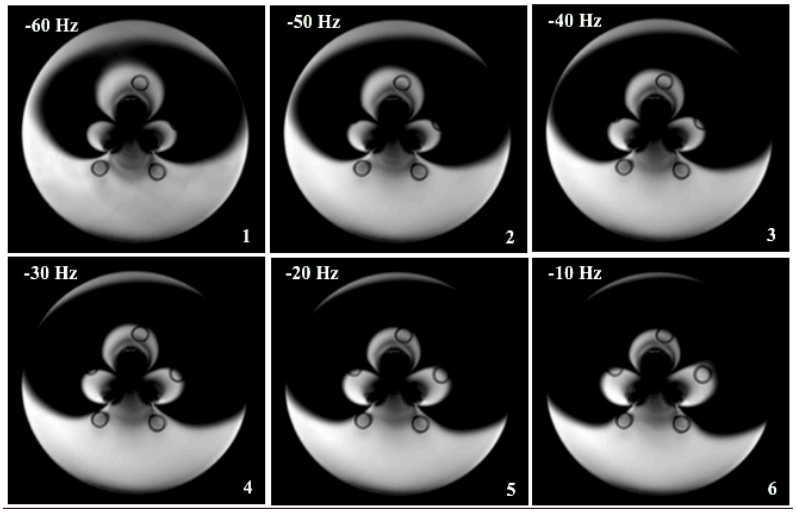

Figure 53: IRON images obtained with a TFE sequence (FA = 10, TE = 3.3 ms, TR = 6.8 ms). The bandwidth of the IRON pulse was set to 200 Hz.

The background suppression has improved compared to the TSE experiment. Comparing the two TFE experiments, a broader IRON bandwidth increases the area of the phantom that can be suppressed.

The TSE sequence described above was also tested on phantom D (steel bearing embedded in gelatine). The IRON bandwidth was increased to 200 Hz. The frequency offset was varied from -130 Hz to +20 Hz in steps of 10 Hz. Figure 54 shows a complete cycle, from the onset of background suppression, positive contrast image of the off-resonant protons and back to a negative contrast image. At an offset frequency of -50 Hz, background is fully suppressed and the dipole field of the steel bearing is shown hyperintense.

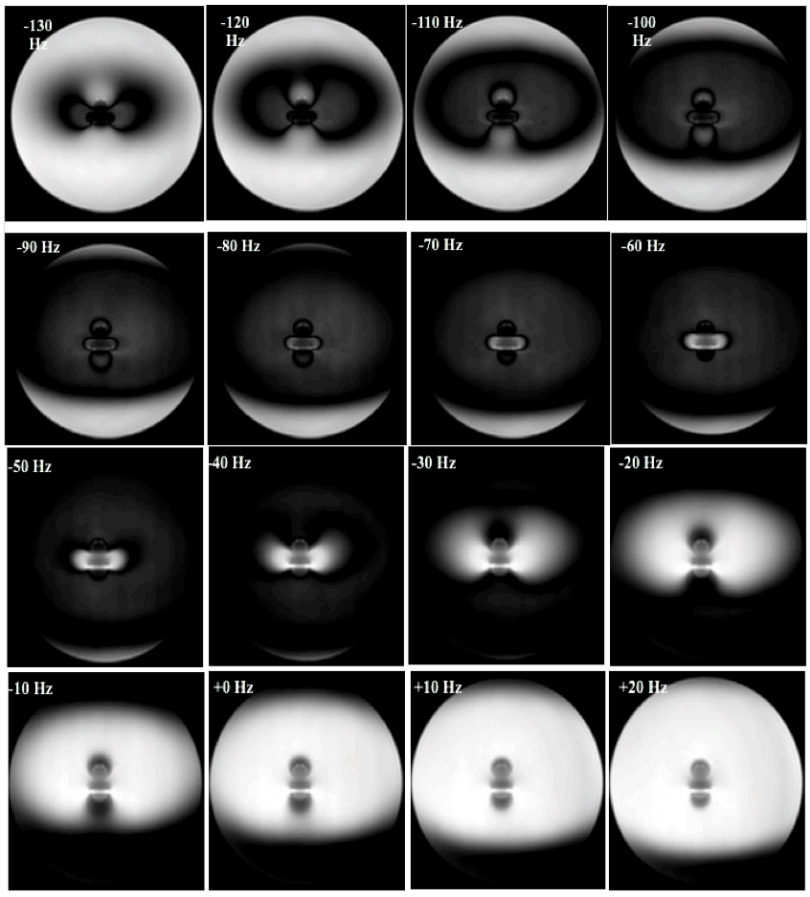

Figure 54: IRON images obtained with a TSE sequence (TE = 11 ms, TR = 855 ms). The bandwidth of the IRON pulse was set to 200 Hz. The figure shows how the on-resonant protons are being suppressed at the right frequency offset and how their signal intensity increases again as the frequency offset is further increases.

The same steel bearing phantom was used to test a TFE sequence with an echo train length of 55, flip angle = 55 degrees, echo time = 1.36 ms and repetition time = 2.69 ms (figure 55). The bandwidth of the IRON pulse was 200 Hz.

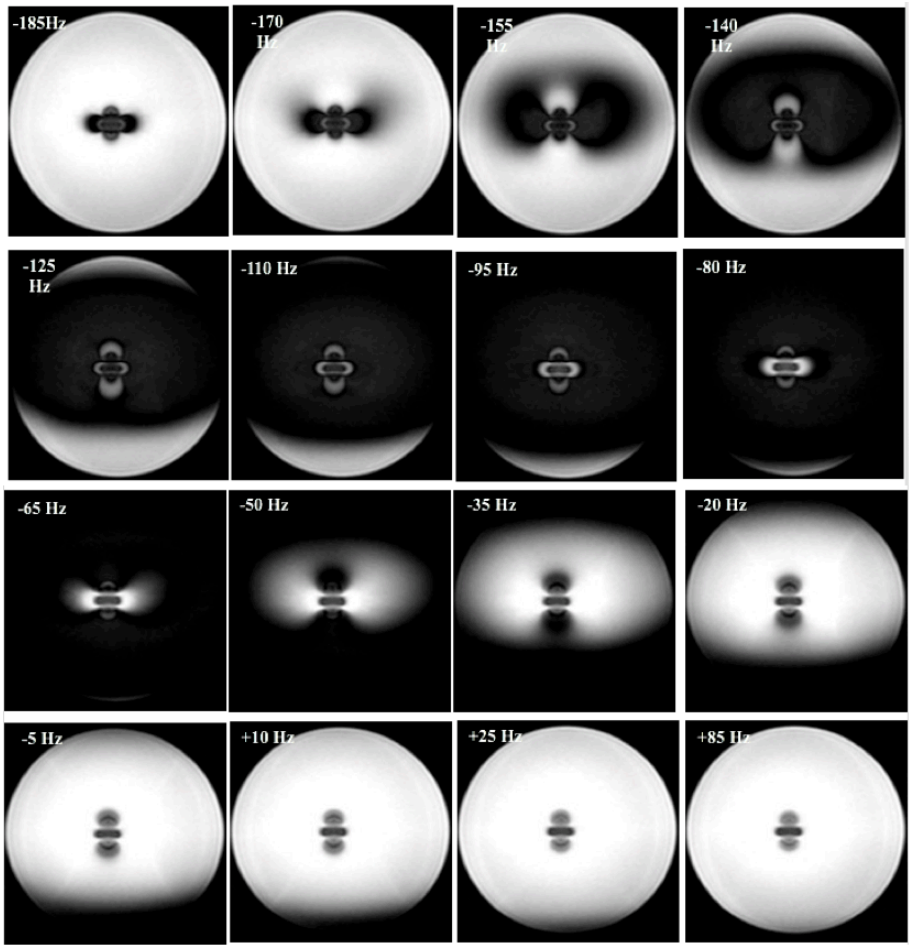

Figure 55: IRON images obtained with a TFE sequence (FA = 55, TE = 1.36 ms, TR = 2.69 ms). The bandwidth of the IRON pulse was 200 Hz. The best positive contrast image is obtained at a frequency offset of -80 Hz.

As seen in figure 54 for a TSE sequence, the whole cycle from zero background suppression via a positive contrast image at -80 Hz frequency offset and back to a negative contrast image can be seen. Compared to the spin echo sequence, the hyperintensity is brighter and the background suppression more convincing.

All further sequence optimisation experiments where conducted on a SPION water phantom with four VSOP vials of different concentrations and a water vial (phantom A and B). Using the exact same TSE sequence as before (TE = 11 ms. TR = 855 ms, IRON bandwidth = 100 Hz) the images shown in figure 56 were obtained.

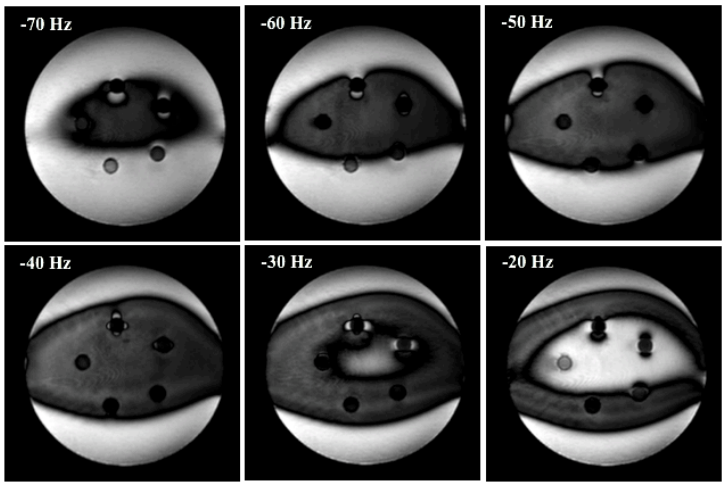

Figure 56: IRON images obtained with a TSE sequence (TE = 11 ms, TR = 855 ms) on phantom A. The bandwidth of the IRON pulse was 100 Hz.

This experiments confirms the weak background suppression as only parts of the water phantom are covered. Furthermore, the background suppression allows to still see the underlying phantom structures. The regions of hyperiontensity are small and mainly present at the vial with the highest and second highest concentration. Hyperintensity is only shown in the dipole field lobes in head/toe and left/right direction, the VSOP solutions do not show any hyperintensity.

In another experiment we attempted to overcome the above described shortcoming by decreasing the repetition time to 517 ms and the IRON bandwidth was increased to 200 Hz. In addition, the water/fat shift was set to 1.5 and SPIR fat suppression was switched on.

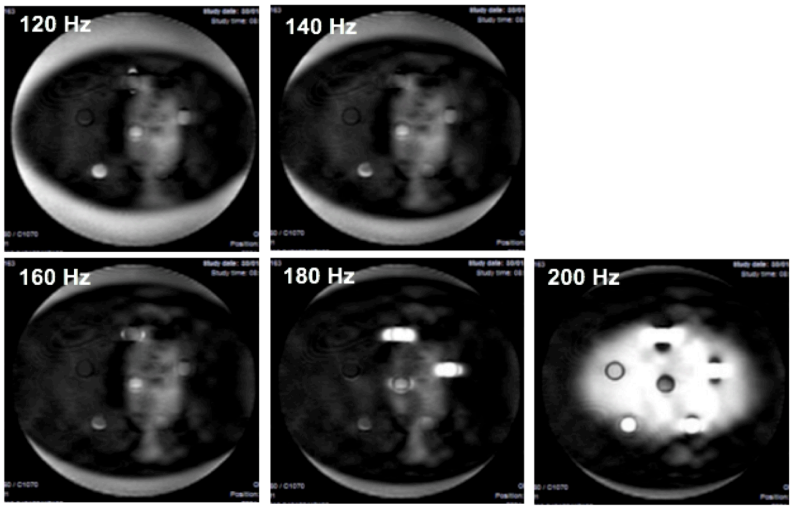

Figure 57: IRON images obtained with a TSE sequence (TE = 11 ms, TR = 517 ms) that used SPIR fat suppression and a water/fat shift of 1.5. The bandwidth of the IRON pulse was 200 Hz.

Figure 57 shows that almost the whole phantom could be suppressed at an offset of 180 Hz with the two highest VSOP vials being brightly visible. Compared to previous experiments, not only the lobes of the dipole field but the vials themselves are hyperintense. The background suppression is inconsistent in the centre of the phantom (patches).

In an optimisation step we increased the TSE factor from 9 to 16 and also increased the echo time to 53 ms. Water fat shift was set to minimum while we kept the SPIR fat suppression activated. At an IRON bandwidth of 200 Hz we obtained the images shown in figure 58.

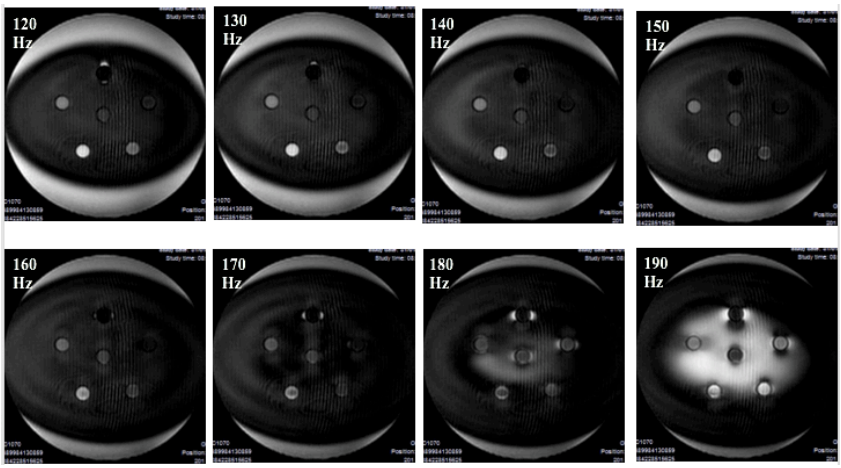

Figure 58: IRON images obtained with a TSE sequence (TE = 53 ms, TR = 517 ms) that used SPIR fat suppression and a minimal water/fat shift. The IRON bandwidth was 200 Hz.

Compared to the previous experiment, the image quality has significantly improved. While most of the phantom could be covered with ON-resonant suppression IRON pulse at 170 Hz (apart from the edges in the head-toe direction), the quality of suppression still lacked intensity and allowed to see underlying structures. Two PCR tubes stand out, the vial with the highest VSOP concentration displays hyperintense lobes in the left/right direction at a lower frequency offset. The vial with the second lowest VSOP concentration appears brighter throughout the experiment.

The above mentioned TFE sequence (echo train length = 15, flip angle = 10, echo time = 3.3 ms, repetition time = 6.8 ms) was tested phantom B (VSOP phantom). The IRON bandwidth was set to 100 Hz (figure 59).

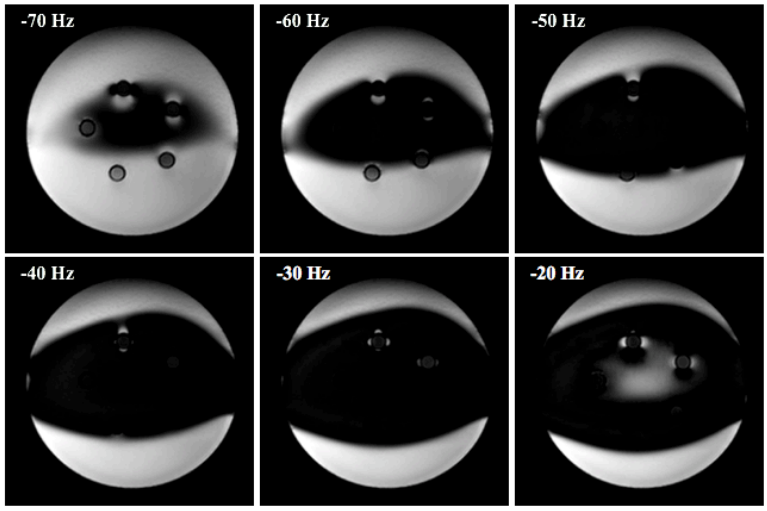

Figure 59: IRON images obtained with a TFE sequence (FA = 15, TE = 3.3 ms, TR = 6.8 ms) on phantom B. The IRON bandwidth was 100 Hz.

The selected IRON bandwidth was not enough to achieve a full background cover of the phantom. However, the background suppression was convincing and at an offset of -30 Hz the dipole lobes of the highest VSOP vial were clearly visible while the signal from the VSOP solution within the vial remained suppressed.

In order to improve the coverage of the background suppression, IRON bandwidth was increased to 200 Hz while also increasing the echo train length to 30. Figure 60 shows the result where the majority of water phantom has successfully been suppressed apart from the edges in head/toe direction. The VSOP vials with two highest Fe concentrations are displayed hyperintense. A positive result from this experiment is that the hyperintensity indicates a possible Fe concentration dependence with the vial with the higher Fe concentration being brighter compared to the vial with the second highest Fe concentration.

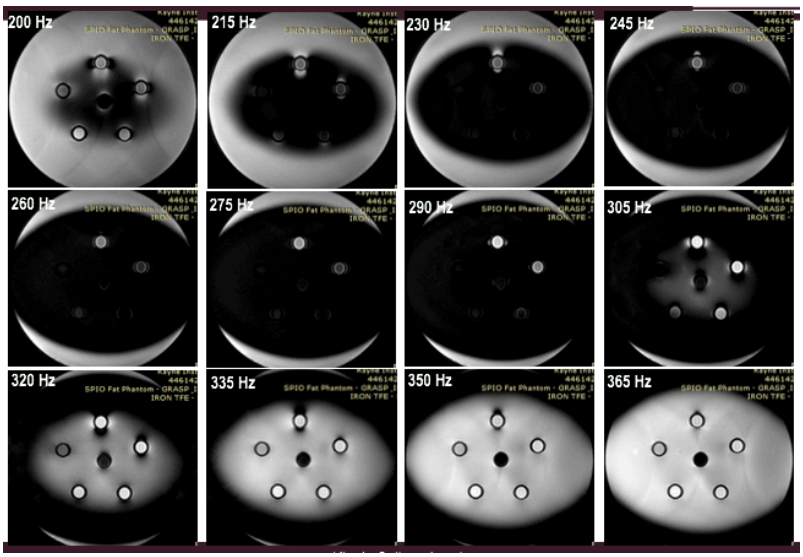

Figure 60: IRON images obtained with a TFE sequence (FA = 15, TE = 3.3 ms, TR = 6.8 ms) on phantom B. The IRON bandwidth was 200 Hz.

In order to further test the influence of the IRON bandwidth on the background suppression, we scanned the phantom with the same sequence but increased the IRON bandwidth to 300 Hz (figure 61).

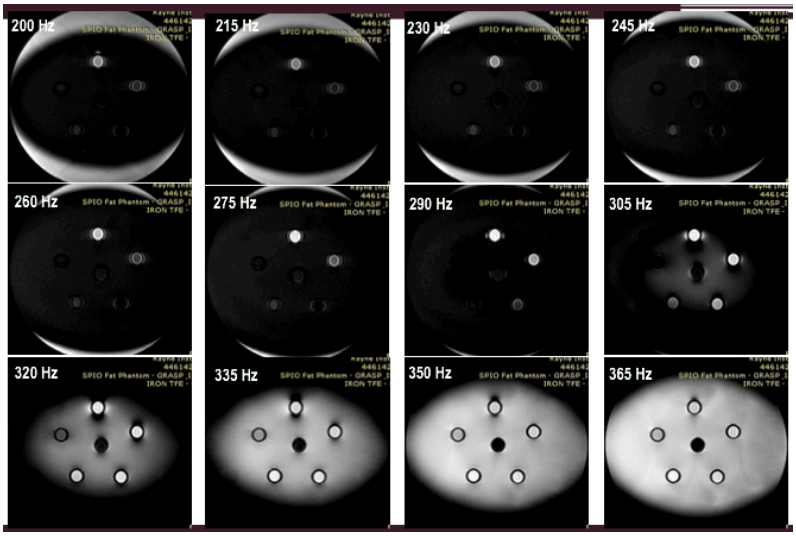

Figure 61: IRON images obtained with a TFE sequence (FA = 15, TE = 3.3 ms, TR = 6.8 ms) on phantom B. The IRON bandwidth was 300 Hz.

At a lower frequency offset, the larger IRON bandwidth pulse is able to achieve background suppression where the narrower pulse fails. The sequence with the 300 Hz bandwidth also resulted in increased hyperintensity of the SPION vials. We plotted the signal intensity over the offset for all VSOP vials, oil vial, water vial and a position within the water phantom (figure 62).

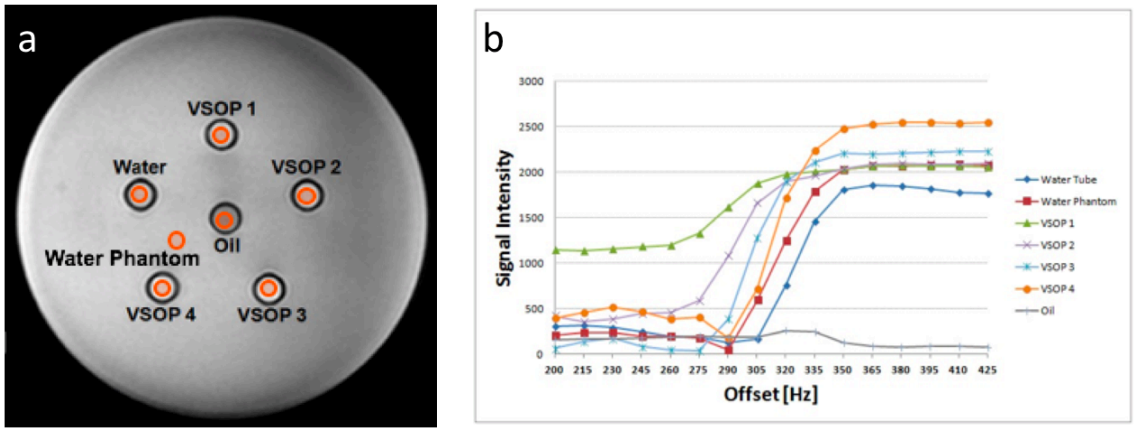

Figure 62: Analysis of IRON TFE sequence. a: Illustration of where ROIs were drawn for the measurement of the signal intensity. As a comparison to the water-filed PCR tube, a ROI was

also drawn in the phantom water. b: Signal intensities of different ROIs (vials) for a range of IRON frequency offsets (200 – 425 Hz). The ideal contrast can be achieved at 290 Hz.

Figure 62 confirms that the best contrast is achieved at 290 Hz. At that offset, VSOP1, VSOP2 and VSOP3 have a higher signal intensity than the other vials. In particular, both water measurements and the oil vial have a very low signal intensity and are therefore suppressed.

Figure 61 showed that an IRON pulse with a broader bandwidth resulted in a better result. As a next step, we evaluated the effect of the water/fat setting on the IRON TFE sequence (figure 63). Scan 201 was conducted with water/fat = 2, scan 301 had the water/fat parameter set to minimum.

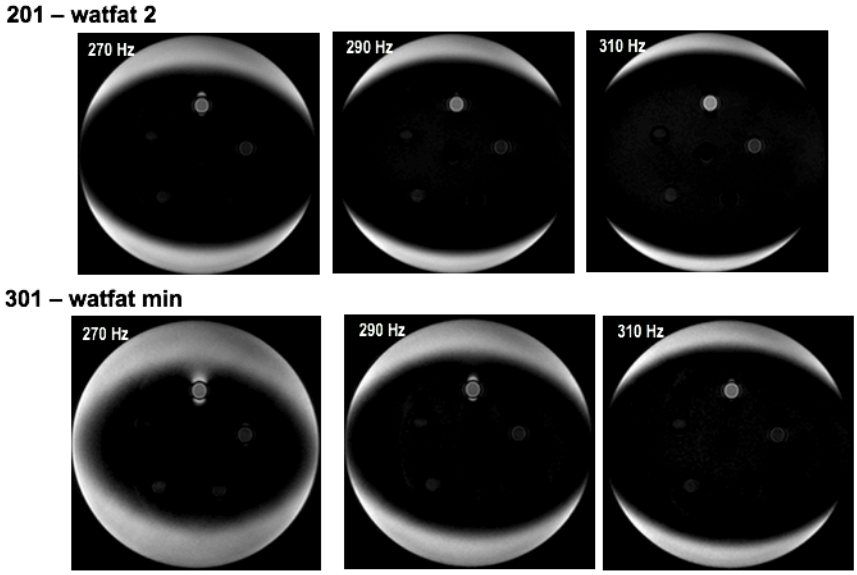

Figure 63: Evaluation of the effect of the water/fat parameter on the IRON image quality. 201: Water/fat =2. 301: Water/fat = minimum.

Scan 201 achieved a better background suppression and became our standard scan for future comparisons. We tested a few more sequences with different scan parameters and compared these to scan 201 from figure 63. A new sequence we tested was an IRON TFE with a flip angle of 15 degrees, an echo time of 1.38 ms, repetition time of 2.7 ms, water/fat set to minimum and an IRON bandwidth of 300 Hz.

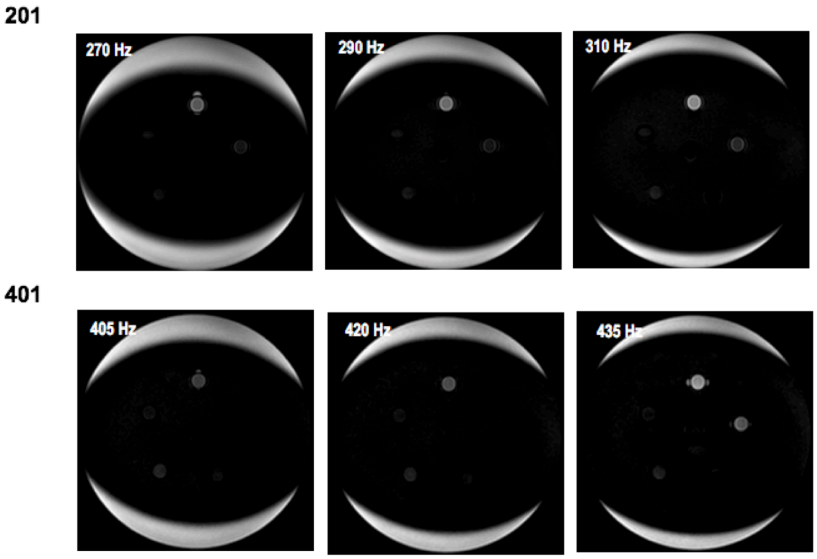

Figure 64: Comparison of two IRON TFE sequences. 201: FA = 15, TE = 3.3 ms, TR = 6.8 ms, water/fat = 2. 401: FA = 15, TE = 1.38 ms, TR = 2.7 ms, water/fat = min.

The different scan parameters resulted in the best images at a very different frequency offset, i.e. 405 Hz, 420 Hz and 435 Hz. While the background suppression was very similar for both scans, 401 also produced hyperintensity at VSOP2 vial. However, the frequency offset had to be changed to achieve good positive contrast images and a direct comparison is therefore difficult. We also tested an IRON TFE with the following parameters: flip angle of 15 degrees, echo time of 1.54 ms, repetition time of 3.9 ms and water/fat set to minimum (figure 65).

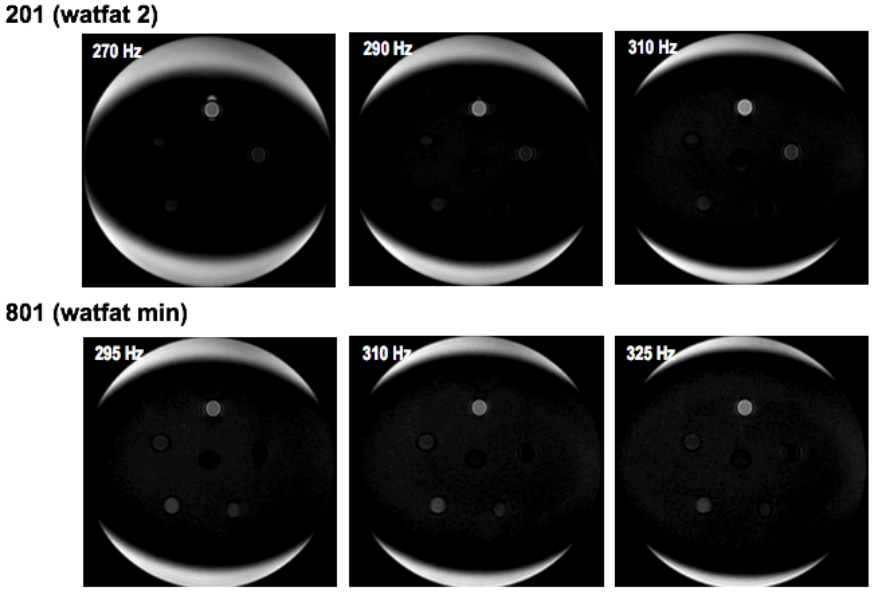

Figure 65: Comparison of two IRON TFE sequences. 201: FA = 15, TE = 3.3 ms, TR = 6.8 ms, water/fat = 2. 401: FA = 15, TE = 1.54 ms, TR = 3.9 ms, water/fat = min.

Despite the good background suppression, the hyperintensity was inconsistent with VSOP4 having a stronger signal than VSOP2 or VSOP3.

The next TFE sequence we tested was based on a sequence described by Stuber et al. [153] with an IRON bandwidth of 300 Hz (figure 66). The scan parameters were: flip angle = 18 degrees, echo time = 3.1 ms, repetition time = 24 ms, water/fat = minimal and SPIR fat suppression. This sequence delivered the best results with almost complete suppression of the water phantom to the edges and hyperintense signal from all VSOP vials. Vials with higher Fe concentration appeared to have a stronger signal. The oil vial in the centre was visible suggesting that fat suppression was not effective. The control water vial on the other hand completely disappeared and blended into the suppressed phantom water.

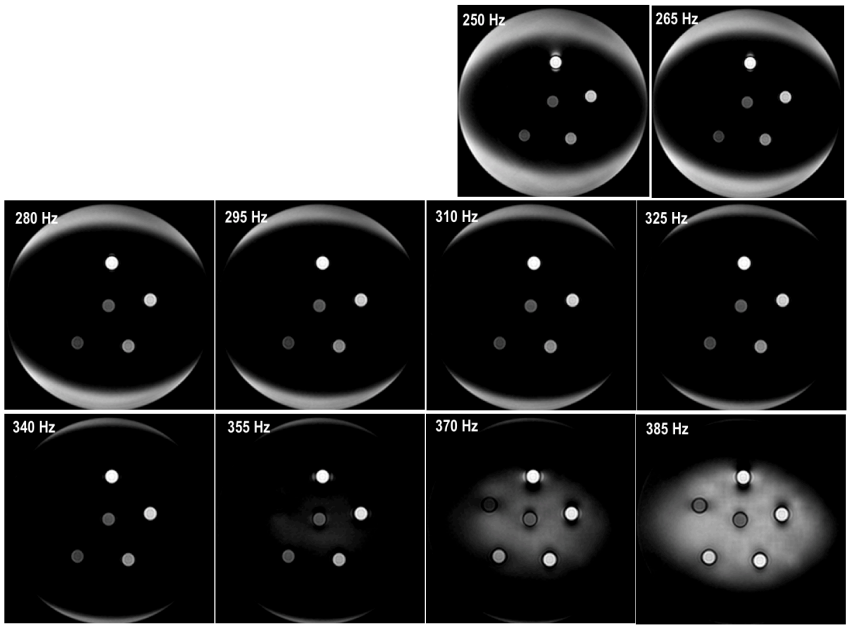

Figure 66: IRON TFE sequence with FA = 18, TE = 3.1 ms, TR = 24 ms, water/fat = min, IRON BW = 300 Hz and SPIR fat suppression.

We repeated this experiment but increased the IRON bandwidth to 679 Hz (figure 67). The increased IRON bandwidth had a significant effect on the ability to suppress the signal of the entire water phantom including the edges where the protons experience slightly different magnetic field.

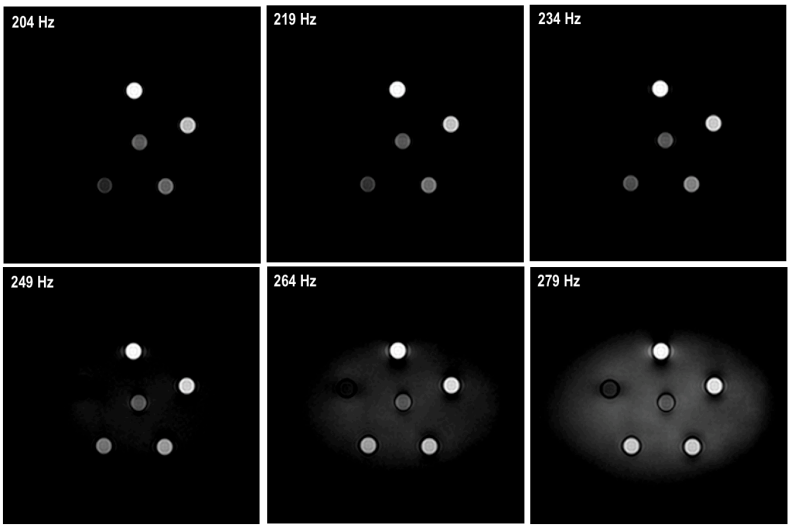

Figure 67: IRON TFE sequence with FA = 18, TE = 3.1 ms, TR = 24 ms, water/fat = min, IRON BW = 679 Hz and SPIR fat suppression.

Because the SPIR fat suppression was not effective, we tested the same sequence but used Dixon as a fat suppression method. The water images are shown in figure 68 for the same frequency offsets the above.

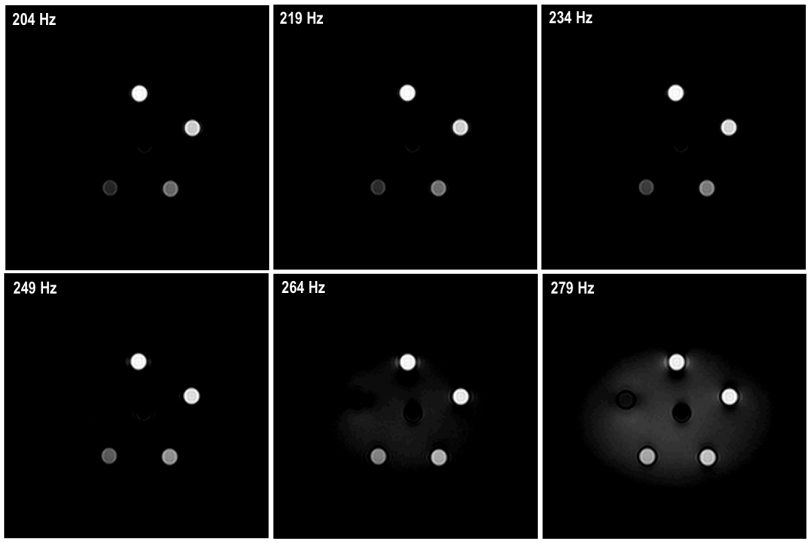

Figure 68: IRON TFE sequence with FA = 18, TE = 3.1 ms, TR = 24 ms, water/fat = min, IRON BW = 679 Hz and Dixon fat suppression (water images are displayed).

Using Dixon as a fat suppression technique was very successful. The oil vial is almost completely suppressed. The vial with the lowest Fe concentration (VSOP4) still achieved a signal intensity > 500 for frequency offsets larger than 234 Hz (figure 69) which allowed it to be very visible on the darkened background. All four VSOP concentrations are visible and display different levels of hyperintensity according to the iron content of the vials.

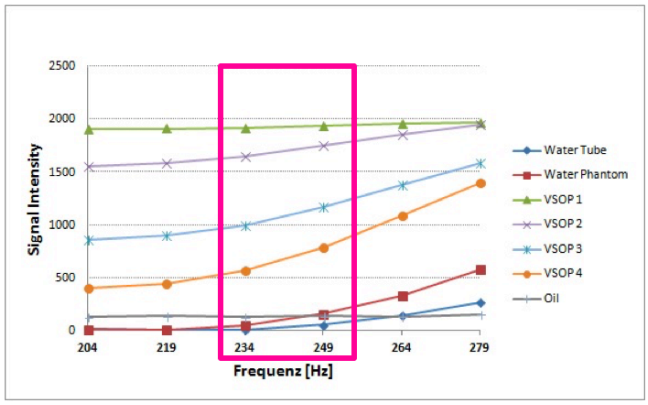

Figure 69: Analysis of signal intensities for different vials within the phantom for IRON TFE sequence with Dixon fat suppression (figure 68).

Using the much increased IRON bandwidth of 679 Hz, we went back to our initial TFE sequence (FA = 10, TE = 3.3 ms, TR = 6.8 ms, water/fat = 2) with SPIR fat suppression (figure 70). Between 249 Hz and 258 Hz frequency offset, good positive contrast images were achieved.

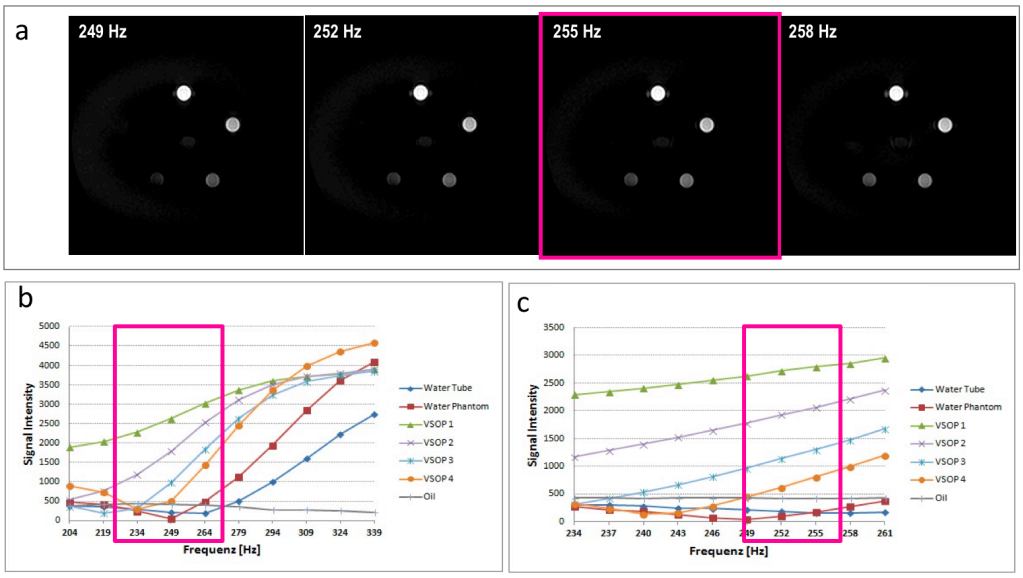

Figure 70: IRON TFE sequence (FA = 10, TE = 3.3 ms, TR = 6.8 ms, water/fat = 2, IRON BW = 679 Hz, SPIR fat suppression) and analysis. a: MR images for four frequency offsets, 249 Hz, 252 Hz, 255 Hz and 258 Hz. b: Analysis of signal intensities for different vials within the phantom over the frequency offset (ideal range highlighted). c: Zoomed in version of (b).

Another TFE sequence we tested had much shorter echo time of 1.36 ms (TR = 6.8, FA = 10, water/fat = min, SPIR fat suppression) (figure 71). As shown in figure 71c, this sequence achieved a linear relationship for the signal intensities of the different VSOP vials.

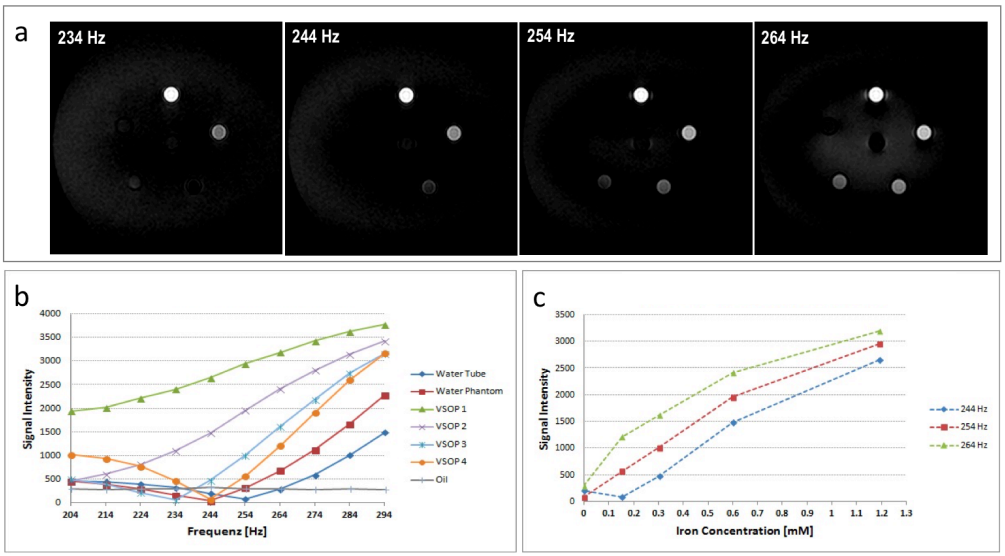

Figure 71: IRON TFE sequence (FA = 10, TE = 1.36 ms, TR = 6.8 ms, water/fat = min, IRON BW = 679 Hz, SPIR fat suppression) and analysis. a: MR images for four frequency offsets, 234 Hz, 244 Hz, 254 Hz and 264 Hz. b: Analysis of signal intensities for different vials within the phantom over the frequency offset. c: Signal intensities over Fe concentration (VSOP1, VSOP2, VSOP3, VSOP4 and water vial) for three frequency offsets (244 Hz, 254 Hz and 264 Hz).

In figures 70 and 71, SPIR fat suppression was successfully applied on an IRON sequence. We went back to the Dixon fat suppression technique but with a very short echo time of 1.36 ms (TE2 = 2.5 ms), a slightly increased excitation angle of 18 degrees. The repetition time was varied from 8 ms (figure 72), 10 ms (figure 73), 12 ms (figure 74) to 24 ms (figure 75).

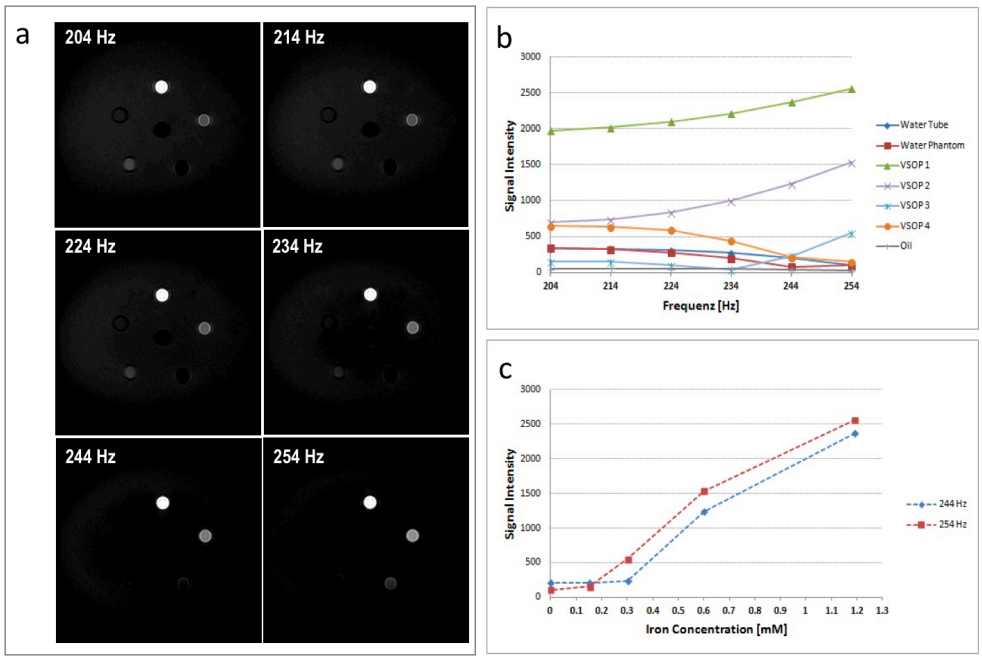

Figure 72: IRON TFE sequence (FA = 18, TE1 = 1.36 ms, TE2 = 2.5 ms, TR = 8 ms, water/fat = min, IRON BW = 679 Hz, Dixon fat suppression) and analysis. a: MR images for six

frequency offsets, 204 Hz, 214 Hz, 224 Hz, 234 Hz, 244 Hz and 254 Hz. b: Analysis of signal intensities for different vials within the phantom over the frequency offset. c: Signal intensities over Fe concentration (VSOP1, VSOP2, VSOP3, VSOP4 and water vial) for two frequency offsets (244 Hz and 254 Hz).

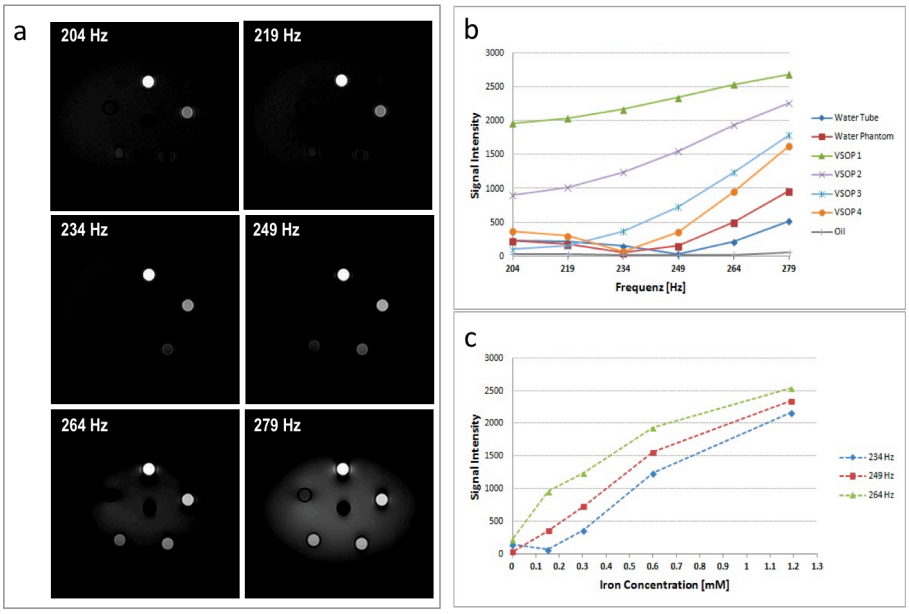

Figure 73: IRON TFE sequence (FA = 18, TE1 = 1.36 ms, TE2 = 2.5 ms, TR = 10 ms, water/fat = min, IRON BW = 679 Hz, Dixon fat suppression) and analysis. a: MR images for six frequency offsets, 204 Hz, 219 Hz, 234 Hz, 249 Hz, 264 Hz and 279 Hz. b: Analysis of signal intensities for different vials within the phantom over the frequency offset. c: Signal intensities over Fe concentration (VSOP1, VSOP2, VSOP3, VSOP4 and water vial) for three frequency offsets (234 Hz, 249 Hz and 254 Hz).

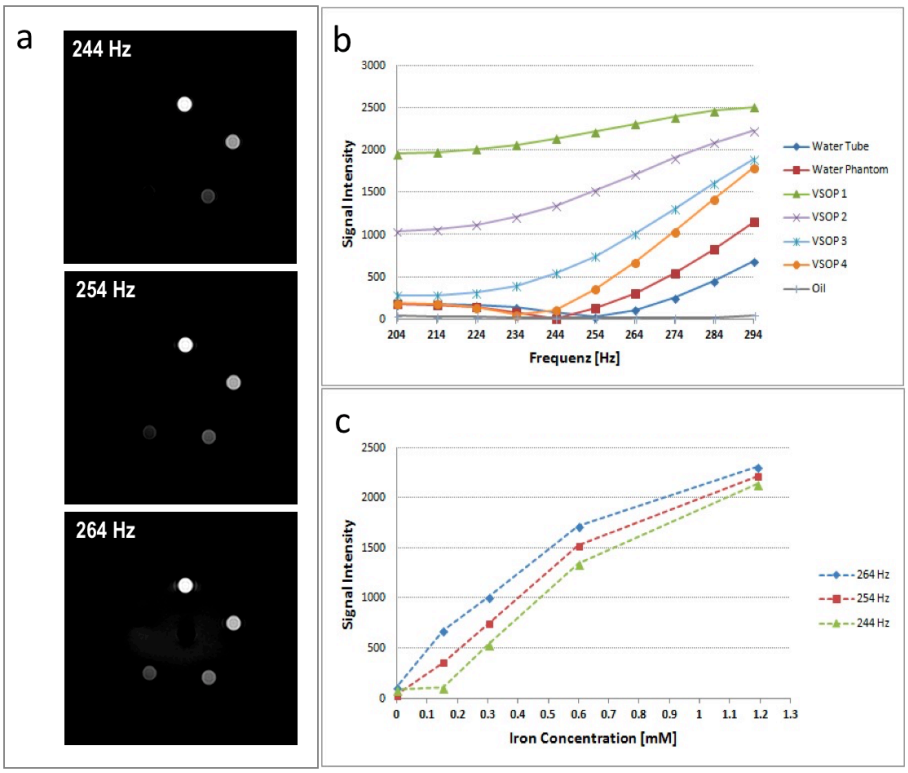

Figure 74: IRON TFE sequence (FA = 18, TE1 = 1.36 ms, TE2 = 2.5 ms, TR = 12 ms, water/fat = min, IRON BW = 679 Hz, Dixon fat suppression) and analysis. a: MR images for three frequency offsets 244 Hz, 254 Hz and 264 Hz. b: Analysis of signal intensities for different vials within the phantom over the frequency offset. c: Signal intensities over Fe concentration (VSOP1, VSOP2, VSOP3, VSOP4 and water vial) for three frequency offsets (244 Hz, 254 Hz and 264 Hz).

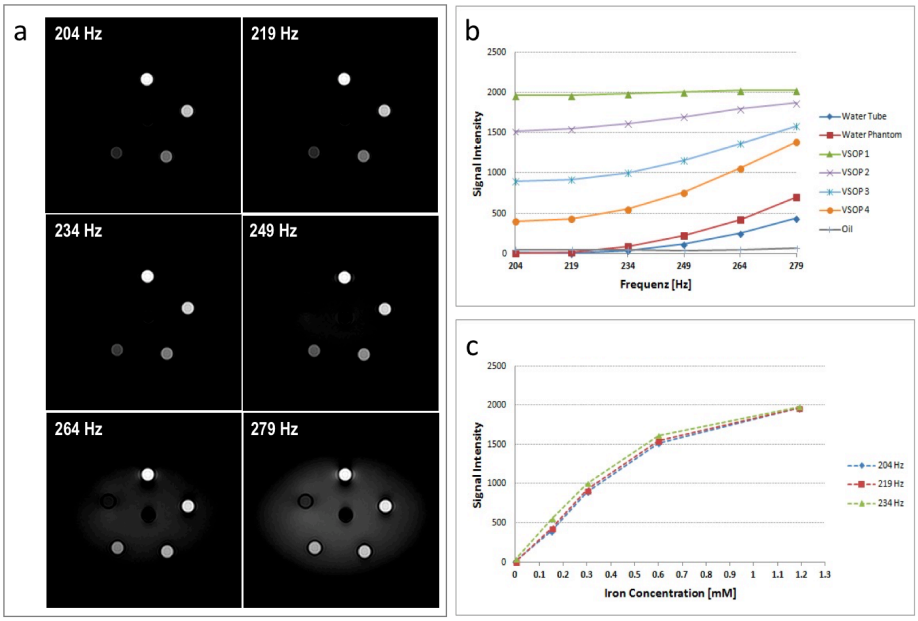

Figure 75: IRON TFE sequence (FA = 18, TE1 = 1.36 ms, TE2 = 2.5 ms, TR = 24 ms, water/fat = min, IRON BW = 679 Hz, Dixon fat suppression) and analysis. a: MR images for six

frequency offsets, 204 Hz, 219 Hz, 234 Hz, 249 Hz, 264 Hz and 279 Hz. b: Analysis of signal intensities for different vials within the phantom over the frequency offset. c: Signal intensities over Fe concentration (VSOP1, VSOP2, VSOP3, VSOP4 and water vial) for three frequency offsets (204 Hz, 219 Hz and 234 Hz).

The best differentiation between the different VSOP vials is achieved with a TR of 24 ms. The best linear correlation between signal intensity and Fe concentration was achieved with a TR of either 10 or 12 ms.

6.5. Susceptibility gradient mapping technique

We did not have to implement SGM as it had already been implemented in Matlab by a former staff member and available in the department. Important parts of the SGM implementation are the program files (m-files) readpar.m and readraw.m. The former reads the scan parameters (i.e. slice number, echo number, dynamic number, phase number, image type, echo time and slice orientation) from exported PAR files. The file readraw.m reads REC files using the information specified in the PAR file. If the parameters from the PAR file are given, the data is reshaped to a specific format, i.e. frequency encoding steps/phase encoding steps/phases/dynamics/echoes/image type. The program file noise_roi.m allows the user to draw a region of interest in the noise area of the image that will be taken into account during the SGM calculations.

The SGM calculation produces a KMAP that includes the echo shift due to the field inhomogeneity and produces the positive contrast image as output. A screenshot of the graphical user interface is shown in figure 76.

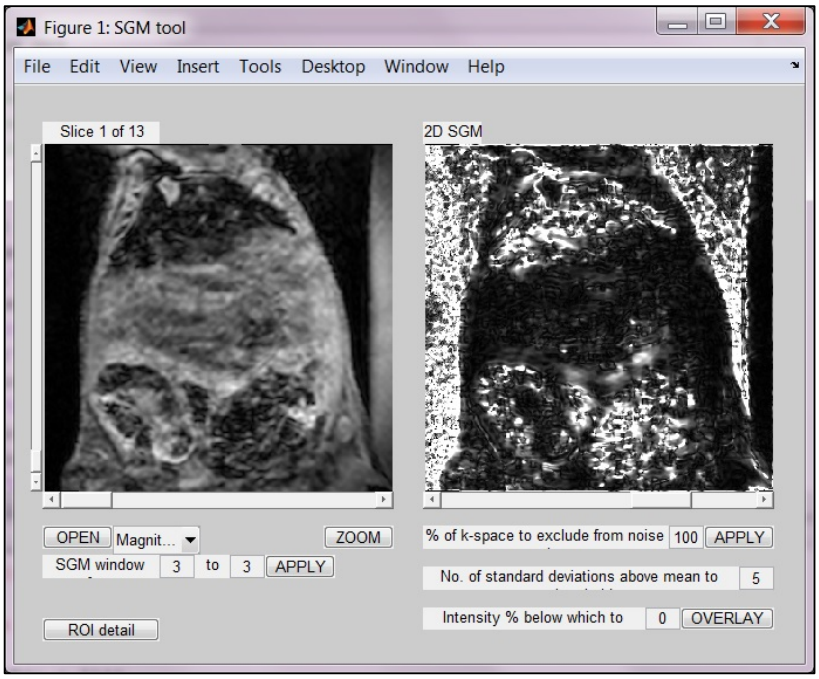

Figure 76: Graphical user interface of SGM implemented in Matlab.

The 'Open' button allows to select a PAR/REC file (either can be selected) and the respective T_2^*-weighted gradient echo image is loaded in the left window in figure 76. Two scroll bars allow to scroll through slices and echoes (i.e. images). When clicking on 'Tools' in the menue bar, it is possible to select a region of interest to be considered as noise. Finally, the SGM window could be defined. This determines the number of neighbouring pixels that are taken into account when the SGM window is scanning the image. The calculation can be started with 'Apply' and the positive contrast image is shown in the right window. The scroll bar allows to look at the positive contrast image when only considering the echo shift in one direction (1D, either x-, y- or z-direction), in two directions (2D, x- and y-direction) and all three directions (3D).

6.6. Discussion

6.6.1. Water phantoms

For the optimisation of our positive contrast sequences, we have used four different phantoms. All phantoms are water phantoms to minimise susceptibility effects from the air to liquid (SPION solution) interface. However, it is impossible to eliminate all inhomogeneities that could affect the measurements. In terms of background suppression, i.e. suppressing the signal from the on-resonant protons (not affected by SPION/steel ball bearing) in our water phantom, it is hardest to achieve a full background suppression around the edges of the phantom. The reason for that is the slightly different Larmor frequency of protons in that region as the

magnetic field is less homogenous as a result of the water/air interface. This was particular apparent in the head/toe direction for the GRASP sequence as that is the direction of the slight select gradient we modified and used for the positive image generation.

We just discussed the inhomogeneity introduced at the edge of the phantom due to the phase interface. Similar inhomogeneities need to be taken into account for phantoms A, B and C that all contained PCR tubes filled with either a SPION solution or olive oil. Inhomogeneities are present at the interface between the water phase of the phantom body and the PCR tube and then again at the interface of the PCR tube with the SPION solution. Because the 1.5 ml PCR tubes we used are thin-walled (approximately 1 mm), inhomogeneities from the two interfaces cannot be differentiated at the resolution we scanned. Phantoms A, B and C had 5 identical PCR tube positions. When these are filled with PCR tubes of different SPION concentrations (including no SPION, i.e. water), it allowed us to estimate the effect of the PCR tube on any visible hyperintensity. In order to minimise PCR tube effects, other researchers have used very thin films shaped as tubes [331] or moulded tube-shaped cavities in a block of hardened gelatine in which they then filled the SPION solution [152]. However, these researchers still reported susceptibility effects as there was still an interface transition. Other researchers have used glass tubes for SPION measurements [332]. It is currently unclear if glass or a polymer material as used for PCR tubes is preferred in reducing susceptibility effects and this might be an interesting question to explore in the future. Furthermore, quantifying the susceptibility effect exerted depending of the wall thickness has not yet been explored and reported in the literature.

The reason we have tested and optimised our sequences on four different phantoms is the following. The difference between phantoms A and B is merely the addition of a PCR tube filled with olive oil which allowed us to test fat suppression techniques in combination with our positive contrast implementations. For this optimisation, we have used vials containing VSOP solutions of different concentrations with the largest being 1.2 mM. We used phantom C which contained five PCR tubes filled with water and one centre vial filled with a SPION solution of very high concentration (135.37 mM) as a control. For once, the water-filled PCR tubes allowed us to estimate the effect the PCR tubes had on a particular sequence and whether there were any differences in the magnetic field strength in the different vial positions within our water phantom. Secondly, the vial with the high concentration SPION solution meant we could test if negative results were due to the implementation or a lack of sensitivity, i.e. not registering lower SPION concentrations.

6.6.2. GRASP

Our implementation of GRASP was straightforward. We initialised three parameters, one to switch GRASP on or off, the strength of the GRASP gradient (i.e. slice-select refocusing gradient) and the gradient step by which the user can make changes to that gradient. As the GRASP technique relies on changing the slice-select refocusing gradient until the off-resonant water protons are refocused, the key is to provide functionality in the code so that the user can exactly do that. The run-time strength of any gradient can be calculated with the equation:

$$GR_1[str] = GR_0[str] + GR[factor] * GR[step]$$

Any run-time gradient can be achieved by adding a gradient step to the current gradient strength. Introducing a gradient factor in this allows for automation by scanning through a range of gradient strengths. If the gradient factor is zero, the gradient does not change, is the factor equal to one, then the gradient increases by the amount defined by the gradient step, for a factor of two the gradient increases by an amount two times the step and so on. In our first implementation, the user could determine the gradient strength on the GUI. However, depending on the sequence, the original slice-select refocusing gradient strength will change. It would therefore be difficult for a user without detailed knowledge of the sequence to be run to select a sensible value for the gradient strength.

In our second implementation, instead of providing gradient strength and step in mT, this was now provided as a percentage of the original gradient. The gradient factor was equal to the number of the dynamic scan variable that starts at zero and increases by one up to a defined end point, e.g. 10 dynamics means the variable increases from zero to nine in steps of one. With this implementation, if the original gradient was 5 mT and the step was selected to be 10%, this would mean for each dynamic scan the gradient would be increased by 0.5 mT.

For the implementation to work, it is crucial to correctly identify the relevant slice-select refocusing gradient variable within the gradient echo and spin-echo code. Providing the gradient strength, step and factor is sufficient for the code then determine the new gradient strength for each dynamic scan.

Our implementation is simple and does not interfere with any other scan functionality or parameter. It allows the user complete control over the GRASP scan in an intuitive measure (percentage) that does not require previous knowledge of the exact gradient strength.

During the optimisation of our GRASP implementation, we initially focused on fast imaging sequences (i.e. turbo field echo and turbo spin echo) with an emphasis on turbo field echo sequences. The sequence had a low excitation angle, an echo time of 3.1 ms and a repetition time of 6.8 ms. We experimented with increasing the flip angle to 19 degrees or the repetition time to 12.8 ms. This sequence failed to produce a good quality positive contrast image of the

phantoms containing VSOP vials. However, when applied to phantom C with the high Fe concentration vial, the introduced dipole field by the SPION solution was depicted hyperintense on a signal suppressed background (figure 37). The dipole field was not symmetric and showed a more protruding lobe in the head-direction. This is likely because of SPION accumulation within the vial as that particular SPION did show a strong tendency to accumulate. The SPION solution did not show any hyperintensity at different refocusing gradient strengths. It could be that the optimal gradient strength was in between the steps we tested or that we did not cover a large enough range of different gradient strengths. However, from -0.5 mT up to 10 mT refocusing gradient strength, the background was suppressed and hyperintensity visible we stopped our measurement at 10 mT). The on-resonant water protons did not recover their signal as the refocusing gradient increased further. Moreover, the off-resonant protons remained hyperintense long after the optimal refocusing gradient. According to the theory, it would be expected that once the gradient is increased beyond the optimal strength for the off-resonant protons, those lose their hyperintensity and eventually the on-resonant protons will increase their signal intensity [151]. This sequence was also able to produce positive contrast images on phantom D (steel bearing embedded in gelatine) (figure 38). A complete background suppression was achieved starting at -2 mT as in the above discussed experiment on phantom C and the dipole field of the steel bearing is visible on the gradient echo as well as GRASP images. The optimal refocusing gradient strength within the values we tested appeared to be -1 mT. In accordance with the above discussed results, the hyperintensity remained as the gradient strength was further increased. These two experiments demonstrate that the sequence was able to produce positive contrast images but not sensitive enough to highlight the different VSOP concentrations (figure 39).

The second set of TFE sequences was based on a sequence described by Vonken at al. [150], excitation pulse of 10 degrees, echo time of 1.64 ms and a repetition time of 3.1 ms (figure 42). A variation of this sequence had an increase echo and repetition time (figure 45). At a refocusing gradient strength of 50% of the original strength, we achieved positive contrast image that showed a VSOP concentration dependence and a satisfactory background suppression. Contrary to the images obtained with our first TFE sequence, here the SPION solution appeared hyperintense and no dipole field was visible on the positive contrast images that protruded outside of the PCR tube walls. The PCR tubes did not produce visible inhomogeneity. However, in figure 47 the content of the water-filled PCR tube has a much higher signal intensity than the phantom water. This suggests that the magnetic field inside the PCR tube is slightly different compared to the rest of the water phantom. The other PCR tubes containing VSOP solutions displayed an increased signal intensity as a result of the VSOPs that

was dependent of the VSOP concentration. The overall concentration dependence showed a linear relationship.

The final TFE sequence we tested had a much increased flip angle of 30 degrees, an echo time of 23 ms and a repetition time 1.36 ms (figure 50). This experiment further clarified the detection limit. Positive contrast images were obtained for a range of different refocusing gradient strengths and throughout the two lower VSOP concentrations could not be differentiated from the water vial by visual inspection of the images. This suggests that for a given sequence implementation and iron oxide nanoparticle, an experiment should be designed determining the detection limit before proceeding to any further measurements or *in vivo* work.

In contrast to the previously discussed TFE experiments, we also tested a field echo sequence with a flip angle of 25 degrees, a short echo time of 1.36 ms and a repetition time of 100 ms/50 ms. This sequence showed a much improved hyperintensity of the VSOP vials compared to water-filled tube. As shown in figure 49, the concentration dependence shows a linear correlation. VSOP particles also display a T_1 effect [243]. A gradient echo sequence with a flip angle of 25 degrees and a very short echo time (1.36 ms) has a strong T_1 weighting which contributed to the hyperintensity of the VSOP vials. SPIONs with a small r_1 value and therefore low T_1 effect are unlikely to show the same effect when scanned with this sequence.

6.6.3. IRON

We implemented IRON by using the already available SPIR code in the pulse programming environment. There were three SPIR implementations, spir1, spir2 and spir3. The former is used for the SPIR fat suppression functionality. Spir2 is used for the respiratory navigator. We used spir3 to be able to use spir1 for fat suppression together with our IRON pulse. The majority of the implementation was therefore done in the global source file mpuspir_g.c. Our implementation satisfies two important criteria: First, we utilise existing code framework which minimises the margin for error and usually results in a mode solid scan performance. Second, we were able to implement IRON while allowing for fat suppression functionality through SPIR or Dixon.

From our optimisation experiments it is clear that our IRON implementation can be used in combination with gradient and spin echo sequences. However, there is a strong difference in the quality of the background suppression when using a TFE sequence compared to a TSE sequence. While the amount of background suppression for a given IRON bandwidth was comparable between both types of sequences, background suppression with a TSE sequence

was a lot less dense and allowed for the underlying structures to be seen. We are unsure about the origin of this difference. Positive contrast experiments using IRON reported in the literature use predominantly gradient echo sequences and our results agree with that.

From testing various sequences with different parameters, the IRON bandwidth needs to be larger than 600 Hz (we used 679 Hz) in order to achieve a complete background suppression of our phantom (diameter 14 cm). As expected, the bigger the IRON bandwidth the larger the area which can be covered with the IRON pulse. The protons in a phantom will not all "see" the same magnetic field. Those protons closest to the phantom edges or around structures such as vials will experience a slightly different magnetic field. Moreover, the magnetic field in a MRI scanner is never perfectly homogenous and even within a small phantom such as ours, slight spatial differences exist. It is therefore important to select an IRON bandwidth that is wide enough account for those magnetic field imperfections and therefore is able to effectively suppress signal from on-resonant protons. However, the IRON bandwidth must not be too wide or it will otherwise also suppress the protons affected by the SPIONs. Depending on the SPION and the magnetic inhomogeneity they introduce, the IRON bandwidth will need to be optimised.

In figure 24, only the lobes of the dipole field of the VSOP1 vial are shown hyperintense. In figure 25, the same sequence was used but here the VSOP solution within the vial is shown hyperintense. The main difference between both scans was the frequency offset. Using a higher frequency offset around 250 Hz and above, hyperintensity could be induced in the VSOP vial. Not all vials were visible in figure 25 which meant that a higher VSOP concentration would also result in increased positive contrast.

Table 1: Selection of turbo field echo sequences that provided the best positive contrast IRON images.

Sequ	**Type**	**Flip angle [degrees]**	**Echo time [ms]**	**Repetition time [ms]**	**Water/fat setting**	**IRON BW [Hz]**	**Fat suppression**
1	TFE	10	3.3	6.8	2	679	SPIR
2	TFE	10	1.36	6.8	min	679	SPIR
3	TFE	18	3.1	24	min	679	SPIR
4	TFE	18	TE1=1.36 TE2=2.5	24	min	679	Dixon

In terms of image quality, the four sequences do not differentiate by much. The detection limit for the three sequences that used SPIR fat suppression was the concentration of the VSOP2 vial (0.6 mM). VSOP2 was visible and according to the figure 36c and figure 37c, the signal

intensity of VSOP3 and VSOP 4 did not differentiate much and had a similar signal intensity then the water vial. When using Dixon as fat suppression (figure 39) VSOP3 has a much higher signal intensity than water and also VSOP4 (0.15 mM) can be differentiated from water for 254 Hz and 264 Hz. The relation of the signal intensities between the different VSOP vials in figure 39 is linear. This suggests that the optimal range for quantitative imaging would be towards the upper end of the frequency spectrum, just before the background suppression starts to break up again in the centre of the phantom. At that frequency, even lower SPION concentrations can be detected while still maintaining a good suppression of the on-resonant protons.

7. Positive contrast imaging using a Dixon-based technique

7.1. Introduction

In this chapter the implementation and optimisation of Dixon as a positive contrast imaging technique is described. MR images were acquired of a water phantom loaded with a range of different SPION concentrations. Dixon was compared with other, more established positive contrast methods such as GRASP, IRON and SGM which were described in the previous chapter.

The Dixon method is a technique developed for effective fat suppression in MR imaging. It was first described by Thomas Dixon in 1984 for spectroscopic imaging [333]. In 1991, Glover and Schneider demonstrated the use of Dixon for the decomposition of water and fat signal in MRI [334], [335]. The technique relies on the chemical shift difference between the water and fat resonant frequencies. Ultimately, the Dixon method is a postprocessing technique as it translates the chemical shift difference in a signal phase. In the original two-point Dixon method, two images are acquired to separate water and fat. The phase angle α of the fat signal relative to the water signal is given as

$$\alpha = \gamma B_0 \sigma \Delta TE \tag{167}$$

where σ is the chemical shift of fat with respect to water and γ is the gyromagnetic ratio of protons. The images are acquired at different echo times which are selected so that for one image the water and fat resonant frequencies will be in-phase ($\alpha = 0$) and for the other they will be out-of-phase ($\alpha = 180°$, opposed-phase). The complex in-phase (I_0) and out-of-phase (I_1) images can then be mathematically combined to receive a water (W) and a fat (F) image

$$I_0 = (W + F)e^{i\phi_0} \tag{168}$$

$$I_1 = (W - F)e^{i(\phi_0 + \phi)} \tag{169}$$

with $\phi = \gamma(\Delta B_0)\Delta TE$ being the accumulated phase during the echo shift ΔTE due to field inhomogeneities (ΔB_0) and ϕ_0 contains all other phase errors. The in-phase and out-of-phase echo times can be determined from the phase angle by knowing that the main contributor to the fat signal is methylene whose resonance frequency is 3.5 ppm away from that of water [91], [336].

The two-point Dixon method has the disadvantage that it works under the assumption that water is perfectly on resonance. Limitations therefore exist if B_0-field inhomogeneities are present. A further development of the two-point Dixon method is the three-point Dixon technique [334] where three rather than two images are acquired for postprocessing [336]. As in the original method, in-phase and out-of-phase images are acquired by selecting the TEs accordingly. In

case of large magnetic field variations, three-point Dixon still suffers from errors in the assignment of water and fat pixels. In order to overcome this problem Szumowski et al. [337] have suggested a phase unwrapping technique. However, phase unwrapping techniques are limited due to their low SNR [338]. Several methods have been reported [339]–[342] that also estimate a field map in addition to the water and fat images. The advantage of these methods is that they are more robust than phase unwrapping and that TEs can be selected arbitrarily making the sequence design more flexible. The main applications for the Dixon technique remain fat suppression and fat quantification. However, with the development of above mentioned field map techniques, other applications can be considered as well.

If the Dixon technique is capable of successfully separating the frequencies of water and fat, it may also be possible to use Dixon to separate on- and off-resonant protons as a means to produce a positive contrast image of off-resonant protons affected by the dipole field of SPIONs. The T_2^* shortening effect of SPIONs means that the signal decay is of the order of the Dixon echo shift. As described above, the Dixon fat suppression is inaccurate when the T_2^* is very short [343], [344]. If modified appropriately, the Dixon method should be able to visualize magnetic susceptibility markers [345]. An example is **I**terative **D**ecomposition of water and fat with **E**cho **A**symmetry and **L**east-squares estimation (IDEAL) [339], [340]. IDEAL was developed for effective water and fat decomposition and uses an iterative reconstruction algorithm that allows for multiple echoes with flexible TEs. IDEAL however is unable to measure the transverse relaxation time because T_2^* mapping could interfere with the quantification of the fat signal.

Yu et al. [346] have described a development of the IDEAL reconstruction algorithm capable to estimate T_2^*, fat and water content. The algorithm was modified in order to allow for the simultaneous estimation of a complex field map that would allow T_2^* estimation in addition to water and fat decomposition.

The T_2^*-IDEAL reconstruction makes the assumption that in the presence of SPIONs, water and fat have similar T_2^* values. For k number of echoes that are acquired at echo times TE_i ($i = 1, 2, 3 \dots k$), the signal (S_i) of any given voxel is

$$\begin{aligned} S_i &= \left(w + f \cdot e^{j2\pi\sigma TE_i}\right) \cdot e^{j2\pi\psi TE_i} \cdot e^{-R_2^* TE_i} + n_i \\ &= \left(w + f \cdot e^{j2\pi\sigma TE_i}\right) \cdot e^{j2\psi TE_1} + n_i \end{aligned} \tag{170}$$

The B_0 field inhomogeneity and noise are represented by ψ and n_i, respectively. With ψ, a complex field map can be estimated

$$\hat{\psi} = \psi + j\frac{R_2^*}{2\pi} \quad (171)$$

$RE\{\hat{\psi}\}$ is the field offset usually given in Hz and $R_2^*/2\pi$ is the imaginary part ($IM\{\widehat{\psi}\}$). Applying the T_2^*-IDEAL implementation for the imaging of susceptibility marker such as SPIONs, w would refer to on-resonance protons instead of water while f would refer to the off-resonance signals affected by the dipole field of the SPIONs [150], [346].

7.1.1. Purpose of present work

The purpose of this study was to implement and test Dixon as a method for positive contrast imaging. We aimed to assess the imaging capabilities of a simple implementation that utilises all of the pre-installed and optimised functionality on a Philips Achieva MRI scanner. Our Dixon positive contrast method will be tested on three different SPIONs of different coatings, size and magnetic moment. We investigated the feasibility to produce positive contrast images using the Dixon technique and compared it to already established techniques such as SGM, GRASP, and IRON. Finally, we compared the fat suppression ability of SPIR and Dixon when acquiring positive contrast images with the IRON technique.

7.2. Methods

7.2.1. Dixon implementation

We used a simple implementation to test whether positive contrast images could be generated *in vitro* using the already available Dixon functionality. The idea was to change the user interface so that the water-fat shift could be changed manually. This would therefore no longer represent the water-fat shift and could potentially be used to display water protons affected by the dipole fields of superparamagnetic iron oxide nanoparticles.

As a first step, we created a new parameter that we called EX_ACQ_Dixon_freq_shift. The parameter was added to the IEX_contrast_pars parameter group of the include file mpuexrcd.h.

We added the parameter to the text file mpiacqtxt.txt where it was given a name tag (XNIACQ128) and a label ("Freq Shift") for its display on the user interface.

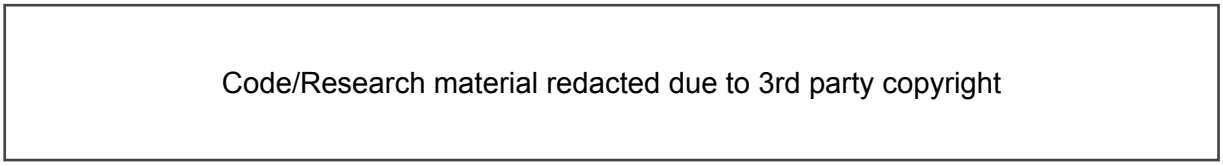

In the file mpuacqrcd.h, the parameter was further defined as a float with a set range, default value and adjust value. The previously defined name tag was provided to link the parameter properties to the parameter name in the mpiacqtxt.txt file and the user interface.

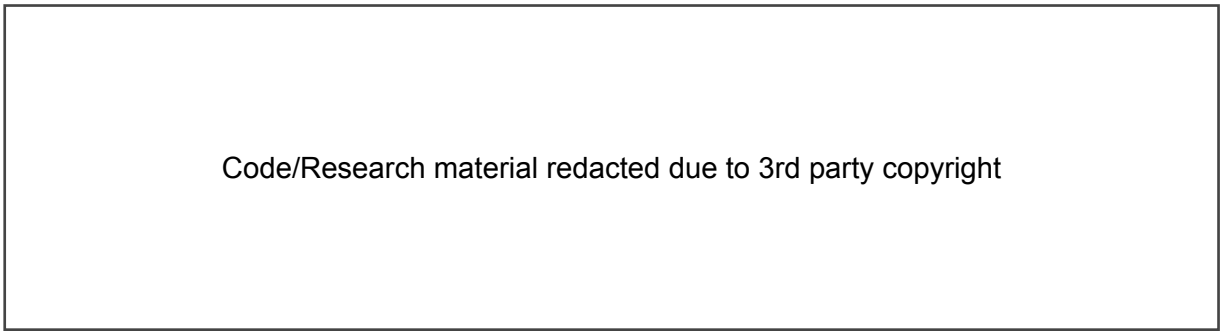

The water-fat shift parameter (MGG_PPM_WATER_FAT_SHIFT) is defined in the file mggrcd.h.

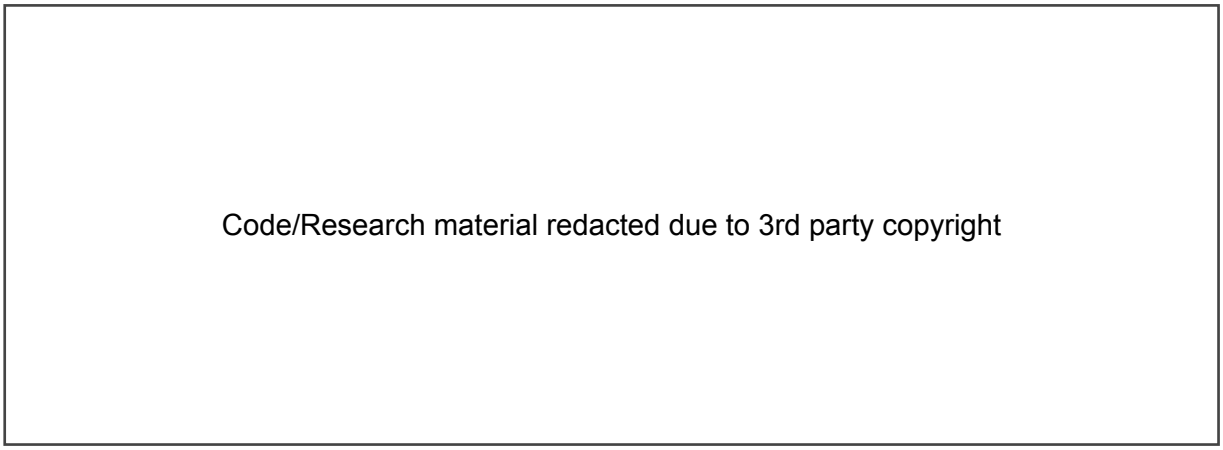

MGG_PPM was defined as 0.000001 which is the equivalent of one part per million (ppm). The water fat shift was defined as 3.4 ppm. Our parameter had to be enabled in the file mpuacq_g.c. It was added to the uacq1_Dixon group. When the Dixon functionality is activated on the user interface, the Dixon parameter EX_ACQ_dixon is enabled as well as our Dixon frequency shift parameter.

Code/Research material redacted due to 3rd party copyright

In order to control the frequency shift manually whenever Dixon is used, we replaced MGG_PPM_WATER_FAT_SHIFT with our frequency shift parameter, e.g. mparc.h:

Code/Research material redacted due to 3rd party copyright

and in the file mpudef_comb_g.c:

Code/Research material redacted due to 3rd party copyright

and in the file mpiffe_sq_g.c:

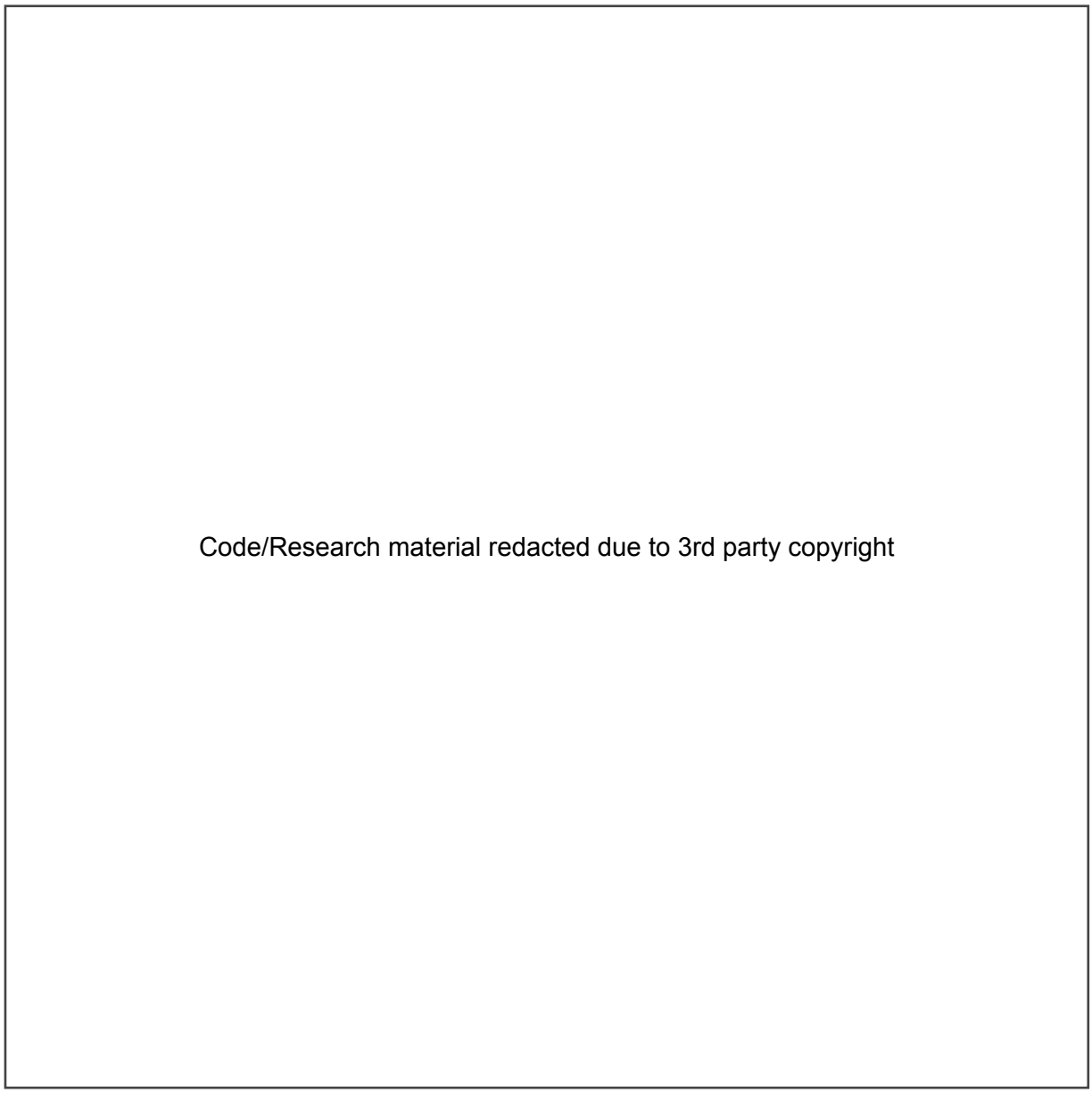

7.2.2. Superparamagnetic Iron Oxide

We compared four different SPIONs (table 2) *in vitro* to investigate their behaviour as positive MR contrast agents. Two SPIONs (MF66-DMSA and MF66-PEG) were synthesised as part of the MultiFun project (European Community's Seventh Framework Programme, grant agreement number 262943). Ferumoxytol is a commercially available and clinically approved MR contrast agent and VSOP-C200 is a very small superparamagnetic iron oxide particle (Ferropharm, Teltow, Germany) that is no longer available.

Table 2: Superparamagnetic iron oxide nanoparticles investigated in this study with their core size, hydrodynamic diameter, coating material, surface charge, pH in water, and transverse relaxivity r_2.

SPION	Particle Size TEM [nm]	Hydrodynamic Size [nm]	Nature of coating	Surface Charge [mV]	pH	r_2^* Relaxivity $[mM^{-1}s^{-1}]$
Ferumoxytol	3.25	23.6	PSC	-43.2	7	90.8
MF66-DMSA	11.7	85	DMSA	-47	4.9	243.1
MF66-PEG	12	111.3	PEG	-28.3	7.4	307.0
VSOP-C200	5	9	Citrate	anionic	7.4	49.8

7.2.3. Experimental Setup

For each SPION we prepared eight different concentrations (1.6 mM, 1.2 mM, 0.8 mM, 0.6 mM, 0.4 mM, 0.2 mM, 0.1 mM and 0.05 mM) by two-fold serial dilution in 2 ml non-conical Eppendorf tubes. We used inductively coupled plasma mass spectrometry (ICP-MS) to determine the exact iron concentration. All contrast agents were treated for 15 minutes in an ultrasound bath before scanning to avoid agglomeration. The Eppendorf tubes containing the SPION solutions were placed in a 5 mm thick custom-made Perspex holder perpendicular to the main magnetic field and suspended in water within a 140 mm crystallising dish (Technische Glasswerke Ilmenau GmbH, Ilmenau, Germany) (figure Figure 77). To assess the homogenous distribution of the SPIO nanoparticles in solution, we visually inspected the phantom before and after the scan session to ensure that there were no accumulations. The slice orientation for all scans was chosen to be coronal. Imaging was performed with a slice in the middle of the water level to achieve optimal magnetic field homogeneity. The phantom was positioned between the two elements of a medium-sized SENSE flex coil to receive the MR signal. Imaging was performed on a clinical 3T Philips Achieva MRI scanner (Philips Healthcare, Best, The Netherlands).

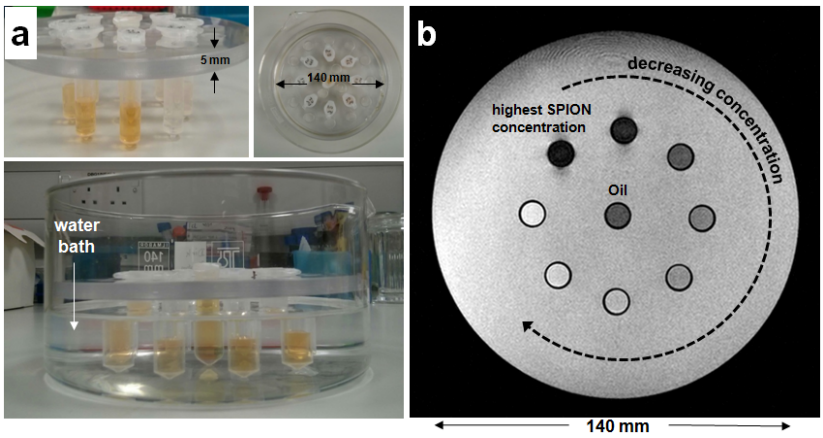

Figure 77: MRI water phantom containing eight SPION concentrations and an Eppendorf tube containing olive oil in the centre. a: Photos illustrating the design of the phantom and the Perspex disc used to hold the Eppendorf tubes. b: Coronal MR image (gradient-echo acquisition) of the water phantom.

7.2.4. Positive Contrast Imaging

All scans were performed with a 2D gradient-echo acquisition where k-space was filled in a Cartesian fashion. The acquisition pixel size was 1 x 1 mm^2 with a field of view of 170 x 170 mm^2. Apart from the T_2^*-weighted imaging sequence used for the SGM technique, all acquisitions had a reconstructed pixel size of 0.53 x 0.53 mm^2 and the SGM input data had a reconstructed pixel size of 0.27 x 0.27 mm^2. The readout direction was foot-head. Shimming was performed using the build-in volume shim function where the region of interest included the entire water phantom. We saved modulus, real, and imaginary DICOM images from all acquisitions for future analysis.

For the GRASP and IRON implementations we devised and developed a dynamic preparation phase to optimise the positive contrast imaging parameters by dynamically loop through the user-defined rephasing gradient strengths (GRASP) or frequency offset (IRON).

7.2.4.1. SGM

The postprocessing technique was applied to images acquired with a T_2^*-weighted multi-shot fast gradient echo sequence (five echoes) with a TFE factor of 1, a user defined shot interval of 300 ms (170 shots), TR/TE1/ΔTE = 10/2.2/1.7, a flip angle of 25°, and 3 mm slice thickness.

7.2.4.2. GRASP

Images were acquired with a user defined TR of 50 ms and the shortest TE possible (1.36 ms). The flip angle was 25° and the slice thickness was 7 mm. GRASP was run with SPIR fat suppression. We ran two acquisitions with 11 dynamics each. The first acquisition started at a rephasing gradient strength of 100% which was reduced by 10% with each dynamic. The second acquisition was based on the most promising area for positive contrast achievement. In our case, the second acquisition contained 11 dynamics and started at a rephasing gradient strength of 60% of the original strength which was decreased by 2% with each dynamic.

7.2.4.3. IRON

IRON was acquired with a multi-shot turbo field echo sequence (TFE factor = 12) with ten start up echoes and a user defined shot interval of 1000 ms (14 shots), TR (user defined)/TE (shortest) = 10/1.36, a flip angle of 18°, and 20 mm slice thickness. The IRON pulse was selected with an offset frequency of 135 Hz and a bandwidth of 679 Hz. We used six dynamics and for each dynamic the frequency was increased by 15 Hz. We ran IRON with SPIR and multi-echo Dixon in order to compare both fat suppression techniques with respect to effective fat suppression for positive contrast imaging. For the Dixon technique (figure 78) the number of

echoes was increased to two with TE2 (shortest) = 2.5 ms and the Dixon frequency shift set to 3.4 ppm, to account for the water-fat frequency shift.

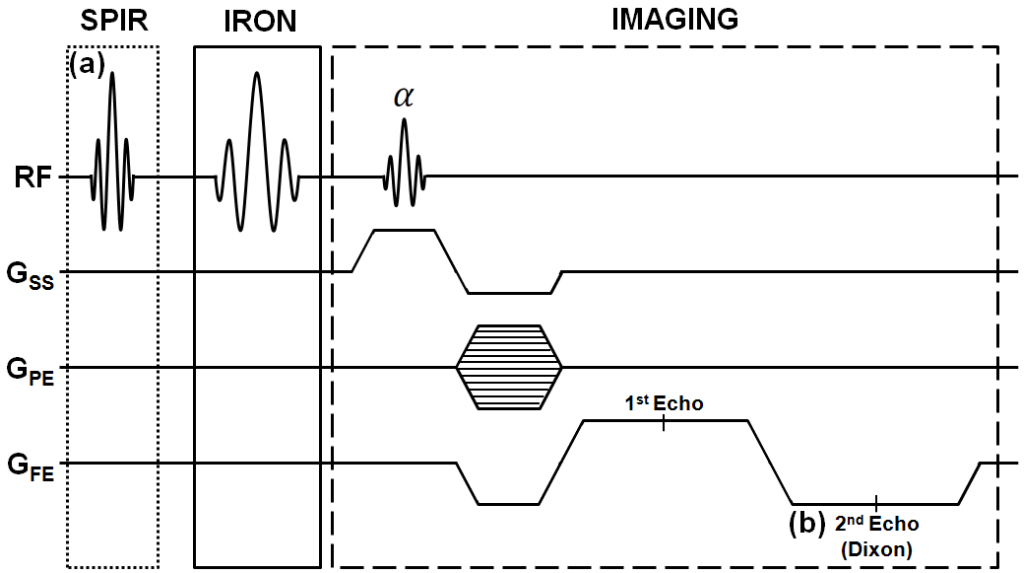

Figure 78: Sequence diagram IRON. a: Gradient-echo sequence with SPIR pre-pulse followed by a frequency-selective IRON pre-pulse. One echo is acquired in the imaging part. b: Only one pre-pulse (IRON) but two echoes are acquired to generate in- and out-of-phase images (i.e. multi-echo Dixon).

7.2.4.4. Dixon

The Dixon technique used for the acquisition of positive contrast images was performed with a multi-shot turbo field echo sequence (TFE factor = 12) with ten start up echoes and a user defined shot interval of 1000 ms (14 shots), TR (user defined)/TE_1 (shortest)/TE_2 (shortest) = 24/3.5/9.3, a flip angle of 18°, and 3 mm slice thickness. We saved the water, in-phase, out-of-phase, and fat images for each acquisition for further analysis in DICOM format. The Dixon frequency shift was varied from 3.4 ppm to 0 ppm in steps of 0.1. The water fat shift was set to 2 pixels (108.45 Hz/pixel).

7.2.5. Image Analysis

Regions of interest (0.12 cm^2) were centred over the coronal images of the Eppendorf tubes to obtain the signal intensity (SI) for each ROI. The operator ensured to stay clear of the tube edge in order to avoid local inhomogeneities caused by the Eppendorf tubes which could distort the measurement. In order to measure the noise, a ROI of 10.20 cm^2 was placed outside the phantom in the background of the MR image. The area of positive contrast enhancement was determined by visual inspection and a region of interest was drawn by an operator in ClearCanvas (Synaptive Medical, Toronto, Canada).

7.3. Dixon optimisation

To get an indication for the positive contrast imaging capacity of Dixon for a given SPION water phantom, we manually altered the frequency shift between the in-phase and out-of-phase images from 0.1 ppm up to 3.4 ppm in steps of 0.1 ppm. The SPION used were VSOPs (VSOP-C200, anionic citrat coating, 5 mm core, 9 mm hydrodynamic diameter) of 1.2 mM, 0.6 mM, 0.3 mM and 1.5 mM. In addition, the phantom contained a vial filled with water as a control and a centre vial filled with olive oil. The aim of this optimisation step was two-fold. First, we wanted to test if with the simple code alteration we implemented that allows us to manually change the frequency shift, we could generate positive contrast images where the VSOPs would be hyperintense while the signal from water phantom would be suppressed. Second, we wanted to find the optimal frequency shift for which the difference in contrast between VSOPs and water was maximised.

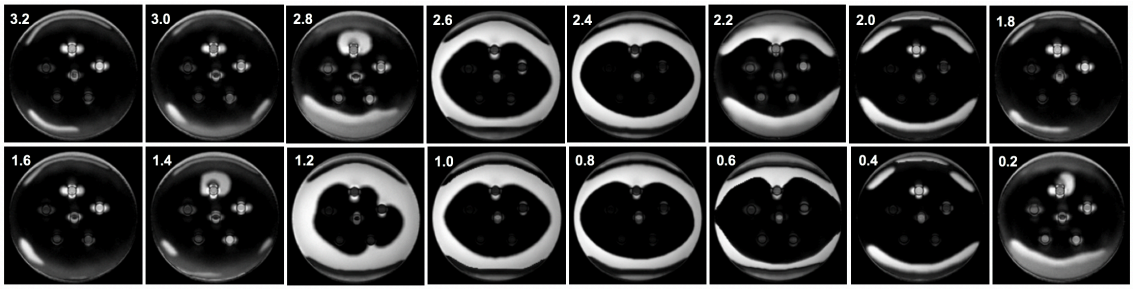

Figure 79: Depiction of Dixon fat images for a range of frequency shifts from 3.2 ppm to 0.2 ppm and the resulting change in contrast behaviour. As the frequency shift was changed, the out-of-phase echo time increased.

Figure 79 shows that Dixon is in general able to produce positive contrast images. There appear to be several ranges of frequency shift where good positive contrast images are possible. Each of these is followed by a range of less well suited frequency shifts. The ideal frequency shift for positive contrast imaging was determined by quantifying the signal intensity of the vial with the highest VSOP concentration (1.2 mM), olive oil, and water and to identify regions where the VSOP signal intensity was greatest while those of olive oil and water were low (figure 80). We measured the water signal in the phantom body as well as within the control PCR tube to detect any effects the PCR tube itself could potentially have on the contrast display.

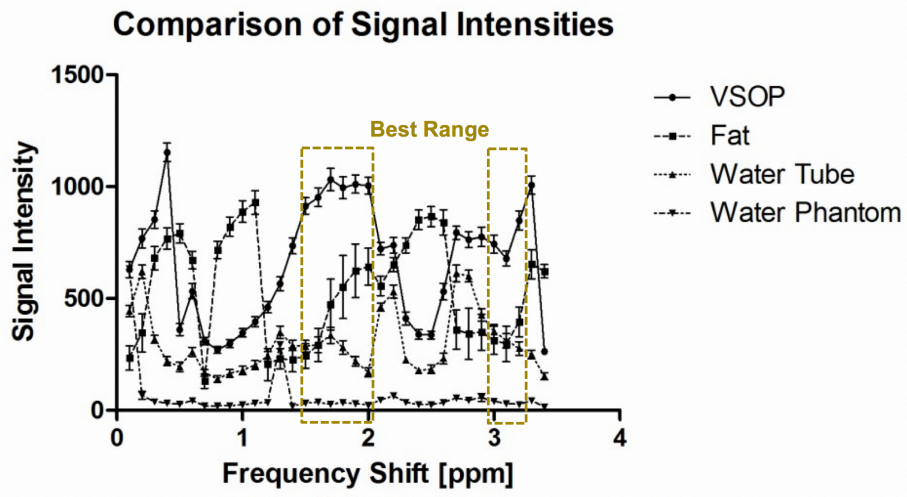

Figure 80: Graphical representation of the signal intensity of the highest VSOP concentration, olive oil mimicking fat, water, and the signal intensity of the phantom water for frequency shifts ranging from 0.1 ppm to 3.4 ppm in steps of 0.1 ppm.

Figure 80 confirms that there are several ranges of frequency shifts where the iron oxide particles display a higher signal intensity compared to the water phantom. The ideal imaging range lies between 1.5 and 2.0 ppm as well as 2.4 ppm and 2.5 ppm where the VSOP vial possess the highest signal intensity.

All of the above was done on the so-called fat images. However, Dixon produces in total 4 different images. It records the in-phase and out-of-phase images from which it calculates the water and fat images. Even though we are not looking to employ Dixon for fat suppression, we will keep the terminology of water and fat images. Below we show the water, in-phase and out-of-phase images obtained for scanning across the range of frequency shifts (figure 81).

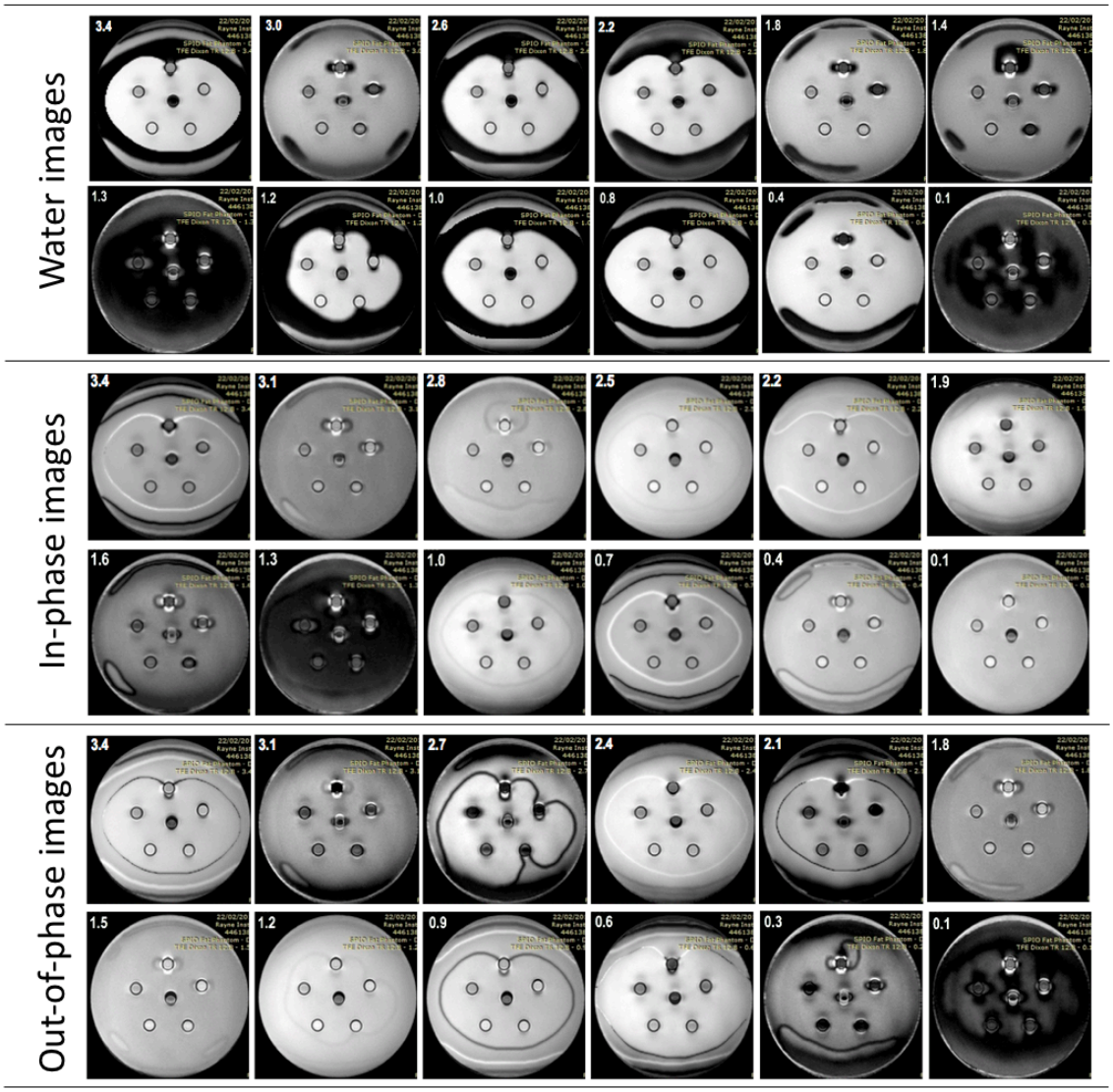

Figure 81: Depiction of Dixon water, in-phase and out-of-phase images. Selection of images with a frequency shift between 3.4 ppm and 0.1 ppm.

The signal from water protons in the phantom appear to be low at frequency shifts of 1.3 ppm and 0.1 ppm. Contrary to the Dixon fat images from figure 79, the VSOP solutions themselves are not highlighted in any of the images. Instead, the dipole field of VSOP1 and VSOP2 are visible on several images across water, in-phase and out-of-phase images. Neither the on-resonant signal suppression nor the hyperintensity of off-resonant protons is comparable to the Dixon fat images.

7.4. Results

In order to explore our simple Dixon implementation for SPION positive contrast imaging, we conducted a range of experiments assessing the contrast behaviour of different SPIONs with

Dixon, compared Dixon to other more established positive contrast imaging methods in terms of image appearance and SPION concentration dependence of hyperintense contrast.

7.4.1. Comparison of Ferumoxytol, MF66-DMSA and MF66-PEG with Dixon positive contrast imaging

Based on the above described optimisation experiments, we selected a frequency shift at which we felt optimal positive contrast images could be achieved. We compared three different SPIONs in terms of their contrast behaviour, Ferumoxytol, MF66-DMSA and MF66-PEG. The MF66 particles are identical apart from their coating which determines surface charge and hydrodynamic diameter.

Dixon fat images were acquired at a frequency shift of 1.9 ppm for ferumoxytol and MF66-DMSA and at 1.8 ppm for MF66-PEG. Figure 82 shows the positive contrast images obtained with the Dixon method for eight different SPION concentrations (1.6 mM, 1.2 mM, 0.8 mM, 0.6 mM, 0.4 mM, 0.2 mM, 0.1 mM, and 0.05 mM). The higher SPION concentrations display the dipole field as positive contrast.

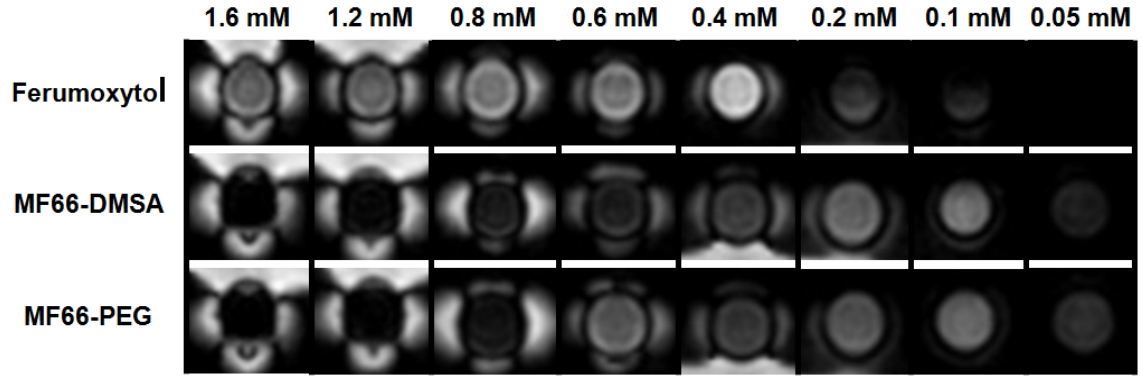

Figure 82: Positive contrast images Dixon fat images of eight different concentrations of ferumoxytol, MF66-DMSA, and MF66-PEG. Higher SPION concentrations display the lobes of the dipole field extending outside of the tube hyperintense whereas lower concentrations show hyperintensity inside the tube compared to the dark, signal suppressed water of the phantom.

On first sight, there appears to be a difference in terms of contrast behaviour and detection limit for the two types of SPIONs, ferumoxytol and the MF66 nanoparticles. Differences between the different SPIONs are also visible on Dixon water images at a frequency shift of 2.5 ppm. The images of figure 83 show good background suppression of the water signal while displaying areas affected by the SPIONs with hyperintense signal.

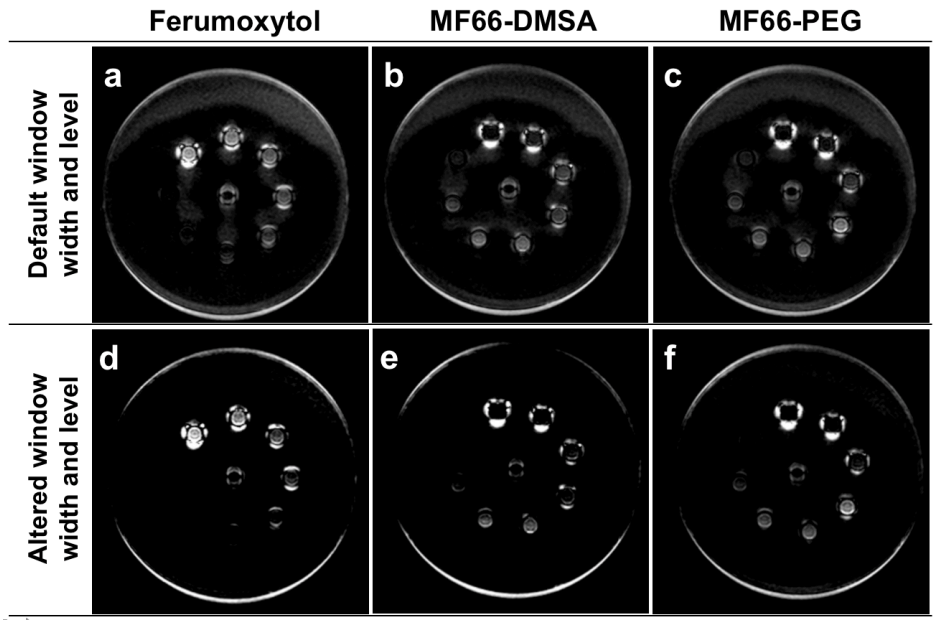

Figure 83: Dixon water images at a frequency shift of 2.5 ppm for ferumoxytol (a,d), MF66-DMSA (b,e) and MF66-PEG (c,f). Images a-b are the original with the default window width and level. For images d-f the window width and level was altered to highlight features.

Compared to the whole phantom fat images from figure 79, the background suppression achieved is more convincing and only fails at the edge of the phantom in the head-toe direction. The SPIO nanoparticles and their associated dipole fields are clearly visible as hyperintense signal while the vial containing water is not.

7.4.2. Comparison of SGM, GRASP, IRON, and Dixon for Novel MRI Contrast agents

An overview of the different positive contrast imaging techniques for three different SPIONs is presented in figure 84 which also includes T_2^* -weighted gradient echo images that are the input for the calculation of the SGM images. Ferumoxytol, MF66-DMSA, and MF66-PEG were measured with a phantom that allowed to fit up to nine PCR tubes while the phantom used for the VSOP measurements only caters for up to six PCR tubes. The SGM images were calculated by taking into account three neighbouring pixels. The GRASP images were acquired at a refocusing gradient strength of 52% of its original strength.

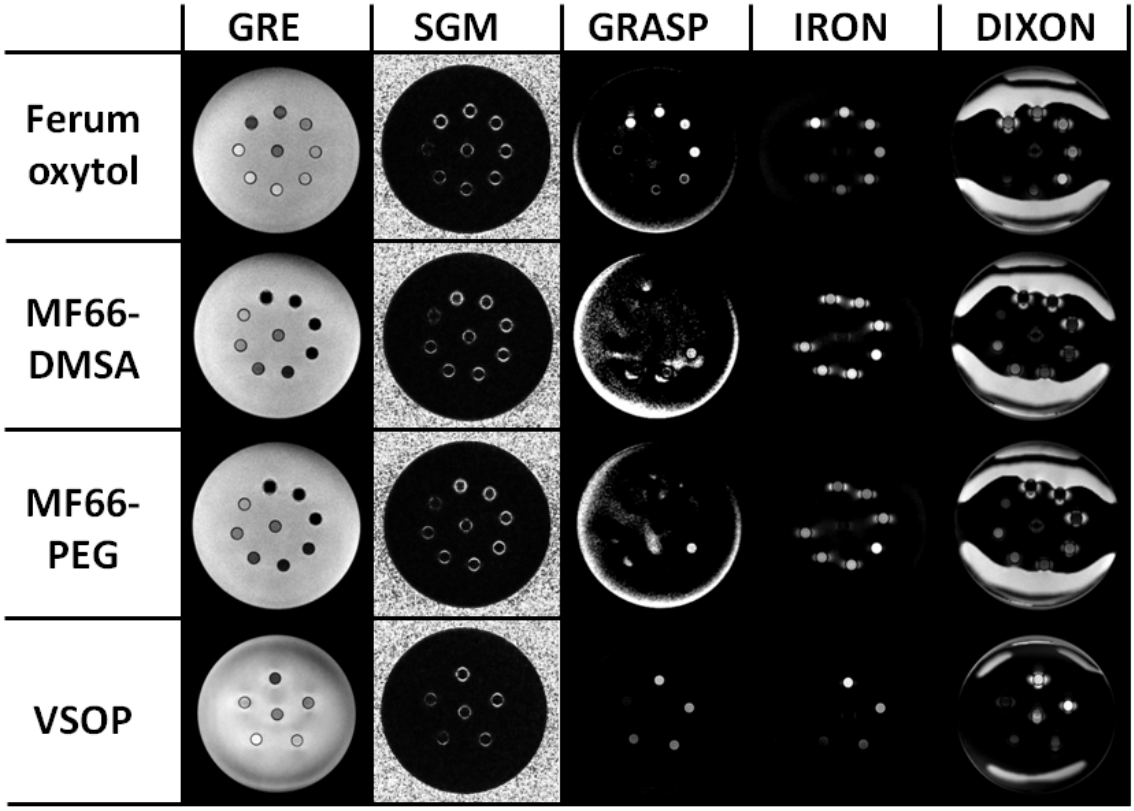

Figure 84: Summary of four different positive contrast techniques (SGM, GRASP, IRON, and Dixon) for four different superparamagnetic iron oxide nanoparticle (ferumoxytol, MF66-DMSA, MF66-PEG, VSOP).

We were unable to obtain good positive contrast images with GRASP for the MultiFun SPIONs (MF66-DMSA and MF66-PEG). The IRON images were acquired at a frequency shift of 180 Hz which led to good background signal suppression while preserving the hyperintense signal of the SPION vials. In the case of ferumoxytol and VSOP, the signal intensity appears to be concentration dependent. Suppression of signal from the centre tube that contained olive oil was achieved by using the SPIR technique. The Dixon images were acquired at frequency shifts of 1.9 ppm (ferumoxytol, MF66-DMSA), 1.8 ppm (MF66-PEG), and 1.6 ppm (VSOP). Background suppression with the Dixon technique was compromised in the phantom used to measure ferumoxytol, MF66-DMSA, and MF66-PEG.

7.4.3. Concentration Dependence of Positive Contrast Techniques

We investigated the relationship between the positive contrast achieved (i.e. SNR or hyperintense area) and the concentration of the SPIONs investigated. For GRASP and IRON, the positive contrast does not normally extend outside of the borders of the measurement tube. We determined the signal-to-noise ratio (SNR) and plotted that over the concentration of the SPION. For the SGM and Dixon techniques where the positive contrast is mostly visible in

form of a dipole field that extends outside of the tube border, we determined the volume of the hyperintensely enhanced area and plotted that over the SPION concentration. Figure 85. summarises the results of concentration dependent measurements.

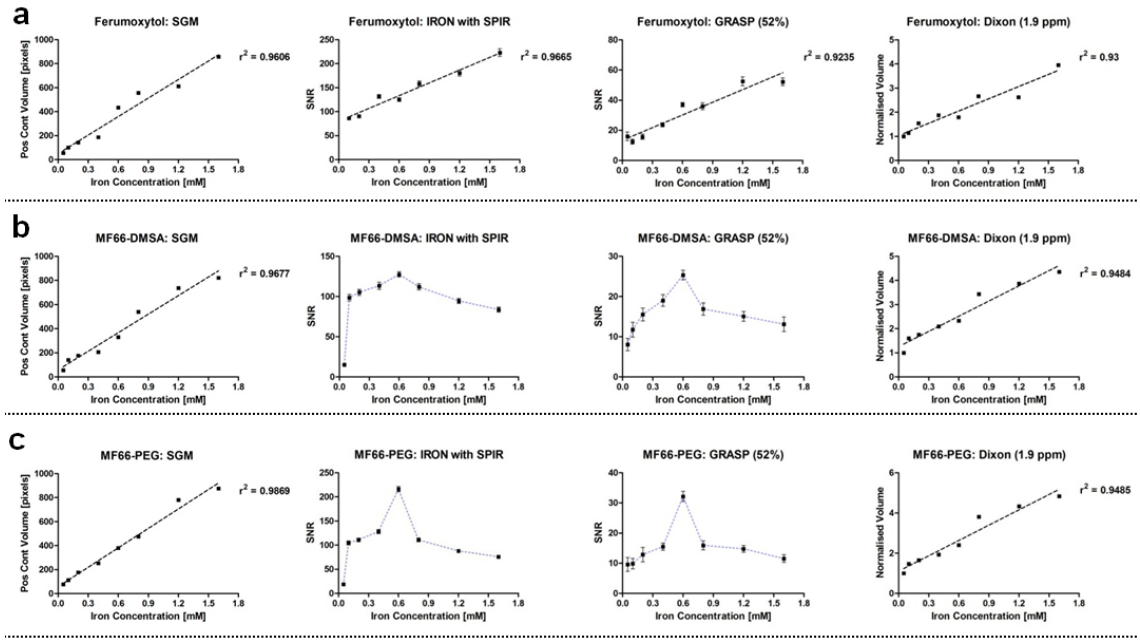

Figure 85: Relationship of positive contrast and SPION concentration for SGM, GRASP, IRON, and Dixon fat image for ferumoxytol (a), MF66-DMSA (b), and MF66-PEG (c). A linear relationship is observed for ferumoxytol whereas GRASP and IRON for MF66-DMSA and MF66-PEG behave in a non-linear fashion.

It can be seen from figure 85 that ferumoxytol follows a linear relationship for all positive contrast techniques. The MultiFun samples MF66-DMSA and MF66-PEG produce a linear relationship only for those techniques that measured the area of positive contrast.

7.4.4. Fat suppression for positive contrast imaging with IRON: SPIR vs Dixon

In the previous sections, we have introduced Dixon as a new positive contrast imaging technique that allows visualising iron-oxide based contrast agents. In the literature however, Dixon is described as a fat suppression technique and essential in many *in vivo* applications.

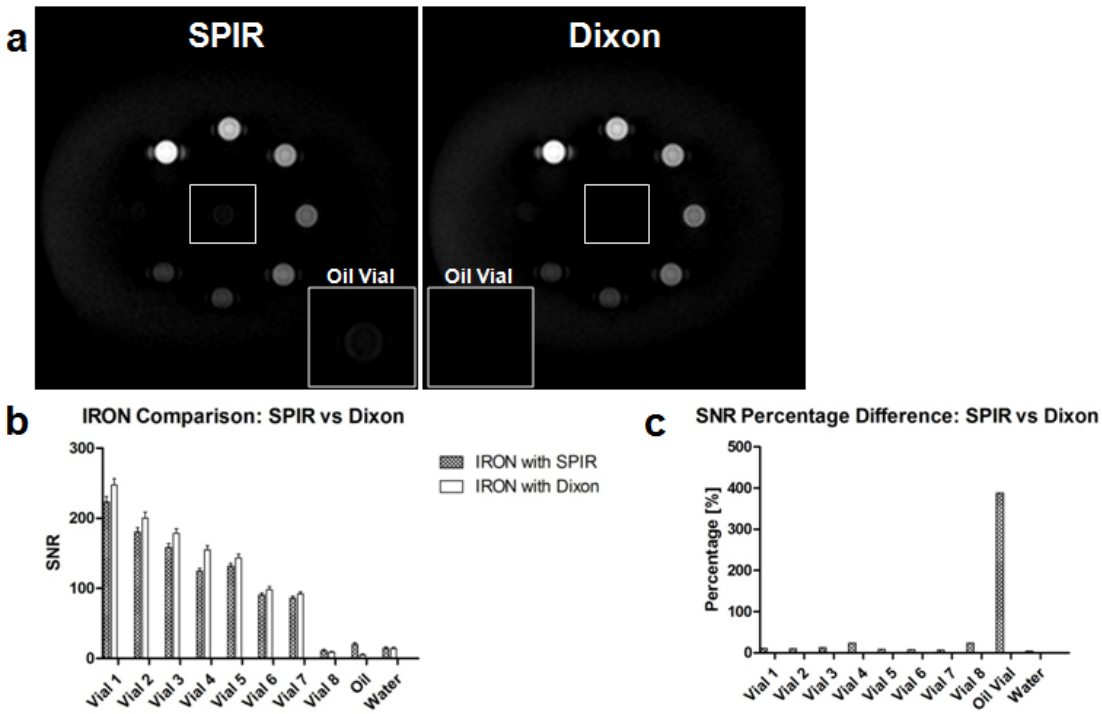

Figure 86: Comparison of SPIR and Dixon fat suppression in combination with IRON positive contrast imaging. a: IRON image of eight ferumoxytol concentrations and a tube containing olive oil (centre) using SPIR and Dixon, respectively. b: Comparison of SNR of each vial (SPION concentration and fat) for IRON. c: Percentage difference of the SNRs from figure 86b showing the largest difference for the fat signal.

The positive contrast methods presented in figure 84 used SPIR as a fat suppression technique. Instead, Dixon can also be used to effectively suppress fat signal in GRASP and IRON acquisitions as it is a highly effective fat suppression technique [347]–[349]. Here we compare IRON acquisitions with SPIR and Dixon fat suppression for positive contrast imaging. Figure 86a presents two images of the ferumoxytol phantom acquired with IRON. The two scans only differ in the fat suppression technique used.

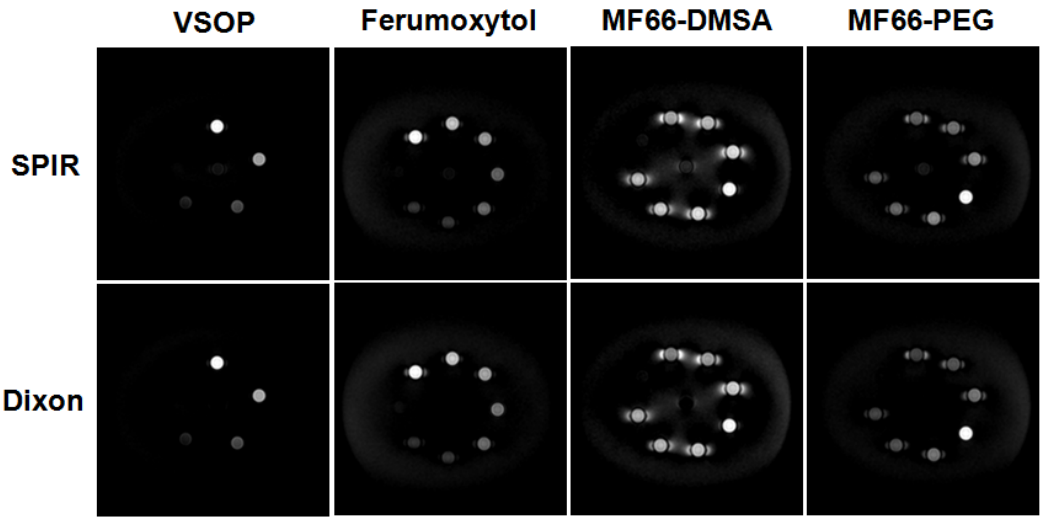

Figure 87: Positive contrast images acquired with IRON for ferumoxytol, MF66-DMSA, MF66-PEG, and VSOP. The top row shows images acquired with SPIR fat suppression and the bottom row shows water images acquired using Dixon. For all SPIONs, the Dixon fat suppression is superior to SPIR.

The tube with olive oil sits in the centre and a better signal suppression is achieved when Dixon is used. For quantification we determined the SNR of all eight SPION vials as well as the oil and water signals and presented these in a bar diagram in figure 86b. The biggest difference in SNR between the two images is observed for the oil tube. This becomes clearer from figure 86c where we have plotted the percentage difference between the SNR bars from figure 86b. This illustrates that the SNR difference between the ferumoxytol vials are very small while there is a large difference between the SNR of the oil tube when using Dixon instead of SPIR. Furthermore, figure 87 shows that for positive contrast imaging with IRON, Dixon results in superior fat suppression than SPIR irrespective of which SPION is used.

7.5. Discussion

7.5.1. Dixon optimisation

The Dixon fat images of figure 79 demonstrate that positive contrast imaging using Dixon is feasible. A problem at all frequency shifts in vitro is the lack of water suppression at the edge of the phantom near the air/water interface along the readout direction (foot-head). The ideal frequency shifts to achieve a positive contrast image were between 1.5 – 2.0 ppm and 3.0 – 3.2 ppm. At 3T, these frequency shifts correspond to 189 – 252 MHz and 378 – 403.2 MHz, respectively. At these frequency shifts, the signal from fat remained high. Between 0.5 – 0.6 ppm, 0.8 – 1.1 ppm, 2.3 – 2.6 ppm and 3.4 ppm, fat had a stronger signal intensity than VSOP1. At the other frequency shifts, the VSOP signal was superior but the fat signal remained high. As

lower VSOP concentrations will result in weaker signal intensity, it will be challenging to differentiate fat from those.

The best image was obtained at a frequency shift of 1.6 ppm. The overall appearance of the image is that the signal from the water phantom is predominantly suppressed resulting in a darkened image. There are bands towards the phantom edges in the head-toe direction where the signal increases. A bright patch is visible towards the right-toe edge of the phantom. As the edge of the phantom is an area of inhomogeneity due to the phase transition, the overall signal suppression of on-resonant protons was successful. The PCR tubes containing VSOP1 and VSOP 2 (i.e. 1.2 mM and 0.6 mM) are hyperintense. VSOP3 and VSOP4 appear similar to the control vial containing water. The small increase in signal in these three vials must be attributed to the PCR vial itself rather than the VSOP solution. Looking at figure 80, the signal intensity of the control vial is more than 5 times higher than that of the phantom water and similar to the signal intensity of fat. The signal intensity of the phantom water was measured in the space between the centre tube (fat) and the control vial filled with water. Comparison of the SNR in the control tube and the surrounding water in the phantom demonstrates that the PCR tubes change the local magnetic field which results in a frequency offset.

The detection limit of any SPION-based contrast agent depends on the concentration and the special resolution of the MRI scan. The latter is predominantly determined by the strength of the B_0 field [350]. The detection threshold for VSOP particles is 0.6 mM. VSOP1 and VSOP2 introduce field inhomogeneity that protrudes outside the PCR tubes visible in the hyperintense dipole field lobes. The vial containing fat also shows small dipole lobes in the left-right direction. A small band of hyperintensity is visible towards the edge of the PCR tube in the toe-direction. A key challenge for further development will be an effective fat suppression method.

It is not surprising that the water, in-phase and out-of-phase images did not lead to superior positive contrast images compared to the fat images. For a given chemical shift value, the in-phase image is acquired at a TE so that the two signal components separate by that given chemical shift are in phase. The out-of-phase image is acquired at a ΔTE later where those two components are 180° out of phase. The signal that leads to the in-phase image is therefore a combination (i.e. addition) of the two signal components that are separated by a given chemical shift value. The opposite is true for the out-of-phase image where the overall signal is a subtraction of the two signal components. The resulting images still display various shades (i.e. signals) because we never operate in a perfectly homogenous magnetic field and there are many more than just two signal components. By definition, neither the in-phase nor the out-of-phase acquisition should result in the isolation of a particular proton signal. The water and fat images

are obtained from mathematically combining the in-phase and out-of-phase images. As the chemical shift we change is always in relation to a set standard, in this case water, the water image will be the same as for any Dixon fat suppression acquisition and highlight the on-resonant water protons. The water image obtained for a frequency shift of 1.3 ppm is interesting in that respect. The range of different signals in a water phantom like we used is obviously complex. There are not just two or three different, sharply defined signals. While the two signal components that are separated by a chemical shift of 1.3 ppm are being perfectly in-phase and out-of-phase, signals slightly off of that will not be. This is not surprising as the PCR tubes, the phantom walls and the inhomogeneity of the magnetic field itself contribute to a range of different resonant frequencies. The display of the water image at 1.3 ppm supports this as the VSOP itself in the PCR tubes are not shown while the background suppression is a lot weaker compared to the fat images. Apart from that, the images shown in figure 81 confirm what was expected that for the correct chemical shift that relates to the off-resonant protons affected by the SPIONs, the fat images will be displayed as positive contrast images for a given SPIO nanoparticle.

7.5.2. Comparison of Ferumoxytol, MF66-DMSA and MF66-PEG with Dixon Positive Contrast Imaging

The lower the concentration of the SPIONs, the more signal appears to be within the PCR tube. We used the shortest echo time possible for the Dixon imaging experiment. As a result, the sequence was T_1-weighted which explains the T_1 effect we observed for lower SPION concentrations. The main difference between ferumoxytol and the two MF66 nanoparticles is that ferumoxytol exhibits a T_1 effect even at higher concentrations. The hyperintense signal as a result of the off-resonant protons due to the SPIONs that affected the magnetic field is clearly visible for the three highest concentrations (0.8 mM, 1.2 mM and 1.6 mM) in the form of dipole field lobes. Dipole field lobes are still visible for 0.6 mM and 0.4 mM for all three SPIONs but significantly less distinct. For the lowest concentrations (i.e. below 0.2 mM), these are absent as the magnetic moment of the SPIONs is not strong enough to extend outside of the PCR tube. Not considering the contrast resulting from the T_1 effect, the detection limit is at 0.4 mM for all three SPIONs. Both are lower than the detection threshold of VSOP used for the optimisation. The reason for the detection limit is that very small concentrations might only lead to intravoxel dephasing. This means there will be no change in the magnetic field from one voxel to another.

7.5.3. Dixon Water Images

The water images of Ferumoxytol and the MF66 particles at 2.5 ppm (315 MHz) compare to the water image of the VSOP phantom at 1.3 ppm in terms of contrast quality. In the unaltered images (figure 83a-c), a 1 cm grey band is visible along the edge of the phantom in head-direction where the on-resonant water suppression failed. The reason for that is the change in the magnetic field strength across the phantom that is less homogenous towards the phantom edges. A much narrower grey band is observed in the toe-direction suggesting the phantom has not be perfectly placed the isocentre of the magnet. By slightly altering the window width and level, we obtained figure 83d-f where the features of a positive contrast image for SPION detection are enhanced. Figure 83 confirms the results of figure 82 with regards to the different positive contrast behaviour of the three SPIONs. Both MF66 particles display a very similar contrast. This was expected as the particle and its magnetic moment that is responsible for changing the Larmor frequency of surrounding water protons is the primary driver for the contrast behaviour. The coating on the other hand seems almost negligible with regards to contrast behaviour and is primary responsible for stabilising the nanoparticle, functionalisation and physiological targeting. At lower concentrations, the MF66 solutions are hyperintense while at higher concentrations, only the only the lobes of the dipole field affecting the surrounding protons are visible. The ferumoxytol phantom displayed a different behaviour. As the SPION concentration increases and the hyperintense dipole fields become larger and more pronounced, the positive contrast of the ferumoxytol solution increases as well. MF66 particles have a higher transverse relaxivity value than ferumoxytol (table 2) which means they have a stronger magnetic moment. For the highly concentrated vials, the offset is likely to be too high to register and instead the surrounding water protons affected by the SPION solution are hyperintense as the effect is weaker there and the Larmor frequency lies within the range that is being highlighted. As the concentration is decreased, the MF66 solution itself will fall within the visible range. For MF66-PEG, the optimal concentration appears to be at 0.6 mM where the solution has the strongest signal. As ferumoxytol has a weaker magnetic field, the signal from the ferumoxytol solution increases with concentration. The control water vial is not visible in figure 83 indicating effective on-resonant water suppression.

7.5.4. Comparison of SGM, GRASP, IRON, and Dixon for novel MRI contrast agents and assessment of their concentration dependence

In figure 84 we compared the different SPIONs for their positive contrast imaging capabilities across a range of different positive contrast imaging techniques (i.e. SGM, GRASP, IRON and Dixon). In figure 85 we summarised the quantitative capabilities of ferumoxytol, MF66-DMSA, and MF66-PEG.

The T_2^*-weighted gradient-echo images (5th echo) of figure 84 show a stronger darkening of the MF66 nanoparticles. This is in agreement with the above discussion and the higher magnetic moment of the MF66 nanoparticles. Furthermore, these SPIONs also have higher transverse relaxivities compared to ferumoxytol and VSOP as shown by table 2. With the T_2^* mapping images as input for the SGM algorithm, the MF66 nanoparticles produce larger hyperintense areas. Comparing the SGM images of the different SPIONs, the signal intensity and area of the hyperintense signal does not correspond to transverse relaxivity or the negative contrast achieved on GRE images. The MF66 particles have a much stronger magnetic moment and also show a much more intense darkening on GRE images. However, the positive contrast achieved on the SGM images is only marginally stronger than that of ferumoxytol and VSOP. Looking at the capability to quantify, we plotted the area of positive contrast over iron concentration (figure 85) which showed a linear relationship. Visual inspection of the SGM images does not initially suggest that the method can be used for quantification due to the small positive contrast area for all MF66 concentrations tested here. The detection limit with SGM appears to be quite low. For all SPIONs, the vial with the lowest concentration produces a hyperintense rim and is visible on the SGM images. The control vial filled with water is also visible demonstrating that the PCR tube has an effect. However, the vial with the lowest SPION concentration had a clearly increased positive contrast for ferumoxytol and the MF66 nanoparticles. Hence, a detection threshold of at least 0.05 mM (possible lower) can be assumed. For the much weaker VSOP particles, a clear difference between the control vial and the VSOP vial was only visible at an iron concentration of 0.3 mM.

We were unable to obtain good positive contrast images using GRASP for the MF66 nanoparticles. Strong hyperintensity is observed for the ferumoxytol vials containing 1.6 mM, 1.2 mM, 0.8 mM and 0.6 mM. A small hyperintense dipole lobe is visible in the head-direction at two highest concentrations. Apart from that, the contrast in those four vials appear similar (visual inspection of GRSAP image) and unrelated to the SPION concentration which was confirmed with figure 85. At 0.4 mM, hyperintensity within the PCR tube disappears and instead a hyperintense rim is visible. The PCR tube containing 0.2 mM is only marginally more pronounced than the control vial. In comparison to the control PCR tube, 0.4 mM can be seen as the detection limit. However, given the change in contrast leading to hyperintensity of the ferumoxytol solution itself, a detection limit of 0.6 mM is more convincing. Plotting the signal-to-noise ratio measured with ferumoxytol over the iron concentration (figure 85) displays a linear relationship with an r^2 value of 0.9235 which suggests a very good linear correlation.

We achieved IRON images with all four nanoparticles. Fat suppression of centre vial (olive oil) was successful for all SPIONs. In comparison with ferumoxytol and VSOP, the signal intensity of the MF66 nanoparticles was lower and did not correlate with the SPION concentration (figure 85). As the concentration increases, more MF66 nanoparticles will be contained within the PCR tubes. As the particles have a strong magnetic moment, it is likely that at higher concentrations, they start to accumulate very quickly. This will affect the T_2^* measurements but not the negative contrast on GRE images as the tubes overall will still introduce strong inhomogeneities in the main magnetic field. As the particles accumulate, it is likely that the frequency offset changed and we did not have the correct setting to accurately image the off-resonant protons for the vials with higher concentrations. In figure 85 we can see a linear relationship for the MF66 nanoparticles up to 0.4 mM/0.6 mM which is the tipping point. For higher concentrations, the SNR decreases again linearly as the concentration is increased further.

Dixon is a phase-based technique and we have discussed the image appearance above. In comparison to the other positive contrast techniques, Dixon shows a greater tendency to also display the dipole field lobes which is the dominant feature for Dixon across all SPIONs investigated in this study. To assess its capability of iron quantification, we plotted area of the hyperintensely displayed dipole lobes over the iron concentration (figure 85) which gave a linear relationship. However, there are several limitations with that result. For once, lower concentrations display almost no dipole lobes. Secondly, for the MF66 nanoparticles there is a change in contrast appearance from showing the lobes hyperintensely to also displaying the MF66 solution itself when moving towards lower concentrations. In the case of ferumoxytol, the SPION solutions themselves have increased signal intensity for all concentrations but these are not concentration dependent and our results rely on the dipole field area alone. As discussed above, it is likely that for the range of SPION concentrations that we had within our phantom (not considering the VSOP phantom which contained a narrower range), one setting (here: phase difference) is not able to provide the optimal imaging parameter that leads to the optimal contrast for all concentrations. This suggests that our simple implementation of Dixon positive contrast imaging could potentially be used to detect SPIONs but is unlikely to provide reliable results for iron quantification.

7.5.5. Fat Suppression for Positive Contrast Imaging with IRON: SPIR vs Dixon

We investigated the merits of SPIR and Dixon for fat suppression in combination with the IRON technique (figure 86a). The vial containing olive oil was suppressed more successfully with Dixon than with SPIR. To demonstrate that the Dixon fat suppression does not have a

negative effect on signal generation of protons affected by SPIONs, we measured the SNR of all vials for Dixon and SPIR (figure 86b). SNR of the bulk water was determined from the average of four ROIs placed around the centre tube. For seven out of eight vials (i.e. vials 1-7), the SNR of IRON with Dixon was higher than that with SPIR which demonstrates that Dixon achieves a better fat suppression while simultaneously increasing the positive contrast effect of the iron-based nanoparticles. Even though the same ROI was used for the analysis, a limitation is that the ROI had to be placed manually on the hyperintense SPION vials and position variation could have attributed differences in the signal intensity between the two scans. From visual comparison of figure 86a, the only noticeable difference is in the fat suppression. This is confirmed in figure 86c where we show the percentage difference between the SNRs measured with Dixon and SPIR (figure 86b). These findings confirm that Dixon was superior to SPIR and thus the preferred fat suppression method in combination with the IRON sequence. As a chemical-shift based technique, SPIR is affected by susceptibility effects introduced by field inhomogeneities (e.g. SPIONs, PCR tubes etc) in both the B_0 and B_1 fields [351]. These can lead to incomplete fat suppression and also water suppression. Dixon on the other hand is known to be less sensitive to B_0 and B_1 field inhomogeneity [352] which leads to improved SPION signal and superior fat suppression compared to SPIR.

In order to expand the validity of these results, we also compared IRON scans with Dixon and SPIR for other iron-based MR contrast agents (VSOP, MF66-DMSA, MF66-PEG). These are shown in figure 87 and confirm that for all SPIONs, a superior fat suppression was achieved with Dixon while maintaining the hyperintense contrast of the SPION filled vials.

8. Measurement of r_2/r_2^* and r_1 relaxivities in novel iron-oxide nanoparticles

8.1. Introduction

When brought into an applied magnetic field, different materials display different magnetic properties. In chapter 5 the different types of magnetism that molecules and materials can adopt have been described. These are diamagnetism, paramagnetism, ferromagnetism and superparamagnetism. Iron oxides can be synthesised in many forms with different stoechiometric relations between iron and oxygen. They are characterised by a large magnetic moment when brought into an external magnetic field. The two most prominent forms for MRI applications as contrast agents are magnetite and maghemite [224] whose inverse spinel structure and general characteristics are described as well in chapter 5.

8.1.1. Relaxation

Molecules and particles in a fluid diffuse at temperatures above absolute zero. In an aqueous solution of iron oxide nanoparticles, the diffusion correlation time for water is

$$\tau_D = \frac{R^2}{D} \tag{172}$$

with R being the radius of the nanoparticle and D being the diffusion coefficient of water [224]. Because the magnetic moment of the iron oxide nanoparticles is much larger than the nuclear moment of the hydrogen atoms of the surrounding water molecules, magnetic dipole interactions occur [353] which is explained by the outer-sphere relaxation theory [354], [355]. According to that, proton relaxation is based on the diffusion of water molecules in the vicinity of the iron oxide nanoparticles. The nuclear spins of the water protons dephase due to the inhomogeneous magnetic field established by the iron oxide nanoparticles. The relaxation due to the outer sphere theory extends to large distances due to the large size of iron oxide nanoparticles [354]. The magnetic moment of the nanoparticles increases as the external magnetic field is increased. Changing the magnetic moment of the nanoparticles can induce proton relaxation and this is referred to as Curie spin relaxation [356].

When water molecules diffuse in the magnetic field of the iron oxide nanoparticles, the water protons experience a magnetic field difference of $\Delta B_{diff} = -\frac{1}{3}\Delta\chi_m B_0$ with B_0 being the external magnetic field strength and $\Delta\chi_m$ being the difference in magnetic susceptibility between water and the iron oxide nanoparticle [353].

In aqueous solution the magnetic moment of iron oxide nanoparticles is influenced by two different rotation modes, Néel [357] and Brownian [358] relaxation. Néel relaxation is the basis of the iron oxide nanoparticles' superparamagnetic behaviour. A characteristic of iron oxide nanoparticles is that they are smaller than a single magnetic domain. The magnetic moment of each nanoparticle aligns along certain preferred axes which are called easy axes or easy directions. This would mean that the nanoparticles are permanently magnetised even when not exposed to an external magnetic field. However, the magnetisation vector fluctuates between different easy directions which mean the time-averaged magnetisation is equal to zero. This fluctuation is described with a correlation time τ_N and called Néel relaxation. τ_N becomes infinite when an external magnetic field is applied and the magnetic moments align with the external magnetic field.

Néel relaxation describes any rotation of the magnetisation vector within the nanoparticle, whether it is fluctuation between different easy axes or the rotation associated with the alignment with an externally applied magnetic field [357]. The Néel rotation correlation time is given by

$$\tau_N = 10^{-9} e^{(E_c + E_s)/k_b T} \tag{173}$$

E_c is the anisotropy energy of magnetite and E_s is an additional anisotropy energy term that accounts for the fact that in reality iron oxide nanoparticles are not perfect spheres [353]. While Néel relaxation describes the rotation of the magnetisation vector within the nanoparticle, Brownian relaxation is the rotation of the whole nanoparticle which consequently also rotates the magnetisation vector [358]. The Brown rotation correlation time is given by

$$\tau_B = \frac{3V\eta}{k_b T} \tag{174}$$

with V being the volume of the nanoparticle and η is the viscosity of the fluid. The overall rotation correlation time is defined by taking both the Néel and Brown relaxation correlation times into account.

$$\frac{1}{\tau_c} = \frac{1}{\tau_N} + \frac{1}{\tau_B} \tag{175}$$

The Néel contribution to the rotation of the magnetization of a magnetic nanoparticle in a colloidal suspension goes up exponentially as the volume of the nanoparticle increases. For that reason, the Brownian relaxation contribution becomes more dominant for larger nanoparticles [353].

8.1.2. T_2 relaxation

Depending on the size of the iron oxide nanoparticles, different processes dominate the transversal relaxation behaviour in MRI. For small nanoparticles of less than 14 nm in diameter,

the T_2 relaxation is governed by Néel relaxation and diffusion $\frac{1}{\tau} = \frac{1}{\tau_N} + \frac{1}{\tau_D}$. The water diffusion is extremely fast for small nanoparticles which means that the spatial variation of the magnetic field vector is averaged out. Relaxivity is therefore determined by the outer sphere theory. The ratio of the transversal and longitudinal relaxivities (see below) is low in this case [359].

For larger nanoparticles up to a few hundred nanometres in diameter, Néel relaxation becomes negligible and T_2 relaxation is predominantly governed by rapid diffusion $\frac{1}{T_2^{CA}} = a\, f\, \langle \Delta\omega^2 \rangle \tau_D$ with f being the effective volume fraction of nanoparticles in solution which depends on the nanoparticle concentration. The parameter a is a scaling factor which increases for larger particles as motional averaging becomes ineffective. Overall, the outer sphere theory governs the relaxation behaviour of nanoparticles of this size.

Iron oxide nanoparticles that are bigger than a few hundred nanometers but less than a few micrometers fall within the intermediate regime where τ_D^{-1} is of similar order as the change in Larmor frequency ($\Delta\omega$). The behaviour of nanoparticles of this size presents a difficult case because the approximation of motional narrowing is not valid anymore due to the much slower water diffusion. However, the nanoparticles are not big enough to be considered static. Nanoparticles of this size produce a clear and distinct difference in the measurement of T_2 (spin echo) and T_2^* (gradient echo) [353].

For SPIONs that are larger than several micrometers, the static dephasing regime applies. Diffusion does contribute negligibly to the reorientation ($\tau_D^{-1} \ll \Delta\omega$) because the water protons can be considered static. In this case, T_2^{-1} is directly proportional to the change in the Larmor frequency [360]

$$\frac{1}{T_2^{CA}} = a\, f\, \Delta\omega \tag{176}$$

For stationary nanoparticles, the scaling factor a is equal to $2\pi(3\sqrt{3})$ [361]. The same equation is valid for T_2^* when using a gradient echo instead of a spin echo sequence.

8.1.3. Comparing contrast agents – the relaxivity

Contrast agents shorten the relaxation time constants T_1, T_2 and T_2^*. Some contrast agents shorten T_1 and T_2 to the same extend. These are called T_1 agents or positive contrast agents. Others will mainly shorten the transversal relaxation time constant and they are called T_2 agents or negative contrast agents. A way of quantifying the effect a contrast agent has on T_1, T_2 and T_2^* is by measuring its relaxivity. In the case of T_2, the following equation can be defined

$$\frac{1}{T_2} = \frac{1}{T_{2,0}} + r_2[CA] \tag{177}$$

$T_{2,0}$ is the T_2 measured when no contrast agent is in solution, T_2 is the relaxation time constant with contrast agent present. T_2^{-1} is called relaxation rate and [CA] is the contrast agent concentration. The constant of proportionality is the relaxivity which is the slope of the linear function obtained when plotting the relaxation rate with contrast agent over the the concentration of the contrast agent. The relaxivity is usually given in $mM^{-1}s^{-1}$. The relaxivities for T_1 and T_2^* can be defined analogous to the above. Determination of the relaxivity provides a quantity independent of the contrast agent's concentration that allows *in vitro* comparison of its efficiency to increase the respective relaxation rate [353], [356].

8.1.4. The effect of clustering on the relaxivity

The formation of clusters through the aggregation of iron oxide nanoparticles has an effect on the T_1, T_2 and T_2^* relaxivities. Clusters can be loosely or tightly packed. T_2 and T_2^* relaxivities generally increase through agglomeration. In the case of loosely packed clusters this increase is expected to be linear with cluster size. As long as water access to the iron oxide cluster is not limited through aggregation, longitudinal relaxation is expected to remain constant even when the cluster size increases. At the clinical field strength of 3T, T_1 relaxivity is expected to decrease while T_2 and T_2^* relaxivities strongly increase. The latter to a much greater extend than r_2 [356].

8.1.5. Compartmentalisation of iron oxide nanoparticles

Compartmentalisation is another effect, observed in *in vivo* applications of contrast agents, that has an effect on the measured relaxivities. Compartmentalisation refers to the trapping of nanoparticles in a confined space where water exchange is limited. An example is the internalisation by cells where nanoparticles can be trapped in cytoplasmic, subcellular and vesicular (i.e. endosomal and lysosomal) compartments. It was observed that the relaxation time of iron oxide nanoparticles internalised by cells increases well beyond what was measured with the same contrast agent concentration in a control experiment. An increase in the relaxation time results in a decrease of the respective relaxivity. The reason for that is the limited water exchange which ultimately leads to a saturation of the relaxivity. When plotting the relaxation rate over the contrast agent concentration, the obtained graph would be no longer linear but start to plateau.

Water exchange is an important concept when discussing compartmentalisation of MRI contrast agents. In the case of a fast exchange regime, water exchanges very quickly between

compartments, i.e. the water exchange rate is faster than the relaxation rate difference between different biological compartments. The result is that the relaxation behaviour of the contrast agent is as if it was distributed uniformly across the compartments. If the water exchange rate is considerably slower than relaxation rate difference between compartments, the concept of one relaxivity value for the tissue under consideration becomes meaningless. In this slow exchange regime, different compartments relax completely independently and have their separate relaxation times. The most common case however is that water exchange is neither slow nor fast (intermediate exchange regime) and the relaxation behaviour becomes bi-exponential [353], [356].

8.1.6. T_2^* relaxometry

T_2^* relaxometry allows to gain information about microscopic magnetic field inhomogeneities. At the same time, it is desirable to avoid macroscopic field distortions such as those intrinsic to the main magnetic field B_0 and inhomogeneities originating from air-tissue interfaces [141]. Macroscopic susceptibility artefacts lead to an overestimation of R_2^*. Reduction of the echo time and the selection of a high spatial resolution (i.e. small voxel size) minimise the macroscopic effects [362]. By analytically evaluating the background gradient and transverse relaxation it was shown that with the optimisation of three successive slice-refocusing gradients an optimal signal recovery at a particular TE can be achieved [147]. Calculation of the ΔB_0 values can also be used for a post-processing correction algorithm of the T_2^* map. The advantage of this correction is that no additional scan is needed as the ΔB_0values can be extracted from T_2^* weighted multislice data [143]. It has recently been reported that the measurement of the B_0 field to correct for field inhomogeneities to perform R_2^* mapping has been extended to 3D acquisitions. This method also allows for water-fat separation by using a sequence based on the chemical-shift in combination with short echo spacing [363].

8.1.7. Purpose of present work

In this chapter the MRI characterisation (i.e. the T_1, T_2 and T_2^* mapping in order to determine the SPIONs respective relaxivity value) of 23 novel iron-oxide nanoparticles is presented. These nanoparticles were developed by the MultiFun project and synthesised by collaborators from different laboratories. Four commercial samples (FeraSpin XS, FeraSpin XXL, Ferumoxytol and VSOPs) were also included in the study for comparison. The nanoparticles under investigation vary in terms of their core and hydrodynamic diameter, coating material and surface charge.

We first optimised the experimental setup for the MRI characterisation. This consisted of the development and optimisation of the MRI phantom, the selection of the correct receiver coil

setup and the determination of the range of SPION concentrations and number of different concentrations. This was followed by the optimisation of the T_1, T_2 and T_2^* mapping sequences in terms of number of echoes acquired, echo time, repetition time and resolution.

In order to evaluate and optimise the technique used for analysing the MRI data and calculating the relaxivity values, we compared three techniques (1. In-house Matlab algorithm, 2. Free software ImageJ, 3. In-house Excel worksheet and algorithm). This was done with a commercial sample for which a reference relaxivity was available in the literature.

The main purpose of this investigation was the determination of the r_1, r_2 and r_2^* relaxivities of all 24 novel iron-oxide nanoparticles in water as well as the four commercial samples. This study provides the opportunity compare and discuss all three relaxivities (i.e. r_1, r_2 and r_2^*) for a wide range of iron-oxide nanoparticles of different sizes, coating materials and surface charges. Based on these results we selected SPIONs to be characterised in breast and pancreatic cancer cells. We looked at two things in particular, the first being the effect of sonication on the relaxivity of cancer cells incubated with iron-oxide nanoparticles. Furthermore, it has been reported in the literature that R_2 and R_2^* mapping can be used to differentiate between free and cell-bound SPIONs by MRI. Cell-bound SPIONs show higher R_2^* values compared with free SPIONs whereas R_2 is higher for free iron [118]. The second goal of our in-vitro study was therefore to reproduce these results with our novel iron-oxide nanoparticles. Literature reports suggest that this was only done in one type of SPION. We therefore aimed to extend this investigation by comparing five selected SPIONs of different characteristics (size, coating material) to evaluate if the type of SPION has any effect on this behaviour.

8.2. Methods

8.2.1. Superparamagnetic Iron Oxide

We investigated 27 different SPIONs (table 3) regarding their T_1, T_2 and T_2^* contrast characteristics using a 3T clinical MR scanner. Of those 27 SPIONs, four are commercially available (FeraSpin XS, FeraSPin XXL, Ferumoxytol and VSOP) and Ferumoxytol is also a clinically approved MR contrast agent. VSOP is the smallest particle in this study with a hydrodynamic diameter of 9 nm. Ferumoxytol has the smallest core with 3.25 nm. All other SPIONs are novel and were synthesised for use as multifunctionalised nanoparticles for cancer targeting, detection, and treatment [364]. Most SPIONs in this investigation were either coated with dimercaptosuccinic acid (DMSA), polyethylene glycol (PEG) or dextran. The intracellular and *in vivo* characteristics of MR iron-oxide based contrast agents strongly depend on the coating, charge as well as on the hydrodynamic particle size. Therefore, we investigated SPIONs with different hydrodynamic diameters ranging from 9 nm up to 1238 nm. Table 3 summarises all SPIONs investigated in this study and lists their respective characteristics (i.e.

iron oxide core size, hydrodynamic diameter, coating, and surface charge). Anionic SPIONs were selected because they have been shown to have a high affinity for the cell membrane and are their efficiency to be internalised is therefore significantly higher compared to neutral or positively charged SPIONs [365]. DMSA, PEG, and Dextran coating has been proven to be well suited for biomedical applications due to their good stability and low toxicity [366]–[368].

Table 3: Superparamagnetic iron oxide nanoparticles investigated with their core size, hydrodynamic diameter, coating material, surface charge and pH in aqueous solution.

SPION	Particle Size TEM [nm]	Hydro-dynamic Size [nm]	Nature of coating	Surface Charge [mV]	Concen-tration [mg Fe/ml]	pH
ADNH	6	150	Aminodextran	35	5.5	7
ASi	8.5	60	Aminosilane	35	7.5	7
A	35	175	No coating	-10	20	7
A22APS	17.5	98	Aminopropyl-silane (APS)	---	5	---
OD7	7	60	DMSA	-40	13.5	7
OD10	10	60	DMSA	-40	1.9	7
OD15	15	60	DMSA	-40	0.5	7
OD18	18	60	DMSA	-40	2.6	7
OD7-P2	7	?	PEG	Anionic	?	7
OD15-P5	15	95	PEG	Anionic	?	7
OD15-P10	15	103	PEG	Anionic	?	7
OD15-P20	15	110	PEG	Anionic	?	7
FF-NX-PAA	5	97	Polyacrylacid	-37.8	4.19	7
FF-NX-PVP	7	279	PVP	?	0.35	7
F1566	8.5	45	Dextran	-6.5	10	6.8
F1563	10	1235	PEI	-26.5	10	4.1
F1706	11.7	159	Dextran T40	-18	10	7.1
F1780	10	101	DMSA	-44	3.3	?
MF66-DMSA	12	85	DMSA	-47	10	4.9
MF66-PEG	12	111.3	PEG	-28.3	5.3	7.4
MF66-N6L	12	140.8	DMSA	-45.3	2.4	7.5
MF71	12	203	CM-Dextran	-35	7	5.1
MF74	12	90	DMSA	-49	10.4	5.6
FeraSpin XS	---	18	Carboxy Dextran	-24	0.56	7

FeraSpin XXL	---	65	Dextran	-24	0.56	7
Ferumoxytol	3.25	23.6	PSC	-43.2	30	7
VSOP	5	9	Citrate	Anionic	---	7

8.2.2. Phantom preparation

We prepared five different concentration of each SPION by two-fold serial dilution (1.2 mM, 0.6 mM, 0.3 mM, 0.15 mM and 0.075 mM). The dilutions were prepared to a volume of 1.5 ml and contained in 2 ml non-conical Eppendorf tubes. The exact concentration of iron was determined by inductively coupled plasma mass spectrometry (ICP-MS). All contrast agents were suspended in an ultrasound bath for 15 minutes shortly before the MR measurements. This ensured a homogenous distribution of the iron oxide particles and to avoid large agglomerations or sedimentation.

We used a 140 mm crystallizing dish (Technische Glasswerke Ilmenau GmbH, Ilmenau, Germany) as a water phantom (figure 88). A 5 mm thick custom-made Perspex disk was used as tube holder. The Eppendorf tubes were immersed in the water phantom for all imaging experiments. A slice in the middle of the water volume was selected for all scans to minimise B_0 field inhomogeneity effects.

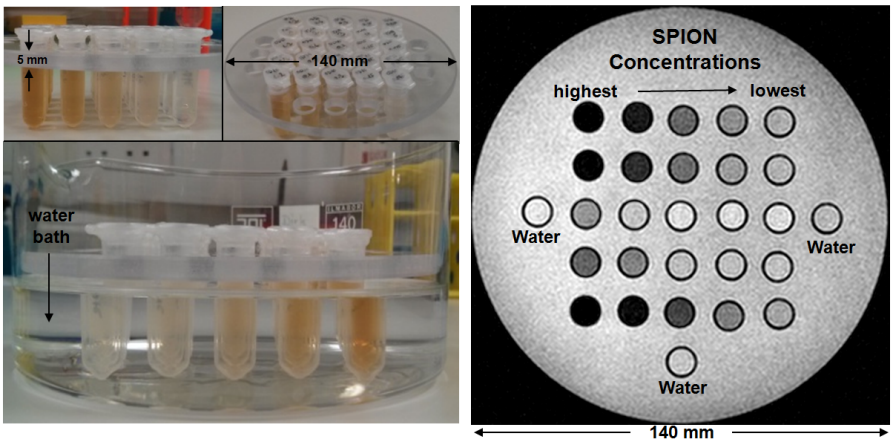

Figure 88: MRI water phantom showing five SPIONs being measured at the same time each of them with five different concentrations.

8.2.3. Cell Culture and Cell Labelling

MDA-MB-231 cells (ATCC, Wesel, Germany) were maintained in Dulbecco's modified Eagle's medium (DMEM) 25 mM glucose, 1 mM sodium pyruvate and 44 mM sodium bicarbonate, supplemented with 10% heat-inactivated fetal bovine serum (FBS), 2 mM L-

Glutamine, 100 units/mL penicillin, and 100 µg/mL streptomycin. All reagents were purchased from Sigma, Poole, United Kingdom. Cultures were seeded into flasks containing supplemented medium and maintained at 37°C in a humidified atmosphere of 5% CO_2 and 95% air. All cells used in this study were used at a low passage number (<13). For assays, MDA-MB-231 cells were sub-cultured in 6-well plates at a seeding density of 120000 cells per well. The following day, sterile stock solutions of the SPIONs were sonicated and serial dilutions were prepared in complete medium without FBS to prevent nanoparticle aggregation. Cells were then incubated for 24 h with 5 different concentrations of the SPIONs (1.2, 0.6, 0.3, 0.15, 0.075 and 0.038 mM_{Fe}). After the incubations, cells were gently but thoroughly washed with PBS, detached and resuspended in 750 µl DMEM, transferred to polypropylene tubes and mixed with 750 µl of 5% polyvinyl alcohol (PVA; Sigma, Poole, United Kingdom) to increase viscosity and allow for MR imaging of a homogeneous distribution of cells inside the tubes. PVA is nontoxic and is currently used as eye lubricant. It has been shown to be suitable for various biomedical applications [369]–[374]. Sterile stock solutions of the SPIONs were sonicated again and new serial dilutions of the SPIONs (750 µl at the aforementioned concentrations: 1.2, 0.6, 0.3, 0.15, 0.075 and 0.038 mM Fe) were freshly prepared in complete medium without FBS, mixed with 750 µl of 5% PVA and placed in a phantom alongside the cell suspensions for MRI.

8.2.4. MR Imaging of Phantom

MR imaging was performed with a two element SENSE flex coil M on a clinical 3T Philips Achieva MRI scanner (Philips Healthcare, Best, The Netherlands). T_1 maps were acquired by using a 2D sequence that employs two non-selective inversion pulses ranging from 20 to 2000 ms, followed by eight segmented readouts for eight individual images [99]. The two imaging trains result in a set of 16 images per slice with increasing inversion times (3.2 repetition time [TR], 1.6 ms time to echo [TE], 10° flip angle, FOV 200x200 mm^2, acquisition matrix 200x179, in-plane resolution 1x1.12 mm^2, 3 mm slice thickness = 3 mm). T_2 maps were obtained with a 2D multi-spin-echo sequence. For each spin-echo, the full k-space data was collected. Five images were reconstructed at five different echo times to provide equidistant samples along the decay curve of transverse magnetisation for T_2 determination (725 ms TR, 10 ms echo spacing [TE], 90° flip angle, FOV 200x200 mm^2, acquisition matrix 200x200, 3 mm slice thickness). T_2^* maps were acquired with a 2D multi-gradient-echo sequence. We sampled the full k-space for each gradient-echo and acquired five echoes for T_2^* determination (11 ms TR, 1.95 ms to first echo, 1.7 ms interval between subsequent echoes, 25° flip angle, FOV 200x200 mm^2, acquisition matrix 200x200, 3 mm slice thickness).

The Eppendorf tubes were placed in the water phantom so they were perpendicular to the main magnetic field (B_0). The slice orientation for the T_1, T_2 and T_2^* mapping sequences was chosen to be coronal because in axial acquisitions, corrections for through-slice field variations would need to be made. Whether in plane corrections for coronal and sagittal acquisitions are necessary is unclear [363]. For this reason we acquired coronal slices for the determination of T_2^* to avoid macroscopic B_0 inhomogeneities in the slice direction which could corrupt our measurements. Regions of interest (ROI, mean size 14.29 ± 1.71 mm^2) were centred over the coronal images of the Eppendorf tubes to obtain the signal intensity (SI) for each ROI. The SI was plotted over the echo spacing and a monoexponential general reduced gradient algorithm (Microsoft Excel, Microsoft, Redmond, Washington, U.S.) was used to determine the T_2 and T_2^* values for each SPION concentration. These transverse relaxation times were converted to relaxation rates R_2 and R_2^* and plotted over their respective concentrations for each SPION. To assess the homogenous distribution of the iron oxide particles in solution and of the iron oxide incubated cells suspended in polyvinyl alcohol (PVA) we visually inspected the phantom before and after the scan session to ensure that there were no accumulations of SPIONs or SPION-loaded cells in our Eppendorf tubes.

8.2.5. Inductively Coupled Plasma Mass Spectrometry (ICP-MS)

Iron concentrations of all the previously MRI scanned serial dilutions of SPIONs and cell suspensions were determined by ICP-MS. Briefly, samples were digested in 70% nitric acid overnight at room temperature, followed by dilution in deionised water. A standard curve was acquired with each sample set for iron concentration determination.

8.3. Results

8.3.1. Phantom development and optimisation for relaxivity measurements

The first step for the accurate measurement of relaxivities was the development of a suitable MRI phantom. We used 0.5 ml Eppendorf tubes with five different SPION concentration that were arranged in a circle around a mass of blu-tec putty and pressed into the putty to stay in place (figure 89). The blu-tec putty was enclosing the Eppendorf tubes from one side which had an effect on the effective magnetic field in the vials and hence on the relaxivity measurements.

Figure 89: First MRI phantom. 0.5 ml Eppendorf tubes arranged around blu-tec putty. a: Several phantoms, one for each SPION. b: Four phantoms in a flex receiver coil. c: Eight phantoms in two flex receiver coils.

The next phantom was custom-built from two Eppendorf tube racks (for 0.5 ml tubes) made of plastic (figure 90). It allowed for easy exchange of the tubes and we produced prototypes in various sizes and shapes (squared, circular). The problem with this setup was the small volume of the Eppendorf tubes which made it difficult to accurately prepare the different SPION concentrations. The small cross section of the Eppendorf tubes meant that we had difficulties drawing a region of interest during data analysis by leaving sufficient space to the tube wall. The major limitation was the difficulty to transform this design to a water phantom.

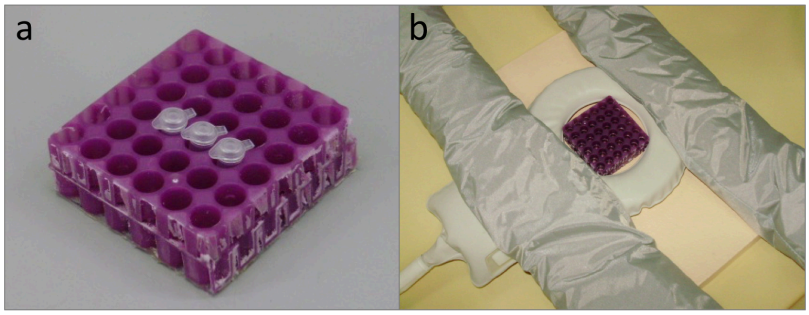

Figure 90: Second MRI phantom custom built from Eppendorf tube racks. a: Example of a squared phantom. b: Phantom in a flex coil setup.

In order to achieve a more homogenous magnetic field within the measured samples, a water phantom was considered favourable. To overcome the limitations of the 0.5 ml Eppendorf tubes, they were replaced with 1.5 ml Eppendorf tubes. A circular tube holder was made from cork. The holder had holes drilled into it that would hold the Eppendorf tubes. The cork holder with sample tubes could stand in a 140 mm crystalizing dish that could be filled with water (figure 91). Sample tubes were arranged in a circle with enough distance between the edge of the phantom (air/water interface) and each other to minimise field interferences. During longer measurements the cork tube holder would start to soak up the water and increase in size which resulted in problems with phantom dissemble and sample exchanges.

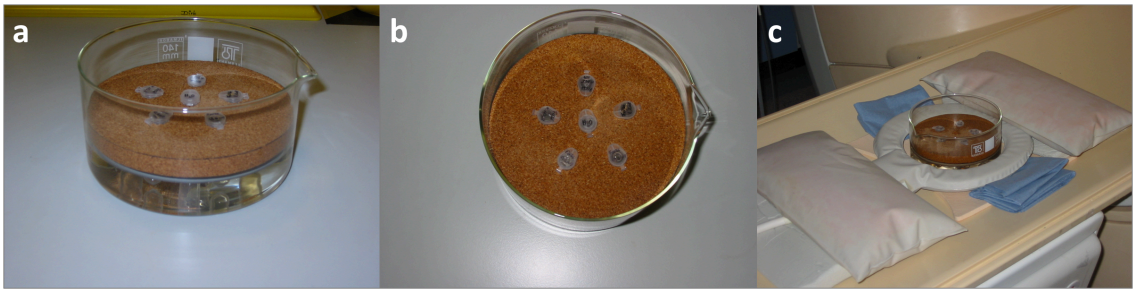

Figure 91: Third MRI phantom (water phantom). Tube holder made from cork with holes to hold 1.5 ml Eppendorf tubes. a: Water phantom from the side. Cork holder thickness was 1 cm. b: Phantom from the top showing circular arrangement of sample tubes. c: Water phantom shown in measurement setup with a flex coil.

As a result, we replaced the cork tube holder with one made from Perspex (figure 92). In order to stay in place, the Eppendorf tubes were sealed with Parafilm that stopped the tubes from moving. We developed two Perspex holders, one with a circular arrangement that could hold up to six sample tubes for a single measurement and another one designed to measure several SPIONs at once with a total of 37 holes as sample holders (figure 88).

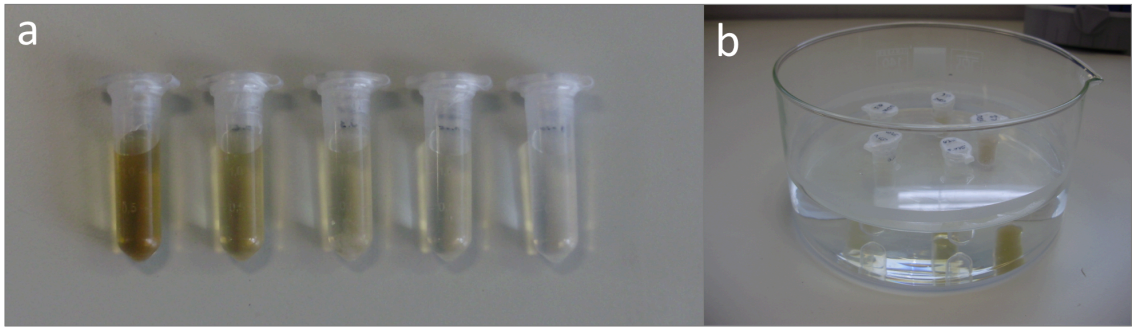

Figure 92: Final water phantom using a Perspec tube holder. A: 1.5 cm Eppendorf tubes with SPIONs of different Fe concentrations. The top is sealed with Parafilm.

In order to assess the homogeneity in the main magnetic field within the phantom (figure 93a) a B_0 field map (figure 93c) was acquired. A B_0 field map represents the phase difference of two images at different echo times acquired with a gradient-echo sequence (multishot TFE, 7.4 ms TR, 3.8 ms TE, 25° flip angle, FOV 200x200 mm^2, acquisition matrix 400x400, 3 mm slice thickness). It depends on the phase evolution $\Delta\Theta$ over ΔTE under the local magnetic field and can be calculated with $\Delta B_0(x,y,z) = \frac{1}{2\pi\gamma\Delta TE}\,\Delta\Theta(x,y,z)$. By extracting the phase evolution from the difference of two images at different echo times, effects common to both images are eliminated and represent the field inhomogeneity [375], [376]. We have defined areas within the phantom for comparison that comprise a collection of Eppendorf tubes (phantom positions) as shown in figure 93b. The B_0 field susceptibility in the core9 area lies between -26.06 Hz and -

8.67 Hz, the core16 area is ranges from -6.78 Hz to 41.11 Hz, and the core25 area which is core9 and core16 combined therefore contains B_0 field susceptibility values from -26.06 Hz up to 41.11 Hz. The averages of the outerHEAD and outerTOE area are 76.03 $\pm$ 3.28 Hz and 90.12 $\pm$ 3.05 Hz, respectively. Both averages are higher than the highest phase value from the core25 area which is 41.11 $\pm$ 12.10 Hz. The average phase value of the outerLEFT and outerRIGHT areas are 13.62 $\pm$ 1.98 Hz and 23.33 $\pm$ 2.14 Hz, respectively. These are similar to the phase values of the core25 area. B_0 field susceptibility measurements directly at the edge of the phantom close to the water/air interface for the head, toe, left, and right positions were 224.43 $\pm$ 25.38 Hz, 261.97 $\pm$ 28.90 Hz, 34.61 $\pm$ 11.38 Hz, and 47.75 $\pm$ 12.91 Hz, respectively.

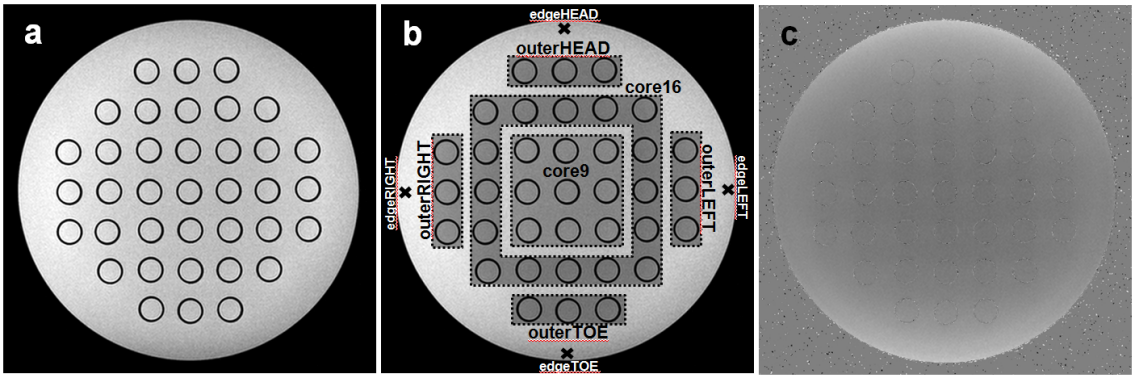

Figure 93: Assessment of water phantom for B_0 homogeneity. a: 2D gradient-echo image displaying the water phantom with 37 Eppendorf tubes filled with tap water. b: Areas defined in the phantom in order to compare phase values and assess B_0 homogeneity. c: B_0 field map used to assess the homogeneity of the main magnetic field inside the water phantom.

8.3.2. MRI sequence optimisation

The T_1 mapping sequence had been optimised by previous lab members and a detailed sequence description is available in the literature [99]. The sequence had to be used in combination with a patch and required a heart rate simulator as it was initially developed for cardiovascular imaging. We adapted the field of view to our phantom size. No further optimisation was required.

For T_2 and T_2^* mapping the literature suggests to treat even and odd echoes separately in order to avoid phase influences that could impact the measurement [143]. In order to evaluate this effect on our measurements, we changed our mapping sequences to allow an echo train with 20 echoes. This results in 10 echoes that can be used for the relaxivity calculations for either even or odd echoes. For the turbo spin echo sequence (T_2), the time to first echo, echo spacing and

repetition time were set to shortest. For the turbo field echo sequence (T_2^*), the repetition time was set to 420 ms while the time to first echo and echo spacing were set to shortest.

T_2 mapping parameters: Multishot TSE (20 echoes), TSE factor = 20, TE1 = 16 ms, echo spacing = 3.9 ms TR = 786 ms, slice thickness = 6 mm.

T_2^* mapping parameters: Multishot TFE (20 echoes), TFE factor = 1, TE1 = 2.4 ms, echo spacing = 1.8 ms, TR = 420 ms, FA = 25.

We measured the r_2 and r_2^* relaxivities with above described sequences in three SPIONs. Two novel SPIONs, i.e. OD7-P2 and MF66-PEG, and one commercial sample (Ferumoxytol). The results are summarised in figure 94 presented as a bar diagram for easy comparison. The second graph shows the percentage difference of the above sequence using only even or odd echoes compared to using all echoes.

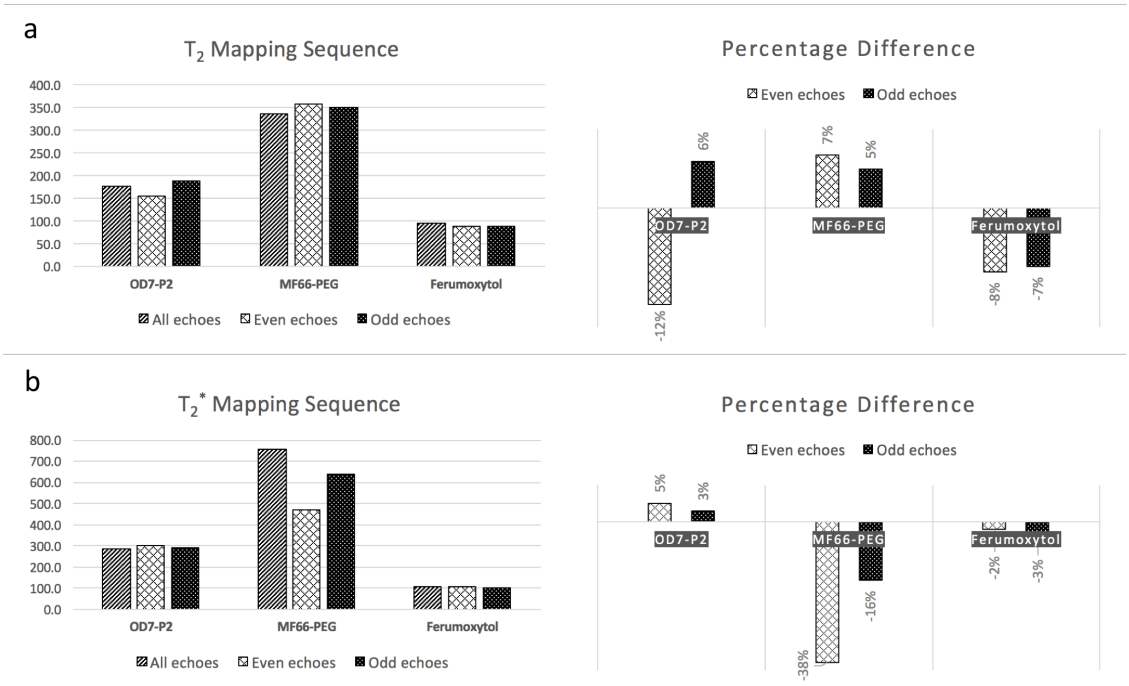

Figure 94: Comparison of even and odd echoes for relaxivity determination. The comparison was conducted for three SPIONs, OD7-P2, MF66-PEG and Ferumoxytol. The second graph shows the percentage difference of using only even or odd echoes compared to using all echoes of the echo train. a: Spin echo sequence for T_2 mapping. b: Gradient echo sequence for T_2^* mapping.

According to figure 94, the biggest variation in percentage difference is shown for the T_2^* mapping result of MF66-PEG where the relaxivity measured with only even or odd echoes is 38% and 16% lower compared to when using all echoes, respectively. For all other SPIONs tested, the percentage difference between considering only even or odd echoes compared with using all echoes was between 2% and 12%. We concluded that the effective impact on our measurements when using all echoes was low enough to consider all echoes in future measurements.

8.3.3. Optimisation of data analysis

We had three different methods available to us to analyse relaxation time mapping data. For one commercial particle (VSOP) all three methods were tested and compared. Literature values for the relaxivities of VSOP at 3T was available.

8.3.3.1. Matlab algorithm

Two Matlab applications were available in the department, one for the analysis of T_1 mapping data and one for T_2 mapping data. The application reads either the PAR or REC file recorded during data acquisition. The file formats of PAR or REC are favourable for image analysis applications over Dicom and can be read into our Matlab application using a specific read algorithm.

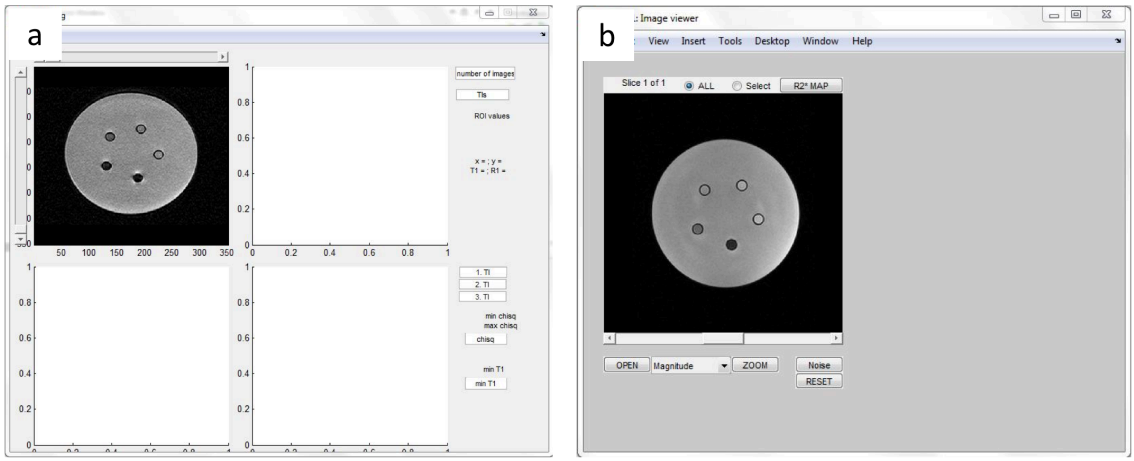

Figure 95: Graphical user interfaces for T_1 mapping data (a) and T_2 mapping data (b).

The Matlab application opens with a graphical user interface (figure 95). Scroll bars allow to scroll through slices (vertical) and echoes/images (horizontal) of the loaded dataset. The application allows the calculation of a T_1 or T_2 map (figure 96). Drawing a ROI on the T_1/T_2 map provides the user with the average relaxation rate (R_1 or R_2).

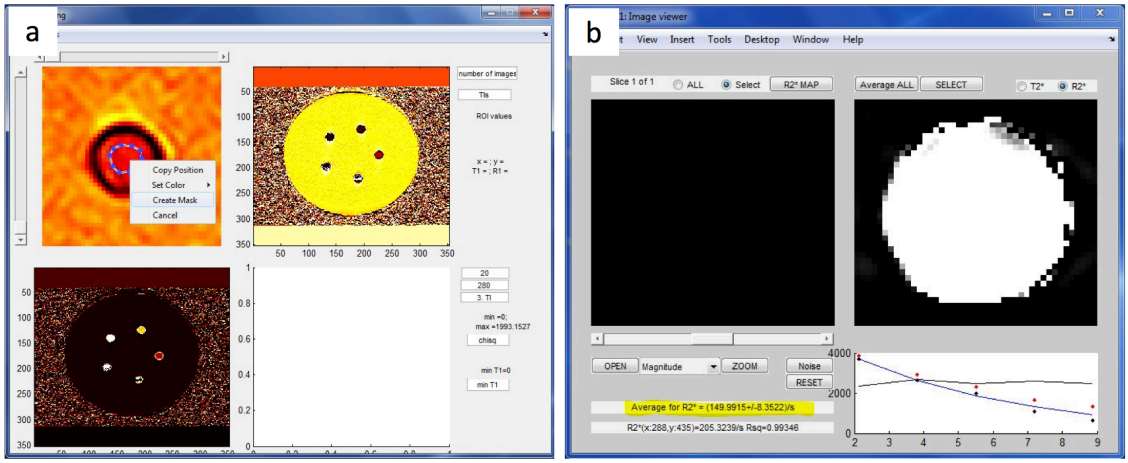

Figure 96: Graphical user interfaces for T_1 mapping data (a) and T_2 mapping data (b).

8.3.3.2. ImageJ software

ImageJ is an image analysis software tool freely available for download. Several add-ons are available to extent the basic functionality of the software package. Dicom images can be loaded in the software and ROIs can be drawn. A specific add-on was installed and used to for the calculation of R_1 and R_2 maps. ImageJ requires the user to input time delays between echoes (images) as well as a cut off value.

8.3.3.3. Osirix and Excel worksheet

Instead of a Matlab algorithm, the relaxation rates can also be calculated using an MS Excel spreadsheet. Both templates (T_1 mapping, T_2 mapping) are available in the appendix of this thesis. We first used Osirix to read in the Dicom files. ROIs were drawn and the signal intensities from all relevant vials were exported. The signal intensities were imported into Excel.

The signal intensities from the T_2 and T_2^* mapping sequences provided by Osirix for each vial should decrease as the echo number increases. Should this not be the case (outliers), the operator can choose to disregard a value. The decrease of signal intensity with increasing echo number is described using an exponential equation from which the relaxation rate can be calculated (figure 97).

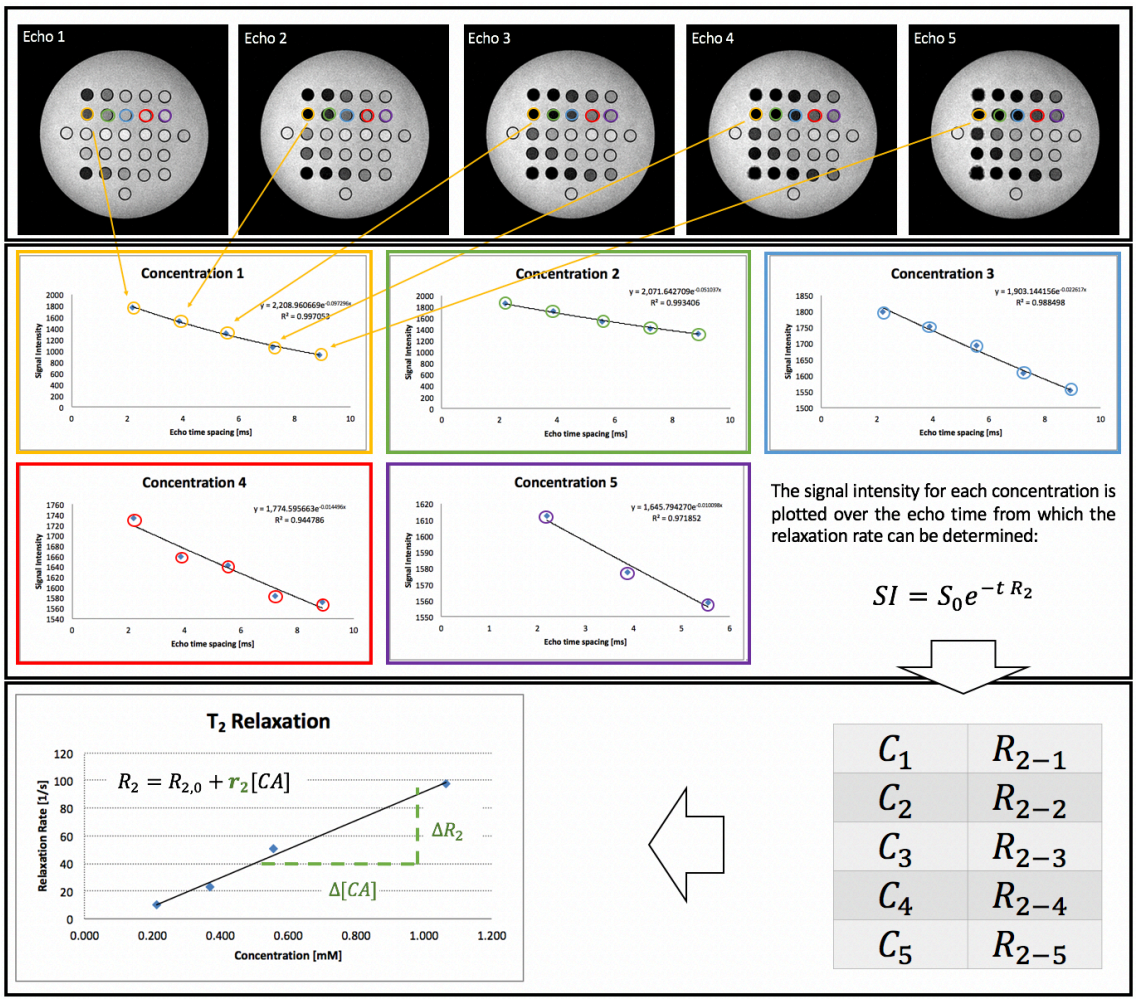

Figure 97: Summary of manual data analysis of $T_2^{(*)}$ data.

The T_1 mapping data is acquired with a sequence of two trains of 8 acquisitions. The echo times are chosen so that the two trains are interleaved. Therefore, the images need to be sorted in the correct order upon loading into Excel.

We used a Leven-Marquadt algorithm to model $M_z(t) = M_0^* - (M_0 + M_0^*)e^{-t/T_1^*}$ to the signal intensity data for each vial. The data is modelled by minimising the sum of squared differences between the measured and predicted signal intensity by changing M_0, M_0^* and R_1^*. From that, we receive a value for the effective relaxation rate R_1^*, which can be converted to R_1 with $T_1 = T_1^* \left(\frac{M_0 + M_0^*}{M_0^*} - 1\right)$ [99]. The analysis has been summarised in figure 98.

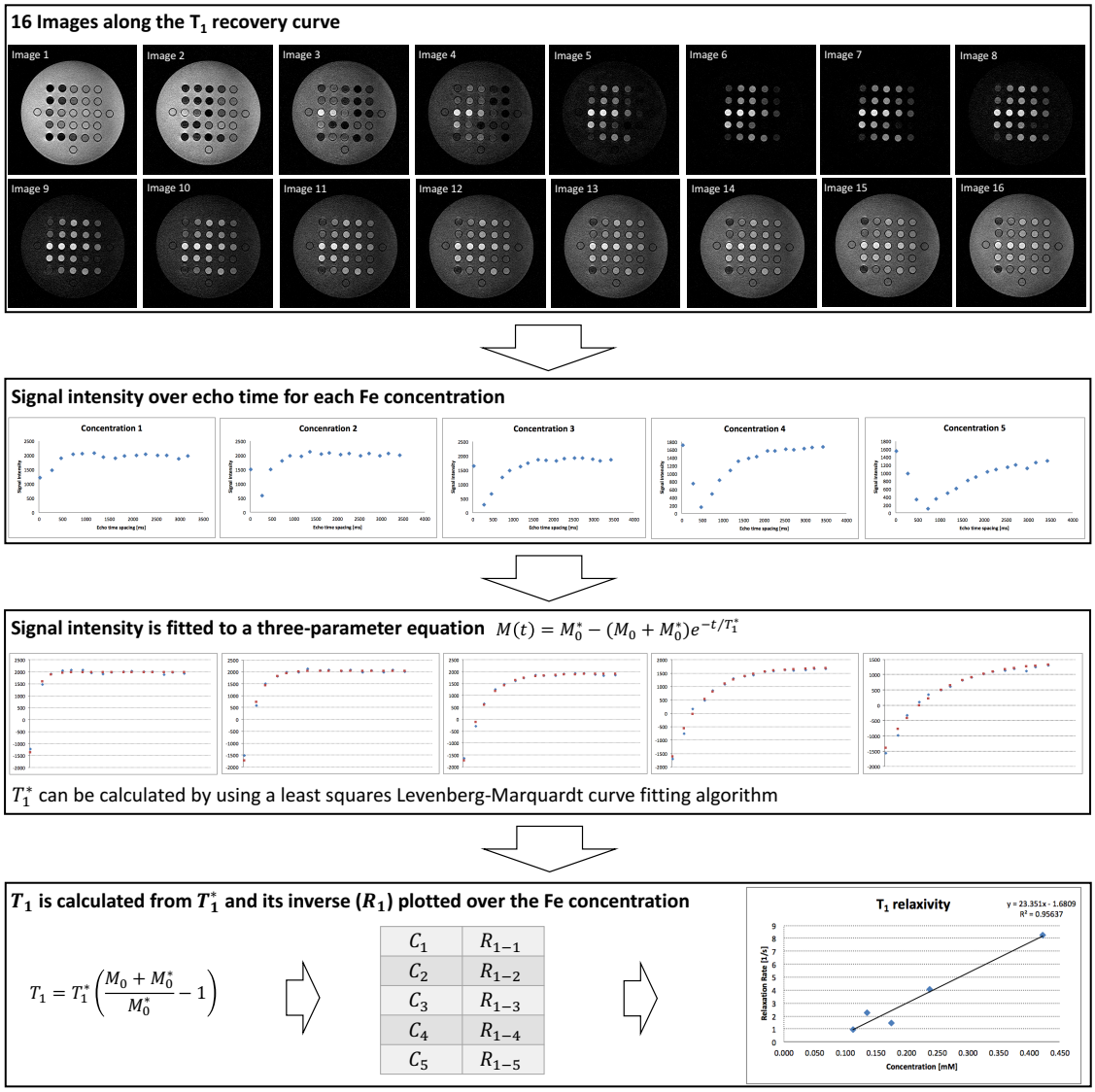

Figure 98: Summary of manual data analysis of T_1 data.

8.3.3.4. Comparison of analysis techniques

The relaxation rates obtained from the different analysis techniques have been plotted over the SPION concentrations (figure 99). This comparison shows that we are getting a very good correlation for all plots. The same set of mapping imaging data was used for all three analysis techniques and any differences in relaxivity are due to the different technique used.

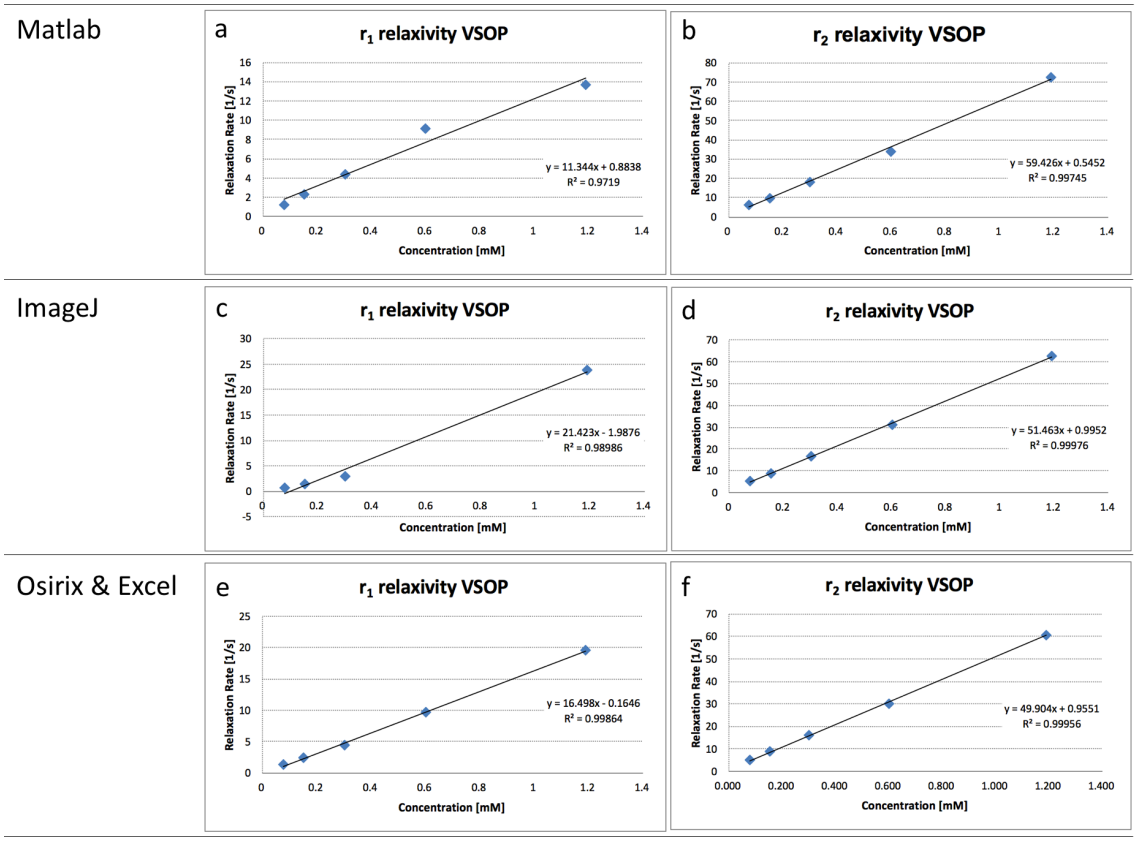

Figure 99: Comparison of methods for calculating the relaxation rates used for relaxivity determination. a: Matlab algorithm (r_1). b: Matlab algorithm (r_2). c: ImageJ add-on (r_1) – The data point for the 2nd highest Fe concentration was omitted (outlier). Only four data points were used for this relaxivity which can impact robustness of the result. d: ImageJ add-on (r_2). e: Osirix and MS Excel (r_1). f: Osirix and MS Excel (r_2).

The preferred data analysis technique for us was the combination of Osirix and MS Excel. The Matlab application might be accurate at times but we also had occasions where it failed to record a value or was not able to calculate a relaxivity map. The handling of ImageJ, especially the drawing of ROIs, was cumbersome and not as straight forward to use.

Table 4: VSOP relaxivity values calculated with three different techniques, a Matlab application, ImageJ and Osirix in combination with MS Excel.

	$\mathbf{r_1}$ $[\mathrm{mM^{-1}s^{-1}}]$	$\mathbf{r_2}$ $[\mathrm{mM^{-1}s^{-1}}]$
Matlab	11.3	59.4
ImageJ	21.4	51.5
Osirix & Excel	16.5	49.9

Table 4 shows a wide range of values for measuring the same relaxivities with different techniques. As the ROIs were drawn manually for each technique, this is likely to account for the discrepancies. To overcome ROI differences, we calculated the average for r_1 and r_2 from the values in table 4 as 16.4 $mM^{-1}s^{-1}$ and 53.6 $mM^{-1}s^{-1}$, respectively. The linear plots (figure 99) of relaxation rate over SPION concentration had an R^2 of more than 0.97 for all three techniques (figure 99c only used 4 data points due to an outlier) indicating good precision. The r_1 and r_2 values were summarised in table 4. The literature reports 20.1 $mM^{-1}s^{-1}$ and 37.1 $mM^{-1}s^{-1}$ for the longitudinal and transverse relaxivities of VSOP at 0.94 T, respectively [377]. Reference values at 3 T were not available in the literature. With increasing magnetic field strength, r_1 decreases and r_2 increases [378]. Comparing the average values (at 3 T) with the literature values at 0.94 T shows that the measured values are within the expected range according to the literature. The advantage of the manual Excel method was that we had full control over the analysis, could select outliers if necessary and had confidence in the accuracy which is why we selected that method for all future measurements.

8.3.4. Relaxivities in water

The measured relaxivities (r_1, r_2 and r_2^*) of SPIONs investigated in this study are summarised in table 5. The longitudinal relaxivities vary from below 1 to 17.5 $mM^{-1}s^{-1}$. Transverse relaxivities are significantly larger and in most cases are of the order of several hundreds. For all SPIONs, r_2^* is larger than r_2 relaxivity. This is expected as T_2^* should always be shorter than T_2 because of the lack of a refocusing RF pulse in gradient echo sequences.

Table 5: Summary of longitudinal and transverse relaxivities in aqueous solution of a wide range of SPIONs investigated in this study. Commercial particles are marked with an asterix (*).

SPION	$\mathbf{r_1}$ $[mM^{-1}s^{-1}]$	$\mathbf{r_2}$ $[mM^{-1}s^{-1}]$	$\mathbf{r_2^*}$ $[mM^{-1}s^{-1}]$
ADNH	8.0	289.9	929.2
ASi	11.1	118.0	272.0
A	1.3	340.5	6207.2
A22APS	0.01	15.1	77.3
OD7	17.5	375.0	270.8
OD10	5.6	63.0	144.7
OD15	9.0	142.3	508.2

OD18	7.8	282.6	518.4
OD7-P2	6.84	232.3	297.5
OD15-P5	6.0	246.8	302.1
OD15-P10	2.7	109.6	317.5
OD15-P20	8.2	510.1	794.0
FF-NX-PAA	5.0	40.5	49.7
FF-NX-PVP	0.7	---	---
F1566	14.8	63.0	88.7
F1563	5.6	150	861.9
F1706	3.1	145.1	289.2
F1780	6.7	275.2	370.2
MF66-DMSA	2.4	242.5	390.1
MF66-PEG	7.72	306.7	1082.2
MF66-N6L	0.18	7.5	68.0
MF71	1.4	110	287.8
MF74	0.9	98.8	264.0
FeraSpin XS*	9.0	58.0	75.9
FeraSpin XXL*	5.8	130.0	502.8
Ferumoxytol*	11.8	90.8	103.7
VSOP*	13.0	49.7	51.5

For comparison, we have included four commercial particles that are displayed at the bottom of table 5 and marked with an asterix (*). For better illustration, the measured relaxivity values have been summarised in the below bar diagrams (figure 100).

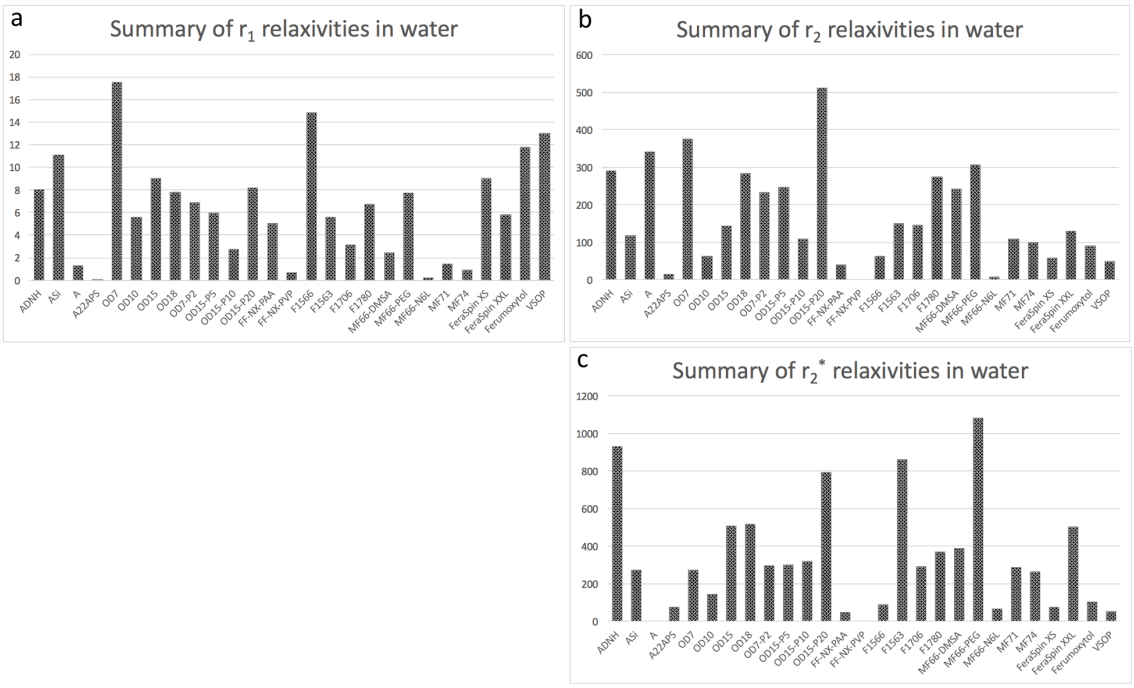

Figure 100: Comparison of longitudinal (a) and transversal (b and c) relaxivities in aqueous solution for a variety of SPIONs. The r_2^* relaxivity of particle A has been excluded for scaling reasons of the ordinate axis in graph c.

From figure 100 it is obvious that both transversal relaxivities generally follow a similar pattern, i.e. a particle that displays a high r_2 relaxivity also has a high r_2^* relaxivity compared to the other particles investigated. The r_2^* relaxivity of particle A has been excluded in figure 100c due to scaling reasons of the ordinate axis. The commercial samples generally have a lower transverse relaxivity compared to the other novel particles. This is not the case for the longitudinal relaxivities where the commercial samples show a stronger r_1 effect.

8.3.5. Relaxivities in cells

A selection of SPIONs was incubated in breast (MDA-MB-231) and pancreatic (PANC-1) cancer cells. *In vitro* measurements in living cells contain cell media. To assess the influence of cell media on the relaxivity measurements we prepared SPION concentrations in cell media and measured r_1, r_2 and r_2^* (table 6).

Table 6: Transverse relaxivities (r_1, r_2 and r_2^*) of selected SPIONs (different coatings, sizes and charges) measured in cell media and polyvinyl alcohol.

SPION	$\mathbf{r_1}$ $[\mathrm{mM^{-1}s^{-1}}]$	$\mathbf{r_2}$ $[\mathrm{mM^{-1}s^{-1}}]$	$\mathbf{r_2^*}$ $[\mathrm{mM^{-1}s^{-1}}]$

A22APS	1.4	93.8	4122.8
OD10	1.0	40.1	605.3
OD15	1.1	47.3	1187.5
OD18	2.0	217.6	5874.3
F1563	3.8	187.2	4770.7
F1706	1.5	369.0	407.2
F1780	3.2	254.5	1348.1
MF66-DMSA	4.0	121.9	2084.5
MF66-PEG	0.5	8.9	913.1
MF71	15.0	1184.9	6705.6
MF74	1.2	77.7	1040.0
Ferumoxytol	23.4	151.2	170.7

From table 6 it is obvious that the order of magnitude of r_1 and r_2 measurements is similar to the results in water (table 5). The r_2^* measurements however are several orders of magnitude larger. To allow a better comparison, figure 101 compares the relaxivity measurements in water and cell media.

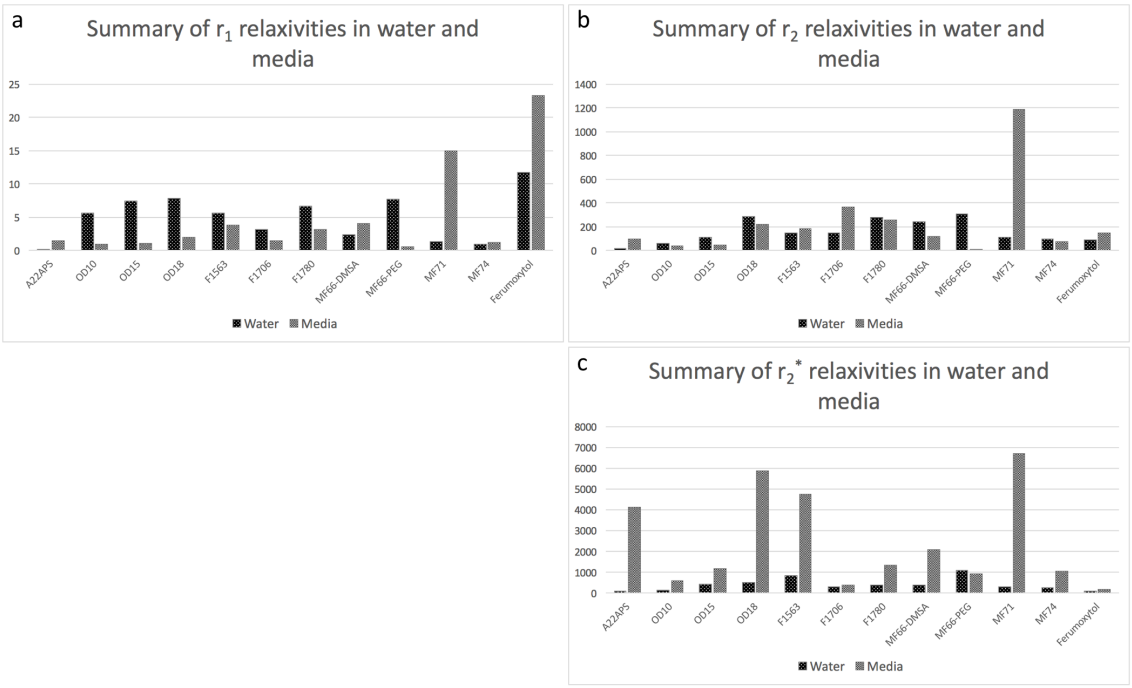

Figure 101: Comparison of longitudinal (a) and transversal (b and c) relaxivities in water and cell media for a variety of SPIONs.

Figure 101a shows that there is no general trend for the longitudinal relaxivity. For some particles r_1 decreases in cell media compared to the measurement in water and for other it increases. Figure 101b and c show a different situation for the transverse relaxation. Except for

MF66-PEG and MF71, the r_2 relaxivity in cell media and water are in good agreement, i.e. the same order of magnitude. For the r_2^* relaxivity, the cell media measurement is significantly larger than the one in water. The only exception to that is MF66-PEG.

Table 7: Transverse relaxivities (r_1, r_2 and r_2^*) of selected SPIONs (different coatings, sizes and charges) measured after incubation in cancer cells in cell media and polyvinyl alcohol.

	Breast Cancer Cells			**Pancreatic Cancer Cells**		
SPION	$\mathbf{r_1}$ $[mM^{-1}s^{-1}]$	$\mathbf{r_2}$ $[mM^{-1}s^{-1}]$	$\mathbf{r_2^*}$ $[mM^{-1}s^{-1}]$	$\mathbf{r_1}$ $[mM^{-1}s^{-1}]$	$\mathbf{r_2}$ $[mM^{-1}s^{-1}]$	$\mathbf{r_2^*}$ $[mM^{-1}s^{-1}]$
A22APS	2.2	156.4	6330.3	1.4	472.2	3643.3
OD10	1.0	28.6	3392.9	2.0	17.5	157.2
OD15	1.7	---	1583.5	1.6	65.3	1929.4
OD18	1.4	116.2	931.7	1.5	114.8	3397.4
F1563	---	251.6	8222.0	0.7	29.8	2733.6
F1706	9.1	21.9	160.6	---	---	---
F1780	35795	153.7	8174.7	---	---	---
MF66-DMSA	2.7	185.8	3414.9	---	---	---
MF66-PEG	0.5	138.8	1157.8	---	---	---
MF74	1.3	42.3	1081.9	---	---	---
Ferumoxytol	0.4	5.1	95.0	---	---	---

The relaxivity measurements in living breast and pancreatic cancer cells are summarised in table 7. To allow for better comparison of the relaxivities presented in table 7, the results were summarised in figure 102. We show three bar diagrams for r_1, r_2 and r_2^* where we compare relaxivities measured in cell media and the two cancer cell lines.

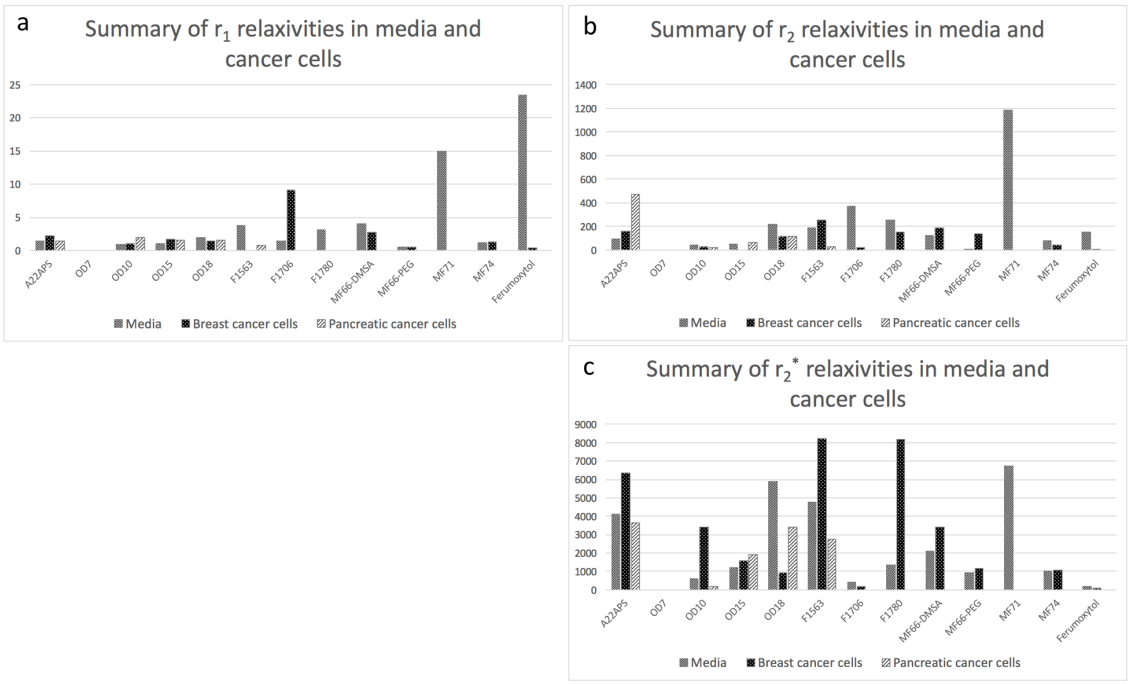

Figure 102: Comparison of longitudinal (a) and transversal (b and c) relaxivities in cell media, incubated in MB-MDA-231 breast cancer cells and PANC-1 pancreatic cancer cells for a variety of SPIONs.

Particle F1706 stands out as displaying a strong longitudinal relaxivity when incubated in cancer cells (figure 102a). The r_2 values of cell incubated particles are generally lower than those particles measured in cell media or water. Figure 102c shows that the r_2^* values of particles incubated in MD-MBE-231 cancer cells increases compared to measurements in media.

8.3.6. Effect of cell sonication on relaxivity measurements

Sonication of living cells in an ultrasound bath results in cell death. To determine whether relaxivity is the same in living and death cells, cancer cells incubated with nine different SPIONs was sonicated and their relaxivity measured again. All cancer cells were thoroughly washed before any imaging experiment commenced to ensure all SPIONs we detect with MRI are either internalised by the cells or stably bound to the surface of the cells. Results are summarised in table 8.

Table 8: Longitudinal and transversal relaxivities of a selection of nine SPIONs measured after incubation in cancer cells (living) and then again after sonicating the SPION-incubated cells for 10 min in an ultrasound bath. For two particles, marked with an asterix (*), not all relaxivities could be determined.

	$\mathbf{r_1}$ $[\mathrm{mM^{-1}s^{-1}}]$		$\mathbf{r_2}$ $[\mathrm{mM^{-1}s^{-1}}]$	
SPION	**Before**	**After**	**Before**	**After**
A22APS	2.2	2.3	156.4	194.5
OD10 (BCC)	1.0	7.7	28.6	300.1
OD10 (PCC)	2.0	1.5	17.5	105.5
OD15 (BCC)*	1.7	2.5	---	---
OD15 (PCC)*	---	---	65.3	364.7
OD18	1.4	6.1	116.2	167.6
F1563	0.7	4.9	29.8	1139.1
F1780	3.6	2.8	153.7	81.7
F1706*	9.1	2.0	---	---
MF66-DMSA	2.7	1.2	185.8	235.3
MF74	1.3	3.7	42.3	147.4

To compare pre- and post-sonication relaxivities for the above listed SPIONs, these have been illustrated in a bar diagram (figure 103).

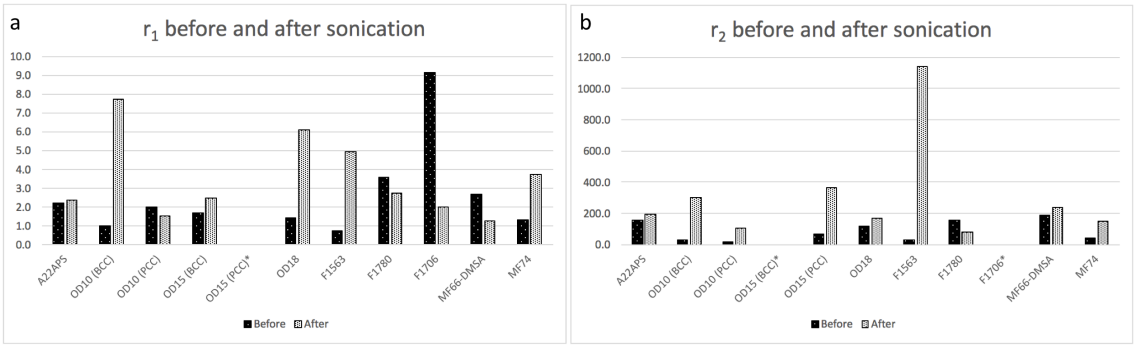

Figure 103: Comparison of pre- and post-sonication relaxivity measurements in a selection of different SPIONs. a: Longitudinal relaxivities. b: Transversal relaxivities.

As can be seen from figure 103, post-sonication relaxivities are different from the pre-sonication measurements. Out of ten SPIONs, the r_1 relaxivity increased for six after sonication. 60% of SPIONs had a post sonication r_1 that was more than 50% different to the pre-sonication value. For r_2, eight of nine SPIONs showed a higher relaxivity post sonication. More than 50% of SPIONs were measured with a post-sonication value which was more than 50% different to its pre-sonication value. There does not appear to be a general trend and sonication seems to be more important for some SPIONs compared to others. The effect of sonication on the relaxivity measurement will be dependent on the colloidal stability of a particular SPION.

8.3.7. Free vs cell-bound SPIONs

It was reported in the literature that relaxivity behaviour is different between free SPIONs and particles bound to cells [118]. It was attempted to reproduce these results with a selection of five SPIONs, i.e. OD10, MF66-DMSA, MF66-PEG, F1706 and Ferumoxytol (table 9).

Table 9: Superparamagnetic iron oxide nanoparticles investigated with their core size, hydrodynamic diameter, coating material, and surface charge.

SPION	Particle Size TEM [nm]	Hydrodynamic Size [nm]	Nature of coating	Surface Charge [mV]	Concentration [mg Fe/ml]	pH
Ferumoxytol	3.25	23.6	PSC	-43.2	30	7
OD10	10	60	DMSA	-40	1.9	7
MF66-DMSA	11.7	85	DMSA	-47	10	4.9
MF66-PEG	12	111.3	PEG	-28.3	5.3	7.4
F1706	11.7	159	Dextran T40	-18	10	7.1

Of those five SPIONs, Ferumoxytol is a commercially available and clinically approved MR contrast agent. The iron-oxide core of ferumoxytol is coated with polyglucose sorbitol carboxymethyl ether (PSC) and is the smallest of all SPIONs in this study with 23.6 nm. The other four SPIONs (OD10, MF66-DMSA, MF66-PEG, and F1706) are novel and were synthesised for use as multifunctionalised nanoparticles for cancer targeting, detection, and treatment [364]. Apart from PSC, SPIONs in this investigation were either coated with dimercaptosuccinic acid (DMSA), polyethylene glycol (PEG) or dextran T40. The intracellular and *in vivo* characteristics of MR iron-oxide based contrast agents strongly depend on the coating, charge as well as on the hydrodynamic particle size. Therefore, we investigated SPIONs with different hydrodynamic diameters ranging from 23.6 nm up to 159 nm. Table 9 summarises all SPIONs investigated in this study and lists their respective characteristics (i.e. iron oxide core size, hydrodynamic diameter, coating, and surface charge). Anionic SPIONs were selected because they have been shown to have a high affinity for the cell membrane and are their efficiency to be internalised is therefore significantly higher compared to neutral or positively charged SPIONs [365]. DMSA, PEG, and Dextran coating has been proven to be well suited for biomedical applications due to their good stability and low toxicity [366]–[368].

The measured r_2 and r_2^* values of all five SPIONs investigated in this study are summarised in table 10. The r_2^* relaxivity is always larger than the r_2 relaxivity. Because of the lack of a refocusing RF pulse T_2^* is always shorter than T_2 for gradient echo sequences. The problem is that the background gradient produced by the iron oxide particles is not cancelled by the GRE sequence [141]. Therefore, the relaxation rate (inverse of relaxation time) R_2^* will always be larger than R_2. The same is true for the relaxivities as they are simply the relaxation rates made independent of the iron concentration.

Table 10: Transverse relaxivities (r_2 and r_2^*) of ferumoxytol, OD10, MF66-DMSA, MF66-PEG, and F1704 measured in aqueous solution, cell media, and bound to or internalised by MDA-MB-231 breast cancer cells.

SPION	**Water**		**Cell Media**		**MDA-MB-231**	
	$\mathbf{r_2}$ $[\mathrm{mM^{-1}s^{-1}}]$	$\mathbf{r_2^*}$ $[\mathrm{mM^{-1}s^{-1}}]$	$\mathbf{r_2}$ $[\mathrm{mM^{-1}s^{-1}}]$	$\mathbf{r_2^*}$ $[\mathrm{mM^{-1}s^{-1}}]$	$\mathbf{r_2}$ $[\mathrm{mM^{-1}s^{-1}}]$	$\mathbf{r_2^*}$ $[\mathrm{mM^{-1}s^{-1}}]$
Ferumoxytol	90.8	103.7	165.2	174.3	5.1	95.0
OD10	108.2	144.7	43.3	658.9	46.9	1256.3
MF66-DMSA	243.1	391.7	145.1	1567.7	185.8	3414.9
MF66-PEG	307.0	1081.6	8.9	913.1	138.8	1157.8
F1706	144.8	291.4	363.1	572.2	21.9	160.6

The MR signal intensity, which is related to the T_2 and T_2^* relaxation times in spin echo and gradient echo MR sequences, varies for different concentrations of the same SPION as well as from one sample to another. As the SPION concentration in water, media or cells increases in a sample vial, the MR signal decreases. In the magnetic field of an MRI scanner, SPIONs introduce field inhomogeneities within their microenvironment which leads to a shortening of the T_2 time constant as the magnetic moments of protons dephase. From comparison of the free SPIONs in aqueous solution with the free SPION measurements in cell media, both transverse relaxivities of ferumoxytol and F1706 increased while MF66-PEG decreased. For OD10 and MF66-DMSA r_2 decreased and r_2^* increased. When comparing the relaxivities of free SPIONs in water with bound SPIONs (i.e. bound to the cell surface of the cell membrane or internalised and compartmentalised by the cell), ferumoxytol and F1706 behave in the same way as both transverse relaxivities decrease. OD10, MF66-DMSA, and MF66-PEG show the behaviour described by Kuhlpeter et al. [118] where r_2 decreases and r_2^* increases. The relaxivities of these three nanoparticles increase from the free state in media to the bound state. In cells, these three SPIONs achieve extremely high r_2^* values which is different for OD10 and MF66-DMSA

to their free r_2^* values in aqueous solution. MF66-PEG was measured with high relaxivity values in all three states (free in water, free in media, and bound in cells) but in particular the r_2^* value in water is unusually high.

The aforementioned decrease of r_2 and increase of r_2^* when SPIONs are bound to cells is illustrated in figure 104. We have plotted the $R_2^{(*)}$ values of each SPION over the iron oxide concentration. The gradient of the linear fit is the relaxivity $r_2^{(*)}$ summarised in table 10. Ferumoxytol shows a decrease in its r_2^* value from free to bound. However, there is a clear increase in the angle between the R_2 and R_2^* fits (figure 104a). This is also the case for OD10 (figure 104b), MF66-DMSA (figure 104c), and to a lesser extent for MF66-PEG (figure 104d). The $r_2^{(*)}$ values of F1706 decrease from free to bound conditions with no noticeable change in the angle between both fits (figure 104e).

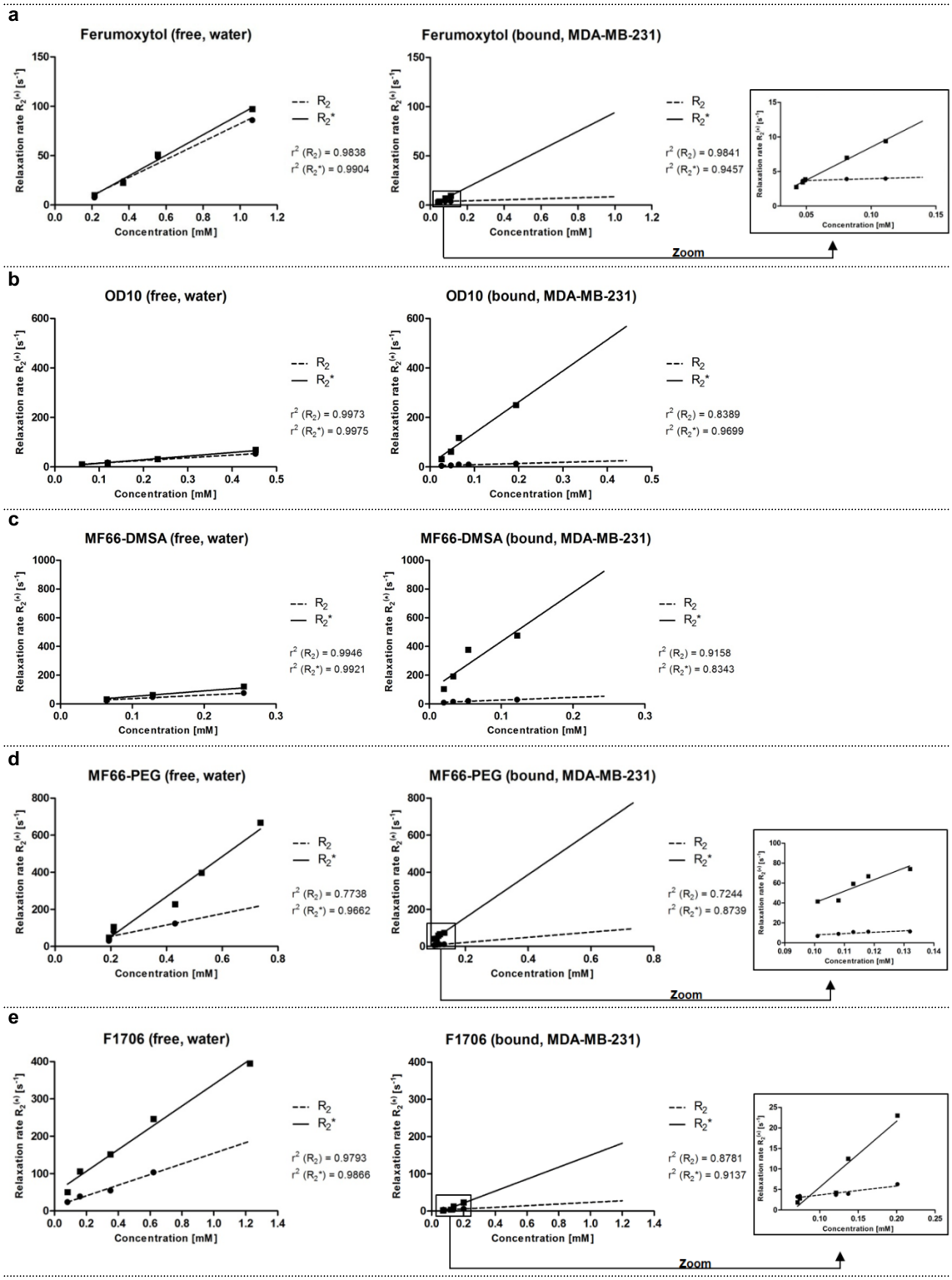

Figure 104: Graphs displaying linear relationship of R_2 and R_2^* for ferumoxytol (a), OD10 (b), MF66-DMSA (c), MF66-PEG (d), and F1706 (e) in aqueous solution (free SPION) and cells (bound SPION). When bound, r_2 decreases and r_2^* increases compared to the free state which means the angle between the R_2 and R_2^* fits increases.

8.4. Discussion

8.4.1. Phantom development and optimisation

The phantom used for the relaxivity measurements has developed from an improvised Blu Tack mould core surrounded with sample tubes to a water phantom. A water phantom was used to minimise all magnetic field distortions (e.g. at phase transitions between air and aqueous solution) except those caused by the superparamagnetic contrast agents. All distortions cause intra-voxel spin dephasing and a reduction in signal. It is therefore essential to minimise B_0 inhomogeneities to measure SPION relaxivities accurately.

Spatial variation of B_0 can originate from the different magnetic susceptibilities in the various tissues in the body to be scanned. For *in vitro* studies, the phantom's shape and composition are major factors influencing main magnetic field homogeneity.

Inhomogeneities in the main magnetic field (e.g. in a body or around an object such as a MRI phantom) can be assessed with a B_0 field map [379], [380]. Two gradient echo images are acquired at different echo times and the phase difference is calculated [380], [381]. The B_0 phase map will be skewed from intrinsic T_2^* decay, imperfections in the excitation phase or if the signal maximum is not recorded in the centre of k-space [375].

Phantom development for this study was motivated by three considerations. First, to minimise sharp edges. All objects or bodies introduced in a magnetic field causes field distortions to a certain extent. Objects that are round without any sharp edges and made up of a homogenous, non-magnetic material cause minimal B_0 field disturbance. Second, the size (volume) of the tubes or vials containing the SPION solutions needed to be big enough to prepare solutions of different SPION concentrations with a two-fold serial dilution and to conveniently draw regions of interest during the later analysis while avoiding the tube edges. Finally, the difference of magnetic susceptibility of the medium surrounding the tubes and the SPION solution needed to be minimised. Susceptibility effects are known to occur on phase interfaces such as air / polypropylene tube / SPION solution. By measuring the SPION vials in a water phantom we achieve more homogenous phase interfaces.

A limitation of the final water phantom with Perspex holder that was used for all measurements are the larger 1.5 ml Eppendorf tubes which have a thicker polypropylene tube wall than other tubes that could have been used. Thin-walled NMR tubes made of glass might have been a suitable alternative to further minimise susceptibility effects. As shown in our B_0 field map

(figure 93), a larger phantom should have been used to ensure greater distance of the tubes from the phantom edges. Finally, the effects the magnetised SPION solutions could potentially have on each other was not evaluated. SPIONs can establish a strong magnetic moment when brought in a magnetic field and the magnetic field effects of each SPION tube in relation to the neighbouring tubes should have been evaluated.

In this phantom study, the highest spatially varying susceptibility gradients were present at the edge of the curved phantom at the air/water interface (figure 93c). This is particularly pronounced in the head-toe direction along the field lines of the main magnetic field. The 37 water-filled Eppendorf tubes can also be seen in the B_0 field map due to the susceptibility gradients at the water/Eppendorf tube/water interfaces. These gradients do not extent into the tube centre and have therefore negligible influence on the relaxivity measurements.

The greatest homogeneity of B_0 field susceptibility values is present in the innermost core9 area. The homogeneity is greatly improved in the core25 area compared to the entire phantom because of the strong susceptibility effects at the phantom edge. The four phantom positions at the corner of the core25 area have slightly higher B_0 field susceptibility values then all other core25 position because of the lack of shielding from other Eppendorf tubes as well as their position towards the head and toe edge of the phantom. The core25 area offers sufficient magnetic field inhomogeneity while allowing measuring multiple samples at the same time in a time-efficient manner.

8.4.2. Relaxation

We have measured a range of different SPIONs in water, cell media and cells. But how does the medium in which the superparamagnetic iron oxide nanoparticles are dispersed effect the relaxivity measurements?

Multiple studies have shown that the characteristics of a SPION contrast agent, whether for MR imaging, cell internalisation and tracking or simply in terms of biocompatibility depend on magnetic susceptibility, shape, size, size distribution and surface modification [382]–[385].

SPION relaxation is the result of a dipolar mechanism as fluctuating dipoles can result in spin relaxation due to the induction of spin transitions. This dipolar coupling depends on the distance between the magnetic moment of the hydrogen nucleus of the surrounding water and the electron magnetic moment of the iron II/iron III ion [386]. The Curie spin relaxation is the result

of Néel relaxation and water diffusion [356]. The former describes the flipping of the magnetic moment of the SPION particle from one anisotropy state to another [386].

The medium in which the SPIONs are dispersed does not affect the Néel relaxation which depends on the particle size and the magnetic field strength. If the field strength becomes too high, the magnetic moment of the SPIONs will become locked onto the direction of the magnetic field in which case Neél relaxation is not possible [386].

For the relaxation of gadolinium complexes, the concepts of inner and outer sphere relaxation are relevant. There is no inner sphere relaxation for SPIONs. Outer sphere water does not conjugate to the particles as it is the case for Gd-complexes but is diffusing near the crystals. Important for SPION relaxation is the second sphere water. These water molecules hydrate the SPION crystals and their exchange constant is larger than that for water diffusion. Relaxivity relates to the number of water molecules that hydrate the SPION and for how long the water is coordinated to the nanoparticle [387], [388].

8.4.3. Relaxivities in water

We observed a linear relationship between the iron concentration and the R_1 and $R_2^{(*)}$ values in the phantom. Comparison of the relaxivity data presented in table 5 display considerable differences among the different SPIONs. This is because of different susceptibility effects exerted by the examined SPIONs which cause the shortening of the relaxation times.

The highest longitudinal relaxivities were recorded from ASi, OD7, F1566, Ferumoxytol, FeraSpinXS and VSOP. From the range of SPIONs tested, these were the smallest particles according to SPION core (3.25 – 8.5 nm) and in solution (9 – 60 nm). Very low r_1 values were measured for the A-series of particles, one without coating which showed immediate signs of agglomeration and sedimentation and one with APS coating. FF-NX-PVP was also observed to strongly agglomerate in solution. MF66-N6L is the MF66 particle functionalised with an anti-cancer drug. The functionalisation had a clear effect on the particles ability to enhance T_1 contrast. The particle's increased size and functionalisation has in impact on the water exchange capability which results in a lower r_1 value.

The background gradient produced by the iron oxide nanoparticles is not cancelled by the GRE sequence [141]. As a result, the relaxation rate (inverse of relaxation time) R_2^* will always be larger than R_2. The same is true for the relaxivities as they are simply the relaxation rates made independent of the iron concentration. The highest r_2 relaxivity was measured for OD7, OD15-

P20 and MF66-PEG. These were closely followed by ADNH, OD18, OD7-P2, OD15-P5, F1780 and MF66-DMSA. The OD-particles were synthesised according to a co-precipitation method described by Salas et al [364]. The MF66-particles were synthesised according to the same method with the aim to reproduce the favourable OD-particles. The highest r_2^* relaxivity was measured for ADNH, OD15-P20, F1563 and MF66-PEG. Other particles of high r_2^* relaxivity were OD15, OD18, F1780, MF66-DMSA and FeraSpinXXL. Nanoparticles synthesised according to above mentioned method [364], i.e. OD-particles, MF66-particles as well as F1780, showed the strongest r_2^* relaxivity.

Looking at the four commercial samples it is obvious that these have a stronger T_1 effect than a T_2 effect. FeraSpinXXL has the lowest r_1 value among the four but the highest r_2 and r_2^* value. As FeraSpinXS and FeraSpinXXL were synthesised identically, the difference in transverse relaxivity is due to the larger particle size of FeraSpinXXL. It is known that nanoparticle aggregation leads to an enhancement of T_2 and T_2^* contrast [389]. It is possible that among identically synthesised SPIONs, those with larger core sizes have more favourable r_2 characteristics.

Interesting to compare are OD15-P5, OD15-P10 and OD15-P20. These are identical particles synthesised from the same batch but then coated with different PEG chain lengths, i.e. 5k Da, 10k Da and 20k Da. OD15-P20 has the most favourable contrast behaviour across r_1, r_2 and r_2^*. The r_2^* value of OD15-P10 was slightly higher and of the same order of magnitude than that of OD15-P5. The r_1 and r_2 values of OD15-P5 were much higher than that of OD15-P10. Comparing all three nanoparticles, OD15-P10 with a PEG chain length of 10k Da appears to be least suitable of the three as an MRI contrast agents based on its relaxation enhancement capabilities. This shows that the relaxivity behaviour of SPIONs does not increase or decrease linearly with polymer chain length of the coating material. Hanot et al. [390] compared PEGylated SPIONs of 2kDa, 5kDa and 20kDa chain length for their uptake kinetics and cytotoxicity. They did not measure the nanoparticles' relaxivities but found that the smallest particle (2k Da) was taken up to a lesser extent than the others while all three SPIONs had a similar positive surface charge. Among identical particles only varying in terms of the chain length of their polymer coating and therefore overall size, one might think that the smallest particle is taken up the most. This makes it clear that further studies are required combining magnetic and relaxivity comparisons with physicochemical and kinetic studies of identical SPIONs with different coating lengths to gain further knowledge about underlying processes and optimal coating parameters for different SPION applications.

MF66-DMSA and MF66-PEG are the same iron oxide particle but different coating materials. When comparing the two for their relaxivity behaviour, MF66-PEG was measured with higher r_1, r_2 and r_2^* values. MF66-PEG has a physiological pH in aqueous solution making it more suitable for *in vivo* applications compared to the more acidic MF66-DMSA particle. MF66-PEG was measured with an unusually high r_2^* value in water. In media and when incubated in cells, MF66-DMSA displays higher longitudinal and transverse relaxivities. It is likely that DMSA does not effectively protect the MF66-particle in cell media where serum is present. The very high r_2^* values in media and cells are most likely the result of agglomeration after the DMSA coating failed to stabilise the solution. The PEGylated particle has a larger hydrodynamic diameter due to the bigger size of PEG. This could negatively influence *in vivo* behaviour such as pharmacokinetics and target tissue uptake but these were not assessed in this study. The higher relaxivity values in aqueous solution of MF66-PEG can be attributed to its coating as that is the only difference between both particles. Why the particle coated with PEG has more favourable relaxivity characteristics compared to the identical particle coated with DMSA is not clear. PEG as a coating polymer has been shown to provide good stability of a colloidal SPION solutions via steric repulsion [391]. It enables the conjugation of targeting ligands [384] and reliably reduces interactions of the SPION with plasma and serum proteins and that would otherwise lead to undesired opsonisation [224]. The effect PEG coating has on the relaxivity of an iron oxide nanoparticle, in particular r2, is currently unknown. No consistent results have been reported with maximum transverse relaxivity values reported at different molecular weights [384], [385]. This indicates that further studies on the effects of coating materials on a nanoparticles relaxivity behaviour on a molecular and sub-molecular level are required.

8.4.4. Relaxivities in media

Not many studies have focused on determining the relaxivities of SPIONs in cell media and assessed the specific effects this has on the SPION and its relaxivity. The medium in which the magnetic nanoparticles are dispersed has an effect on the water diffusion. Particles in a more viscous suspension diffuse at a lower rate than in a solution of lower viscosity [392]. For the measurements of cell media and cells, PVA was added to the medium to increase viscosity and keep the cells from sedimenting. This should have little effect on the *in vitro* cell measurements as SPIONs are either tightly bound to the cell surfaces or internalised when clustering and compartmentalisation effects are more relevant. However, for the relaxivity measurements of free SPIONs in cell media, the increase in viscosity results in a decrease of diffusion and a lower water exchange rate according to the outer sphere relaxation mechanism [359], [393].

For the majority of SPIONs measured, r_1 is smaller in cell media mixed with PVA than in water. Exception to this are A22APS, MF66-DMSA, MF71, MF74 and Ferumoxytol. In particular the particles MF71 and Ferumoxytol stand out. The r_1 in cell media of the latter is almost twice as much compared to the water measurement and the r_1 of MF71 is more than ten times larger in cell media compared to water. The reason for the strong increase in r_1, especially that of MF71 is not clear. A small discrepancy from the expected behaviour could be attributed to measurement errors. The fact that the r_1 in cell media is considerably larger than in water makes a measurement error unlikely. The characteristics of MF71 do not give any reason to suspect such a behaviour. The particle is quite large in solution with a hydrodynamic diameter of 203 nm and might be prone to agglomeration. However, agglomeration would decrease the longitudinal relaxivity, not increase it [394].

For SPIONs up to a few hundred nanometres in diameter, the transverse relaxation depends mainly on diffusion. Néel relaxation becomes less relevant. A decrease of r_2 in the more viscous cell media would be expected compared to the water measurements. Overall, the r_2 values in media are similar to those in water. MF71 shows a strong increase in transverse relaxivity in cell media compared to water. It is not clear why MF71 displays this behaviour. A strong tendency to cluster could provide an explanation for the r_2 increase if the cluster size is of such that supports an increase in transverse relaxation. As MF71 displayed unexpected relaxation behaviour for both, r_1 and r_2, it would worth to further investigate the origin of that behaviour.

For all measured SPIONs except MF66-PEG, r_2^* in cell media is considerably larger than in water. Particles with PEI coating undergo direct agglomeration in the presence of fetal calf serum [395] which explains the very high r_2^* values for F1563 in media and cells.

Due to the reduction in diffusion, transverse relaxivity is expected to decrease in cell media. Cell media contains a range of components such as nutrients, carboxyhydrates, various metals and minerals (calcium, magnesium, sulphates) and buffering agents (phophates, acetates). These co mponents have an impact on the clustering behaviour of SPIONs. Park et al. [396] reported that SPIONs start to aggregate in DMEM over a time period of hours due to the high salt content. Aggregation occurs because the salt blocks electrostatic repulsion between particles. The same authors reported that no aggregation was observed for hours when bovine calf serum was added to the DMEM. This effect was more pronounced for SPIONs with a negative zeta potential. Further studies have concluded that the adsorption of serum on superparamagnetic iron oxide nanoparticles could potentially hinder cell internalisation [395]. SPIONs in media containing fetal calf serum could undergo depletion stabilisation as a result of the serum

proteins that have a similar size as the SPIONs. Small negatively charged biomolecules could be adsorbed on the SPIONs surface giving the complex a neutral charge and therefore decreased electrostatic interactions and increased stabilisation [397]. Petri-Fink et al. [395] concluded that the serum in cell media had a clear and immediate effect on the agglomeration of some SPIONs but not on others. However, no clear tendency to higher r_2 relaxivities was observed. Superparamagnetic iron oxide nanoparticles are T_2^* contrast agents combining the local inhomogeneities introduced by the SPIONs with the reversible main magnetic field dephasing effect. Our results suggest that agglomeration of SPIONs has a much stronger effect on T_2^* where the reversible bulk field dephasing effects are not eliminated by a 180° inversion pulse. For future relaxivity studies in cell media it would be interesting to investigate the agglomeration behaviour in cell media containing serum and then discussing relaxivity measurements within the context of SPION stability in media with and without serum.

8.4.5. Relaxivity in cells

The aim of SPIONs as MRI contrast agents is to be taken up by target cells in a specific manner. Nonspecific cell internalisation may also occur which is undesired as it will make it difficult to target specific regions and deliver a particular diagnostic or therapeutic modality. In both cases, the uptake of the SPIONs by cells changes with size and shape of the SPION and the physicochemical properties of its surface (e.g. zeta potential) [398]–[401].

Non-specific uptake, which is what has been investigated in this study, occurs via SPION adsorption on the cell surface. We investigated a range of different SPIONs of different core and hydrodynamic sizes, different surface charges and coatings and performed *in vitro* experiments in two different cancer cell lines. Certain coating materials can be synthesised (e.g. PEG [402]) to avoid non-specific uptake by steric hindrance. This would require a particular spatial structure as our PEGylated SPION (MF66-PEG) was adsorbed by cancer cells.

The relaxivity behaviour of SPIONs in cells is inhomogenous. When SPIONs are internalised by cells via the various processes described in the literature [403], a nanoparticle agglomeration or clustering happens within the cells. The clustering as part of a cell internalisation affects the relaxation behaviour. Longitudinal and transverse relaxation respond differently to the clustering of SPIONs and the measured r_1, r_2 and r_2^* relaxivities strongly depend on the size of the cluster [404], [405].

For nanoparticles taken up by the cancer cells, the r_1 value should decrease compared to free SPIONs. This is due to clustering and the confinement in cells and the limit this puts on the outer water exchange (water diffusion) [389]. According to Bulte et al. [394], this trend

continues as the SPION cluster grows bigger. With the exception of F1706, this behaviour was observed in this study for a range of different SPIONs measured in pancreatic and breast cancer cells. The core or hydrodynamic size of F1706 nor its Dextran coating would provide a reason that this nanoparticle behaved differently. The surface charge of F1706 is -18 mV which is lower than many other SPIONs in the study. A possible explanation could be that F1706 was not internalised by the breast cancer cells and instead attached to the surface of the cells. This could potentially have happened because of its less anionic surface charge. This bound state would still influence the relaxation behaviour but not in the same way predicted by the theory from post internalisation clustering. The relaxivities strongly depend on whether the cells are internalised by the cells or merely adsorbed/attached to the surface of the cells. For SPIONs smaller than 120 nm in hydrodynamic diameter, endocytosis has been reported to be the mechanism of uptake [406]. Other SPIONs such as ferucarbotran which is negatively charged as all SIONs in this study, nonspecific phagocytosis was reported for the uptake mechanism in human umbilical vein endothelial cells [407] and carcinoma cells [408].

The behaviour of the transverse relaxivity is more complicated than that of the longitudinal relaxivity. During agglomeration of SPIONs to clusters, the r_2 relaxivity increases. However, the r_2 increase will eventually reach a maximum. After further increase of the SPION cluster, r_2 will decrease again [404], [405]. Rad et al. [409] and Simon et al. [410] also showed that the transverse relaxivity in cells strongly depends of the type of cell. The extremely high relaxivity values of F1563 are consistent with previous reports of SPION particles with a PEI coating agglomerating in serum media [411]. OD10, MF66-DMSA, and MF66-PEG show the behaviour described by Kuhlpeter et al. [118] where r_2 decreases and r_2^* increases. The relaxivities of these three nanoparticles increase from the free state in media to the bound state. In cells, all SPIONs except F1706 and Ferumoxytol achieve extremely high r_2^* values which is different to their free r_2^* values in aqueous solution.

The behaviour of SPIONs when interacting with cells depends predominantly on the coating. The interaction of the coating polymer with the SPION surface is determined by the bonds between the charge carrying functional groups of the coating polymer and the protonated and hydroxylated surface of the iron oxide [412]. The configuration of the coating polymer has a key role in the biological behaviour of the particle but is difficult to control or determine [413]. It is controlled by the molecular weight of the polymer, its concentration, pH, surface charge and ionic strength.

The magnetic relaxivity as well as toxicity of SPIONs depends on the stability of the particles as Park et al. [391] have demonstrated on r_2 measurements on PEG-coated SPIONs. SPION

colloidal stability is directly linked to its relaxation behaviour because cell media has an effect on the stability of SPIONs and their relaxation properties. SPIONs can also aggregate governed by pharmacokinetic processes to produce micron-sized clusters that destablisise the SPION. Several researchers have described this phenomenon [395], [414]–[419]. These clusters might be coated again with a layer of biomacromolecules or proteins which determine the interaction with cells. Furthermore, the characteristics of micron-sized SPION clusters a fundamentally different to single SPIONs in terms of their diffusion and sedimentation and therefore show a different behaviour towards cells. The destabilisation of SPIONs in biological fluid is believed to be due to the adsorption of biomolecules and the removal or exchange of coating polymers with other biomolecules. Due to these processes, the original coating is no longer able to hinder the electrostatic van der Waals forces (attraction) and SPION clustering results. The most important factor to stop destabilisation and therefore not only maintain the nanoparticles physicochemical properties but also its magnetic relaxation characteristics is a well-designed and robust polymer coating [395], [414], [419], [420].

In this study, we only evaluated the SPIONs relaxivity behaviour *in vitro*. For *in vivo* studies additional factors need to be taken into account such as the dependency between the shape of the physiological uptake area and the T_2 shortening of the SPION [421]. Qualitative and quantitative studies reported in the literature suggest that SPIONs are taken up by cancer cells in a dose-dependent matter that possess a saturation [422].

Future studies should focus on providing more general conclusions on how each SPION characteristic influences in vitro relaxation behaviour. This would allow the synthesis of a SPION particle with the exact magnetic relaxation properties required for a given purpose. Furthermore, many researchers explored SPION biocompatibility. Often, this is understood as cytotoxicity [423], [424]. However, studies should also focus on the effects SPIONs have on signal transduction of normal cell physiology [425], [426]. Apart from passively interacting cells and their membranes, SPIONs can also interact with membrane receptors which leads to modulation of the signal transduction pathways [427].

8.4.6. Effect of cell sonication on relaxivity

Ultrasound sonication causes cell death. We therefore wanted to compare relaxivity measurements pre- and post-sonication to evaluate the effect of cell death on the relaxivity. The results for the longitudinal relaxivity are inconclusive. For some particles, i.e. A22APS, OD10 (PCC), OD15 (BCC) and F1780, the pre- and post-sonication relaxivities are similar. For other particles such as OD10 (BCC), OD18, F1563, F1706, MF66-DMSA and MF74, pre- and post-

sonication r_1 values are considerably different. The cells were scanned 15 min post-sonication. SPIONs that have been internalised by cells are not immediately released upon cell death. A clear difference between pre- and post-sonication relaxivity measurements are therefore likely to be seen on cells where the SPIONs mainly adsorbed onto the cell surface which will be released upon sonication. However, the result for the longitudinal relaxivity pre- and post-sonication are inconsistent. There is no clear trend that longitudinal relaxivity increases or decreases post-sonication. Four out of six SPIONs have a higher r_1 value post-sonication. This is expected when more SPIO nanoparticles are freely suspended in solution after release from the cell surface. The additional free SPIONs lead to an increased water exchange.

The r_2 results are more consistent. Except for F1780, the transverse relaxivity increased post-sonication. This result is consistent with Kuhlpeter et al. [118] who described a decrease in r_2 when the SPIONs were bound by cells compared to free SPIONs. The increase in r_2 is most pronounced for F1563. A likely explanation is that F1563 quickly aggregated in media [396] which would explain the very high transverse relaxivity that is normally only achieved for SPION aggregates.

8.4.7. Free vs cell-bound SPIONs

Summary of the relaxivity data for five selected SPIONs presented in table 10 display considerable differences among the different SPIONs. This is because of different susceptibility effects exerted by the examined SPIONs which cause the shortening of the T_2^* relaxation time. A reason that the MF66 particles have a stronger transverse relaxivity is due to the larger crystal size which leads to an increase in magnetisation for magnetite nanoparticles [428], [429].

For superparamagnetic iron oxide nanoparticles, r_2 and r_2^* are particularly important because of the rapid water exchange and diffusion within the surrounding of these particles [430]. Ferumoxytol and F1706 display a T_1 effect on T_2- and T_2^*-weighted MR images. Because the signal intensity also depends on TR/T_1, this can disturb the signal decay for a $T_2^{(*)}$ contrast agent at concentrations where the condition $T_1 \ll TR$ does not apply any more [378]. Therefore, the signal enhancement does not only depend on $r_2^{(*)}$ but also on the longitudinal relaxivity r_1. That means that in addition to a high $r_2^{(*)}$ value, a lower r_1/r_2 ratio can be useful for $T_2^{(*)}$-weighted contrast enhancement with SPIONs. The transverse relaxivity depends on the characteristics of the SPION, e.g. as the coating thickness increases, transverse and longitudinal relaxivities decrease. A change in pH on the other hand does not impact relaxivities [431]. Particles with a positive zeta potential usually have a higher r_2/r_1 ratio [432]. In terms of type

of coating, silica was shown to lead to very high transverse relaxivities within a clinical magnetic field strength (1.5T) when compared to other common coating materials [433]. Furthermore, transverse relaxivity increases as hydrophilicity of the coating increases which makes hydrophilic Polyethylenimine (PEI) a very good choice for SPION coatings [430]. The coating of a SPION can hinder water molecules from diffusing to the particle surface. Coating molecules can also bind to nearby water and therefore immobilise it. Both processes have an impact on the proton relaxation and therefore the relaxivity. Due to the impact the SPION coating can have, even identical SPION cores but with different coatings can exhibit very different magnetic relaxivity behaviours. But in general, the effect of the coating on transverse relaxivity is not fully understood [385]. According to the outer-sphere theory, the transverse relaxivity improves if the thickness of the polymer coating increases while the water diffusion coefficient decreases [354], [355], [359].

It was reported by Bowen et al. [434] that for cell-bound SPIONs, R_2^* measurements have a much higher sensitivity than R_2 measurements. When comparing the free and bound SPIONs, the latter display much higher r_2^* values and significantly lower r_2 values. Therefore, the measurement of both quantities provides information of whether a particular iron-based contrast agent has been bound and compartmentalised by cells. The relaxivities for free SPIONs are much closer together in magnitude. This separation indicates that it is possible to determine whether SPIONs have been internalised by cells or are tightly bound to the surface of cells by MRI. Upon compartmentalisation of SPIONs in cells, a nonuniform field distribution is generated. As a result, the influence of diffusion on the signal is changed [435]. This can be explained with the static dephasing regime [360].

The majority of linear fits of $R_2^{(*)}$ vs. the different SPION concentration (relaxivities reported in table 7) have an $r^2 > 0.9$ with the quality of all fits being higher than 0.7 (figure 104). Ferumoxytol and F1706 did not behave as described by Kuhlpeter et al. [118] where a decrease of r_2 and increase of r_2^* occur from a free to a bound state. A reason for that could be the short TR we used in our T_2^* mapping sequence. Ferumoxytol and F1706 displayed a T_1 effect on T_2- and T_2^*-weighted MR images. Because the signal intensity also depends on TR/T_1, this can disturb the signal decay for a $T_2^{(*)}$ contrast agent at concentrations where the condition $T_1 \ll TR$ does not apply any more [378]. Therefore, the signal enhancement does not only depend on $r_2^{(*)}$ but also on the longitudinal relaxivity r_1. That means that in addition to a high $r_2^{(*)}$ value, a lower r_1/r_2 ratio can be useful for $T_2^{(*)}$-weighted contrast enhancement with SPIONs. In figure 104, MF66-PEG and F1706 show the smallest increase in angle between the R_2 and R_2^* curves.

These two SPIONs have a large hydrodynamic diameter compared to the other particles investigated. This means that compartmentalisation has a lesser effect on larger nanoparticles. MF66-DMSA and MF66-PEG are the same iron oxide nanoparticle but with different coatings. They displayed the highest r_2 and r_2^* values both in aqueous solution and compartmentalised in cells. In particular the r_2^* value of these particles appear very promising.

9. *In vivo* MRI of novel nanoparticles in an animal model of cancer

9.1. Introduction

Superparamagnetic iron oxide nanoparticles (SPIONs) have been widely studied for their potential as MRI contrast agents since it was shown in 1997 that magnetically labelled cells can be detected by MRI [436]. In decreasing the size of the iron oxide core below a single magnetic domain they become superparamagnetic which allows them to be detected by MRI while not having a remnant magnetic moment outside the scanner's magnetic field [191]. SPIONs are not stable in aqueous solutions and therefore need to be coated to ensure that they do not aggregate or precipitate [187] (common coating materials are described in chapter 5). A hydrodynamic diameter between 10 – 50 nm is desirable for a long blood retention time. Particles with a size greater than approximately 50 nm are metabolized by the RES (Kupffer cells, macrophages). Particles smaller than approximately 10 nm are removed from the vasculature by renal filtration [437]. A long blood circulation time increases the probability that particles accumulate in the tumour through leaky neovascularisation combined with reduced lymph drainage at the tumour (EPR effect) [438].

For the *in vivo* testing of SPIONs, both in terms of cancer targeting capability and MRI contrast, human cancer xenografts are often used. In this model, immunodeficient rodents (e.g. athymic nude mice) are being transplanted human cancer cells. This heterotransplantation can be done subcutaneously or directly into the organ from which the cells originated [439], [440]. For the assessment of cancer therapeutics, it was reported that the predictive value of a human cancer xenograft is variable. In particular, the activity of an agent was vastly different *in vitro*, in a subcutaneous xenograft model and a clinical trial [441]–[443]. Others have reported good predictions from xenograft studies that were later confirmed in phase 2 clinical trials [444]. The use of continuous cell lines as a source for a human cancer xenograft is a potential limitation [445]. Cancer xenografts are used in a range of MRI studies, such as the assessment of volume and size of lesions [446], measurement of parameters of the tumour environment such as perfusion, vascular function [447], hypoxia and pH [448]–[453] as well as metabolic studies [454].

Another model is that of genetically engineered mice (GEM). Through the alteration of the genetic profile, genes are overexpressed or mutated that are likely to play a part in tumour malignancy/transformation. The GEM model can be superior to the human cancer xenograft model in some aspects. However, it also has a set of disadvantages and the interested reader is referred to more specialised literature for further information [439], [455], [456].

Overall, cancer MRI studies with multifunctional nanoparticles aim to develop targeted imaging agents and therapeutic vehicles that prove successful in theranostic applications. Part of that is the development of new imaging technology (see chapter 7). In this chapter, we will describe the testing of our novel iron oxide nanoparticles in a human cancer xenograft model. We compare five different SPIONs in terms of their suitability as MRI contrast agents with respect to their size, coating material and surface charge. Further, it has been reported elsewhere that R_2 and R_2^* mapping can be used to differentiate between free and cell-bound SPIONs by MRI. Cell-bound SPIONs show higher R_2^* values compared with free SPIONs whereas R_2 is higher for free iron [118]. The aim of the present work has been to extend this by investigating a relationship between the chemical nature of the SPION (i.e. particle size, charge, coating, functional groups) and the ability to differentiate whether a particular particle is cell-bound or free by MRI.

9.2. Methods

9.2.1. Superparamagnetic Iron Oxide

We investigated two different SPIONs (table 9) regarding their T_2 and T_2^* contrast characteristics *in vivo* using a 3T clinical MR scanner.

Table 11: Superparamagnetic iron oxide nanoparticles investigated with their core size, hydrodynamic diameter, coating material, and surface charge.

SPION	Particle Size TEM [nm]	Hydrodynamic Size [nm]	Nature of coating	Surface Charge [mV]	Concentration [mg Fe/ml]	pH
Ferumoxytol	3.25	23.6	PSC	-43.2	30	7
MF66-PEG	12	111.3	PEG	-28.3	5.3	7.4

Ferumoxytol is a commercially available and clinically approved MR contrast agent. The iron-oxide core of ferumoxytol is coated with polyglucose sorbitol carboxymethyl ether (PSC). The other SPION (MF66-PEG) is a novel PEGylated particle which was synthesised for cancer targeting, detection, and treatment [364]. The intracellular and *in vivo* characteristics of MR iron-oxide based contrast agents strongly depend on the coating, charge as well as on the hydrodynamic particle size. Therefore, we investigated SPIONs with different hydrodynamic diameters. Table 9 summarises the SPIONs investigated in this study and lists their respective characteristics (i.e. iron oxide core size, hydrodynamic diameter, coating, and surface charge). Anionic SPIONs were selected because they have been shown to have a high affinity for the cell

membrane and are their efficiency to be internalised is therefore significantly higher compared to neutral or positively charged SPIONs [365]. PEG coating has been proven to be well suited for biomedical applications due to its good stability and low toxicity [366]–[368].

9.2.2. MR Imaging *in vivo*

All procedures used in these studies were performed in accordance with the European Communities Council Directive 2010/63/EU on the protection of animals used for scientific purposes, and with the British legislation (The Animals (Scientific Procedures) Act 1986). All efforts were made to minimize animal suffering and to reduce the number of animals used. Female athymic nude mice (Hsd:Athymic Nude-Foxn1nu, 8 weeks old) were purchased from Harlan Laboratories (Blackthorn, United Kingdom). Subcutaneous xenograft tumours were induced by injection of 2x106 MDA-MB-231 cells (ATCC, Wesel, Germany) in 100 µl Matrigel™ (BD Biosciences, Bedford, USA) into the right flank of the mice. The experiments were started when the tumour size reached 300 mm^3, as calculated by the formula V = π/6 x (length x width x height of the tumour) [457].

In order to test two selected SPIONs *in vivo*, two tumour-bearing mice were intravenously injected with 11 mg_{Fe}/kg of either MF66-PEG or ferumoxytol, and MR images were acquired using T_2^* mapping sequences. Mice were anaesthetised with 5% and maintained with 1-2% isoflurane in oxygen under spontaneous breathing during the MR imaging experiments. We used a custom-made single-loop surface coil (47 mm diameter) for signal reception. Mice were imaged in prone position before the SPION injection (baseline), 30 min and 48 h after the injection.

The scan protocol consisted of an anatomical scan and a T_2^* mapping sequence. In order to display the anatomy of the mice and plan subsequent scans, 44 coronal slices were acquired with a 3D gradient-echo sequence (26 ms TR, echo time 8.4 ms, 25° flip angle, FOV 40x40x22 mm^3, acquisition matrix 160x160, slice thickness 1 mm, in-plane resolution 0.25x0.25 mm^2, 3 averages, duration 4.32 min). T_2^* mapping was performed with a 2D turbo gradient-echo (2D TFE) sequence (100 ms TR, 4.6 ms to first echo, 6.9 ms interval between subsequent echoes, 6 k-space lines per shot, 35° flip angle, FOV 50x50 mm^2, acquisition matrix 72x69, slice thickness 3 mm, in-plane resolution 0.69x0.72 mm^2, 4 averages, duration 3.12 min).
The T_2^* weighted images were post-processed with the SGM technique where short term Fourier transforms in x- and y-directions are applied to all pixels individually. This technique also takes into account a certain number of neighbouring pixels which is three in our case. A susceptibility

gradient map was calculated from the value of the k^{shift} vector (two-dimensional shift in k-space from the maximum) at every pixel location.

9.3. Results

For the *in vivo* study we acquired three coronal slices in tumour bearing mice. All three slices contained the tumour area and liver. The tumour is the intended target area for our SPIONs and the liver is where most SPIONs accumulate due to the uptake by the mononuclear phagocytic system. Figure 105 shows an anatomical scan illustrating the two areas of interest.

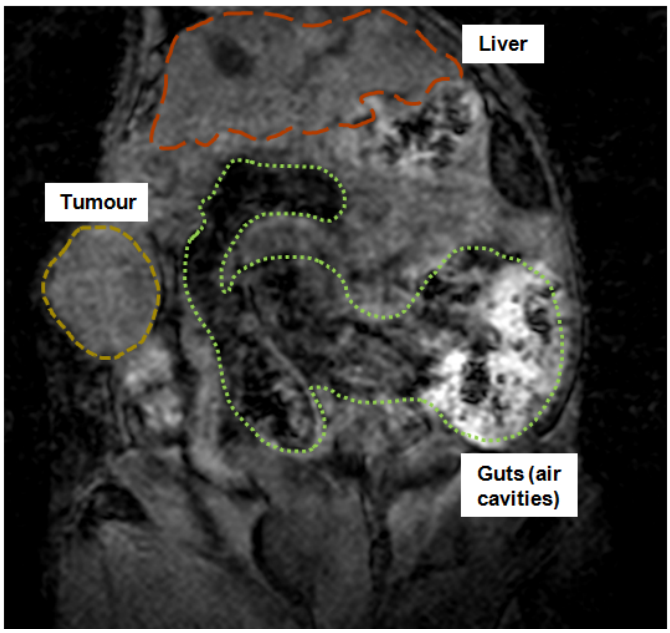

Figure 105: Anatomic scan (coronal) showing the organs of interest for the *in vivo* study.

We injected mice with ferumoxytol (n = 6) and MF66-PEG (n = 3) and acquired coronal T_2^* maps pre-contrast, 30 min post-contrast and 48 hours post-contrast. We determined the transverse relaxation time T_2^* for three slices in the tumour and liver area at all three time points. The mean values are summarised in table 12.

Table 12: Mean transverse relaxation time of three coronal slices in tumour and liver before injection of the contrast agent and at 30 min and 48 hours post-injection.

$\mathbf{T_2^*}$ [ms]	Pre-contrast		30 min post-contrast		48h post-contrast	
	Liver	Tumour	Liver	Tumour	Liver	Tumour
Ferumoxytol mouse (n = 6)	22.13 ± 1.70	35.87 ± 11.75	7.52 ± 2.62	25.99 ± 9.56	15.13 ± 4.73	30.28 ± 13.48

MF66-PEG mouse (n = 3)	22.82 ± 2.63	35.71 ± 11.28	10.16 ± 6.10	36.44 ± 11.33	9.29 ± 6.63	37.53 ± 3.94

The mean T_2^* values were plotted in figure 106 showing the statistical significance of changes at the 30 min and 48 hour time points compared to the pre-contrast measurement.

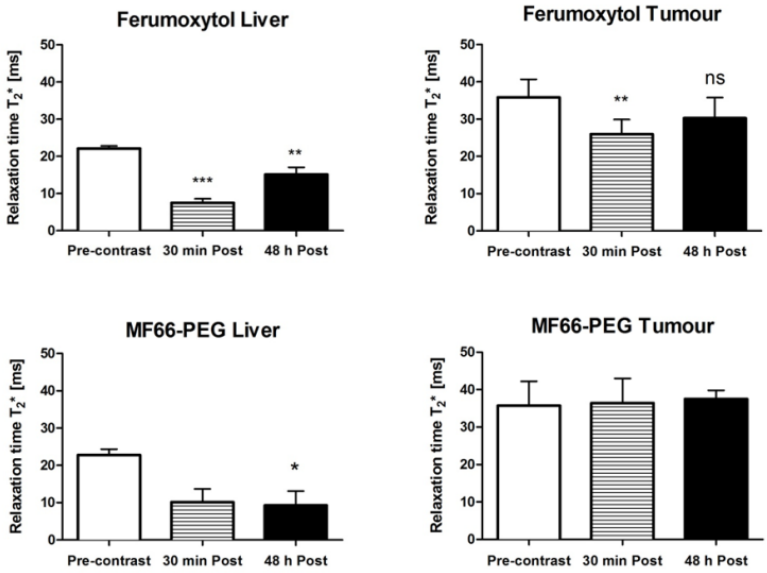

Figure 106: Mean T_2^* values of mice injected with ferumoxytol (n = 6) and MF66-PEG (n = 3) for two areas of interest (i.e. liver and tumour. The bar diagrams indicate whether the change at the post-injection time points was significant compared to the pre-contrast measurement.

The decrease in T_2^* recovers slightly after 48 hours for ferumoxytol while both post-contrast time points of the MF66-PEG mice are similar. We have measured the iron content in liver (n = 3) and tumour (n = 2) of mice injected with ferumoxytol (figure 107). There is significantly more iron in the liver at 48 hours post injection whereas no significant increase in iron content could be detected in the tumour.

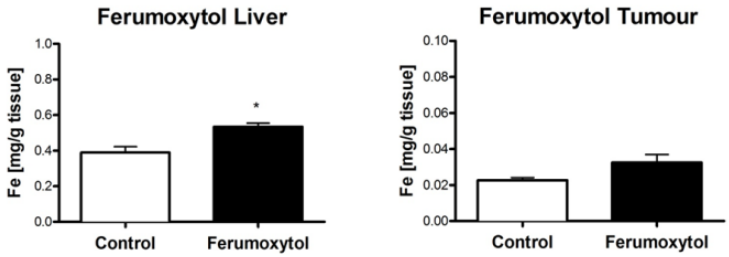

Figure 107: Mean iron content in liver (n = 3) and tumour (n = 2) measured with ICP-MS in controlled animals injected with saline and in ferumoxytol injected mice culled after the 48 h time point.

Coronal T_2^* maps of the two mice, one injected with ferumoxytol and one with MF66-PEG are shown in figure 108 and 109, respectively. In both cases a clear darkening of the liver can be observed 30 min post injection. The presence of SPIONs in the liver is still visible 48h post injection with a clear increase in negative contrast in the case of ferumoxytol and a slight increase with MF66-PEG. We determined the transverse relaxation time T_2^* for three slices in the tumour and liver area at all three time points. The mean values are summarised in table 12. Positive contrast images have been generated from the GRE images of the mice injected with ferumoxytol and MF66-PEG in a postprocessing step with the susceptibility gradient mapping tool. No direct uptake of the two SPIONs is seen in the tumour area.

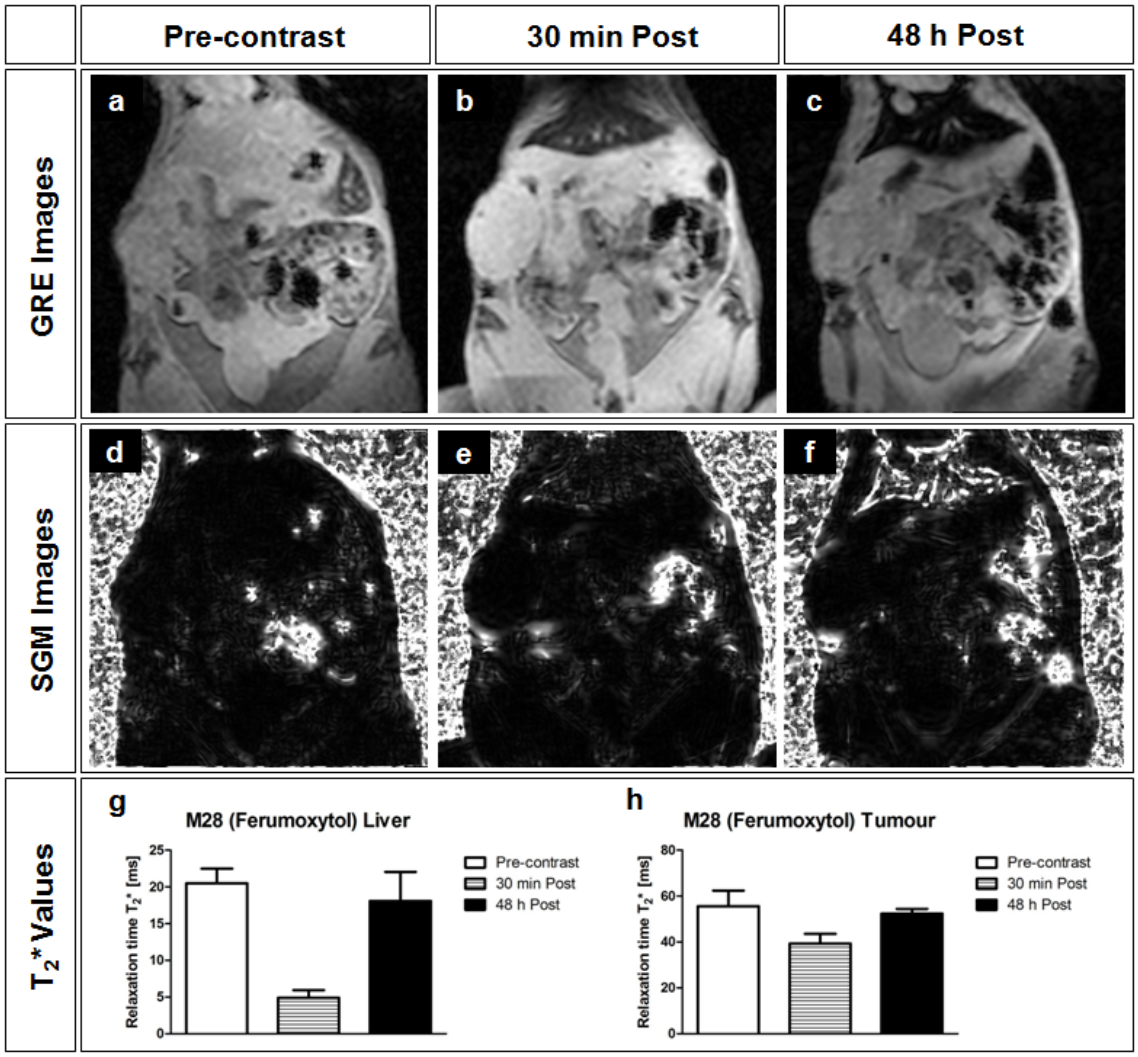

Figure 108: Results of a mouse injected with ferumoxytol. a – c: Coronal 2D gradient-echo images before injection with ferumoxytol, 30 min and 48h post injection. d – f: SGM images constructed from their respective gradient echo images highlighting areas of large susceptibility gradients in white (positive contrast). g – h: Bar diagrams showing the T_2^* values in the liver (g) and tumour (h) pre-contrast, 30 min and 48 hours post contrast.

In figure 108a, a dark patch at the inferior edge of the tumour can be seen that increases in area and intensity with time after injection (figure 108b and 108c). This contrast behaviour is consistent with the liver where the contrast agent is expected to be found because of removal from the circulation due to macrophages. The SGM images confirm this observation (figure 108d – f).

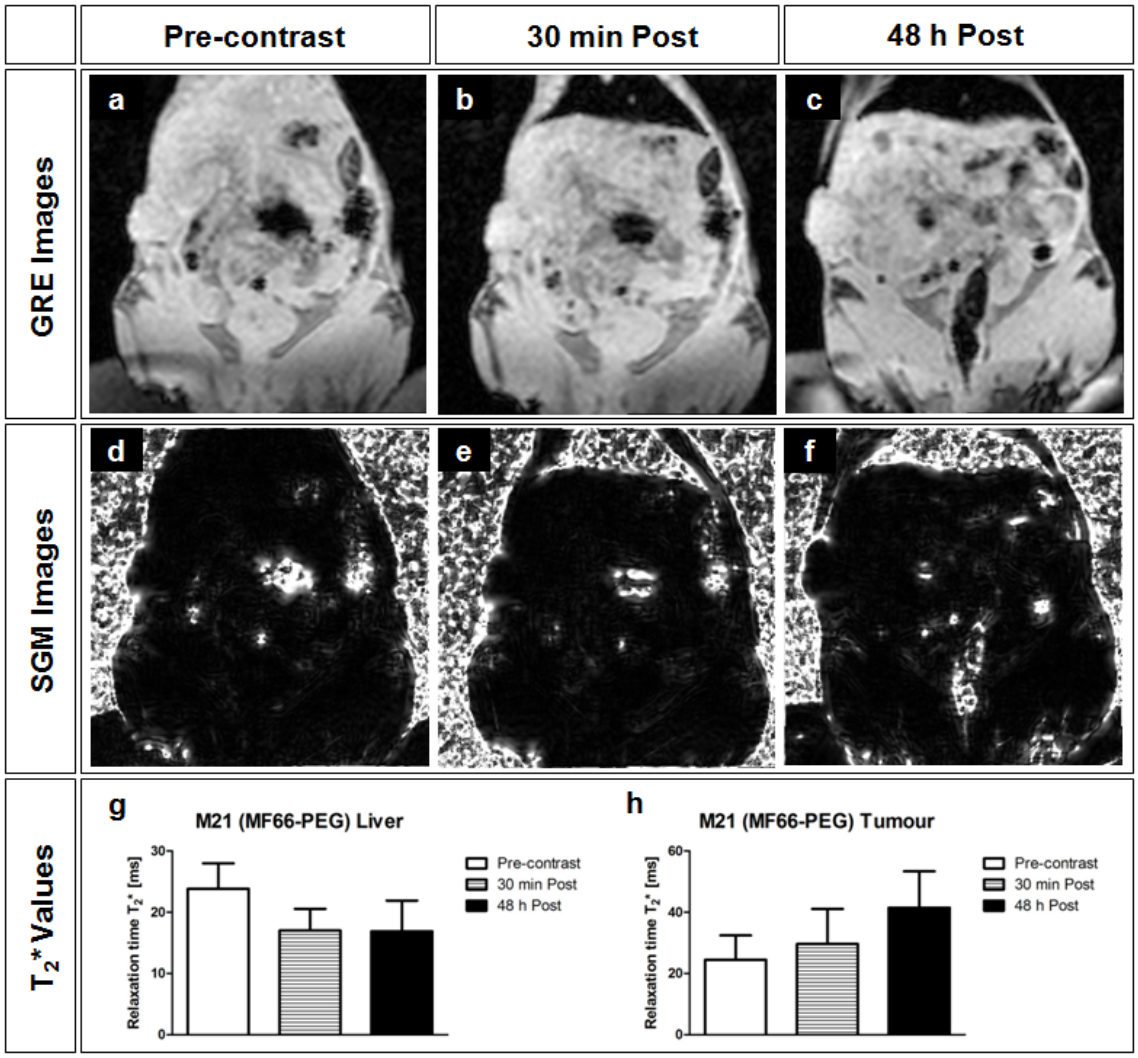

Figure 109: Results of a mouse injected with MF66-PEG. a – c: Coronal 2D gradient-echo images before injection with MF66-PEG, 30 min and 48h post injection. d – f: SGM images constructed from their respective gradient echo images highlighting areas of large susceptibility gradients in white (positive contrast). g – h: Bar diagrams showing the T_2^* values in the liver (g) and tumour (h) pre-contrast, 30 min and 48 hours post contrast.

The SGM images of the mouse injected with MF66-PEG (figure 109d - f) are less convincing despite the obvious negative contrast effect in the liver of the GRE images (figure 109a – c). No

other areas of SPION uptake than the liver can be identified from the images presented in figure 109.

9.4. Discussion

SPIONs, like all contrast agents and therapeutic drugs administered intravenously, need to prove that they do not suffer from major disadvantages that would disqualify them for further use. These are toxicological characteristics, low dose delivery and a resulting low therapeutic efficacy. A key consideration is also the pharmacokinetic profile as SPIONs need to pass various physiological barriers in order to reach the intended target site within the body. These barriers are clearance by the mononuclear phagocyte system (MPS) also referred to as the reticuloendothelial system (RES) in the form of macrophages, monocytes and Kupffer cells, kidney filtration, extravasation from the diseased site and crossing nuclear and plasma membranes [458]–[460].

9.4.1. Liver uptake

We have presented T_2^*-weighted in vivo images of two mice which were acquired at three different time points; images were acquired before as well as 30 minutes and 48 hours after the injection of a SPION contrast agent (i.e. ferumoxytol and MF66-PEG). Anatomical areas of interest in the tumour bearing mice are the tumour, liver and any other regions that show signs of SPION accumulation. SPIONs and other nanoparticles developed for biomedical applications are taken up by macrophages when injected into the bloodstream. Tissues that are rich of macrophages are the bone marrow, spleen and liver (Kupffer cells). A key aim for SPIONs designed for passive tumour targeting is therefore to increase blood circulation time by decreasing the uptake rate by macrophages ("stealth" characteristics). Blood half-lives of SPIONs depend on various factors such as particle size, coating (e.g. hydrophilic polymers), charge and dose and can vary considerably from 1 to 36 hours [461]. Several authors have reported that as the size of the SPION increases so does the liver uptake [462]. However, this might not be a general rule as other studies have also presented contradictory results [463].

The negative contrast produced by ferumoxytol in the liver in figure 108 increases in area and decreases in signal intensity at 48 hours post injection. A reason that SPIONs accumulate in large amounts in the liver is due to phagocytosis of scavenger molecules of the RES [464]. The liver uptake of MF66-PEG in figure 109 is similar to ferumoxytol with a visible presence of SPIONs 30 min after the injection. SPIONs are very quickly (i.e. within minutes) recognised by the RES after intravenous injection and therefore cause changes in contrast in the liver shortly after injection [465], [466]. The negative contrast in the liver weakens over time. The time it

takes for the contrast to come back to baseline can vary from one SPION to another and depends on a particular SPION's size, composition, coating and charge. However, some SPIONs might be retained by organs for a very long time which could potentially lead to toxicity effects [466]. In our mouse injected with MF66-PEG, no difference in area or signal intensity can be seen between the 30 min and 48-hour time points. When comparing the 48-hour time points of both SPIONs, MF66-PEG produces more darkening. This is in agreement with table 10; MF66-PEG has a higher relaxivity.

9.4.2. Tumour uptake

In figure 108 the central tumour area does not darken on the GRE images post ferumoxytol injection at any time point. In contrast, in the inferior tumour periphery a dark patch becomes visible as early as 30 minutes post ferumoxytol injection and remains visible also on the 48 hour images. Moore et al. reported from experiments on brain tumours that dextran-coated SPIONs showed a higher accumulation in the periphery of the tumour with more heterogeneous particle locations in the tumour centre near supplying blood vessels [24], [270]. As passive targeting is governed by the EPR effect [467], this can be explained with a higher microvascular density in the tumour periphery. In figure 109 no negative contrast in either tumour core or periphery is observed post injection of MF66-PEG. A possible reason for that could be that the surface area-to-volume ratio was too high that led to aggregation and interactions with plasma proteins. This would result in fast clearance from the vasculature by the RES [468], [469]. In general, this is an important consideration for in vivo biomedical applications of SPIONs. Proteins and other biomolecules will attach to the surface of the SPION which is referred to as the protein corona [470]–[472]. A result of the formation of the protein corona is that active targeting sites on the SPION surface may not be functional. But the protein corona can also lead to undesirable biodistribution including rapid RES clearance for SPIONs that relied on passive targeting [473]–[475].

9.4.3. Size and coating

Because of the defective blood vessel structure of tumours, as explained by the EPR effect [476], the hydrodynamic size of SPIONs is the key factor that determines passive tumour uptake and biodistribution. A hydrodynamic diameter in the range of 20-200 nm is best suited for molecular imaging. If SPIONs are too small (i.e. below 10 nm) and biodegradable, it is likely that they will be cleared from the vasculature by the kidneys [464]. Some authors have reported that within the range of 20-200 nm, smaller SPIONs (below 100 nm) show improved uptake efficiency while larger particles stay in the area where they were injected [477]–[480]. However, Natarjan et al. demonstrated that such a linear size-tumour uptake relationship may

not be true and that other factors need to be taken into consideration as well [481]. One of the novel SPIONs we used in this study was coated with PEG which together with dextran is among the most popular SPION coating materials [464]. PEGylated SPIONs have been reported to reduce interactions between plasma proteins and SPIONs *in vivo* which contributes to their "stealth" characteristic [479], [482]. Cui et al. reported that increasing the length of the PEG chains from 45 (2 kDa, positive zeta potential) to around 227 (10 kDa, negative zeta potential) of otherwise identical SPIONs does delay the clearance by the RES [479]. SPIONs coated with dextran have been reported to be more vulnerable to RES clearance due to the formation of protein corona [473], [483].

9.4.4. Cell biology

Within a tumour, SPIONs have been identified in various different cell types such as tumour macrophages, tumour cells and to some extent in endothelial cells. SPIONs have been shown to transcytose in endothelial cells as a way to enter the interstitium of the tumour [287]. When a tumour grows, monocytes enter the neoplasm from the circulation which give rise to macrophages that infiltrate the tumour and internalise SPIONs [484]–[486]. Macrophages can make up 40-60% of a tumour. Phagocytic cell infiltration in tumours depends on tumour angiogenesis and developmental stage [487], [488] and *in situ* cytokine production [489] among others. Because cell uptake of SPIONs in tumours is not saturable [490], cell internalisation of SPIONs within the tumour is likely governed by endocytosis as has been proven for the transport of other hydrophilic biomolecules. Cells such as macrophages absorbs SPIONs through enclosure in vesicles. There are different types of endocytosis and the exact internalisation process depends on the particular SPION and its characteristics such as shape, size, composition, surface charge and chemistry [491].

9.4.5. Relaxation time constant T_2^* in tumour and liver

In the case of ferumoxytol the mean T_2^* in the tumour drops 30 min after contrast injection from 35.87 ± 11.75 ms to 25.99 ± 9.56 ms (table 12). A more significant drop in T_2^* is observed in the liver from 22.13 ± 1.70 ms to 7.52 ± 2.62 ms. Liu et al. reported an enhancement of the tumour after 60 min post injection of superparamagnetic polymersomes in normal and nude (bearing HeLa tumours). This is up to six times longer than for the liver [492]. It is well known from pre-clinical studies, particularly in mice, that SPIONs become measurable and visible in MR images after a very short time window (e.g. 10 min) post injection in the tail vein. In the above mentioned study by Liu et al, the negative contrast in the liver after intravenous injection was strongest at 50 min post injection. The same authors compared liver and spleen uptake. The later was only half as fast which is another indication that SPIONs are taken up by macrophages

via phagocytosis. The T_2^* value increased again at 48 hours post injection compared to the 30 min time point in the tumour and liver. This is surprising as the liver still shows a significant negative contrast at 48 hours indicating the presence of SPIONs. Several processes are involved in the clearance of SPIONs. The iron particles themselves are being degraded followed by binding to serum proteins such as transferrin. The iron might also be redistributed to other cells and eventually is eliminated. This can be measured through a decline of the serum iron levels. Jain et al. reported SPION clearance required more than 3 weeks [493]. Bourrinet et al. reported more than 7 weeks for the clearance of Fe-Ferumoxtran-10 (dextran coated) [494]. However, other authors have also reported faster clearance times [495]. The reasons for the difference in reported clearance times are different sizes and coatings which have a direct effect on biodistribution but also degradation. In the case of slow clearing SPIONs, it is worth considering that iron from injected and degraded SPIONs has been reported to add to the body's iron storage. The iron will be incorporated into haemoglobin [493]. A slightly different behaviour can be observed in the average T_2^* values of mice (n = 3) injected with MF66-PEG. There is almost no change in the T_2^* in the tumour at 30 min and 48 hours post injection indicating that MF66-PEG does not accumulate in the tumour within that time frame. The liver region shows a rapid drop in T_2^* at 30 min post injection and the T_2^* further decreases slightly at the 48 hour time point.

We did not measure the T_2^* in blood in order to compare it to our measurements in liver and tumour tissue. Tanimoto et al. reported that the T_2 in the liver was lower than in blood after USPIO injection. The likely reason is intracellular compartmentalisation that restricts the water diffusion. Furthermore, iron oxide nanoparticles are distributed more heterogeneously in tissue compared to blood [496]. As the SPION concentration in tissue increases, a saturation effect would be expected based on water exchange [359].

Before we have discussed the formation of the protein corona on SPIONs in vivo. With regards to T_2 and T_2^* measurements in vivo, the protein corona can also alter the magnetic properties of SPIONs which would lead to changes in the MRI contrast behaviour [497]–[499]. The transverse relaxivity depends on water diffusion and exchange in the SPION surrounding. If the functional groups of the coating material are covered with proteins and biomolecules, this will change the water diffusion rate, the hydrodynamic diameter as well as the surface charge. As discussed above, these changes will have a direct impact on the relaxivity characteristics of the SPION [432], [499], [500].

9.4.6. Positive contrast images with SGM

The positive contrast images constructed with the SGM method shown in figure 108 and 109 highlight areas of susceptibility. The SGM images of the ferumoxytol injected mouse (figure 108c – f) confirm the growing area of susceptibility inferior to the tumour. This positive contrast signal increases in accordance with the increasing positive signal in the liver at the 48 hour time point. No positive contrast could be detected inside the tumour area. This shows that the presence of SPIONs in the tumour indicated in the decrease of the T_2^* value in figure 108h is below the detection limit. The contrast behaviour in the liver is surprising. According to figure 108g, the image at 30 min should show the highest positive contrast because the T_2^* value recovers back to the baseline value thereafter. However, the SGM image at the 48 hour time point is the most convincing. In figure 104 the R_2^* curves decreased significantly upon internalisation of the ferumoxytol particles. A similar effect is seen *in vivo* where the T_2^* value recovers after 48 hours because the SPIONs in the liver have been mostly internalised in cells. Evidently, this does not limit the detection capabilities of these SPIONs with the SGM technique. One problem could be the dilution of internalised SPIONs by tumour cells as the tumour growths and proliferates [161]. However, how rapid a particular SPION that successfully targeted tumorous tissue is cleared and falls below the detection limit depends on the SPION and the amount of SPIONs that make it to the tumour. In comparison, the GRE images (figure 108b and 108c) do not display the increased accumulation and internalisation of SPIONs at 48 hours. Thus, SGM images (figure 108e and 108f) are better suited to detect accumulation or internalisation of SPIONs over time which seems to be associated with a change in susceptibility.

In the case of the mouse injected with MF66-PEG, SGM images show no contrast in the tumour and strong positive contrast in the liver at both post injection time points. This is in agreement with the GRE images (figure 109b and 109c) and the behaviour of the T_2^* values (figure 109g) that show no difference in liver contrast between the 30 min and 48 hour time points. However, comparison of the *in vivo* images acquired with ferumoxytol and MF66-PEG suggest that MF66-PEG is better suited due to the much better positive contrast achieved. One potential reason could be that higher amounts of MF66-PEG particles have been accumulated in the liver 48 hours post injection leading to a stronger signal void. This would mean that MF66-PEG was more effectively taken up by the MPS. Under the assumption that both SPIONs investigated predominantly accumulate in the liver, another effect could be responsible for the difference in contrast at 30 minutes. MF66-PEG has much stronger magnetic susceptibility effect as shown in table 10 compared to ferumoxytol. The drop in T_2^* in the liver (figure 109g) remains consistent for both post injection time points which is reflected in similar amount of positive contrast in

figure 109e and 109f. Despite the higher T_2^* values of MF66-PEG post SPION injection (figure 109g) compared to ferumoxytol (figure 108g), the positive contrast achieved in the MF66-PEG injected mouse is more convincing. Overall the *in vivo* data demonstrates that the superior magnetic susceptibility characteristics of MF66-PEG evident through extremely high transverse relaxivity values measured in a phantom, translates to superior *in vivo* imaging behaviour over a commercial sample. Due to the greater susceptibility difference of MF66-PEG, this particle is more likely to be detected by SGM. The magnetic field disturbance caused by the SPIONs must spread beyond the imaging voxel in order to be detected by SGM [152]. For that reason, SPIONs with stronger magnetic moments and areas of higher SPION density are more likely to produce a change in contrast.

A drawback of SGM is that it does not differentiate between susceptibilities introduced by SPIONs and other sources of field inhomogeneities (e.g. air cavities in the guts) [161]. This might be reduced by only taking into account a certain direction of the susceptibility gradients [501]. SGM offers the opportunity for retrospective parameter optimisation. The main advantage however is that SGM does not suffer from the problem to mistake an area of low signal intensity as negative contrast originating from a field distorting particle. In many cases SGM provides a specific positive contrast that is also visible as negative contrast on T_2^*-weighted images.

9.5. Conclusion

In this chapter we have presented four novel superparamagnetic iron oxide nanoparticles for biomedical applications. We assessed these SPIONs for their suitability as MRI contrast agents and investigated the differentiation between free and bound states by MRI in vitro. We investigated one novel SPION that demonstrated superior magnetic susceptibility characteristics *in vivo* where it showed superior imaging behaviour on multi echo gradient-echo images and susceptibility gradient maps compared to a commercial sample. We did not assess the density of the SPIONs in the tissue or its distribution. However, it can be assumed that a stronger $T_2^{(*)}$/SGM effect would have been visible if the density of SPIONs was higher. Our study confirms reports the numerous reports in the literature that the liver is the organ that displays the strongest contrast enhancement and the contrast remains there for longest in an *in vivo* experiment. Even though the impact of the SPION coating is not fully understood yet, SPIONs are ideally smaller (less than 100 nm) and have a hydrophilic coating to provide good contrast on T_2-weighted images and avoid rapid RES clearance.

10. Discussion

This chapter will provide a concluding discussion on the results presented in this thesis. It will, chapter by chapter, provide information on the general role and novel aspects of the thesis within the field and conclude with an outlook.

10.1. Chapter 6 – Implementation and optimisation of established positive contrast MRI sequences

In chapter 6 the implementation and optimisation of three positive contrast MRI techniques, GRASP, IRON and SGM, was described. All three techniques are established and well reported in the literature. GRASP was first described by Seppenwoolde et al. [151] in 2003 under the name white marker imaging. The technique has been demonstrated in various applications since it was first described such as using GRASP to determine ferritin deposition in a thrombus model [156] or to dynamically track implanted stem cells in an in vivo mouse model of myocardial infarction [158]. The IRON technique was first described by Stuber et al. [153] and has proven to be successful in depicting particles and objects that possess a strong magnetic susceptibility. However, not much was published since Stuber first described the technique in 2007. Korosogiou et al. [159] showed that IRON images displayed strong positive contrast in paraaortic lymph nodes post SPION injection. The latest paper came from Gitsioudis et al. [160] in 2013 who investigated the suitability or IRON for vessel imaging (MR angiography) in conjunction with a suitable iron-based MR contrast agent. SGM is the youngest of the three techniques first described by Dahnke et al. [152] in 2008. It has been applied to successfully image prostate marker seeds (in a phantom study) [162], SPION-labelled C6 glioma cells in nude rats [161] and to assess the progression of atherosclerotic plaques in $ApoE^{-/-}$ mice [163]. Published papers so far have focused on the theoretical description of GRASP, IRON and SGM as well as demonstrating their application *in vitro* and *in vivo*. Detailed and practical descriptions of the implementation of these techniques is missing in the literature. We are aware that there are different ways to implement these techniques and implementation will also vary from MR scanner manufacturer. In this thesis we have presented our approach to implement GRASP and IRON in the pulse programming environment for the Philips Achieva scanner. We have incorporated the dynamic function to allow the iteration of a scan with increasing or decreasing one parameter by a pre-defined value for each iteration.

We described the optimisation of GRASP and IRON using different phantoms. Because of the limited number of published positive contrast studies, this work provides an overview of the contrast capabilities of GRASP and IRON on a SPION water phantom as well as a steel ball

bearing in a block of hardened gelatine. For both positive contrast techniques, our results highlight the importance of thorough sequence optimisation. Optimal positive contrast images are only achieved at a particular set of parameters that need to be carefully determined and re-determined when the setup or SPION concentration changes. As part of the optimisation documented in chapter 6, we also present a range of Null results. These are valuable in order to record what does not work. This is particularly important as some of the sequences we tested with our implementations were taken directly from published papers but used with a different MR scanner and setup. This demonstrates again that positive results often do not translate to a different setup/implementation.

The majority of our phantom experiments were done with VSOPs that are no longer available. VSOP-C184 has been assessed by Taupitz et al. [243] who reported a r_1 of 13.97 $mM^{-1}*s^{-1}$ and a r_2 of 33.45 $mM^{-1}*s^{-1}$ at 1.4T. This shows that the nanoparticle also has a strong T_1 effect with a moderate T_2 effect. In this thesis, we present the first positive contrast images obtained on a VSOP phantom where we showed that very convincing positive contrast images could be achieved with our GRASP and SPION implementations. Finally, chapter 6 provides a summary table of IRON sequences that gave in our optimisation the best positive contrast images.

10.2. Chapter 7 – Positive contrast imaging with Dixon

Following on from chapter 6, we implemented and tested a simple modification to the Dixon fat suppression technique for positive contrast imaging of SPIO nanoparticles. Dixon is able to separately image water and fat due to their different resonant frequencies. By modifying Dixon, it must therefore be possible to also separately image off-resonant protons whose Larmor frequency has been affected by the magnetic moment of nearby SPIO nanoparticles. Reeder et al. [339], [340] has described a modified Dixon technique termed IDEAL where water and fat signals are iteratively decomposed. Yu et al. [346] have described a development of the IDEAL reconstruction algorithm that allows T_2^* estimation in addition to water and fat decomposition. This technique allows to image the off-resonance signals that result due to SPION presence.

The IDEAL technique described by Reeder and Yu is a sophisticated post-processing technique that was initially developed for T_2^* quantification while separating water and fat signals. It was never fully assessed and applied for positive contrast imaging of SPIONs. What we have done in this thesis is a simple proof of concept study that shows that the fat suppression implementation of Dixon on a Philips Achieva scanner can be used for to gain positive contrast images of a SPION phantom by changing the water-fat shift parameter. Compared to Reeder and Yu's IDEAL technique, this is simpler to implement and very robust as we utilise the on-

board Dixon implementation that is optimised by Philips. A disadvantage is in the quality of the images we obtained. The simpler approach meant there was less opportunity to specifically optimise the technique for positive contrast imaging. As a future project it might be worth looking into adding functionalities that would allow to control the bandwidth, run an automated optimisation scan that determines the optimal sequence parameters and optimise the artefacts we observed.

As part of this thesis, Dixon as a positive contrast imaging technique was assessed *in vitro* with a VSOP water phantom. Our experiments involved free SPIONs but did not include cell internalised SPIONs as cell internalisation will only have a small effect on the field inhomogeneity introduced by the SPIONs (this is only true for as long as the SPIONs have not been degraded, i.e. short temporal frame). However, a vastly different scenario would be the *in vivo* imaging of localised subcutaneously injected SPIONs or the imaging of SPIONs injected intravenously. The question in this case would be to determine the detection threshold at which the modified Dixon sequence is able to detect any SPION accumulations. Furthermore, the more complex *in vivo* situation which will include air cavities and different types of tissues are another aspect to consider and investigate. As part of this thesis we merely aimed to conduct a proof of concept study that shows that Dixon in its "off-the-shelf" implementation is capable of displaying SPIONs with positive contrast images when modifying the water-fat shift to accommodate the resonant frequencies of protons affected by the dipole field of SPIONs and those that are not (on-resonant protons).

Apart from VSOPs, Dixon was applied to three other SPIONs, one commercial and two novel SPIO nanoparticles. The commercial samples have been described before but to our knowledge were never used for positive contrast imaging. The novel SPIONs were synthesised by the MultiFun consortium (European Community's Seventh Framework Programme, grant agreement number 262943) and this is the first time that they are tested with established positive contrast techniques to test their contrast behaviour and detection limit for positive contrast imaging. We compared our Dixon positive contrast implementation to established methods (implementation and optimisation was described in chapter 6) such as GRASP, IRON and SGM in terms of contrast and SPION concentration dependence.

Originally, Dixon is a fat suppression technique. During the optimisation of our IRON implementation, we used SPIR for fat suppression. SPIR and Dixon have been compared before but to our knowledge, have never been tested on the same positive contrast imaging sequence. Here we compared both fat suppression techniques for IRON imaging using a gradient echo

sequence. We showed that while changing the fat suppression technique did not affect SPION contrast, fat suppression was superior with Dixon.

10.3. Chapter 8 – r2/r2* and r1 relaxivities

In chapter 8 the development of a water phantom was described that was used for all *in vitro* relaxivity measurements. We tested a variety of self-made phantoms using different materials and sample tube sizes. There is little information available in the literature about MRI phantoms for relaxivity measurements. Descriptions that do exist are too specific for general use or too sophisticated making these descriptions inaccessible for many labs. Furthermore, MRI phantoms that minimize magnetic field inhomogeneity can be purchased from a range of manufacturer. However, we could not find a simple phantom description that would allow to build an MRI phantom with resources available in most labs. Our objective therefore was to develop an MRI phantom for relaxivity measurements that was easy and cheap to build, minimising customisation and using equipment available in most labs. The phantom should allow for easy handling including the convenient preparation of samples to be measured, the changing of samples and most importantly deliver reliable results by minimising the magnetic field inhomogeneity within the phantom. We appreciate that such a description might be available elsewhere as part of a larger contrast agent study but unless the authors provide relevant keywords, it is almost impossible to find such descriptions. We are therefore considering to make the phantom description and evaluation available by publishing these results as a brief research note about an effective and easy way to build an MRI water phantom for a variety of contrast agent measurements.

This thesis is part of the MultiFun project (European Community's Seventh Framework Programme, grant agreement number 262943) that had the goal to develop and validate a novel and minimally-invasive nanotechnology system to improve cancer diagnosis and treatment. The ultimate goal was to develop multifunctionalised magnetic nanoparticles to selectively target and eliminate breast and pancreatic cancer cells. The nanoparticles should have improved magnetic features which lead to potential medical applications such as contrast agents and magnetic heating inductors. As part of that project, we have assessed a large collection of novel SPIO nanoparticles and reported their longitudinal and transversal relaxivity values in water, media and cells. Similar work has been done in the past by Rohrer et al. [378] who have characterised and compared commercially available contrast agents (Gd chelates and SPIONs) at different field strengths in water, plasma and blood. The novelty in what is presented her is the MRI characterisation of a range of newly developed superparamagnetic iron oxide nanoparticles. The article by Rohrer et al. published in 2005 was cited more than 1,000 times

showing the interest of the contrast agent community in studies that focus on the MRI characterisation without describing the SPION development or *in vivo* assessment and application. Descriptive publications where several contrast agents, either novel or commercial ones, are summarised and compared for their characteristics such as coating, size, surface charge and relaxivity behaviour add value. It allows other researchers to gain an overview of described SPIONs without having to consult multiple publications. Furthermore, other researchers can look up the MRI behaviour of a SPION that shows otherwise similar characteristics than the one they are working on and use that information for predications, comparisons and discussion. We therefore plan to publish the contents of chapter 8 in a brief and descriptive research note or simply deposit the data in a citeable format in order to make it available to other research groups.

10.4. Chapter 9 – In vivo MRI in animal model of cancer

In chapter 9 we assessed four novel superparamagnetic iron oxide nanoparticles previously presented in chapter 8 and one commercially available SPION (Ferumoxytol) and investigated the differentiation between free and bound states by MRI *in vitro*. We reproduced the results of Kuhlpeter et al. [118] who showed that SPIONs bound to cells can be differentiated by MRI from free SPIONs using $R_2^{(*)}$ imaging. To our knowledge, the results of Kuhlpeter et al., who have only drawn the above conclusion based on measurements with one SPIO nanoparticle, have not been confirmed or reproduced elsewhere. We showed that similar results and effects can be achieved in a different lab with a different set of SPIONs. Our extension of Kuhlpeter's results is also valuable as we confirmed the *in vitro* behaviour with several SPIONs of different sizes, coatings and surface charges.

We investigated one novel SPION (MF66-PEG) that demonstrated superior magnetic susceptibility characteristics *in vivo* where it also showed superior imaging behaviour on multi echo gradient-echo images and susceptibility gradient maps compared to a commercial sample (ferumoxytol). Even though the impact of the SPION coating is not fully understood yet, SPIONs are ideally smaller (less than 100 nm) and have a hydrophilic coating to provide good contrast on T_2-weighted images and avoid rapid RES clearance. Because of its size, MF66-PEG is likely to have almost exclusively accumulated in the liver. Together with its high transverse relaxivity values reported in chapter 9, this explains the strong negative and positive contrast observed on gradient-echo and SGM-processed images, respectively.

We did not assess the biodistribution of MF66-PEG or ferumoxytol and focused on assessing presence of SPIONs via relaxometry. However, it can be assumed that a stronger $T_2^{(*)}$/SGM

effect would have been visible in the tumour if the concentration of SPIONs was higher to overcome the detection threshold. A surprising result was presented in chapter 9 where the increased T_2^* value for ferumoxytol in the liver 48h post injection suggested SPION clearance which does not align with the negative and positive contrast on the MR images. We have discussed this and all other observations thoroughly in chapter 9. There are numerous reports in the literature that the liver is the organ that displays the strongest contrast enhancement and the contrast remains there the longest in an *in vivo* experiment because SPIONs that are not functionalised are predominantly taken up by the mononuclear phagocyte system. Our results confirm that this is also the case for the novel SPION MF66-PEG. Our data and results therefore add to the literature by describing the *in vivo* behaviour of one novel superparamagnetic iron oxide nanoparticle and comparing it to a commercially available sample already characterised by other authors.

In most studies where novel SPIONs are tested *in vivo*, the authors report the T_2 and T_2^*-weighted images. However, we had the opportunity to also process our T_2^*-weighted gradient-echo images with SGM in order to evaluate how the negative contrast we see in gradient-echo images compares to the positive contrast in SGM images. This was not only done for our novel SPION but also for a commercially available contrast agent (ferumoxytol) to allow comparison between the contrast behaviour of both SPIONs and be valuable data for other researchers looking to understand iron oxide contrast behaviour better in the future.

10.5. Outlook

The work for this thesis included novel iron oxide nanoparticles for use as MRI contrast agents and the technical development of MR imaging techniques i.e. positive contrast imaging. After gadolinium chelates, SPIONs are the second big group of MRI contrast agents. A lot of research has focused on the development of SPIONs to ensure homogenous size distribution, favourable magnetic characteristics for MR imaging and non-toxicological profiles to enable *in vivo* utilisation. SPIONs can be multifunctionalised as explained in detail in this thesis and the many parameter that can be changed during SPION synthesis opens up endless routes for research. Examples are testing different coating materials, linkers, doping SPIONs with transition metals to change their magnetic characteristics, attach biomolecules such as antibodies to the surface to increase specificity. Some examples of recent developments are polymer-iron oxide composite nanoparticles for EPR-independent drug delivery [502], VEGF-targeted magnetic nanoparticles for MRI visualisation of brain tumour [503], SPIONs for magnetically-guided and magnetically-responsive drug delivery [504] and the design of multifunctional SPIONs/mitoxantrone-loaded liposomes for both magnetic resonance imaging and targeted

cancer therapy [505]. There have been a large number of papers on various new SPION aspects and many more will follow in the years to come. While those developments are important, it has become harder to keep up with the literature. However, it has become clear that knowledge is still missing on the fate of SPIONs *in vivo* and the exact processes by which they are taken up by cells. In particular the recent papers by Volatron et al. [506] and Kolosnjaj et al. [507] are valuable additions to the literature which describe how Ferritin protein regulates the degradation of iron oxide nanoparticles and the biotransformation of magnetic nanoparticles in the body, respectively. This knowledge is crucial in making the step from the lab to the clinic.

Not much has been published recently on positive contrast imaging techniques for SPION detection. The most attention was given to these techniques during the establishment of several prominent methods such as GRASP, IRON, SGM and IDEAL. This work makes a small contribution by showing that Dixon is able to differentiate SPIONs without much customisation. The next step would be to further improve the implementation and customise it for its purpose as a positive contrast imaging technique. However, positive contrast techniques have decreased in popularity due to its limitations. It is still difficult to differentiate between SPION accumulations and other sources of inhomogeneity, even if the detection threshold can be lowered further. I believe the most promising technique will be post-processing techniques such as SGM and PGM. These can be acquired in addition to any negative contrast sequence and do not require any additional scan time. What is needed is a well optimised gradient echo sequence able of imaging SPION accumulations. In general, positive contrast techniques need to become more specific to the imaging of SPIONs and perhaps the next step is to make SPIONs more chemically and magnetically unique so that a second generation of positive contrast techniques display only their signal.

11. Conclusion

In this work I have given an overview of the magnetic characteristics of SPIONs as well as their synthesis and stabilisation strategies. I have reviewed their applications as nanotheranostic particles with an emphasis on diagnostic methods for cancer and cardiovascular applications. The research that was presented in this work focuses on novel SPIONs that were synthesised with the aim of improved MR contrast characteristics while also allow for hyperthermia applications. This work focused on the assessment of the SPIONs for MRI. Some of the novel particles presented in chapter 8 exhibited very high transverse relaxivity values which translated to strong negative contrast characteristics on multi echo gradient-echo images. We showed that MRI can be used to differentiate between free SPIONs and bound SPIONs for these novel iron oxide-based nanoparticles.

The MR imaging in this work was fosuced on positive contrast imaging which offers unique opportunities to imporve the visibility of areas of SPION uptake that would be difficult to see on T_2^*-weighted images. Positive contrast methods do not suffer from the problem to mistake areas of low signal intensity as negative contrast originating from field inhomogeneities introduced by SPIONs. Well established sequences in the literature are GRadient-echo Acqusition for Superparamagnetic particles with Positive contrast (GRASP), Inversion Recovery with ON-resonant water suppression (IRON) and Susceptbility Gradient Mapping (SGM). In this work I have described how GRASP, IRON and SGM generate positive contrast from signal voids introduced by SPIONs reviewed the literature with respect to their successful applications.

The research in this work demonstrated the superior *in vivo* contrast behaviour on T_2^*-weighted images and susceptibility gradient maps acquired in a postprocessing step of a novel superparamagnetic iron oxide formulation compared to a commercial sample. I implemented the GRASP and IRON techniques and further developed these by devising a dynamic preparation phase to optimise the positive contrast imaging parameters such as the rephasing gardient strength for GRASP and the frequency offset for IRON. We have compared GRASP, IRON and SGM for two novel and two commercial SPIONs and found IRON to be the most reliable technique for all iron oxide formulations that also showed superior quantitative positive contrast behaviour. In Chapter 7 I describe a new positive contrast technique developed by us which is based on the Dixon multi echo sequence. We have demonstrated the capability of the Dixon positive contrast technique to successfully produce positive contrast in vitro and that the contrast produced is linearly dependent on the SPION concentration. Finally, we demonstrated that the Dixon method as a fat suppression technique is superior to SPIR in combination with

IRON positive contrast imaging. Overall, this work makes a contribution to the development of novel SPIONs for nanotheranostic applications. Specifically, new developments for positive contrast imaging with SPIONs are presented that could further improve the usability of these techniques in future diagnostic applications.

MR imaging with iron oxide-based contrast agents offer great opportunities for the advancement of medical diagnostics but is also facing considerable challenges such as the efficient targeting and the bypassing of premature uptake by the cells of the monoculear phagocytic system. However, I believe these challenges can be overcome as more knowledge is acquired about the in vivo behaviour of SPIONs. It is therefore expected that superparamagnetic iron oxide nanoparticles and associated diagnostic and therapeutic technologies will remain a focus of biomedical research in the forseeable future and play a key role in benefiting patients in the future of modern medicine.

References

[1] Z. Fan, P. P. Fu, H. Yu, and P. C. Ray, "Theranostic nanomedicine for cancer detection and treatment," *J. Food Drug Anal.*, vol. 22, no. 1, pp. 3–17, 2014.

[2] T. Lammers, F. Kiessling, W. E. Hennink, and G. Storm, "Nanotheranostics and image-guided drug delivery: current concepts and future directions," *Mol. Pharm.*, vol. 7, no. 6, pp. 1899–1912, 2010.

[3] N. Ahmed, H. Fessi, and A. Elaissari, "Theranostic applications of nanoparticles in cancer," *Drug Discov. Today*, vol. 17, no. 17, pp. 928–934, 2012.

[4] J. Xie, S. Lee, and X. Chen, "Nanoparticle-based theranostic agents," *Adv. Drug Deliv. Rev.*, vol. 62, no. 11, pp. 1064–1079, 2010.

[5] Y. Cohen and S. Y. Shoushan, "Magnetic nanoparticles-based diagnostics and theranostics," *Curr. Opin. Biotechnol.*, vol. 24, no. 4, pp. 672–681, 2013.

[6] S. Laurent and M. Mahmoudi, "Superparamagnetic iron oxide nanoparticles: promises for diagnosis and treatment of cancer," *Int. J. Mol. Epidemiol. Genet.*, vol. 2, no. 4, p. 367, 2011.

[7] T. Yu, D. Hubbard, A. Ray, and H. Ghandehari, "In vivo biodistribution and pharmacokinetics of silica nanoparticles as a function of geometry, porosity and surface characteristics," *J. Control. Release*, vol. 163, no. 1, pp. 46–54, 2012.

[8] P. Zou *et al.*, "Superparamagnetic iron oxide nanotheranostics for targeted cancer cell imaging and pH-dependent intracellular drug release," *Mol. Pharm.*, vol. 7, no. 6, pp. 1974–1984, 2010.

[9] P. C. Brooks, R. A. Clark, and D. A. Cheresh, "Requirement of vascular integrin alpha v beta 3 for angiogenesis," *Science (80-.).*, vol. 264, no. 5158, pp. 569–571, 1994.

[10] Y. Matsumura and H. Maeda, "A new concept for macromolecular therapeutics in cancer chemotherapy: mechanism of tumoritropic accumulation of proteins and the antitumor agent smancs," *Cancer Res.*, vol. 46, no. 12 Part 1, pp. 6387–6392, 1986.

[11] N. Schleich *et al.*, "Dual anticancer drug/superparamagnetic iron oxide-loaded PLGA-based nanoparticles for cancer therapy and magnetic resonance imaging," *Int. J. Pharm.*, vol. 447, no. 1, pp. 94–101, 2013.

[12] Y. Ling, K. Wei, Y. Luo, X. Gao, and S. Zhong, "Dual docetaxel/superparamagnetic iron oxide loaded nanoparticles for both targeting magnetic resonance imaging and cancer therapy," *Biomaterials*, vol. 32, no. 29, pp. 7139–7150, 2011.

[13] Y. Ling, K. Wei, F. Zou, and S. Zhong, "Temozolomide loaded PLGA-based superparamagnetic nanoparticles for magnetic resonance imaging and treatment of malignant glioma," *Int. J. Pharm.*, vol. 430, no. 1, pp. 266–275, 2012.

[14] W. Chen *et al.*, "Multifunctional magnetoplasmonic nanoparticle assemblies for cancer

therapy and diagnostics (theranostics)," *Macromol. Rapid Commun.*, vol. 31, no. 2, pp. 228–236, 2010.

[15] J. Kim *et al.*, "Multifunctional uniform nanoparticles composed of a magnetite nanocrystal core and a mesoporous silica shell for magnetic resonance and fluorescence imaging and for drug delivery," *Angew. Chemie Int. Ed.*, vol. 47, no. 44, pp. 8438–8441, 2008.

[16] N. Kohler, C. Sun, A. Fichtenholtz, J. Gunn, C. Fang, and M. Zhang, "Methotrexate-immobilized poly (ethylene glycol) magnetic nanoparticles for MR imaging and drug delivery," *Small*, vol. 2, no. 6, pp. 785–792, 2006.

[17] I.-K. Park *et al.*, "Determination of nanoparticle vehicle unpackaging by MR imaging of a T 2 magnetic relaxation switch," *Biomaterials*, vol. 29, no. 6, pp. 724–732, 2008.

[18] P. Kocbek, S. Kralj, M. E. Kreft, and J. Kristl, "Targeting intracellular compartments by magnetic polymeric nanoparticles," *Eur. J. Pharm. Sci.*, vol. 50, no. 1, pp. 130–138, 2013.

[19] A. Kumari and S. K. Yadav, "Cellular interactions of therapeutically delivered nanoparticles," *Expert Opin. Drug Deliv.*, vol. 8, no. 2, pp. 141–151, 2011.

[20] H. Maeda, "Vascular permeability in cancer and infection as related to macromolecular drug delivery, with emphasis on the EPR effect for tumor-selective drug targeting," *Proc. Jpn. Acad. Ser. B. Phys. Biol. Sci.*, vol. 88, no. 3, p. 53, 2012.

[21] Y. H. Bae and K. Park, "Targeted drug delivery to tumors: myths, reality and possibility," *J. Control. Release*, vol. 153, no. 3, p. 198, 2011.

[22] F. Danhier, O. Feron, and V. Préat, "To exploit the tumor microenvironment: passive and active tumor targeting of nanocarriers for anti-cancer drug delivery," *J. Control. Release*, vol. 148, no. 2, pp. 135–146, 2010.

[23] R. A. Petros and J. M. DeSimone, "Strategies in the design of nanoparticles for therapeutic applications," *Nat. Rev. Drug Discov.*, vol. 9, no. 8, pp. 615–627, 2010.

[24] R. K. Jain and T. Stylianopoulos, "Delivering nanomedicine to solid tumors," *Nat. Rev. Clin. Oncol.*, vol. 7, no. 11, pp. 653–664, 2010.

[25] J. L. Arias *et al.*, "Squalene based nanocomposites: a new platform for the design of multifunctional pharmaceutical theragnostics," *ACS Nano*, vol. 5, no. 2, pp. 1513–1521, 2011.

[26] A. J. Cole, V. C. Yang, and A. E. David, "Cancer theranostics: the rise of targeted magnetic nanoparticles," *Trends Biotechnol.*, vol. 29, no. 7, pp. 323–332, 2011.

[27] A. Prokop and J. M. Davidson, "Nanovehicular intracellular delivery systems," *J. Pharm. Sci.*, vol. 97, no. 9, pp. 3518–3590, 2008.

[28] M. Wang and M. Thanou, "Targeting nanoparticles to cancer," *Pharmacol. Res.*, vol. 62, no. 2, pp. 90–99, 2010.

[29] G. Hong, R. Yuan, B. Liang, J. Shen, X. Yang, and X. Shuai, "Folate-functionalized polymeric micelle as hepatic carcinoma-targeted, MRI-ultrasensitive delivery system of antitumor drugs," *Biomed. Microdevices*, vol. 10, no. 5, pp. 693–700, 2008.

[30] X. Yang *et al.*, "Multifunctional SPIO/DOX-loaded wormlike polymer vesicles for cancer therapy and MR imaging," *Biomaterials*, vol. 31, no. 34, pp. 9065–9073, 2010.

[31] M. Liong *et al.*, "Multifunctional inorganic nanoparticles for imaging, targeting, and drug delivery," *ACS Nano*, vol. 2, no. 5, pp. 889–896, 2008.

[32] N. Kohler, C. Sun, J. Wang, and M. Zhang, "Methotrexate-modified superparamagnetic nanoparticles and their intracellular uptake into human cancer cells," *Langmuir*, vol. 21, no. 19, pp. 8858–8864, 2005.

[33] N. Nasongkla *et al.*, "Multifunctional polymeric micelles as cancer-targeted, MRI-ultrasensitive drug delivery systems," *Nano Lett.*, vol. 6, no. 11, pp. 2427–2430, 2006.

[34] A. H. Schmieder *et al.*, "Three-dimensional MR mapping of angiogenesis with α5β1 (αvβ3)-targeted theranostic nanoparticles in the MDA-MB-435 xenograft mouse model," *FASEB J.*, vol. 22, no. 12, pp. 4179–4189, 2008.

[35] J. S. Guthi *et al.*, "MRI-visible micellar nanomedicine for targeted drug delivery to lung cancer cells," *Mol. Pharm.*, vol. 7, no. 1, pp. 32–40, 2009.

[36] F. Danhier, A. Le Breton, and V. Préat, "RGD-based strategies to target alpha (v) beta (3) integrin in cancer therapy and diagnosis," *Mol. Pharm.*, vol. 9, no. 11, pp. 2961–2973, 2012.

[37] K. Temming, R. M. Schiffelers, G. Molema, and R. J. Kok, "RGD-based strategies for selective delivery of therapeutics and imaging agents to the tumour vasculature," *Drug Resist. Updat.*, vol. 8, no. 6, pp. 381–402, 2005.

[38] J. L Arias, "Drug targeting strategies in cancer treatment: an overview," *Mini Rev. Med. Chem.*, vol. 11, no. 1, pp. 1–17, 2011.

[39] T. Lammers, W. E. Hennink, and G. Storm, "Tumour-targeted nanomedicines: principles and practice," *Br. J. Cancer*, vol. 99, no. 3, pp. 392–397, 2008.

[40] V. P. Torchilin, "Targeted polymeric micelles for delivery of poorly soluble drugs," *Cell. Mol. Life Sci. C.*, vol. 61, no. 19–20, pp. 2549–2559, 2004.

[41] E. Gullotti and Y. Yeo, "Extracellularly activated nanocarriers: a new paradigm of tumor targeted drug delivery," *Mol. Pharm.*, vol. 6, no. 4, pp. 1041–1051, 2009.

[42] S.-T. Feng *et al.*, "pH-Sensitive Nanomicelles for Controlled and Efficient Drug Delivery to Human Colorectal Carcinoma LoVo Cells," *PLoS One*, vol. 9, no. 6, p. e100732, 2014.

[43] X. Li, H. Li, W. Yi, J. Chen, and B. Liang, "Acid-triggered core cross-linked nanomicelles for targeted drug delivery and magnetic resonance imaging in liver cancer cells," *Int. J. Nanomedicine*, vol. 8, p. 3019, 2013.

[44] M. M. Yallapu, S. F. Othman, E. T. Curtis, B. K. Gupta, M. Jaggi, and S. C. Chauhan, "Multi-functional magnetic nanoparticles for magnetic resonance imaging and cancer therapy," *Biomaterials*, vol. 32, no. 7, pp. 1890–1905, 2011.

[45] G. Baldi *et al.*, "In vivo anticancer evaluation of the hyperthermic efficacy of anti-human epidermal growth factor receptor-targeted PEG-based nanocarrier containing magnetic nanoparticles," *Int. J. Nanomedicine*, vol. 9, p. 3037, 2014.

[46] M. Johannsen *et al.*, "Clinical hyperthermia of prostate cancer using magnetic nanoparticles: presentation of a new interstitial technique," *Int. J. Hyperth.*, vol. 21, no. 7, pp. 637–647, 2005.

[47] K. Maier-Hauff *et al.*, "Efficacy and safety of intratumoral thermotherapy using magnetic iron-oxide nanoparticles combined with external beam radiotherapy on patients with recurrent glioblastoma multiforme," *J. Neurooncol.*, vol. 103, no. 2, pp. 317–324, 2011.

[48] G. Malietzis *et al.*, "High-intensity focused ultrasound: advances in technology and experimental trials support enhanced utility of focused ultrasound surgery in oncology," *Br. J. Radiol.*, vol. 86, no. 1024, 2013.

[49] A. Yudina and C. Moonen, "Ultrasound-induced cell permeabilisation and hyperthermia: strategies for local delivery of compounds with intracellular mode of action," *Int. J. Hyperth.*, vol. 28, no. 4, pp. 311–319, 2012.

[50] S. A. Abouelmagd, H. Hyun, and Y. Yeo, "Extracellularly activatable nanocarriers for drug delivery to tumors," *Expert Opin. Drug Deliv.*, vol. 11, no. 10, pp. 1601–1618, 2014.

[51] P.-S. Yang, F.-I. Tung, H.-P. Chen, T.-Y. Liu, and Y.-Y. Lin, "A novel bubble-forming material for preparing hydrophobic-agent-loaded bubbles with theranostic functionality," *Acta Biomater.*, vol. 10, no. 8, pp. 3762–3774, 2014.

[52] A. S. Lübbe *et al.*, "Preclinical experiences with magnetic drug targeting: tolerance and efficacy," *Cancer Res.*, vol. 56, no. 20, pp. 4694–4701, 1996.

[53] H.-W. Yang *et al.*, "An epirubicin–conjugated nanocarrier with MRI function to overcome lethal multidrug-resistant bladder cancer," *Biomaterials*, vol. 33, no. 15, pp. 3919–3930, 2012.

[54] C. Alexiou *et al.*, "Locoregional cancer treatment with magnetic drug targeting," *Cancer Res.*, vol. 60, no. 23, pp. 6641–6648, 2000.

[55] H.-Y. Huang, Y.-T. Shieh, C.-M. Shih, and Y.-K. Twu, "Magnetic chitosan/iron (II, III) oxide nanoparticles prepared by spray-drying," *Carbohydr. Polym.*, vol. 81, no. 4, pp. 906–910, 2010.

[56] J. Riegler, J. A. Wells, P. G. Kyrtatos, A. N. Price, Q. A. Pankhurst, and M. F. Lythgoe, "Targeted magnetic delivery and tracking of cells using a magnetic resonance imaging

system," *Biomaterials*, vol. 31, no. 20, pp. 5366–5371, 2010.

[57] B. Polyak *et al.*, "High field gradient targeting of magnetic nanoparticle-loaded endothelial cells to the surfaces of steel stents," *Proc. Natl. Acad. Sci.*, vol. 105, no. 2, pp. 698–703, 2008.

[58] X. Yang *et al.*, "cRGD-functionalized, DOX-conjugated, and 64 Cu-labeled superparamagnetic iron oxide nanoparticles for targeted anticancer drug delivery and PET/MR imaging," *Biomaterials*, vol. 32, no. 17, pp. 4151–4160, 2011.

[59] P. Pradhan *et al.*, "Targeted temperature sensitive magnetic liposomes for thermo-chemotherapy," *J. Control. Release*, vol. 142, no. 1, pp. 108–121, 2010.

[60] C.-H. Fan *et al.*, "SPIO-conjugated, doxorubicin-loaded microbubbles for concurrent MRI and focused-ultrasound enhanced brain-tumor drug delivery," *Biomaterials*, vol. 34, no. 14, pp. 3706–3715, 2013.

[61] D. Wang *et al.*, "Targeted iron-oxide nanoparticle for photodynamic therapy and imaging of head and neck cancer," *ACS Nano*, vol. 8, no. 7, pp. 6620–6632, 2014.

[62] G. R. Reddy *et al.*, "Vascular targeted nanoparticles for imaging and treatment of brain tumors," *Clin. Cancer Res.*, vol. 12, no. 22, pp. 6677–6686, 2006.

[63] N. Schleich *et al.*, "Comparison of active, passive and magnetic targeting to tumors of multifunctional paclitaxel/SPIO-loaded nanoparticles for tumor imaging and therapy," *J. Control. Release*, vol. 194, pp. 82–91, 2014.

[64] Z. Li *et al.*, "PEG-functionalized iron oxide nanoclusters loaded with chlorin e6 for targeted, NIR light induced, photodynamic therapy," *Biomaterials*, vol. 34, no. 36, pp. 9160–9170, 2013.

[65] S. S. Kelkar and T. M. Reineke, "Theranostics: combining imaging and therapy," *Bioconjug. Chem.*, vol. 22, no. 10, pp. 1879–1903, 2011.

[66] B. Moses and Y. You, "Emerging Strategies for Controlling Drug Release by Using Visible/Near IR Light," *Med. Chem. (Los. Angeles).*, vol. 3, no. 32, 2013.

[67] S. Mura and P. Couvreur, "Nanotheranostics for personalized medicine," *Adv. Drug Deliv. Rev.*, vol. 64, no. 13, pp. 1394–1416, 2012.

[68] L. H. Reddy, J. L. Arias, J. Nicolas, and P. Couvreur, "Magnetic nanoparticles: design and characterization, toxicity and biocompatibility, pharmaceutical and biomedical applications," *Chem. Rev.*, vol. 112, no. 11, pp. 5818–5878, 2012.

[69] S. Laurent, A. A. Saei, S. Behzadi, A. Panahifar, and M. Mahmoudi, "Superparamagnetic iron oxide nanoparticles for delivery of therapeutic agents: opportunities and challenges," *Expert Opin. Drug Deliv.*, vol. 11, no. 9, pp. 1449–1470, 2014.

[70] D. Peer, J. M. Karp, S. Hong, O. C. Farokhzad, R. Margalit, and R. Langer, "Nanocarriers as an emerging platform for cancer therapy," *Nat. Nanotechnol.*, vol. 2,

no. 12, pp. 751–760, 2007.

[71] T. Lammers, F. Kiessling, W. E. Hennink, and G. Storm, “Drug targeting to tumors: principles, pitfalls and (pre-) clinical progress,” *J. Control. Release*, vol. 161, no. 2, pp. 175–187, 2012.

[72] S. Svenson, “Theranostics: are we there yet?,” *Mol. Pharm.*, vol. 10, no. 3, pp. 848–856, 2013.

[73] A. Filler, “The History, Development and Impact of Computed Imaging in Neurological Diagnosis and Neurosurgery: CT, MRI and DTI,” *Internet J. Neurosurg.*, vol. 7, pp. 1–85, 2010.

[74] C. P. Enz, *No Time to be Brief: A scientific biography of Wolfgang Pauli*. Oxford: Oxford University Press, 2010.

[75] I. I. Rabi, J. R. Zacharias, S. Millman, and P. Kusch, “A New Method of Measuring Nuclear Magnetic Moment,” *Phys. Rev.*, vol. 53, no. 4, p. 318, 1938.

[76] “The Nobel Prize in Physics 1944,” *Nobelprize.org. Nobel Media AB 2014*. [Online]. Available: http://www.nobelprize.org/nobel_prizes/physics/laureates/1944/. [Accessed: 16-Jul-2017].

[77] E. M. Purcell, H. C. Torrey, and R. V Pound, “Resonance Absorption by Nuclear Magnetic Moments in a Solid,” *Phys. Rev.*, vol. 69, no. 1–2, pp. 37–38, 1946.

[78] F. Bloch, “Nuclear Induction,” *Phys. Rev.*, vol. 70, no. 7–8, pp. 460–474, 1946.

[79] Nobelprize.org Nobel Media AB 2014, “The Nobel Prize in Physics 1952.” [Online]. Available: http://www.nobelprize.org/nobel_prizes/physics/laureates/1952/.

[80] R. Damadian, “Tumor Detection by Nuclear Magnetic Resonance,” *Science (80-.).*, vol. 171, no. 3976, pp. 1151–1153, 1971.

[81] P. C. Lauterbur, “Image Formation by Induced Local Interactions: Examples Employing Nuclear Magnetic Resonance,” *Nature*, vol. 242, no. 5394, pp. 190–191, 1973.

[82] A. Kumar, D. Welti, and R. R. Ernst, “NMR Fourier zeugmatography,” *J. Magn. Reson.*, vol. 18, no. 1, pp. 69–83, 1975.

[83] R. N. Bracewell, *The Fourier Transform and Its Applications*. McGraw Hill, 2000.

[84] F. W. Wehrli, “On the 2003 Nobel Prize in medicine or physiology awarded to Paul C. Lauterbur and Sir Peter Mansfield,” *Magn. Reson. Med.*, vol. 51, no. 1, pp. 1–3, 2004.

[85] Nobelprize.org Nobel Media AB 2014, “The Nobel Prize in Physiology or Medicine 2003 .” [Online]. Available: http://www.nobelprize.org/nobel_prizes/medicine/laureates/2003/.

[86] R. A. de Graaf, *In Vivo NMR Spectroscopy*, 2nd editio. Chichester, West Sussex, England: John Wiley & Sons Ltd, 2007.

[87] Z.-P. Liang and P. C. Lauterbur, *Principles of Magnetic Resonance Imaging*. NJ, USA: IEEE Press, 2000.

[88] D. G. Nishimura, *Principles of Magnetic Resonance Imaging*. Rayleigh, North Carolina, US: Lulu.com, 2010.

[89] R. W. Brown, Y.-C. N. Cheng, E. M. Haacke, M. R. Thompson, and R. Venkatesan, *Magnetic Resonance Imaging: Physical Principles and Sequence Design*, 2nd editio. Hoboken, New Jersey, US: John Wiley & Sons, Inc., 2014.

[90] W. R. Nitz and P. Reimer, "Contrast mechanisms in MR imaging," *Eur. Radiol.*, vol. 9, no. 6, pp. 1032–1046, 1999.

[91] M. A. Bernstein, K. F. King, and X. J. Zhou, *Handbook of MRI pulse sequences*. Elsevier, 2004.

[92] D. W. McRobbie, E. A. Moore, M. J. Graves, and M. R. Prince, *MRI from Picture to Proton*. Cambridge university press, 2006.

[93] V. S. Lee, *Cardiovascular MRI: physical principles to practical protocols*. Lippincott Williams & Wilkins, 2006.

[94] M. F. Kircher *et al.*, "A brain tumor molecular imaging strategy using a new triple-modality MRI-photoacoustic-Raman nanoparticle," *Nat. Med.*, vol. 18, no. 5, pp. 829–834, 2012.

[95] P. Kellman and M. S. Hansen, "T1-mapping in the heart: accuracy and precision," *J Cardiovasc Magn Reson*, vol. 16, no. 2, 2014.

[96] D. J. Pennell *et al.*, "Clinical indications for cardiovascular magnetic resonance (CMR): Consensus Panel report," *Eur. Heart J.*, vol. 25, no. 21, pp. 1940–1965, 2004.

[97] D. R. Messroghli, A. Radjenovic, S. Kozerke, D. M. Higgins, M. U. Sivananthan, and J. P. Ridgway, "Modified Look-Locker inversion recovery (MOLLI) for high-resolution T1 mapping of the heart," *Magn. Reson. Med.*, vol. 52, no. 1, pp. 141–146, 2004.

[98] O. P. Simonetti *et al.*, "An Improved MR Imaging Technique for the Visualization of Myocardial Infarction 1," *Radiology*, vol. 218, no. 1, pp. 215–223, 2001.

[99] U. Blume, J. Orbell, M. Waltham, A. Smith, R. Razavi, and T. Schaeffter, "3D T 1-mapping for the characterization of deep vein thrombosis," *Magn. Reson. Mater. Physics, Biol. Med.*, vol. 22, no. 6, pp. 375–383, 2009.

[100] S. C. L. Deoni, "High-resolution T1 mapping of the brain at 3T with driven equilibrium single pulse observation of T1 with high-speed incorporation of RF field inhomogeneities (DESPOT1-HIFI)," *J. Magn. Reson. Imaging*, vol. 26, no. 4, pp. 1106–1111, 2007.

[101] H. Vrenken *et al.*, "Whole-Brain T1 Mapping in Multiple Sclerosis: Global Changes of Normal-appearing Gray and White Matter 1," *Radiology*, vol. 240, no. 3, pp. 811–820, 2006.

[102] R. R. Edelman, D. Chien, and D. Kim, "Fast selective black blood MR imaging,"

Radiology, vol. 181, no. 3, pp. 655–660, 1991.

[103] K. Scheffler and S. Lehnhardt, "Principles and applications of balanced SSFP techniques," *Eur. Radiol.*, vol. 13, no. 11, pp. 2409–2418, 2003.

[104] G. B. Chavhan, P. S. Babyn, B. G. Jankharia, H.-L. M. Cheng, and M. M. Shroff, "Steady-State MR Imaging Sequences: Physics, Classification, and Clinical Applications 1," *Radiographics*, vol. 28, no. 4, pp. 1147–1160, 2008.

[105] S. K. Piechnik *et al.*, "Shortened Modified Look-Locker Inversion recovery (ShMOLLI) for clinical myocardial T1-mapping at 1.5 and 3 T within a 9 heartbeat breathhold," *J. Cardiovasc. Magn. Reson.*, vol. 12, no. 1, p. 69, 2010.

[106] F. Schmitt, M. K. Stehling, and R. Turner, *Echo-planar imaging*. Springer Science & Business Media, 1998.

[107] R. L. DeLaPaz, "Echo-planar imaging," *Radiographics*, vol. 14, no. 5, pp. 1045–1058, 1994.

[108] P. Gowland and P. Mansfield, "Accurate measurement of T1in vivo in less than 3 seconds using echo-planar imaging," *Magn. Reson. Med.*, vol. 30, no. 3, pp. 351–354, 1993.

[109] A. J. Freeman, P. A. Gowland, and P. Mansfield, "Optimization of the ultrafast look-locker echo-planar imaging T 1 mapping sequence," *Magn. Reson. Imaging*, vol. 16, no. 7, pp. 765–772, 1998.

[110] M. Karlsson and B. Nordell, "Phantom and in vivo study of the look–locher T 1 mapping method," *Magn. Reson. Imaging*, vol. 17, no. 10, pp. 1481–1488, 1999.

[111] A. Freeman *et al.*, "DynamicT 1 studies of gadolinium uptake in brain tumors using LL-EPI," *Magn. Reson. Mater. Physics, Biol. Med.*, vol. 2, no. 3, pp. 409–412, 1994.

[112] P. A. Gowland *et al.*, "In vivo relaxation time measurements in the human placenta using echo planar imaging at 0.5 T," *Magn. Reson. Imaging*, vol. 16, no. 3, pp. 241–247, 1998.

[113] A. Haase, J. Frahm, D. Matthaei, W. Hanicke, and K. D. Merboldt, "FLASH imaging. Rapid NMR imaging using low flip-angle pulses," *J. Magn. Reson.*, vol. 67, no. 2, pp. 258–266, 1986.

[114] R. Deichmann and A. Haase, "Quantification of T 1 values by SNAPSHOT-FLASH NMR imaging," *J. Magn. Reson.*, vol. 96, no. 3, pp. 608–612, 1992.

[115] K. Chow, J. A. Flewitt, J. D. Green, J. J. Pagano, M. G. Friedrich, and R. B. Thompson, "Saturation recovery single-shot acquisition (SASHA) for myocardial T1 mapping," *Magn. Reson. Med.*, vol. 71, no. 6, pp. 2082–2095, 2014.

[116] S. C. L. Deoni, B. K. Rutt, and T. M. Peters, "Rapid combined T1 and T2 mapping using gradient recalled acquisition in the steady state," *Magn. Reson. Med.*, vol. 49, no. 3, pp. 515–526, 2003.

[117] H. Z. Wang, S. J. Riederer, and J. N. Lee, "Optimizing the precision in T1 relaxation estimation using limited flip angles," *Magn. Reson. Med.*, vol. 5, no. 5, pp. 399–416, 1987.

[118] R. Kuhlpeter *et al.*, "R2 and R2*mapping for sensing cell-bound superparamagnetic nanoparticles: In vitro and murine in vivo testing," *Radiology*, vol. 245, no. 2, pp. 449–457, 2007.

[119] J. Xie *et al.*, "PET/NIRF/MRI triple functional iron oxide nanoparticles," *Biomaterials*, vol. 31, no. 11, pp. 3016–3022, 2010.

[120] I. Chan *et al.*, "Detection of prostate cancer by integration of line-scan diffusion, T2-mapping and T2-weighted magnetic resonance imaging; a multichannel statistical classifier," *Med. Phys.*, vol. 30, no. 9, pp. 2390–2398, 2003.

[121] D. L. Langer, T. H. van der Kwast, A. J. Evans, J. Trachtenberg, B. C. Wilson, and M. A. Haider, "Prostate cancer detection with multi-parametric MRI: Logistic regression analysis of quantitative T2, diffusion-weighted imaging, and dynamic contrast-enhanced MRI," *J. Magn. Reson. Imaging*, vol. 30, no. 2, pp. 327–334, 2009.

[122] W. Liu *et al.*, "Accelerated T2 mapping for characterization of prostate cancer," *Magn. Reson. Med.*, vol. 65, no. 5, pp. 1400–1406, 2011.

[123] P. Gibbs, D. J. Tozer, G. P. Liney, and L. W. Turnbull, "Comparison of quantitative T2 mapping and diffusion-weighted imaging in the normal and pathologic prostate," *Magn. Reson. Med.*, vol. 46, no. 6, pp. 1054–1058, 2001.

[124] A. H. Aletras *et al.*, "Retrospective determination of the area at risk for reperfused acute myocardial infarction with T2-weighted cardiac magnetic resonance imaging histopathological and displacement encoding with stimulated echoes (DENSE) functional validations," *Circulation*, vol. 113, no. 15, pp. 1865–1870, 2006.

[125] A. E. Arai, S. Leung, and P. Kellman, "Controversies in cardiovascular MR imaging: reasons why imaging myocardial T2 has clinical and pathophysiologic value in acute myocardial infarction," *Radiology*, vol. 265, no. 1, pp. 23–32, 2012.

[126] H. Abdel-Aty *et al.*, "Diagnostic performance of cardiovascular magnetic resonance in patients with suspected acute myocarditis: comparison of different approaches," *J. Am. Coll. Cardiol.*, vol. 45, no. 11, pp. 1815–1822, 2005.

[127] H. B. W. Larsson *et al.*, "Assessment of demyelination, edema, and gliosis by in vivo determination of T1 and T2 in the brain of patients with acute attack of multiple sclerosis," *Magn. Reson. Med.*, vol. 11, no. 3, pp. 337–348, 1989.

[128] A. Pitkanen *et al.*, "Severity of hippocampal atrophy correlates with the prolongation of MRI T sub 2 relaxation time in temporal lobe epilepsy but not in Alzheimer's disease," *Neurology*, vol. 46, no. 6, pp. 1724–1730, 1996.

[129] T. Carr and P. Conlon, “Frontal, temporal, and striatal proton relaxation times in schizophrenic patients and normal comparison subjects,” *Am J Psychiatry*, vol. 1, no. 49, p. 549, 1992.

[130] S. C. L. Deoni, T. M. Peters, and B. K. Rutt, “High-resolution T1 and T2 mapping of the brain in a clinically acceptable time with DESPOT1 and DESPOT2,” *Magn. Reson. Med.*, vol. 53, no. 1, pp. 237–241, 2005.

[131] A. Haase, “Snapshot flash mri. applications to t1, t2, and chemical-shift imaging,” *Magn. Reson. Med.*, vol. 13, no. 1, pp. 77–89, 1990.

[132] T. Gneiting, S. Nekolla, J. Sysha, M. Kienlin, and A. Haase, “Fast T2 imaging with Carr-Purcell snapshot-flash,” in *SMRM, 11th Annual Meeting*, 1992, p. 1346.

[133] J. H. Brittain, G. Wight, J. Pauly, and D. G. Nishimura, “Flow-insensitive magnetization-prepared T2 measurement,” in *SMRM, 12th Annual Meeting*, 1993, p. 1216.

[134] J. H. Brittain, B. S. Hu, G. A. Wright, C. H. Meyer, A. Macovski, and D. G. Nishimura, “Coronary angiography with magnetization-prepared T2 contrast,” *Magn. Reson. Med.*, vol. 33, no. 5, pp. 689–696, 1995.

[135] M. H. Levitt, R. Freeman, and T. Frenkiel, “Broadband heteronuclear decoupling,” *J. Magn. Reson.*, vol. 47, no. 2, pp. 328–330, 1982.

[136] A. J. Shaka, S. P. Rucker, and A. Pines, “Iterative carr-purcell trains,” *J. Magn. Reson.*, vol. 77, no. 3, pp. 606–611, 1988.

[137] M. H. Levitt and R. Freeman, “Compensation for pulse imperfections in NMR spin-echo experiments,” *J. Magn. Reson.*, vol. 43, no. 1, pp. 65–80, 1981.

[138] H. Ding *et al.*, “Three-dimensional whole-heart T2 mapping at 3T,” *Magn. Reson. Med.*, vol. 74, no. 3, pp. 803–816, 2014.

[139] R. Nezafat, M. Stuber, R. Ouwerkerk, A. M. Gharib, M. Y. Desai, and R. I. Pettigrew, “B1-insensitive T2 preparation for improved coronary magnetic resonance angiography at 3 T,” *Magn. Reson. Med.*, vol. 55, no. 4, pp. 858–864, 2006.

[140] S. Baudrexel *et al.*, “Rapid single-scan T 2*-mapping using exponential excitation pulses and image-based correction for linear background gradients,” *Magn. Reson. Med.*, vol. 62, no. 1, pp. 263–268, 2009.

[141] G. B. Chavhan, P. S. Babyn, B. Thomas, M. M. Shroff, and E. M. Haacke, “Principles, Techniques, and Applications of T2*-based MR Imaging and Its Special Applications,” *Radiographics*, vol. 29, no. 5, pp. 1433-U272, 2009.

[142] X. Yang, S. Sammet, P. Schmalbrock, and M. V Knopp, “Postprocessing correction for distortions in T2* decay caused by quadratic cross-slice B0 inhomogeneity,” *Magn. Reson. Med.*, vol. 63, no. 5, pp. 1258–1268, 2010.

[143] H. Dahnke and T. Schaeffter, “Limits of detection of SPIO at 3.0 T using T-2* relaxometry,” *Magn. Reson. Med.*, vol. 53, no. 5, pp. 1202–1206, 2005.

[144] J. Dennie, J. B. Mandeville, J. L. Boxerman, S. D. Packard, B. R. Rosen, and R. M. Weisskoff, “NMR imaging of changes in vascular morphology due to tumor angiogenesis,” *Magn. Reson. Med.*, vol. 40, no. 6, pp. 793–799, 1998.

[145] R. J. Ordidge, J. M. Gorell, J. C. Deniau, R. A. Knight, and J. A. Helpern, “Assessment of relative brain iron concentrations using T2-weighted and T2*-weighted MRI at 3 Tesla,” *Magn. Reson. Med.*, vol. 32, no. 3, pp. 335–341, 1994.

[146] Z. H. Cho and Y. M. Ro, “Reduction of susceptibility artifact in gradient-echo imaging,” *Magn. Reson. Med.*, vol. 23, no. 1, pp. 193–200, 1992.

[147] J. M. Wild, W. R. W. Martin, and P. S. Allen, “Multiple gradient echo sequence optimized for rapid, single-scan mapping of R-2(*) at high B-0,” *Magn. Reson. Med.*, vol. 48, no. 5, pp. 867–876, 2002.

[148] M. A. Fernández-Seara and F. W. Wehrli, “Postprocessing technique to correct for background gradients in image-based R* 2 measurements,” *Magn. Reson. Med.*, vol. 44, no. 3, pp. 358–366, 2000.

[149] J. R. Reichenbach, R. Venkatesan, D. A. Yablonskiy, M. R. Thompson, S. Lai, and E. M. Haacke, “Theory and application of static field inhomogeneity effects in gradient-echo imaging,” *J. Magn. Reson. Imaging*, vol. 7, no. 2, pp. 266–279, 1997.

[150] E. Vonken, M. Schär, J. Yu, C. J. G. Bakker, and M. Stuber, “Direct in vitro comparison of six three-dimensional positive contrast methods for susceptibility marker imaging,” *J. Magn. Reson. Imaging*, vol. 38, no. 2, pp. 344–357, 2013.

[151] J. H. Seppenwoolde, M. A. Viergever, and C. J. G. Bakker, “Passive tracking exploiting local signal conservation: The white marker phenomenon,” *Magn. Reson. Med.*, vol. 50, no. 4, pp. 784–790, 2003.

[152] H. Dahnke, W. Liu, D. Herzka, J. A. Frank, and T. Schaeffter, “Susceptibility gradient mapping (SGM): A new postprocessing method for positive contrast generation applied to superparamagnetic iron oxide particle (SPIO)-labeled cells,” *Magn. Reson. Med.*, vol. 60, no. 3, pp. 595–603, 2008.

[153] M. Stuber *et al.*, “Positive contrast visualization of iron oxide-labeled stem cells using inversion-recovery with ON-Resonant water suppression (IRON),” *Magn. Reson. Med.*, vol. 58, no. 5, pp. 1072–1077, 2007.

[154] R. Dharmakumar, I. Koktzoglou, and D. Li, “Generating positive contrast from off-resonant spins with steady-state free precession magnetic resonance imaging: theory and proof-of-principle experiments,” *Phys. Med. Biol.*, vol. 51, no. 17, p. 4201, 2006.

[155] V. Mani, K. C. Briley-Saebo, V. V Itskovich, D. D. Samber, and Z. A. Fayad, “GRadient

echo Acquisition for Superparamagnetic particles with positive contrast (GRASP): Sequence characterization in membrane and glass superparamagnetic iron oxide phantoms at 1.5T and 3T," *Magn. Reson. Med.*, vol. 55, no. 1, pp. 126–135, 2006.

[156] V. Mani, K. C. Briley-Saebo, F. Hyafil, and Z. A. Fayad, "Feasibility of in vivo identification of endogenous ferritin with positive contrast MRI in rabbit carotid crush injury using GRASP," *Magn. Reson. Med.*, vol. 56, no. 5, pp. 1096–1106, 2006.

[157] J. H. Seppenwoolde, K. L. Vincken, and C. J. G. Bakker, "White-marker imaging - Separating magnetic susceptibility effects from partial volume effects," *Magn. Reson. Med.*, vol. 58, no. 3, pp. 605–609, 2007.

[158] V. Mani *et al.*, "Serial in vivo positive contrast MRI of iron oxide-labeled embiryonic stem cell-derived cardiac precursor cells in a mouse model of myocardial infarction," *Magn. Reson. Med.*, vol. 60, no. 1, pp. 73–81, 2008.

[159] G. Korosogiou *et al.*, "Positive contrast MR-lymphography using inversion recovery with ON-resonant water suppression (IRON)," *J. Magn. Reson. Imaging*, vol. 27, no. 5, pp. 1175–1180, 2008.

[160] G. Gitsioudis *et al.*, "Steady-state equilibrium phase inversion recovery ON-resonant water suppression (IRON) MR angiography in conjunction with superparamagnetic nanoparticles. A robust technique for imaging within a wide range of contrast agent dosages," *J. Magn. Reson. Imaging*, vol. 38, no. 4, pp. 836–844, 2013.

[161] W. Liu, H. Dahnke, E. K. Jordan, T. Schaeffter, and J. A. Frank, "In vivo MRI using positive-contrast techniques in detection of cells labeled with superparamagnetic iron oxide nanoparticles," *Nmr Biomed.*, vol. 21, no. 3, pp. 242–250, 2008.

[162] G. Varma *et al.*, "Utilizing different methods for visualizing susceptibility from a single multi-gradient echo dataset," *Magn. Reson. Mater. Phys. Biol. Med.*, vol. 22, no. 5, pp. 297–308, 2009.

[163] M. R. Makowski *et al.*, "Noninvasive Assessment of Atherosclerotic Plaque Progression in ApoE(-/-) Mice Using Susceptibility Gradient Mapping," *Circ. Imaging*, vol. 4, no. 3, pp. 295-U153, 2011.

[164] G. Varma *et al.*, "Positive Visualization of Implanted Devices With Susceptibility Gradient Mapping Using the Original Resolution," *Magn. Reson. Med.*, vol. 65, no. 5, pp. 1483–1490, 2011.

[165] R. Dharmakumar, I. Koktzoglou, and D. Li, "Factors influencing fast low angle positive contrast steady-state free precession (FLAPS) magnetic resonance imaging," *Phys. Med. Biol.*, vol. 52, no. 11, p. 3261, 2007.

[166] I. Koktzoglou, D. Li, and R. Dharmakumar, "Dephased FLAPS for improved visualization of susceptibility-shifted passive devices for real-time interventional MRI," *Phys. Med. Biol.*, vol. 52, no. 13, pp. N277–N286, 2007.

[167] H. Zhu, K. Demachi, and M. Sekino, “Phase gradient imaging for positive contrast generation to superparamagnetic iron oxide nanoparticle-labeled targets in magnetic resonance imaging,” *Magn. Reson. Imaging*, vol. 29, no. 7, pp. 891–898, 2011.

[168] C. H. Cunningham, T. Arai, P. C. Yang, M. V McConnell, J. M. Pauly, and S. M. Conolly, “Positive contrast magnetic resonance imaging of cells labeled with magnetic nanoparticles,” *Magn. Reson. Med.*, vol. 53, no. 5, pp. 999–1005, 2005.

[169] P. Balchandani, M. Yamada, J. Pauly, P. Yang, and D. Spielman, “Self-refocused spatial-spectral pulse for positive contrast imaging of cells labeled with SPIO nanoparticles,” *Magn. Reson. Med.*, vol. 62, no. 1, pp. 183–192, 2009.

[170] N. Mascheri, R. Dharmakumar, Z. Zhang, T. Paunesku, G. Woloschak, and D. Li, “Fast low-angle positive contrast steady-state free precession imaging of USPIO-labeled macrophages: theory and in vitro experiment,” *Magn. Reson. Imaging*, vol. 27, no. 7, pp. 961–969, 2009.

[171] T. Çukur, M. Yamada, W. R. Overall, P. Yang, and D. G. Nishimura, “Positive contrast with alternating repetition time SSFP (PARTS): A fast imaging technique for SPIO-labeled cells,” *Magn. Reson. Med.*, vol. 63, no. 2, pp. 427–437, 2010.

[172] Y. B. Kim, K. H. Bae, S.-S. Yoo, T. G. Park, and H. Park, “Positive contrast visualization for cellular magnetic resonance imaging using susceptibility-weighted echo-time encoding,” *Magn. Reson. Imaging*, vol. 27, no. 5, pp. 601–610, 2009.

[173] O. M. Girard *et al.*, “Optimization of iron oxide nanoparticle detection using ultrashort echo time pulse sequences: Comparison of T1, T2*, and synergistic T1 − T2* contrast mechanisms,” *Magn. Reson. Med.*, vol. 65, no. 6, pp. 1649–1660, Jun. 2011.

[174] Y. Dong, Z. Chang, G. Xie, G. Whitehead, and J. X. Ji, “Susceptibility-based positive contrast MRI of brachytherapy seeds,” *Magn. Reson. Med.*, vol. 74, no. 3, pp. 716–726, 2015.

[175] L. A. Crowe *et al.*, “A Novel Method for Quantitative Monitoring of Transplanted Islets of Langerhans by Positive Contrast Magnetic Resonance Imaging,” *Am. J. Transplant.*, vol. 11, no. 6, pp. 1158–1168, Jun. 2011.

[176] X. Deligianni, D. Jirák, Z. Berková, M. Hájek, K. Scheffler, and O. Bieri, “In vivo visualization of cells labeled with superparamagnetic iron oxides by a sub-millisecond gradient echo sequence,” *Magn. Reson. Mater. Physics, Biol. Med.*, vol. 27, no. 4, pp. 329–337, Aug. 2014.

[177] P. R. Seevinck, H. de Leeuw, C. Bos, and C. J. G. Bakker, “Highly localized positive contrast of small paramagnetic objects using 3D center-out radial sampling with off-resonance reception,” *Magn. Reson. Med.*, vol. 65, no. 1, pp. 146–156, 2011.

[178] J. Rahmer, U. Blume, and P. Börnert, “Selective 3D ultrashort TE imaging: comparison

of ‘dual-echo’ acquisition and magnetization preparation for improving short-T 2 contrast,” *Magn. Reson. Mater. Physics, Biol. Med.*, vol. 20, no. 2, pp. 83–92, 2007.

[179] P. H. Mills and E. T. Ahrens, “Enhanced positive-contrast visualization of paramagnetic contrast agents using phase images,” *Magn. Reson. Med.*, vol. 62, no. 5, pp. 1349–1355, 2009.

[180] Q. Zhao, J. Langley, S. Lee, and W. Liu, “Positive contrast technique for the detection and quantification of superparamagnetic iron oxide nanoparticles in MRI,” *NMR Biomed.*, vol. 24, no. 5, pp. 464–472, 2011.

[181] F. Eibofner, G. Steidle, R. Kehlbach, R. Bantleon, and F. Schick, “Positive contrast imaging of iron oxide nanoparticles with susceptibility-weighted imaging,” *Magn. Reson. Med.*, vol. 64, no. 4, pp. 1027–1038, 2010.

[182] S. Posse, “Direct imaging of magnetic field gradients by group spin-echoselection,” *Magn. Reson. Med.*, vol. 25, no. 1, pp. 12–29, 1992.

[183] C. J. G. Bakker, H. de Leeuw, K. L. Vincken, E. Vonken, and J. Hendrikse, “Phase gradient mapping as an aid in the analysis of object-induced and system-related phase perturbations in MRI,” *Phys. Med. Biol.*, vol. 53, no. 18, pp. N349–N358, 2008.

[184] H. Leeuw, P. Seevinck, and G. Maat, “High resolution phase gradient mapping as a tool for the detection and analysis of local field disturbances,” *Proc. Intl. Soc. Mag.*, 2009.

[185] E. M. Haacke, Y. Xu, Y.-C. N. Cheng, and J. R. Reichenbach, “Susceptibility weighted imaging (SWI),” *Magn. Reson. Med.*, vol. 52, no. 3, pp. 612–618, Sep. 2004.

[186] S. Saini, R. B. Frankel, D. D. Stark, and J. T. Ferrucci Jr, “Magnetism: a primer and review,” *Am. J. Roentgenol.*, vol. 150, no. 4, pp. 735–743, 1988.

[187] A. K. Gupta and M. Gupta, “Synthesis and surface engineering of iron oxide nanoparticles for biomedical applications,” *Biomaterials*, vol. 26, no. 18, pp. 3995–4021, 2005.

[188] C. P. Bean and J. D. Livingston, “Superparamagnetism,” *J. Appl. Phys.*, vol. 30, no. 4, pp. S120–S129, 1959.

[189] J. E. Rosen, L. Chan, D. B. Shieh, and F. X. Gu, “Iron oxide nanoparticles for targeted cancer imaging and diagnostics,” *Nanomedicine-Nanotechnology Biol. Med.*, vol. 8, no. 3, pp. 275–290, 2012.

[190] R. M. Cornell and U. Schwertmann, *The iron oxides: structure, properties, reactions, occurrences and uses*. John Wiley & Sons, 2006.

[191] A. S. Teja and P. Y. Koh, “Synthesis, properties, and applications of magnetic iron oxide nanoparticles,” *Prog. Cryst. Growth Charact. Mater.*, vol. 55, no. 1–2, pp. 22–45, 2009.

[192] N. A. Frey, S. Peng, K. Cheng, and S. H. Sun, “Magnetic nanoparticles: synthesis, functionalization, and applications in bioimaging and magnetic energy storage,” *Chem.*

Soc. Rev., vol. 38, no. 9, pp. 2532–2542, 2009.

[193] D. L. J. Thorek, A. K. Chen, J. Czupryna, and A. Tsourkas, "Superparamagnetic iron oxide nanoparticle probes for molecular imaging," *Ann. Biomed. Eng.*, vol. 34, no. 1, pp. 23–38, 2006.

[194] C. Fang and M. Zhang, "Multifunctional magnetic nanoparticles for medical imaging applications," *J. Mater. Chem.*, vol. 19, no. 35, pp. 6258–6266, 2009.

[195] P. Majewski and B. Thierry, "Functionalized magnetite nanoparticles—synthesis, properties, and bio-applications," *Crit. Rev. Solid State Mater. Sci.*, vol. 32, no. 3–4, pp. 203–215, 2007.

[196] S. Klotz, G. Steinle-Neumann, T. Strässle, J. Philippe, T. Hansen, and M. J. Wenzel, "Magnetism and the Verwey transition in Fe 3 O 4 under pressure," *Phys. Rev. B*, vol. 77, no. 1, p. 12411, 2008.

[197] G. H. Kwei, R. B. Von Dreele, A. Williams, J. A. Goldstone, A. C. Lawson, and W. K. Warburton, "Structure and valence from complementary anomalous X-ray and neutron powder diffraction," *J. Mol. Struct.*, vol. 223, pp. 383–406, 1990.

[198] K. Haneda and A. H. Morrish, "Vacancy ordering in γ-Fe 2 O 3 small particles," *Solid State Commun.*, vol. 22, no. 12, pp. 779–782, 1977.

[199] A. Bee, R. Massart, and S. Neveu, "Synthesis of very fine maghemite particles," *J. Magn. Magn. Mater.*, vol. 149, no. 1, pp. 6–9, 1995.

[200] G. W. Reimers and S. E. Khalafalla, *Preparing magnetic fluids by a peptizing method*, vol. 59. US Dept. of the Interior, 1972.

[201] R. Massart, "Ferrofluids." Google Patents, 1982.

[202] R. Massart, "Preparation of aqueous magnetic liquids in alkaline and acidic media," *IEEE Trans. Magn.*, pp. 1247–1248, 1981.

[203] R. S. Molday, "Magnetic iron-dextran microspheres." Google Patents, 1984.

[204] G. C. Hadjipanayis and R. W. (Richard W. . Siegel, *Nanophase Materials : Synthesis - Properties - Applications*. Springer Netherlands, 1994.

[205] C. E. Sjøgren, K. Briley-Sæbø, M. Hanson, and C. Johansson, "Magnetic characterization of iron oxides for magnetic resonance imaging," *Magn. Reson. Med.*, vol. 31, no. 3, pp. 268–272, 1994.

[206] F. A. Cotton and G. Wilkinson, "Advanced Inorganic Chemistry, 5th Edit," *New york*, p. 705, 1988.

[207] A. K. Gupta and S. Wells, "Surface-modified superparamagnetic nanoparticles for drug delivery: preparation, characterization, and cytotoxicity studies," *NanoBioscience, IEEE Trans.*, vol. 3, no. 1, pp. 66–73, 2004.

[208] S. Qu *et al.*, "Magnetite nanoparticles prepared by precipitation from partially reduced ferric chloride aqueous solutions," *J. Colloid Interface Sci.*, vol. 215, no. 1, pp. 190–192,

1999.

[209] S. Sun *et al.*, "Monodisperse MFe2O4 (M= Fe, Co, Mn) nanoparticles," *J. Am. Chem. Soc.*, vol. 126, no. 1, pp. 273–279, 2004.

[210] S. Yamamuro, T. Ando, K. Sumiyama, T. Uchida, and I. Kojima, "Monodisperse metallic iron nanoparticles synthesized from noncarbonyl complex," *Jpn. J. Appl. Phys.*, vol. 43, no. 7R, p. 4458, 2004.

[211] S. Sun and H. Zeng, "Size-controlled synthesis of magnetite nanoparticles," *J. Am. Chem. Soc.*, vol. 124, no. 28, pp. 8204–8205, 2002.

[212] T. M. Tillotson, A. E. Gash, R. L. Simpson, L. W. Hrubesh, J. H. Satcher, and J. F. Poco, "Nanostructured energetic materials using sol–gel methodologies," *J. Non. Cryst. Solids*, vol. 285, no. 1, pp. 338–345, 2001.

[213] R. P. Bagwe, J. R. Kanicky, B. J. Palla, P. K. Patanjali, and D. O. Shah, "Improved drug delivery using microemulsions: rationale, recent progress, and new horizons," *Crit. Rev. Ther. Drug Carrier Syst.*, vol. 18, no. 1, p. 77, 2001.

[214] Y. Deng, L. Wang, W. Yang, S. Fu, and A. Elaıssari, "Preparation of magnetic polymeric particles via inverse microemulsion polymerization process," *J. Magn. Magn. Mater.*, vol. 257, no. 1, pp. 69–78, 2003.

[215] V. Pillai, P. Kumar, M. J. Hou, P. Ayyub, and D. O. Shah, "Preparation of nanoparticles of silver halides, superconductors and magnetic materials using water-in-oil microemulsions as nano-reactors," *Adv. Colloid Interface Sci.*, vol. 55, pp. 241–269, 1995.

[216] C. T. Seip, E. E. Carpenter, C. J. O'Connor, V. T. John, and S. Li, "Magnetic properties of a series of ferrite nanoparticles synthesized in reverse micelles," *Magn. IEEE Trans.*, vol. 34, no. 4, pp. 1111–1113, 1998.

[217] M. J. Lawrence and G. D. Rees, "Microemulsion-based media as novel drug delivery systems," *Adv. Drug Deliv. Rev.*, vol. 45, no. 1, pp. 89–121, 2000.

[218] V. Ng, Y. V Lee, B. T. Chen, and A. O. Adeyeye, "Nanostructure array fabrication with temperature-controlled self-assembly techniques," *Nanotechnology*, vol. 13, no. 5, p. 554, 2002.

[219] M. P. Pileni, "Reverse micelles as microreactors," *J. Phys. Chem.*, vol. 97, no. 27, pp. 6961–6973, 1993.

[220] J. Rockenberger, E. C. Scher, and A. P. Alivisatos, "A new nonhydrolytic single-precursor approach to surfactant-capped nanocrystals of transition metal oxides," *J. Am. Chem. Soc.*, vol. 121, no. 49, pp. 11595–11596, 1999.

[221] D. L. Huber, "Synthesis, properties, and applications of iron nanoparticles," *Small*, vol. 1, no. 5, pp. 482–501, 2005.

[222] D. Farrell, S. A. Majetich, and J. P. Wilcoxon, "Preparation and characterization of

monodisperse Fe nanoparticles," *J. Phys. Chem. B*, vol. 107, no. 40, pp. 11022–11030, 2003.

[223] Z. Li, H. Chen, H. Bao, and M. Gao, "One-pot reaction to synthesize water-soluble magnetite nanocrystals," *Chem. Mater.*, vol. 16, no. 8, pp. 1391–1393, 2004.

[224] S. Laurent *et al.*, "Magnetic iron oxide nanoparticles: synthesis, stabilization, vectorization, physicochemical characterizations, and biological applications," *Chem. Rev.*, vol. 108, no. 6, pp. 2064–2110, 2008.

[225] T. Hyeon, S. S. Lee, J. Park, Y. Chung, and H. Bin Na, "Synthesis of highly crystalline and monodisperse maghemite nanocrystallites without a size-selection process," *J. Am. Chem. Soc.*, vol. 123, no. 51, pp. 12798–12801, 2001.

[226] Z. Li, Q. Sun, and M. Gao, "Preparation of water-soluble magnetite nanocrystals from hydrated ferric salts in 2-pyrrolidone: mechanism leading to Fe3O4," *Angew. Chemie Int. Ed.*, vol. 44, no. 1, pp. 123–126, 2005.

[227] P. Tartaj, M. del Puerto Morales, S. Veintemillas-Verdaguer, T. Gonzalez-Carreno, and C. J. Serna, "The preparation of magnetic nanoparticles for applications in biomedicine," *J. Phys. D. Appl. Phys.*, vol. 36, no. 13, p. R182, 2003.

[228] I. W. Hamley, "Nanotechnology with soft materials," *Angew. Chemie Int. Ed.*, vol. 42, no. 15, pp. 1692–1712, 2003.

[229] Y. Sahoo *et al.*, "Aqueous ferrofluid of magnetite nanoparticles: Fluorescence labeling and magnetophoretic control," *J. Phys. Chem. B*, vol. 109, no. 9, pp. 3879–3885, 2005.

[230] N. Fauconnier, A. Bee, J. Roger, and J. N. Pons, "Adsorption of gluconic and citric acids on maghemite particles in aqueous medium," in *Trends in Colloid and Interface Science X*, Springer, 1996, pp. 212–216.

[231] N. Fauconnier, J. N. Pons, J. Roger, and A. Bee, "Thiolation of maghemite nanoparticles by dimercaptosuccinic acid," *J. Colloid Interface Sci.*, vol. 194, no. 2, pp. 427–433, 1997.

[232] G. Tanguy, F. Hindre, E. Rump, J. J. Le Jeune, and P. Jallet, "Phosphorylcholine coating of iron oxide nanoparticles," *J. Colloid Interface Sci.*, vol. 209, no. 1, pp. 66–71, 1999.

[233] Y. Sahoo *et al.*, "Alkyl phosphonate/phosphate coating on magnetite nanoparticles: a comparison with fatty acids," *Langmuir*, vol. 17, no. 25, pp. 7907–7911, 2001.

[234] C. C. Berry, S. Wells, S. Charles, and A. S. G. Curtis, "Dextran and albumin derivatised iron oxide nanoparticles: influence on fibroblasts in vitro," *Biomaterials*, vol. 24, no. 25, pp. 4551–4557, 2003.

[235] R. Gref *et al.*, "'Stealth'corona-core nanoparticles surface modified by polyethylene glycol (PEG): influences of the corona (PEG chain length and surface density) and of the core composition on phagocytic uptake and plasma protein adsorption," *Colloids*

Surfaces B Biointerfaces, vol. 18, no. 3, pp. 301–313, 2000.

[236] P. Tartaj, T. Gonzalez-Carreno, and C. J. Serna, "Single-Step Nanoengineering of Silica Coated Maghemite Hollow Spheres with Tunable Magnetic Properties," *Adv. Mater.*, vol. 13, no. 21, pp. 1620–1624, 2001.

[237] S. Santra, R. Tapec, N. Theodoropoulou, J. Dobson, A. Hebard, and W. Tan, "Synthesis and characterization of silica-coated iron oxide nanoparticles in microemulsion: the effect of nonionic surfactants," *Langmuir*, vol. 17, no. 10, pp. 2900–2906, 2001.

[238] M. Chen, S. Yamamuro, D. Farrell, and S. A. Majetich, "Gold-coated iron nanoparticles for biomedical applications," *J. Appl. Phys.*, vol. 93, no. 10, pp. 7551–7553, 2003.

[239] W. L. Zhou, E. E. Carpenter, J. Lin, A. Kumbhar, J. Sims, and C. J. O'Connor, "Nanostructures of gold coated iron core-shell nanoparticles and the nanobands assembled under magnetic field," *Eur. Phys. J. D-Atomic, Mol. Opt. Plasma Phys.*, vol. 16, no. 1, pp. 289–292, 2001.

[240] A. M. Morawski *et al.*, "Targeted nanoparticles for quantitative imaging of sparse molecular epitopes with MRI," *Magn. Reson. Med.*, vol. 51, no. 3, pp. 480–486, 2004.

[241] H. K. Xu, C. M. Sorensen, K. J. Klabunde, and G. C. Hadjipanayis, "Aerosol synthesis of gadolinium iron garnet particles," *J. Mater. Res.*, vol. 7, no. 3, pp. 712–716, 1992.

[242] S. Wagner, J. SCHNORR, H. Pilgrimm, B. Hamm, and M. Taupitz, "Monomer-coated very small superparamagnetic iron oxide particles as contrast medium for magnetic resonance imaging: preclinical in vivo characterization," *Invest. Radiol.*, vol. 37, no. 4, pp. 167–177, 2002.

[243] M. Taupitz *et al.*, "Phase I clinical evaluation of citrate-coated monocrystalline very small superparamagnetic iron oxide particles as a new contrast medium for magnetic resonance imaging," *Invest. Radiol.*, vol. 39, no. 7, pp. 394–405, 2004.

[244] G. S. R. Krishnamurti and P. M. Huang, "Influence of citrate on the kinetics of Fe (II) oxidation and the formation of iron oxyhydroxides," *Clays Clay Min.*, vol. 39, pp. 28–34, 1991.

[245] C. Liu and P. M. Huang, "Atomic force microscopy and surface characteristics of iron oxides formed in citrate solutions," *Soil Sci. Soc. Am. J.*, vol. 63, no. 1, pp. 65–72, 1999.

[246] N. Fauconnier, A. Bee, J. Roger, and J. N. Pons, "Synthesis of aqueous magnetic liquids by surface complexation of maghemite nanoparticles," *J. Mol. Liq.*, vol. 83, no. 1, pp. 233–242, 1999.

[247] K. Kandori, Y. Kawashima, and T. Ishikawa, "Effects of citrate ions on the formation of monodispersed cubic hematite particles," *J. Colloid Interface Sci.*, vol. 152, no. 1, pp. 284–288, 1992.

[248] D. Portet, B. Denizot, E. Rump, J.-J. Lejeune, and P. Jallet, "Nonpolymeric coatings of iron oxide colloids for biological use as magnetic resonance imaging contrast agents," *J.*

Colloid Interface Sci., vol. 238, no. 1, pp. 37–42, 2001.

[249] L. F. Gamarra, G. E. S. Brito, W. M. Pontuschka, E. Amaro, A. H. C. Parma, and G. F. Goya, "Biocompatible superparamagnetic iron oxide nanoparticles used for contrast agents: a structural and magnetic study," *J. Magn. Magn. Mater.*, vol. 289, pp. 439–441, 2005.

[250] R. S. Molday and D. Mackenzie, "Immunospecific ferromagnetic iron-dextran reagents for the labeling and magnetic separation of cells," *J. Immunol. Methods*, vol. 52, no. 3, pp. 353–367, 1982.

[251] I. Raynal, P. Prigent, S. Peyramaure, A. Najid, C. Rebuzzi, and C. Corot, "Macrophage endocytosis of superparamagnetic iron oxide nanoparticles: mechanisms and comparison of ferumoxides and ferumoxtran-10," *Invest. Radiol.*, vol. 39, no. 1, pp. 56–63, 2004.

[252] P. Reimer and T. Balzer, "Ferucarbotran (Resovist): a new clinically approved RES-specific contrast agent for contrast-enhanced MRI of the liver: properties, clinical development, and applications," *Eur. Radiol.*, vol. 13, no. 6, pp. 1266–1276, 2003.

[253] W. Li *et al.*, "First-pass contrast-enhanced magnetic resonance angiography in humans using ferumoxytol, a novel ultrasmall superparamagnetic iron oxide (USPIO)-based blood pool agent," *J. Magn. Reson. Imaging*, vol. 21, no. 1, pp. 46–52, 2005.

[254] P. Tartaj, M. P. Morales, S. Veintemillas-Verdaguer, T. Gonzalez-Carreño, and C. J. Serna, "Synthesis, properties and biomedical applications of magnetic nanoparticles," *Handb. Magn. Mater.*, vol. 16, no. 5, pp. 403–482, 2006.

[255] L. X. Tiefenauer, A. Tschirky, G. Kühne, and R. Y. Andres, "In vivo evaluation of magnetite nanoparticles for use as a tumor contrast agent in MRI," *Magn. Reson. Imaging*, vol. 14, no. 4, pp. 391–402, 1996.

[256] S. M. Moghimi, A. C. Hunter, and J. C. Murray, "Long-circulating and target-specific nanoparticles: theory to practice," *Pharmacol. Rev.*, vol. 53, no. 2, pp. 283–318, 2001.

[257] H. W. Kang, L. Josephson, A. Petrovsky, R. Weissleder, and A. Bogdanov, "Magnetic resonance imaging of inducible E-selectin expression in human endothelial cell culture," *Bioconjug. Chem.*, vol. 13, no. 1, pp. 122–127, 2002.

[258] F. Llanes, D. H. Ryan, and R. H. Marchessault, "Magnetic nanostructured composites using alginates of different M/G ratios as polymeric matrix," *Int. J. Biol. Macromol.*, vol. 27, no. 1, pp. 35–40, 2000.

[259] P. V Finotelli, M. A. Morales, M. H. Rocha-Leao, E. M. Baggio-Saitovitch, and A. M. Rossi, "Magnetic studies of iron (III) nanoparticles in alginate polymer for drug delivery applications," *Mater. Sci. Eng. C*, vol. 24, no. 5, pp. 625–629, 2004.

[260] B. Schöpf *et al.*, "Methodology description for detection of cellular uptake of PVA coated superparamagnetic iron oxide nanoparticles (SPION) in synovial cells of sheep,"

J. Magn. Magn. Mater., vol. 293, no. 1, pp. 411–418, 2005.

[261] B. Xue and Y. Sun, "Protein adsorption equilibria and kinetics to a poly (vinyl alcohol)-based magnetic affinity support," *J. Chromatogr. A*, vol. 921, no. 2, pp. 109–119, 2001.

[262] J. Lee, T. Isobe, and M. Senna, "Preparation of ultrafine Fe 3 O 4 particles by precipitation in the presence of PVA at high pH," *J. Colloid Interface Sci.*, vol. 177, no. 2, pp. 490–494, 1996.

[263] M. Knutson and M. Wessling-Resnick, "Iron metabolism in the reticuloendothelial system," *Crit. Rev. Biochem. Mol. Biol.*, vol. 38, no. 1, pp. 61–88, 2003.

[264] Y. Zhang, N. Kohler, and M. Zhang, "Surface modification of superparamagnetic magnetite nanoparticles and their intracellular uptake," *Biomaterials*, vol. 23, no. 7, pp. 1553–1561, 2002.

[265] G. Storm, S. O. Belliot, T. Daemen, and D. D. Lasic, "Surface modification of nanoparticles to oppose uptake by the mononuclear phagocyte system," *Adv. Drug Deliv. Rev.*, vol. 17, no. 1, pp. 31–48, 1995.

[266] J. Folkman, "Angiogenesis in cancer, vascular, rheumatoid and other disease," *Nat. Med.*, vol. 1, no. 1, pp. 27–30, 1995.

[267] Y. Noguchi *et al.*, "Early phase tumor accumulation of macromolecules: a great difference in clearance rate between tumor and normal tissues," *Cancer Sci.*, vol. 89, no. 3, pp. 307–314, 1998.

[268] L. Brannon-Peppas and J. O. Blanchette, "Nanoparticle and targeted systems for cancer therapy," *Adv. Drug Deliv. Rev.*, vol. 64, pp. 206–212, 2012.

[269] H. Maeda, J. Wu, T. Sawa, Y. Matsumura, and K. Hori, "Tumor vascular permeability and the EPR effect in macromolecular therapeutics: a review," *J. Control. Release*, vol. 65, no. 1–2, pp. 271–284, 2000.

[270] A. Moore, E. Marecos, A. Bogdanov Jr, and R. Weissleder, "Tumoral Distribution of Long-circulating Dextran-coated Iron Oxide Nanoparticles in a Rodent Model 1," *Radiology*, vol. 214, no. 2, pp. 568–574, 2000.

[271] W. S. Enochs, G. Harsh, F. Hochberg, and R. Weissleder, "Improved delineation of human brain tumors on MR images using a long-circulating, superparamagnetic iron oxide agent," *J. Magn. Reson. Imaging*, vol. 9, no. 2, pp. 228–232, 1999.

[272] C. Zimmer, R. Weissleder, K. Poss, A. Bogdanova, S. C. Wright Jr, and W. S. Enochs, "MR imaging of phagocytosis in experimental gliomas," *Radiology*, vol. 197, no. 2, pp. 533–538, 1995.

[273] I. Hilger and W. A. Kaiser, "Iron oxide-based nanostructures for MRI and magnetic hyperthermia," *Nanomedicine*, vol. 7, no. 9, pp. 1443–1459, 2012.

[274] H. E. Daldrup-Link *et al.*, "Targeting of Hematopoietic Progenitor Cells with MR Contrast Agents 1," *Radiology*, vol. 228, no. 3, pp. 760–767, 2003.

[275] A. Jordan *et al.*, “Endocytosis of dextran and silan-coated magnetite nanoparticles and the effect of intracellular hyperthermia on human mammary carcinoma cells in vitro,” *J. Magn. Magn. Mater.*, vol. 194, no. 1, pp. 185–196, 1999.

[276] F. K. H. van Landeghem *et al.*, “Post-mortem studies in glioblastoma patients treated with thermotherapy using magnetic nanoparticles,” *Biomaterials*, vol. 30, no. 1, pp. 52–57, 2009.

[277] R. Weissleder *et al.*, “Superparamagnetic iron oxide: enhanced detection of focal splenic tumors with MR imaging,” *Radiology*, vol. 169, no. 2, pp. 399–403, 1988.

[278] M. G. Harisinghani *et al.*, “Noninvasive detection of clinically occult lymph-node metastases in prostate cancer,” *N. Engl. J. Med.*, vol. 348, no. 25, pp. 2491–2499, 2003.

[279] R. K. Gilchrist, R. Medal, W. D. Shorey, R. C. Hanselman, J. C. Parrott, and C. B. Taylor, “Selective inductive heating of lymph nodes,” *Ann. Surg.*, vol. 146, no. 4, p. 596, 1957.

[280] R. T. Gordon, J. R. Hines, and D. Gordon, “Intracellular hyperthermia a biophysical approach to cancer treatment via intracellular temperature and biophysical alterations,” *Med. Hypotheses*, vol. 5, no. 1, pp. 83–102, 1979.

[281] J.-C. Bolomey, M. H. Seegenschmiedt, P. Fessenden, and C. C. Vernon, *Thermoradiotherapy and Thermochemotherapy: Volume 1: Biology, Physiology, and Physics*, vol. 1. Springer Science & Business Media, 1995.

[282] S. Wada, K. Tazawa, I. Furuta, and H. Nagae, “Antitumor effect of new local hyperthermia using dextran magnetite complex in hamster tongue carcinoma,” *Oral Dis.*, vol. 9, no. 4, pp. 218–223, 2003.

[283] A. Jordan and K. Maier-Hauff, “Magnetic nanoparticles for intracranial thermotherapy,” *J. Nanosci. Nanotechnol.*, vol. 7, no. 12, pp. 4604–4606, 2007.

[284] P. Wust *et al.*, “Magnetic nanoparticles for interstitial thermotherapy - Feasibility, tolerance and achieved temperatures,” *Int. J. Hyperth.*, vol. 22, no. 8, pp. 673–685, 2006.

[285] T. J. Vogl *et al.*, “Superparamagnetic iron oxide--enhanced versus gadolinium-enhanced MR imaging for differential diagnosis of focal liver lesions,” *Radiology*, vol. 198, no. 3, pp. 881–887, 1996.

[286] P. Reimer *et al.*, “Hepatic Lesion Detection and Characterization: Value of Nonenhanced MR Imaging, Superparamagnetic Iron Oxide-enhanced MR Imaging, and Spiral CT—ROC Analysis 1,” *Radiology*, vol. 217, no. 1, pp. 152–158, 2000.

[287] R. Weissleder, G. Elizondo, J. Wittenberg, A. S. Lee, L. Josephson, and T. J. Brady, “Ultrasmall superparamagnetic iron oxide: an intravenous contrast agent for assessing lymph nodes with MR imaging,” *Radiology*, vol. 175, no. 2, pp. 494–498, 1990.

[288] Y. Anzai *et al.*, “Evaluation of Neck and Body Metastases to Nodes with Ferumoxtran 10–enhanced MR Imaging: Phase III Safety and Efficacy Study 1,” *Radiology*, vol. 228,

no. 3, pp. 777–788, 2003.

[289] S. M. Cromer Berman, P. Walczak, and J. W. M. Bulte, "Tracking stem cells using magnetic nanoparticles," *Wiley Interdiscip. Rev. Nanomedicine Nanobiotechnology*, vol. 3, no. 4, pp. 343–355, 2011.

[290] S. D. Conner and S. L. Schmid, "Regulated portals of entry into the cell," *Nature*, vol. 422, no. 6927, pp. 37–44, 2003.

[291] K. G. Neoh and E. T. Kang, "Surface modification of magnetic nanoparticles for stem cell labeling," *Soft Matter*, vol. 8, no. 7, pp. 2057–2069, 2012.

[292] J. Zhu, L. Zhou, and F. XingWu, "Tracking neural stem cells in patients with brain trauma," *N. Engl. J. Med.*, vol. 355, no. 22, pp. 2376–2378, 2006.

[293] C. Toso *et al.*, "Clinical magnetic resonance imaging of pancreatic islet grafts after iron nanoparticle labeling," *Am. J. Transplant.*, vol. 8, no. 3, pp. 701–706, 2008.

[294] F. Callera and C. M. T. P. de Melo, "Magnetic resonance tracking of magnetically labeled autologous bone marrow CD34+ cells transplanted into the spinal cord via lumbar puncture technique in patients with chronic spinal cord injury: CD34+ cells' migration into the injured site," *Stem Cells Dev.*, vol. 16, no. 3, pp. 461–466, 2007.

[295] D. Karussis *et al.*, "Safety and immunological effects of mesenchymal stem cell transplantation in patients with multiple sclerosis and amyotrophic lateral sclerosis," *Arch. Neurol.*, vol. 67, no. 10, pp. 1187–1194, 2010.

[296] I. J. M. de Vries *et al.*, "Magnetic resonance tracking of dendritic cells in melanoma patients for monitoring of cellular therapy," *Nat. Biotechnol.*, vol. 23, no. 11, pp. 1407–1413, 2005.

[297] P. Walczak, D. A. Kedziorek, A. A. Gilad, B. P. Barnett, and J. W. M. Bulte, "Applicability and limitations of MR tracking of neural stem cells with asymmetric cell division and rapid turnover: the case of the shiverer dysmyelinated mouse brain," *Magn. Reson. Med.*, vol. 58, no. 2, pp. 261–269, 2007.

[298] N. Lee *et al.*, "Magnetosome-like ferrimagnetic iron oxide nanocubes for highly sensitive MRI of single cells and transplanted pancreatic islets," *Proc. Natl. Acad. Sci.*, vol. 108, no. 7, pp. 2662–2667, 2011.

[299] H. Wang *et al.*, "Durable mesenchymal stem cell labelling by using polyhedral superparamagnetic iron oxide nanoparticles," *Chem. Eur. J.*, vol. 15, no. 45, pp. 12417–12425, 2009.

[300] H.-M. Fan *et al.*, "Quantum dot capped magnetite nanorings as high performance nanoprobe for multiphoton fluorescence and magnetic resonance imaging," *J. Am. Chem. Soc.*, vol. 132, no. 42, pp. 14803–14811, 2010.

[301] L. M. Parkes *et al.*, "Cobalt nanoparticles as a novel magnetic resonance contrast agent—relaxivities at 1.5 and 3 Tesla," *Contrast Media Mol. Imaging*, vol. 3, no. 4, pp.

150–156, 2008.

[302] M. J. Baek *et al.*, “Water-soluble MnO nanocolloid for a molecular T 1 MR imaging: a facile one-pot synthesis, in vivo T 1 MR images, and account for relaxivities,” *ACS Appl. Mater. Interfaces*, vol. 2, no. 10, pp. 2949–2955, 2010.

[303] K. Thorstensen and I. Romslo, “The transferrin receptor: its diagnostic value and its potential as therapeutic target,” *Scand. J. Clin. Lab. Investig.*, vol. 53, no. S215, pp. 113–120, 1993.

[304] A. Moore, J. P. Basilion, E. A. Chiocca, and R. Weissleder, “Measuring transferrin receptor gene expression by NMR imaging,” *Biochim. Biophys. Acta (BBA)-Molecular Cell Res.*, vol. 1402, no. 3, pp. 239–249, 1998.

[305] Z. M. Qian, H. Li, H. Sun, and K. Ho, “Targeted drug delivery via the transferrin receptor-mediated endocytosis pathway,” *Pharmacol. Rev.*, vol. 54, no. 4, pp. 561–587, 2002.

[306] A. C. Antony, “Folate receptors,” *Annu. Rev. Nutr.*, vol. 16, no. 1, pp. 501–521, 1996.

[307] H. Choi, S. R. Choi, R. Zhou, H. F. Kung, and I.-W. Chen, “Iron oxide nanoparticles as magnetic resonance contrast agent for tumor imaging via folate receptor-targeted delivery 1,” *Acad. Radiol.*, vol. 11, no. 9, pp. 996–1004, 2004.

[308] J. Sudimack and R. J. Lee, “Targeted drug delivery via the folate receptor,” *Adv. Drug Deliv. Rev.*, vol. 41, no. 2, pp. 147–162, 2000.

[309] A. Moore, Z. Medarova, A. Potthast, and G. Dai, “In vivo targeting of underglycosylated MUC-1 tumor antigen using a multimodal imaging probe,” *Cancer Res.*, vol. 64, no. 5, pp. 1821–1827, 2004.

[310] Z. Kachra *et al.*, “Expression of matrix metalloproteinases and their inhibitors in human brain tumors,” *Clin. Exp. Metastasis*, vol. 17, no. 7, pp. 555–566, 1999.

[311] D. Artemov, N. Mori, R. Ravi, and Z. M. Bhujwalla, “Magnetic resonance molecular imaging of the HER-2/neu receptor,” *Cancer Res.*, vol. 63, no. 11, pp. 2723–2727, 2003.

[312] M. A. Funovics *et al.*, “MR imaging of the her2/neu and 9.2. 27 tumor antigens using immunospecific contrast agents,” *Magn. Reson. Imaging*, vol. 22, no. 6, pp. 843–850, 2004.

[313] P. Reimer, R. Weissleder, A. S. Lee, J. Wittenberg, and T. J. Brady, “Receptor imaging: application to MR imaging of liver cancer,” *Radiology*, vol. 177, no. 3, pp. 729–734, 1990.

[314] G. A. F. van Tilborg *et al.*, “Annexin A5-functionalized bimodal nanoparticles for MRI and fluorescence imaging of atherosclerotic plaques,” *Bioconjug. Chem.*, vol. 21, no. 10, pp. 1794–1803, 2010.

[315] A. Ito, M. Shinkai, H. Honda, and T. Kobayashi, “Heat-inducible TNF-alpha gene therapy combined with hyperthermia using magnetic nanoparticles as a novel tumor-

targeted therapy," *Cancer Gene Ther.*, vol. 8, no. 9, pp. 649–654, 2001.

[316] E. Ruoslahti, "RGD and other recognition sequences for integrins," *Annu. Rev. Cell Dev. Biol.*, vol. 12, no. 1, pp. 697–715, 1996.

[317] L. O. Johansson, A. Björnerud, H. K. Ahlström, D. L. Ladd, and D. K. Fujii, "A targeted contrast agent for magnetic resonance imaging of thrombus: implications of spatial resolution," *J. Magn. Reson. Imaging*, vol. 13, no. 4, pp. 615–618, 2001.

[318] R. A. S. Ariëns, T.-S. Lai, J. W. Weisel, C. S. Greenberg, and P. J. Grant, "Role of factor XIII in fibrin clot formation and effects of genetic polymorphisms," *Blood*, vol. 100, no. 3, pp. 743–754, 2002.

[319] F. A. Jaffer and R. Weissleder, "Seeing within molecular imaging of the cardiovascular system," *Circ. Res.*, vol. 94, no. 4, pp. 433–445, 2004.

[320] R. Weissleder, A. S. Lee, B. A. Khaw, T. Shen, and T. J. Brady, "Antimyosin-labeled monocrystalline iron oxide allows detection of myocardial infarct: MR antibody imaging," *Radiology*, vol. 182, no. 2, pp. 381–385, 1992.

[321] K. A. Kelly, J. R. Allport, A. Tsourkas, V. R. Shinde-Patil, L. Josephson, and R. Weissleder, "Detection of vascular adhesion molecule-1 expression using a novel multimodal nanoparticle," *Circ. Res.*, vol. 96, no. 3, pp. 327–336, 2005.

[322] P. T. Chapman, F. Jamar, E. Keelan, A. M. Peters, and D. O. Haskard, "Use of a radiolabeled monoclonal antibody against e-selectin for imaging of endothelial activation in rheumatoid arthritis," *Arthritis Rheum.*, vol. 39, no. 8, pp. 1371–1375, 1996.

[323] B. M. Kräling *et al.*, "E-selectin is present in proliferating endothelial cells in human hemangiomas," *Am. J. Pathol.*, vol. 148, no. 4, p. 1181, 1996.

[324] M. Zhao, D. A. Beauregard, L. Loizou, B. Davletov, and K. M. Brindle, "Non-invasive detection of apoptosis using magnetic resonance imaging and a targeted contrast agent," *Nat. Med.*, vol. 7, no. 11, pp. 1241–1244, 2001.

[325] B. Lobel, O. Eyal, N. Kariv, and A. Katzir, "Temperature controlled CO2 laser welding of soft tissues: Urinary bladder welding in different animal models (rats, rabbits, and cats)," *Lasers Surg. Med.*, vol. 26, no. 1, pp. 4–12, 2000.

[326] K. Sokolov *et al.*, "Real-time vital optical imaging of precancer using anti-epidermal growth factor receptor antibodies conjugated to gold nanoparticles," *Cancer Res.*, vol. 63, no. 9, pp. 1999–2004, 2003.

[327] J. W. M. Bulte *et al.*, "Magnetodendrimers allow endosomal magnetic labeling and in vivo tracking of stem cells," *Nat. Biotechnol.*, vol. 19, no. 12, pp. 1141–1147, 2001.

[328] C. Chouly, D. Pouliquen, I. Lucet, J. J. Jeune, and P. Jallet, "Development of superparamagnetic nanoparticles for MRI: effect of particle size, charge and surface nature on biodistribution," *J. Microencapsul.*, vol. 13, no. 3, pp. 245–255, 1996.

[329] T. Kubo, T. Sugita, S. Shimose, Y. Nitta, Y. Ikuta, and T. Murakami, "Targeted delivery

of anticancer drugs with intravenously administered magnetic liposomes in osteosarcoma-bearing hamsters," *Int. J. Oncol.*, vol. 17, no. 2, pp. 309–324, 2000.

[330] S. A. Gomez-Lopera, R. C. Plaza, and A. V Delgado, "Synthesis and characterization of spherical magnetite/biodegradable polymer composite particles," *J. Colloid Interface Sci.*, vol. 240, no. 1, pp. 40–47, 2001.

[331] C. Billotey, C. Wilhelm, M. Devaud, J. C. Bacri, J. Bittoun, and F. Gazeau, "Cell internalization of anionic maghemite nanoparticles: quantitative effect on magnetic resonance imaging," *Magn. Reson. Med.*, vol. 49, no. 4, pp. 646–654, 2003.

[332] R. Tavaré *et al.*, "Monitoring of In Vivo Function of Superparamagnetic Iron Oxide Labelled Murine Dendritic Cells during Anti-Tumour Vaccination," *PLoS One*, vol. 6, no. 5, p. e19662, May 2011.

[333] W. T. Dixon, "Simple proton spectroscopic imaging," *Radiology*, vol. 153, no. 1, pp. 189–194, 1984.

[334] G. H. Glover and E. Schneider, "Three-point dixon technique for true water/fat decomposition with B0 inhomogeneity correction," *Magn. Reson. Med.*, vol. 18, no. 2, pp. 371–383, 1991.

[335] G. H. Glover, "Multipoint dixon technique for water and fat proton and susceptibility imaging," *J. Magn. Reson. Imaging*, vol. 1, no. 5, pp. 521–530, Sep. 1991.

[336] J. Ma, "Dixon techniques for water and fat imaging," *J. Magn. Reson. Imaging*, vol. 28, no. 3, pp. 543–558, 2008.

[337] J. Szumowski, W. R. Coshow, F. Li, and S. F. Quinn, "Phase unwrapping in the three-point Dixon method for fat suppression MR imaging," *Radiology*, vol. 192, no. 2, pp. 555–561, 1994.

[338] P. Kellman *et al.*, "Multiecho dixon fat and water separation method for detecting fibrofatty infiltration in the myocardium," *Magn. Reson. Med.*, vol. 61, no. 1, pp. 215–221, 2009.

[339] S. B. Reeder *et al.*, "Multicoil Dixon chemical species separation with an iterative least-squares estimation method," *Magn. Reson. Med.*, vol. 51, no. 1, pp. 35–45, 2004.

[340] S. B. Reeder *et al.*, "Iterative decomposition of water and fat with echo asymmetry and least-squares estimation (IDEAL): application with fast spin-echo imaging," *Magn. Reson. Med.*, vol. 54, no. 3, pp. 636–644, 2005.

[341] H. Yu, S. B. Reeder, A. Shimakawa, J. H. Brittain, and N. J. Pelc, "Field map estimation with a region growing scheme for iterative 3-point water-fat decomposition," *Magn. Reson. Med.*, vol. 54, no. 4, pp. 1032–1039, 2005.

[342] D. Hernando, J. P. Haldar, B. P. Sutton, J. Ma, P. Kellman, and Z. Liang, "Joint estimation of water/fat images and field inhomogeneity map," *Magn. Reson. Med.*, vol.

59, no. 3, pp. 571–580, 2008.

[343] H. K. Hussain *et al.*, "Hepatic fat fraction: MR imaging for quantitative measurement and display—Early experience," *Radiology*, vol. 237, no. 3, pp. 1048–1055, 2005.

[344] M. Bydder, M. Middleton, P. Gatehouse, and A. Chavez, "Fat quantification by modeling the variation in signal amplitude with TE," *Proc ISMRM*, 2006.

[345] S. Reeder, A. Faranesh, I. Chen, and C. Gard, "Off-resonance separation for positive contrast imaging of iron-oxide labeled cells," *Proc.*, 2006.

[346] H. Yu *et al.*, "Multiecho reconstruction for simultaneous water-fat decomposition and T2* estimation," *J. Magn. Reson. Imaging*, vol. 26, no. 4, pp. 1153–1161, Oct. 2007.

[347] J. Simon *et al.*, "Fat-suppression MR imaging of the orbit," *Am. J. Neuroradiol.*, vol. 9, no. 5, pp. 961–968, 1988.

[348] S. W. Atlas *et al.*, "Orbital lesions: proton spectroscopic phase-dependent contrast MR imaging," *Radiology*, vol. 164, no. 2, pp. 510–514, 1987.

[349] D. L. Daniels *et al.*, "MR imaging of the optic nerve and sheath: correcting the chemical shift misregistration effect," *Am. J. Neuroradiol.*, vol. 7, no. 2, pp. 249–253, 1986.

[350] J. Bulte and D. Kraitchman, "Iron oxide MR contrast agents for molecular and cellular imaging," *NMR Biomed.*, vol. 17, no. 7, pp. 484–499, 2004.

[351] E. Kaldoudi, S. C. R. Williams, G. J. Barker, and P. S. Tofts, "A chemical shift selective inversion recovery sequence for fat-suppressed MRI: theory and experimental validation," *Magn. Reson. Imaging*, vol. 11, no. 3, pp. 341–355, 1993.

[352] J. Ma, A. T. Vu, J. B. Son, H. Choi, and J. D. Hazle, "Fat-suppressed three-dimensional dual echo dixon technique for contrast agent enhanced MRI," *J. Magn. Reson. Imaging*, vol. 23, no. 1, pp. 36–41, 2006.

[353] G. J. Strijkers and K. Nicolay, "Relaxivity of nanoparticles for magnetic resonance imaging," *Handb. Nanophysics Nanomedicine Nanorobotics. CRC Press Boca Rat.*, pp. 1–23, 2011.

[354] D. Kruk, T. Nilsson, and J. Kowalewski, "Outer-sphere nuclear spin relaxation in paramagnetic systems: a low-field theory," *Mol. Phys.*, vol. 99, no. 17, pp. 1435–1445, 2001.

[355] E. Toth, L. Helm, and A. E. Merbach, "Relaxivity of MRI contrast agents," *Contrast Agents I*, vol. 221, pp. 61–101, 2002.

[356] P. Caravan, "Physicochemical principles of MR contrast agents," *Mol. Cell. MR Imaging*, pp. 13–36, 2007.

[357] L. Néel, "Theory of magnetic viscosity of fine grained ferromagnetics with application to baked clays," *Ann. Geophys*, vol. 5, no. 99–136, p. 41, 1949.

[358] W. F. Brown Jr, "Thermal fluctuations of a single-domain particle," *J. Appl. Phys.*, vol.

34, no. 4, pp. 1319–1320, 1963.

[359] A. Roch, R. N. Muller, and P. Gillis, “Theory of proton relaxation induced by superparamagnetic particles,” *J. Chem. Phys.*, vol. 110, no. 11, pp. 5403–5411, 1999.

[360] D. A. Yablonskiy and E. M. Haacke, “Theory of NMR signal behavior in magnetically inhomogeneous tissues: the static dephasing regime,” *Magn. Reson. Med.*, vol. 32, no. 6, pp. 749–763, 1994.

[361] R. J. S. Brown, “Distribution of fields from randomly placed dipoles: Free-precession signal decay as result of magnetic grains,” *Phys. Rev.*, vol. 121, no. 5, p. 1379, 1961.

[362] I. R. Young, I. J. Cox, D. J. Bryant, and G. M. Bydder, “The Benefits of Increasing Spatial-Resolution as a Means of Reducing Artifacts Due to Field Inhomogeneities,” *Magn. Reson. Imaging*, vol. 6, no. 5, pp. 585–590, 1988.

[363] D. Hernando, K. K. Vigen, A. Shimakawa, and S. B. Reeder, “R-2(*) mapping in the presence of macroscopic B-0 field variations,” *Magn. Reson. Med.*, vol. 68, no. 3, pp. 830–840, 2012.

[364] G. Salas, C. Casado, F. J. Teran, R. Miranda, C. J. Serna, and M. P. Morales, “Controlled synthesis of uniform magnetite nanocrystals with high-quality properties for biomedical applications,” *J. Mater. Chem.*, vol. 22, no. 39, pp. 21065–21075, 2012.

[365] C. Wilhelm, C. Billotey, J. Roger, J. N. Pons, J.-C. Bacri, and F. Gazeau, “Intracellular uptake of anionic superparamagnetic nanoparticles as a function of their surface coating,” *Biomaterials*, vol. 24, no. 6, pp. 1001–1011, 2003.

[366] M. Calero *et al.*, “Characterization of interaction of magnetic nanoparticles with breast cancer cells,” *J. Nanobiotechnology*, vol. 13, no. 1, p. 16, 2015.

[367] A. Prina-Mello, K. Crosbie-Staunton, G. Salas, M. del Puerto Morales, and Y. Volkov, “Multiparametric toxicity evaluation of SPIONs by high content screening technique: identification of biocompatible multifunctional nanoparticles for nanomedicine,” *Magn. IEEE Trans.*, vol. 49, no. 1, pp. 377–382, 2013.

[368] N. Schleich, F. Danhier, and V. Préat, “Iron oxide-loaded nanotheranostics: Major obstacles to in vivo studies and clinical translation,” *J. Control. Release*, vol. 198, pp. 35–54, 2015.

[369] F. Yi, J.-W. Lu, Z.-X. Guo, and J. Yu, “Mechanical properties and biocompatibility of soluble eggshell membrane protein/poly (vinyl alcohol) blend films,” *J. Biomater. Sci. Polym. Ed.*, vol. 17, no. 9, pp. 1015–1024, 2006.

[370] A. Gupta, R. Kumar, N. K. Upadhyay, P. Surekha, and P. K. Roy, “Synthesis, characterization and efficacy of chemically crosslinked PVA hydrogels for dermal wound healing in experimental animals,” *J. Appl. Polym. Sci.*, vol. 111, no. 3, pp. 1400–1408, 2009.

[371] M. Kobayashi, J. Toguchida, and M. Oka, “Development of the shields for tendon injury

repair using polyvinyl alcohol—hydrogel (PVA-H)," *J. Biomed. Mater. Res.*, vol. 58, no. 4, pp. 344–351, 2001.

[372] Z. Peng and Y. Shen, "Study on biological safety of polyvinyl alcohol/collagen hydrogel as tissue substitute (I)," *Polym. Plast. Technol. Eng.*, vol. 50, no. 3, pp. 245–250, 2011.

[373] R. H. Schmedlen, K. S. Masters, and J. L. West, "Photocrosslinkable polyvinyl alcohol hydrogels that can be modified with cell adhesion peptides for use in tissue engineering," *Biomaterials*, vol. 23, no. 22, pp. 4325–4332, 2002.

[374] C. Weis, E. K. Odermatt, J. Kressler, Z. Funke, T. Wehner, and D. Freytag, "Poly (vinyl alcohol) membranes for adhesion prevention," *J. Biomed. Mater. Res. Part B Appl. Biomater.*, vol. 70, no. 2, pp. 191–202, 2004.

[375] K. Bartusek, Z. Dokoupil, and E. Gescheidtova, "Magnetic field mapping around metal implants using an asymmetric spin-echo MRI sequence," *Meas. Sci. Technol.*, vol. 17, no. 12, p. 3293, 2006.

[376] C. Hutton, A. Bork, O. Josephs, R. Deichmann, J. Ashburner, and R. Turner, "Image distortion correction in fMRI: a quantitative evaluation," *Neuroimage*, vol. 16, no. 1, pp. 217–240, 2002.

[377] M. F. Reiser, W. Semmler, and H. Hricak, Eds., *Magnetic Resonance Tomography*. Berlin, Heidelberg: Springer Berlin Heidelberg, 2008.

[378] M. Rohrer, H. Bauer, J. Mintorovitch, M. Requardt, and H.-J. Weinmann, "Comparison of magnetic properties of MRI contrast media solutions at different magnetic field strengths," *Invest. Radiol.*, vol. 40, no. 11, pp. 715–724, 2005.

[379] J. P. Marques and R. Bowtell, "Application of a Fourier-based method for rapid calculation of field inhomogeneity due to spatial variation of magnetic susceptibility," *Concepts Magn. Reson. Part B Magn. Reson. Eng.*, vol. 25B, no. 1, pp. 65–78, Apr. 2005.

[380] E. Schneider and G. Glover, "Rapid in vivo proton shimming," *Magn. Reson. Med.*, vol. 18, no. 2, pp. 335–347, 1991.

[381] L. Li and J. S. Leigh, "Quantifying arbitrary magnetic susceptibility distributions with MR," *Magn. Reson. Med.*, vol. 51, no. 5, pp. 1077–1082, May 2004.

[382] A. Bjørnerud and L. Johansson, "The utility of superparamagnetic contrast agents in MRI: theoretical consideration and applications in the cardiovascular system," *NMR Biomed.*, vol. 17, no. 7, pp. 465–477, Nov. 2004.

[383] T. Allkemper, C. Bremer, L. Matuszewski, W. Ebert, and P. Reimer, "Contrast-enhanced Blood-Pool MR Angiography with Optimized Iron Oxides: Effect of Size and Dose on Vascular Contrast Enhancement in Rabbits," *Radiology*, vol. 223, no. 2, pp. 432–438, May 2002.

[384] L. E. W. LaConte *et al.*, "Coating thickness of magnetic iron oxide nanoparticles affects

R2 relaxivity," *J. Magn. Reson. Imaging*, vol. 26, no. 6, pp. 1634–1641, Dec. 2007.

[385] S. Tong, S. Hou, Z. Zheng, J. Zhou, and G. Bao, "Coating Optimization of Superparamagnetic Iron Oxide Nanoparticles for High T2 Relaxivity," *Nano Lett.*, vol. 10, no. 11, pp. 4607–4613, Nov. 2010.

[386] Y. Gossuin, P. Gillis, A. Hocq, Q. L. Vuong, and A. Roch, "Magnetic resonance relaxation properties of superparamagnetic particles," *Wiley Interdiscip. Rev. Nanomedicine Nanobiotechnology*, vol. 1, no. 3, pp. 299–310, 2009.

[387] J. H. Freed, "Dynamic effects of pair correlation functions on spin relaxation by translational diffusion in liquids. II. Finite jumps and independent T1 processes," *J. Chem. Phys.*, vol. 68, no. 9, p. 4034, 1978.

[388] G. J. Ayant Y, Belorizky E, Alizon J, "Calculation of spectral density resulting from random translational movement with relaxation by magnetic dipolar interac- tion in liquids," *J Phys A*, no. 36, pp. 991 – 1004, 1975.

[389] Y. Ge *et al.*, "Effect of surface charge and agglomerate degree of magnetic iron oxide nanoparticles on KB cellular uptake in vitro," *Colloids Surfaces B Biointerfaces*, vol. 73, no. 2, pp. 294–301, 2009.

[390] C. Hanot, Y. Choi, T. Anani, D. Soundarrajan, and A. David, "Effects of Iron-Oxide Nanoparticle Surface Chemistry on Uptake Kinetics and Cytotoxicity in CHO-K1 Cells," *Int. J. Mol. Sci.*, vol. 17, no. 1, p. 54, 2015.

[391] Y. Park *et al.*, "Stability of Superparamagnetic Iron Oxide Nanoparticles at Different pH Values: Experimental and Theoretical Analysis," *Langmuir*, vol. 28, no. 15, pp. 6246–6255, Apr. 2012.

[392] A. Einstein, "Zur Theorie der Brownschen Bewegung," *Ann. Phys.*, vol. 324, no. 2, pp. 371–381, 1906.

[393] P. Gillis and S. H. Koenig, "Transverse relaxation of solvent protons induced by magnetized spheres: Application to ferritin, erythrocytes, and magnetite," *Magn. Reson. Med.*, vol. 5, no. 4, pp. 323–345, 1987.

[394] J. W. M. Bulte, M. de Cuyper, D. Despres, and J. A. Frank, "Preparation, relaxometry, and biokinetics of PEGylated magnetoliposomes as MR contrast agent," *J. Magn. Magn. Mater.*, vol. 194, no. 1–3, pp. 204–209, 1999.

[395] A. Petri-Fink, B. Steitz, A. Finka, J. Salaklang, and H. Hofmann, "Effect of cell media on polymer coated superparamagnetic iron oxide nanoparticles (SPIONs): Colloidal stability, cytotoxicity, and cellular uptake studies," *Eur. J. Pharm. Biopharm.*, vol. 68, no. 1, pp. 129–137, 2008.

[396] Y. C. Park *et al.*, "Effect of PEG molecular weight on stability, T2 contrast, cytotoxicity, and cellular uptake of superparamagnetic iron oxide nanoparticles (SPIONs)," *Colloids Surfaces B Biointerfaces*, vol. 119, pp. 106–114, 2014.

[397] A. Vonarbourg, C. Passirani, P. Saulnier, and J.-P. Benoit, “Parameters influencing the stealthiness of colloidal drug delivery systems,” *Biomaterials*, vol. 27, no. 24, pp. 4356–4373, 2006.

[398] J. Huang *et al.*, “Effects of Nanoparticle Size on Cellular Uptake and Liver MRI with Polyvinylpyrrolidone-Coated Iron Oxide Nanoparticles,” *ACS Nano*, vol. 4, no. 12, pp. 7151–7160, 2010.

[399] N. Oh and J.-H. Park, “Endocytosis and exocytosis of nanoparticles in mammalian cells,” *Int. J. Nanomedicine*, vol. 9 Suppl 1, no. Suppl 1, pp. 51–63, 2014.

[400] L. Shang, K. Nienhaus, and G. Nienhaus, “Engineered nanoparticles interacting with cells: size matters,” *J. Nanobiotechnology*, vol. 12, no. 1, p. 5, 2014.

[401] O. P. Perumal, R. Inapagolla, S. Kannan, and R. M. Kannan, “The effect of surface functionality on cellular trafficking of dendrimers,” *Biomaterials*, vol. 29, no. 24–25, pp. 3469–3476, 2008.

[402] T. A. Kelf *et al.*, “Non-specific cellular uptake of surface-functionalized quantum dots,” *Nanotechnology*, vol. 21, no. 28, p. 285105, Jul. 2010.

[403] F. M. Kievit and M. Q. Zhang, “Surface Engineering of Iron Oxide Nanoparticies for Targeted Cancer Therapy,” *Acc. Chem. Res.*, vol. 44, no. 10, pp. 853–862, 2011.

[404] A. Roch, Y. Gossuin, R. N. Muller, and P. Gillis, “Superparamagnetic colloid suspensions: Water magnetic relaxation and clustering,” *J. Magn. Magn. Mater.*, vol. 293, no. 1, pp. 532–539, 2005.

[405] B. A. Larsen, M. A. Haag, N. J. Serkova, K. R. Shroyer, and C. R. Stoldt, “Controlled aggregation of superparamagnetic iron oxide nanoparticles for the development of molecular magnetic resonance imaging probes,” *Nanotechnology*, vol. 19, no. 26, p. 265102, 2008.

[406] J. Rauch, W. Kolch, S. Laurent, and M. Mahmoudi, “Big Signals from Small Particles: Regulation of Cell Signaling Pathways by Nanoparticles,” *Chem. Rev.*, vol. 113, no. 5, pp. 3391–3406, 2013.

[407] T. Schlorf, M. Meincke, E. Kossel, C.-C. Glüer, O. Jansen, and R. Mentlein, “Biological properties of iron oxide nanoparticles for cellular and molecular magnetic resonance imaging,” *Int. J. Mol. Sci.*, vol. 12, no. 1, pp. 12–23, 2010.

[408] A. Lindemann, K. Lüdtke-Buzug, B. M. Fräderich, K. Gräfe, R. Pries, and B. Wollenberg, “Biological impact of superparamagnetic iron oxide nanoparticles for magnetic particle imaging of head and neck cancer cells,” *Int. J. Nanomedicine*, vol. 9, pp. 5025–40, 2014.

[409] A. M. Rad, A. S. Arbab, A. S. M. Iskander, Q. Jiang, and H. Soltanian-Zadeh, “Quantification of superparamagnetic iron oxide (SPIO)-labeled cells using MRI,” *J. Magn. Reson. Imaging*, vol. 26, no. 2, pp. 366–374, 2007.

[410] G. H. Simon *et al.*, “T1 and T2 relaxivity of intracellular and extracellular USPIO at 1.5T and 3T clinical MR scanning,” *Eur. Radiol.*, vol. 16, no. 3, pp. 738–745, 2006.

[411] M. Neu, D. Fischer, and T. Kissel, “Recent advances in rational gene transfer vector design based on poly (ethylene imine) and its derivatives,” *J. Gene Med.*, vol. 7, no. 8, pp. 992–1009, 2005.

[412] L. Lee and P. Somasundaran, “Adsorption of polyacrylamide on oxide minerals,” *Langmuir*, vol. 5, no. 3, pp. 854–860, 1989.

[413] J. Schutjens, G. Fleer, and M. Stuart, “End effects in polymer adsorption: A tale of tails,” *Colloids and Surfaces*, vol. 21, pp. 285–306, 1986.

[414] M. Auffan *et al.*, “In vitro interactions between DMSA-coated maghemite nanoparticles and human fibroblasts: a physicochemical and cyto-genotoxical study,” *Environ. Sci. Technol.*, vol. 40, no. 14, pp. 4367–4373, 2006.

[415] K. Boldt, O. T. Bruns, N. Gaponik, and A. Eychmüller, “Comparative examination of the stability of semiconductor quantum dots in various biochemical buffers,” *J. Phys. Chem. B*, vol. 110, no. 5, pp. 1959–1963, 2006.

[416] D. N. Williams, S. H. Ehrman, and T. R. Pulliam Holoman, “Evaluation of the microbial growth response to inorganic nanoparticles,” *J. Nanobiotechnology*, vol. 4, no. 1, p. 3, 2006.

[417] B. Díaz *et al.*, “Assessing methods for blood cell cytotoxic responses to inorganic nanoparticles and nanoparticle aggregates,” *Small*, vol. 4, no. 11, pp. 2025–2034, 2008.

[418] Z. E. Allouni, M. R. Cimpan, P. J. Høl, T. Skodvin, and N. R. Gjerdet, “Agglomeration and sedimentation of TiO 2 nanoparticles in cell culture medium,” *Colloids Surfaces B Biointerfaces*, vol. 68, no. 1, pp. 83–87, 2009.

[419] A. Villanueva *et al.*, “The influence of surface functionalization on the enhanced internalization of magnetic nanoparticles in cancer cells,” *Nanotechnology*, vol. 20, no. 11, p. 115103, 2009.

[420] M. Safi, H. Sarrouj, O. Sandre, N. Mignet, and J.-F. Berret, “Interactions between sub-10-nm iron and cerium oxide nanoparticles and 3T3 fibroblasts: the role of the coating and aggregation state,” *Nanotechnology*, vol. 21, no. 14, p. 145103, 2010.

[421] S. H. Koenig, K. E. Kellar, D. K. Fujii, W. H. H. Gunther, K. Briley-Sæbø, and M. Spiller, “Three Types of Physical Measurements Needed to Characterize Iron Oxide Nanoparticles for MRI and MRA,” *Acad. Radiol.*, vol. 9, no. 1, pp. S5–S10, Jan. 2002.

[422] E. Munnier *et al.*, “Doxorubicin delivered to MCF-7 cancer cells by superparamagnetic iron oxide nanoparticles: effects on subcellular distribution and cytotoxicity,” *J. Nanoparticle Res.*, vol. 13, no. 3, pp. 959–971, 2011.

[423] F. Bahring *et al.*, “Suitability of Viability Assays for Testing Biological Effects of Coated Superparamagnetic Nanoparticles,” *IEEE Trans. Magn.*, vol. 49, no. 1, pp. 383–

388, Jan. 2013.

[424] M. Mahmoudi, S. Laurent, M. A. Shokrgozar, and M. Hosseinkhani, “Toxicity Evaluations of Superparamagnetic Iron Oxide Nanoparticles: Cell ‘Vision’ versus Physicochemical Properties of Nanoparticles,” *ACS Nano*, vol. 5, no. 9, pp. 7263–7276, Sep. 2011.

[425] P. H. Hoet *et al.*, “Nanoparticles – known and unknown health risks,” *J. Nanobiotechnology*, vol. 2, no. 1, p. 12, 2004.

[426] J. Rauch, W. Kolch, and M. Mahmoudi, “Cell type-specific activation of AKT and ERK signaling pathways by small negatively-charged magnetic nanoparticles,” *Sci. Rep.*, vol. 2, no. 1, p. 868, 2012.

[427] F. Marano, S. Hussain, F. Rodrigues-Lima, A. Baeza-Squiban, and S. Boland, “Nanoparticles: molecular targets and cell signalling,” *Arch. Toxicol.*, vol. 85, no. 7, pp. 733–741, Jul. 2011.

[428] Y. Jun *et al.*, “Nanoscale Size Effect of Magnetic Nanocrystals and Their Utilization for Cancer Diagnosis via Magnetic Resonance Imaging,” *J. Am. Chem. Soc.*, vol. 127, no. 16, pp. 5732–5733, 2005.

[429] Y. Jun, J. Seo, and J. Cheon, “Nanoscaling laws of magnetic nanoparticles and their applicabilities in biomedical sciences,” *Acc. Chem. Res.*, vol. 41, no. 2, pp. 179–189, 2008.

[430] H. Duan, M. Kuang, X. Wang, Y. A. Wang, H. Mao, and S. Nie, “Reexamining the Effects of Particle Size and Surface Chemistry on the Magnetic Properties of Iron Oxide Nanocrystals: New Insights into Spin Disorder and Proton Relaxivity,” *J. Phys. Chem. C*, vol. 112, no. 22, pp. 8127–8131, 2008.

[431] R. N. Muller, P. Gillis, F. Moiny, and A. Roch, “Transverse relaxivity of particulate MRI contrast media: from theories to experiments,” *Magn. Reson. Med.*, vol. 22, no. 2, pp. 178–182, 1991.

[432] N. Najafian, S. Shanehsazzadeh, F. Hajesmaeelzadeh, A. Lahooti, C. Gruettner, and M. A. Oghabian, “Effect of Functional Group and Surface Charge of PEG and Dextran-Coated USPIO as a Contrast Agent in MRI on Relaxivity Constant,” *Appl. Magn. Reson.*, vol. 46, no. 6, pp. 685–692, 2015.

[433] M. Branca *et al.*, “Towards MRI T2 contrast agents of increased efficiency,” *J. Magn. Magn. Mater.*, vol. 377, pp. 348–353, 2015.

[434] C. V Bowen, X. Zhang, G. Saab, P. J. Gareau, and B. K. Rutt, “Application of the static dephasing regime theory to superparamagnetic iron-oxide loaded cells,” *Magn. Reson. Med.*, vol. 48, no. 1, pp. 52–61, 2002.

[435] R. P. Kennan, J. Zhong, and J. C. Gore, “Intravascular susceptibility contrast mechanisms in tissues,” *Magn. Reson. Med.*, vol. 31, no. 1, pp. 9–21, 1994.

[436] R. Weissleder, H. C. Cheng, A. Bogdanova, and A. Bogdanov, “Magnetically labeled cells can be detected by MR imaging,” *Jmri-Journal Magn. Reson. Imaging*, vol. 7, no. 1, pp. 258–263, 1997.

[437] M. Longmire, P. L. Choyke, and H. Kobayashi, “Clearance properties of nano-sized particles and molecules as imaging agents: considerations and caveats,” *Nanomedicine*, vol. 3, no. 5, pp. 703–717, 2008.

[438] F. M. Kievit and M. Q. Zhang, “Cancer Nanotheranostics: Improving Imaging and Therapy by Targeted Delivery Across Biological Barriers,” *Adv. Mater.*, vol. 23, no. 36, pp. H217–H247, 2011.

[439] A. Richmond and Y. Su, “Mouse xenograft models vs GEM models for human cancer therapeutics,” *Dis. Model. Mech.*, vol. 1, no. 2–3, pp. 78–82, 2008.

[440] J. R. Whittle, M. T. Lewis, G. J. Lindeman, and J. E. Visvader, “Patient-derived xenograft models of breast cancer and their predictive power,” *Breast Cancer Res.*, vol. 17, no. 1, p. 17, 2015.

[441] J. I. Johnson *et al.*, “Relationships between drug activity in NCI preclinical in vitro and in vivo models and early clinical trials,” *Br. J. Cancer*, vol. 84, no. 10, pp. 1424–1431, 2001.

[442] R. E. Bellet, V. Danna, M. J. Mastrangelo, and D. Berd, “Evaluation of a ‘Nude’ Mouse-Human Tumor Panel as a Predictive Secondary Screen for Cancer Chemotherapeutic Agents,” *JNCI J. Natl. Cancer Inst.*, vol. 63, no. 5, pp. 1185–1188, 1979.

[443] E. Boven, B. Winograd, Ø. Fodstad, M. W. Lobbezoo, and H. M. Pinedo, “Preclinical phase II studies in human tumor lines: a European multicenter study,” *Eur. J. Cancer Clin. Oncol.*, vol. 24, no. 3, pp. 567–573, 1988.

[444] T. Voskoglou-Nomikos, J. L. Pater, and L. Seymour, “Clinical predictive value of the in vitro cell line, human xenograft, and mouse allograft preclinical cancer models,” *Clin. Cancer Res.*, vol. 9, no. 11, pp. 4227–39, 2003.

[445] C. L. Morton and P. J. Houghton, “Establishment of human tumor xenografts in immunodeficient mice,” *Nat. Protoc.*, vol. 2, no. 2, pp. 247–250, 2007.

[446] G. P. Schmidt, H. Kramer, M. F. Reiser, and C. Glaser, “Whole-body magnetic resonance imaging and positron emission tomography-computed tomography in oncology,” *Top. Magn. Reson. Imaging*, vol. 18, no. 3, pp. 193–202, 2007.

[447] T. Barrett, M. Brechbiel, M. Bernardo, and P. L. Choyke, “MRI of tumor angiogenesis,” *J. Magn. Reson. Imaging*, vol. 26, no. 2, pp. 235–249, 2007.

[448] I. Stasinopoulos, M.-F. Penet, Z. Chen, S. Kakkad, K. Glunde, and Z. M. Bhujwalla, “Exploiting the tumor microenvironment for theranostic imaging,” *NMR Biomed.*, vol. 24, no. 6, 2011.

[449] R. P. Mason, W. Rodbumrung, and P. P. Antich, “Hexafluorobenzene: a sensitive 19F

NMR indicator of tumor oxygenation," *NMR Biomed.*, vol. 9, no. 3, pp. 125–134, 1996.

[450] Z. M. Bhujwalla, D. Artemov, P. Ballesteros, S. Cerdan, R. J. Gillies, and M. Solaiyappan, "Combined vascular and extracellular pH imaging of solid tumors," *NMR Biomed.*, vol. 15, no. 2, pp. 114–119, 2002.

[451] R. J. Gillies, N. Raghunand, M. L. Garcia-Martin, and R. A. Gatenby, "pH imaging," *IEEE Eng. Med. Biol. Mag.*, vol. 23, no. 5, pp. 57–64, 2004.

[452] Y. Wu, T. C. Soesbe, G. E. Kiefer, P. Zhao, and A. D. Sherry, "A responsive europium (III) chelate that provides a direct readout of pH by MRI," *J. Am. Chem. Soc.*, vol. 132, no. 40, pp. 14002–14003, 2010.

[453] G. Liu, Y. Li, V. Sheth, and M. Pagel, "Imaging in vivo extracellular pH with a single paramagnetic chemical exchange saturation transfer magnetic resonance imaging contrast agent," *Mol. Imaging*, vol. 11, no. 1, 2012.

[454] K. Glunde, D. Artemov, M.-F. Penet, M. A. Jacobs, and Z. M. Bhujwalla, "Magnetic resonance spectroscopy in metabolic and molecular imaging and diagnosis of cancer," *Chem. Rev.*, vol. 110, no. 5, pp. 3043–3059, 2010.

[455] J. Jung, "Human tumor xenograft models for preclinical assessment of anticancer drug development," *Toxicol. Res.*, vol. 30, no. 1, pp. 1–5, 2014.

[456] J. J. Tentler *et al.*, "Patient-derived tumour xenografts as models for oncology drug development," *Nat. Rev. Clin. Oncol.*, vol. 9, no. 6, pp. 338–350, 2012.

[457] L. A. Dethlefsen, J. M. S. Prewitt, and M. L. Mendelsohn, "Analysis of tumor growth curves," *J. Natl. Cancer Inst.*, vol. 40, no. 2, pp. 389–405, 1968.

[458] K. Kataoka, A. Harada, and Y. Nagasaki, "Block copolymer micelles for drug delivery: design, characterization and biological significance," *Adv. Drug Deliv. Rev.*, vol. 47, no. 1, pp. 113–131, 2001.

[459] M. Ferrari, "Cancer nanotechnology: opportunities and challenges," *Nat. Rev. Cancer*, vol. 5, no. 3, pp. 161–171, 2005.

[460] R. Jain, "Barriers to drug delivery in solid tumors.," *Sci. Am.*, vol. 271, pp. 58–65, 1994.

[461] C. Corot, P. Robert, J.-M. Idée, and M. Port, "Recent advances in iron oxide nanocrystal technology for medical imaging," *Adv. Drug Deliv. Rev.*, vol. 58, no. 14, pp. 1471–1504, 2006.

[462] R. Madru *et al.*, "(68)Ga-labeled superparamagnetic iron oxide nanoparticles (SPIONs) for multi-modality PET/MR/Cherenkov luminescence imaging of sentinel lymph nodes.," *Am. J. Nucl. Med. Mol. Imaging*, vol. 4, no. 1, pp. 60–9, 2013.

[463] A. Natarajan *et al.*, "NanoFerrite particle based radioimmunonanoparticles: binding affinity and in vivo pharmacokinetics," *Bioconjug. Chem.*, vol. 19, no. 6, pp. 1211–1218, 2008.

[464] A. Lahooti, S. Sarkar, S. Laurent, and S. Shanehsazzadeh, "Dual nano-sized contrast

agents in PET/MRI: a systematic review," *Contrast Media Mol. Imaging*, vol. 11, no. 6, pp. 428–447, 2016.

[465] A. F. Thünemann, D. Schütt, L. Kaufner, U. Pison, and H. Möhwald, "Maghemite nanoparticles protectively coated with poly (ethylene imine) and poly (ethylene oxide)-b lock-poly (glutamic acid)," *Langmuir*, vol. 22, no. 5, pp. 2351–2357, 2006.

[466] N. Arsalani, H. Fattahi, S. Laurent, C. Burtea, L. Vander Elst, and R. N. Muller, "Polyglycerol-grafted superparamagnetic iron oxide nanoparticles: highly efficient MRI contrast agent for liver and kidney imaging and potential scaffold for cellular and," *Contrast Media Mol. Imaging*, vol. 7, no. 2, pp. 185–194, 2012.

[467] H. Maeda, L. W. Seymour, and Y. Miyamoto, "Conjugates of anticancer agents and polymers: advantages of macromolecular therapeutics in vivo," *Bioconjug. Chem.*, vol. 3, no. 5, pp. 351–362, 1992.

[468] R. Weissleder, A. Bogdanov, E. A. Neuwelt, and M. Papisov, "Long-circulating iron oxides for MR imaging," *Adv. Drug Deliv. Rev.*, vol. 16, no. 2–3, pp. 321–334, 1995.

[469] A. H. Kaim *et al.*, "MR Imaging with Ultrasmall Superparamagnetic Iron Oxide Particles in Experimental Soft-Tissue Infections in Rats," *Radiology*, vol. 225, no. 3, pp. 808–814, 2002.

[470] M. P. Monopoli *et al.*, "Physical− chemical aspects of protein corona: relevance to in vitro and in vivo biological impacts of nanoparticles," *J. Am. Chem. Soc.*, vol. 133, no. 8, pp. 2525–2534, 2011.

[471] M. Mahmoudi, I. Lynch, M. R. Ejtehadi, M. P. Monopoli, F. B. Bombelli, and S. Laurent, "Protein− nanoparticle interactions: opportunities and challenges," *Chemical*, vol. 111, no. 9, pp. 5610–5637, 2011.

[472] S. Zanganeh, R. Spitler, M. Erfanzadeh, A. M. Alkilany, and M. Mahmoudi, "Protein corona: opportunities and challenges," *Int. J. Biochem. Cell Biol.*, vol. 75, pp. 143–147, 2016.

[473] S. Shanehsazzadeh *et al.*, "Monoclonal antibody conjugated magnetic nanoparticles could target MUC-1-positive cells in vitro but not in vivo," *Contrast Media Mol. Imaging*, vol. 10, no. 3, pp. 225–236, 2015.

[474] E. Mahon, A. Salvati, F. Baldelli Bombelli, I. Lynch, and K. A. Dawson, "Designing the nanoparticle–biomolecule interface for 'targeting and therapeutic delivery,'" *J. Control. Release*, vol. 161, no. 2, pp. 164–174, 2012.

[475] M. Mahmoudi, "Protein corona: The golden gate to clinical applications of nanoparticles," *Int. J. Biochem. Cell Biol.*, vol. 75, no. 75, pp. 141–142, 2016.

[476] J. Fang, H. Nakamura, and H. Maeda, "The EPR effect: unique features of tumor blood vessels for drug delivery, factors involved, and limitations and augmentation of the

effect," *Adv. Drug Deliv. Rev.*, vol. 63, no. 3, pp. 136–151, 2011.

[477] M. P. Desai, V. Labhasetwar, G. L. Amidon, and R. J. Levy, "Gastrointestinal uptake of biodegradable microparticles: effect of particle size," *Pharm. Res.*, vol. 13, no. 12, pp. 1838–1845, 1996.

[478] S. Prabha, W.-Z. Zhou, J. Panyam, and V. Labhasetwar, "Size-dependency of nanoparticle-mediated gene transfection: studies with fractionated nanoparticles," *Int. J. Pharm.*, vol. 244, no. 1–2, pp. 105–115, 2002.

[479] X. Cui *et al.*, "Synthesis, Characterization, and Application of Core–Shell Co0. 16Fe2. 84O4@ NaYF4 (Yb, Er) and Fe3O4@ NaYF4 (Yb, Tm) Nanoparticle as Trimodal (MRI, PET/," *Bioconjug. Chem.*, vol. 27, no. 2, pp. 319–328, 2016.

[480] S.-D. Li and L. Huang, "Pharmacokinetics and biodistribution of nanoparticles," *Mol. Pharm.*, vol. 5, no. 4, pp. 496–504, 2008.

[481] A. Natarajan, C.-Y. Xiong, C. Gruettner, G. L. DeNardo, and S. J. DeNardo, "Development of multivalent radioimmunonanoparticles for cancer imaging and therapy," *Cancer Biother. Radiopharm.*, vol. 23, no. 1, pp. 82–91, 2008.

[482] U. Sakulkhu, M. Mahmoudi, L. Maurizi, J. Salaklang, and H. Hofmann, "Protein corona composition of superparamagnetic iron oxide nanoparticles with various physico-chemical properties and coatings," *Sci. Rep.*, vol. 4, p. 5020, 2014.

[483] S. Shanehsazzadeh, M. A. Oghabian, F. J. Daha, M. Amanlou, and B. J. Allen, "Biodistribution of ultra small superparamagnetic iron oxide nanoparticles in BALB mice," *J. Radioanal. Nucl. Chem.*, vol. 295, no. 2, pp. 1517–1523, 2013.

[484] M. M. Esiri and J. O. McGee, "Monoclonal antibody to macrophages (EMB/11) labels macrophages and microglial cells in human brain.," *J. Clin. Pathol.*, vol. 39, no. 6, pp. 615–21, 1986.

[485] T. Morimura *et al.*, "Monocyte subpopulations in human gliomas: expression of Fc and complement receptors and correlation with tumor proliferation," *Acta Neuropathol.*, vol. 80, no. 3, pp. 287–294, 1990.

[486] S. Y. Leung, M. P. Wong, L. P. Chung, A. S. Y. Chan, and S. T. Yuen, "Monocyte chemoattractant protein-1 expression and macrophage infiltration in gliomas," *Acta Neuropathol.*, vol. 93, no. 5, pp. 518–527, 1997.

[487] P. J. Bugelski, R. L. Kirsh, J. M. Sowinski, and G. Poste, "Changes in the macrophage content of lung metastases at different stages in tumor growth.," *Am. J. Pathol.*, vol. 118, no. 3, pp. 419–24, 1985.

[488] C. H. Blood and B. R. Zetter, "Tumor interactions with the vasculature: angiogenesis and tumor metastasis," *Biochim. Biophys. Acta - Rev. Cancer*, vol. 1032, no. 1, pp. 89–118, 1990.

[489] B. J. Camp, S. T. Dyhrman, V. A. Memoli, L. A. Mott, and R. J. Barth, "In situ cytokine

production by breast cancer tumor-infiltrating lymphocytes," *Ann. Surg. Oncol.*, vol. 3, no. 2, pp. 176–184, 1996.

[490] A. Moore, R. Weissleder, and A. Bogdanov, "Uptake of dextran-coated monocrystalline iron oxides in tumor cells and macrophages," *J. Magn. Reson. Imaging*, vol. 7, no. 6, pp. 1140–1145, 1997.

[491] F. Zhao, Y. Zhao, Y. Liu, X. Chang, C. Chen, and Y. Zhao, "Cellular uptake, intracellular trafficking, and cytotoxicity of nanomaterials," *Small*, vol. 7, no. 10, pp. 1322–1337, 2011.

[492] Q. Liu, L. Song, S. Chen, J. Gao, P. Zhao, and J. Du, "A superparamagnetic polymersome with extremely high T2 relaxivity for MRI and cancer-targeted drug delivery," *Biomaterials*, vol. 114, pp. 23–33, 2017.

[493] T. K. Jain, M. K. Reddy, M. A. Morales, D. L. Leslie-Pelecky, and V. Labhasetwar, "Biodistribution, clearance, and biocompatibility of iron oxide magnetic nanoparticles in rats," *Mol. Pharm.*, vol. 5, no. 2, pp. 316–327, 2008.

[494] P. Bourrinet *et al.*, "Preclinical safety and pharmacokinetic profile of ferumoxtran-10, an ultrasmall superparamagnetic iron oxide magnetic resonance contrast agent," *Invest. Radiol.*, vol. 41, no. 3, pp. 313–324, 2006.

[495] R. Weissleder *et al.*, "Superparamagnetic iron oxide: pharmacokinetics and toxicity," *AJR. Am. J. Roentgenol.*, vol. 152, no. 1, pp. 167–73, 1989.

[496] A. Tanimoto, D. Pouliquen, B. P. Kreft, and D. D. Stark, "Effects of spatial distribution on proton relaxation enhancement by particulate iron oxide," *J. Magn. Reson. Imaging*, vol. 4, no. 5, pp. 653–657, 1994.

[497] V. Mirshafiee, R. Kim, S. Park, M. Mahmoudi, and M. L. Kraft, "Impact of protein pre-coating on the protein corona composition and nanoparticle cellular uptake," *Biomaterials*, vol. 75, pp. 295–304, 2016.

[498] S. Palchetti, D. Pozzi, M. Mahmoudi, and G. Caracciolo, "Exploitation of nanoparticle–protein corona for emerging therapeutic and diagnostic applications," *J. Mater. Chem. B*, vol. 4, no. 25, pp. 4376–4381, 2016.

[499] H. Amiri *et al.*, "Protein corona affects the relaxivity and MRI contrast efficiency of magnetic nanoparticles," *Nanoscale*, vol. 5, no. 18, p. 8656, 2013.

[500] F. Hajesmaeelzadeh, S. Shanehsazzadeh, C. Grüttner, F. J. Daha, and M. A. Oghabian, "Effect of coating thickness of iron oxide nanoparticles on their relaxivity in the MRI," *ranian J. basic Med. Sci.*, vol. 19, no. 2, pp. 166–71, 2016.

[501] H. Dahnke, W. Liu, J. A. Frank, and T. Schaeffter, "Suppression of large scale susceptibility artifacts in positive contrast images," in *Proc Int Soc Magn Reson Med*, 2007, vol. 15, p. 1228.

[502] J. Park *et al.*, "Polymer–iron oxide composite nanoparticles for EPR-independent drug

delivery," *Biomaterials*, vol. 101, pp. 285–295, 2016.

[503] M. A. Abakumov, N. V. Nukolova, M. Sokolsky-Papkov, S. A. Shein, T. O. Sandalova, and H. M. Vishwasrao, "VEGF-targeted magnetic nanoparticles for MRI visualization of brain tumor," *Nanomedicine Nanotechnology, Biol. Med.*, vol. 11, no. 4, pp. 825–833, 2015.

[504] J. Estelrich, E. Escribano, and J. Queralt, "Iron oxide nanoparticles for magnetically-guided and magnetically-responsive drug delivery," *Int. J. Mol. Sci.*, vol. 16, no. 4, pp. 8070–8101, 2015.

[505] Y. He, L. Zhang, D. Zhu, and C. Song, "Design of multifunctional magnetic iron oxide nanoparticles/mitoxantrone-loaded liposomes for both magnetic resonance imaging and targeted cancer therapy," *Int. J. Nanomedicine*, vol. 9, pp. 4055–66, 2014.

[506] J. Volatron, F. Carn, J. Kolosnjaj-Tabi, and Y. Javed, "Ferritin Protein Regulates the Degradation of Iron Oxide Nanoparticles," *Small*, vol. 3, no. 2, p. 1602030, 2017.

[507] J. Kolosnjaj-Tabi *et al.*, "Biotransformations of magnetic nanoparticles in the body," *Nano Today*, vol. 11, no. 3, pp. 280–284, Jun. 2016.

Appendix I: Summary of types of steady-state sequences

12.	**rf-spoiled fast low angle shot sequence**	**Postexcitation refocused sequence**	**Preexcitation refocused sequence**	**Balanced (fully refocused) sequence**
Image weighting	T_1	T_2^*	T_2	T_1 and T_2
Signal source	FID	FID	Spin echo	FID, Spin echo
Common acronyms	SPGR (GE) FLASH (Siemens) T1 FFE (Philips)	GRASS (GE) FISP (Siemens) FFE (Philips) FAST (Picker)	SSFP (GE) PSIF, reversed FISP (Siemens) T2 FFE (Philips) CE-FAST (Picker)	bSSFP or FIESTA (GE) TrueFISP (Siemens) Balanced FFE (Philips)
Description	Residual transverse magnetisation is spoiled with a spoiler gradient to avoid interference with the following excitation pulse.	Residual transverse magnetisation is refocused with a phase-encoding gradient (phase rewinder). The frequency-encoding and slice-select gradients are not balanced.	Based on a time reversal of the frequency-encoding and slice-select gradients (both are not balanced). The refocusing of the signal (echo formation) happens after the next rf excitations.	Between two rf excitations, the sum of all positive gradients exactly matches the sum of all negative gradients for all three gradient types (phase-encoding, frequency-encoding and slice-select). The magnetisation at the beginning and at the end of a TR interval are the same.

Source: [103], [104]

Appendix II: Publications and conference presentations

Co-author publications

- X. Cui, D. Mathe, N. Kovács, I. Horváth, M. Jauregui-Osoro, R. de Rosales, G. Mullen, W. Wong, Y. Yan, D. Krüger, A. Khlobystov, M. Gimenez-Lopez, M. Semjeni, K. Szigeti, D. Veres, H. Lu, I. Hernández, W. Gillin, A. Protti, K. Petik, M. Green and P. Blower, "Syntheis, characterization and application of core-shell $Co_{0.16}Fe_{2.84}O_4$ $NaYF_4$(Yb, Er) and Fe_3O_4@$NaYF_4$(Yb, Tm) nanoparticles as trimodal (MRI, PET/SPECT, and optical) imaging agents", *Bioconjugate Chemistry*, 2016
- X. Cui, S. Belo, D. Krüger, Y. Yan, R. de Rosales, M. Jauregui-Osoro, H. Ye, S. Su, D. Mathe, N. Kovács, I. Horváth, M. Semjeni, K. Sunassee, K. Szigeti, M. Green and P. Blower, "Aluminium hydroxide stabilised MnFe2O4 and Fe3O4 nanoparticles as dual-modality contrast agent for MRI and PET imaging", *Biomaterials*, 2014

Poster presentations at national and international scientific conferences

- Annual meeting of the European Society of Magnetic Resonance in Medicine and Biology, "T_1 and T_2^* mapping of magnetic nanoparticles for the detection of breast and pancreatic cancer cells", Lisbon, 2012
- NCRI Cancer Conference, "Magnetic nanoparticles for the detection and treatment of breast and pancreatic cancer cells", Manchester, 2012
- Annual meeting of the International Society of Magnetic Resonance in Medicine, "T_1 and T_2 mapping of superparamagnetic iron oxide nanoparticles for the detection of breast and pancreatic cancer cells", Salt Lake City, 2013
- Annual meeting of the International Society of Magnetic Resonance in Medicine, Toronto, 2015
    - Abstract 1: A Dixon method for positive contrast imaging of very small superparamagnetic iron oxide nanoparticles in MRI
    - Abstract 2: Dixon fat suppression for off-resonant water imaging of superparamagnetic iron oxide nanoparticles